

Charge, spin and orbital order in the candidate multiferroic material LuFe_2O_4

Von der Fakultät für Mathematik, Informatik und Naturwissenschaften der
RWTH Aachen University zur Erlangung des akademischen Grades
eines Doktors der Naturwissenschaften genehmigte Dissertation

vorgelegt von

Diplom-Physiker

Joost de Groot

aus Nordhorn, Deutschland

Berichter: Juniorprofessor Dr. M. Angst

Universitätsprofessor Dr. M. Wuttig

Tag der mündlichen Prüfung: 28. Juni 2012

Diese Dissertation ist auf den Internetseiten der Hochschulbibliothek online verfügbar.

Abstract

This thesis is a detailed study of the magnetic, structural and orbital order parameters of the candidate multiferroic material LuFe_2O_4 . Multiferroic oxides with a strong magneto-electric coupling are of high interest for potential information technology applications, but they are rare because the traditional mechanism of ferroelectricity is incompatible with magnetism. Consequently, much attention is focused on various unconventional mechanisms of ferroelectricity. Of these, ferroelectricity originating from charge ordering (CO) is particularly intriguing because it potentially combines large electric polarizations with strong magneto-electric coupling. However, examples of oxides where this mechanism occurs are exceedingly rare and none is really well understood.

LuFe_2O_4 is often cited as the prototypical example of CO-based ferroelectricity. In this material, the order of Fe valences has been proposed to render the triangular Fe/O bilayers polar by making one of the two layers rich in Fe^{2+} and the other rich in Fe^{3+} , allowing for a possible ferroelectric stacking of the individual bilayers. Because of this new mechanism for ferroelectricity, and also because of the high transition temperatures of charge order ($T_{CO} \sim 320$ K) and ferro magnetism ($T_N \sim 240$ K) LuFe_2O_4 has recently attracted increasing attention. Although these polar bilayers are generally accepted in the literature for LuFe_2O_4 , direct proof is lacking. An assumption-free experimental determination of whether or not the CO in the Fe/O bilayers is polar would be crucial, given the dependence of the proposed mechanism of ferroelectricity from CO in LuFe_2O_4 on polar bilayers.

This thesis starts with a detailed characterization of the macroscopic magnetic properties, where growing ferrimagnetic contributions observed in magnetization could be ascribed to increasing oxygen off-stoichiometry. The main focus is on samples exhibiting a sharp magnetic transition to long-range spin order at $T_N \sim 240$ K accompanied at $T_{LT} \sim 170$ K by a low temperature phase transition into a phase with glassy magnetic dynamics. It is proposed that this magnetic behavior best approximates the intrinsic defect-free behavior of LuFe_2O_4 . The spin structures of the long-range ordered phases could be refined properly by neutron diffraction as antiferromagnetic (AFM) and ferrimagnetic (fM) spin alignments. The two solutions exhibit a simple geometrical relation, where all spins in half of the bilayers change their sign. Furthermore, it is demonstrated that at T_N and $H=0$ competing AFM and fM spin structures, which correspond respectively to ferro and antiferro stacking of equivalently ordered bilayers, are nearly degenerate. The

observation of diffuse magnetic scattering in neutron diffraction far above T_N indicates the random stacking of still individually ferrimagnetic ordered bilayers.

The first crystal structural refinement, taking into account the superstructure due to the CO in LuFe_2O_4 , was performed on these stoichiometric samples with the help of a monoclinic unit-cell and the $C2/m$ symmetry. By clearly identifying the positions of Fe^{2+} and Fe^{3+} valences in this structure with the Bond Valence Sum (BVS) analysis, a completely new and unexpected CO pattern with charged Fe/O bilayers emerges. This new CO arrangement with charged, and consequently non-polar, bilayers is in strong contrast to all previously suggested CO configurations with polar bilayers. The implications of this result on “ferroelectricity from CO” in LuFe_2O_4 are discussed, addressing the possibility of polarizing the charged bilayers by an external electric or magnetic field, which could not be verified for our samples. In summary, a possible ferroelectric behavior of LuFe_2O_4 from CO is very unlikely. This is discussed in the light of the so far published work, where some doubt about the “ferroelectricity from CO” scenario is already present.

It is worth emphasizing that although the AFM-fM meta-magnetism has not been reported previously and may not be resolvable in the majority of LuFe_2O_4 samples, our results have strong implications for the general nature of magnetism in this material. Additionally, x-ray magnetic circular dichroism (XMCD) measurements are presented which could link the novel CO configuration with the previously determined spin order, further corroborating both the new CO pattern established by x-ray diffraction and the spin structures refined by neutron diffraction. Finally, the relevance of the strict spin-charge coupling to the CO transition is addressed and the possibility of an orbital ordered state in the low temperature phase is discussed.

Kurzfassung

Die vorliegende Arbeit beinhaltet eine detaillierte Studie der magnetischen, strukturellen und orbitalen Ordnungsparameter im möglicherweise multiferroischen Material Lutetium-Eisen-Oxid (LuFe_2O_4). Multiferroische Materialien, welche eine starke Kopplung zwischen der elektrischen und magnetischen Ordnung aufweisen, sind aufgrund des möglichen Einsatzes in zukünftigen Anwendungen der Informationstechnologie von besonderem Interesse. Da der herkömmliche Mechanismus für Ferroelektrizität mit dem für Ferromagnetismus inkompatibel ist, sind daher neue Wege zum Erreichen einer solchen Koexistenz beider Phasen nötig. Ein solcher Lösungsansatz wird in ladungsgeordneten Materialien gesucht, in denen bestimmte Valenz-Anordnungen ein ferroelektrisches Verhalten induzieren können; hier wird oft LuFe_2O_4 mit seiner Fe^{2+} und Fe^{3+} Separation ab $T_{CO} \sim 320$ K als das Musterbeispiel für ein solches Multiferroikum genannt.

Diese Arbeit beginnt mit einer ausführlichen makroskopischen Charakterisierung der magnetischen Eigenschaften verschiedener LuFe_2O_4 Kristalle. Es konnte eine wachsende ferrimagnetische Verunreinigung, welche in der Magnetisierung einzelner Proben beobachtet wurden, einem zunehmenden Sauerstoff Ungleichgewicht in der jeweiligen Probe zugeschrieben werden. Daher ist der hauptsächliche Fokus der vorliegenden Arbeit auf Proben gerichtet, welche einen scharfen magnetischen Übergang zu einer langreichweitigen magnetischen Ordnung unterhalb der Néel Temperatur von $T_N \sim 240$ K zeigen. Es wird diskutiert, dass dieses magnetische Verhalten dem tatsächlichen, magnetisch fehlerfreien Verhalten von LuFe_2O_4 am besten entspricht. Für Proben dieser Qualität konnte erstmalig detailliert das magnetische Phasendiagramm bestimmt werden, indem sich ein weiterer Phasenübergang in eine magnetisch stark inhomogene Phase bei $T_{LT} \sim 170$ K zeigt.

Die Spinstrukturen der beiden magnetisch langreichweitig geordneten Phasen konnten mittels Neutronenstreuung als antiferromagnetische (AFM) und ferrimagnetische (fM) Spinstrukturen identifiziert werden. Diese zwei Strukturen weisen eine erstaunlich einfache geometrische Relation zueinander auf. Diese ist dadurch gekennzeichnet, dass beim Anlegen eines externen magnetischen Feldes die Spinrichtungen der Eisenmomente in einer der beiden Eisendoppelschichten der AFM Struktur ihre Vorzeichen umkehren. Die AFM Struktur geht somit in die ferrimagnetische Struktur über. Die jeweilige Spinstruktur hängt also nur von der jeweiligen Stapelfolge ihrer Doppelschichten ab. Es wird gezeigt, dass bei T_N diese beiden konkurrierenden Lösungen, in der Abwesenheit von

externen magnetischen Feldern, energetisch entartet sind und sich somit oberhalb der magnetischen Ordnungstemperatur eine willkürliche Ausrichtung der Doppelschichtmomente ergibt, welche mittels diffuser Neutronenstreuung nachgewiesen werden konnte. Die Beobachtung dieser diffusen Streuung weit oberhalb von T_N zeigt eine mögliche Kopplung zur Ladungsordnung.

Die erste Kristallstrukturverfeinerung, welche die Überstruktureffekte aufgrund der Ladungsordnung in LuFe_2O_4 berücksichtigt, wurde an diesen stöchiometrischen Proben mithilfe einer monoklinen Einheitszelle und der $C2/m$ Symmetrie durchgeführt. Indem die Positionen der Fe^{2+} und Fe^{3+} Valenzen in dieser Struktur mit Hilfe der Bond Valence Sum Analyse (BVS) identifiziert wurden, taucht ein vollständig neues und unerwartetes Valenzmuster mit geladenen Fe/O Doppelschichten auf. Diese neue Anordnung mit aufgeladenen, und infolgedessen nicht polaren Doppelschichten, steht in starkem Kontrast zu allen bisher vorgeschlagenen Konfigurationen mit intrinsisch polaren Schichten. Die Auswirkungen dieser Erkenntnisse auf das „Ferroelektrisch aufgrund der Ladungsordnung“ Szenario für LuFe_2O_4 werden besprochen. Die Möglichkeit der elektrischen Polarisierung durch ein externes elektrisches oder magnetisches Feld wurde mittels Röntgenbeugung überprüft, konnte aber nicht für die im Rahmen dieser Arbeit untersuchten Proben verifiziert werden. Zusammenfassend ist ein mögliches ferroelektrisches Verhalten von LuFe_2O_4 aufgrund seiner $\text{Fe}^{2+/3+}$ Ladungsordnung sehr unwahrscheinlich, dieses wird angesichts bereits publizierter Arbeiten, in denen ebenfalls Zweifel am multiferroischen Verhalten von LuFe_2O_4 aufkommen, diskutiert.

Zusätzliche magnetische röntgen dichroismus Messungen zeigen eine strikte Kopplung zwischen der Ladungs- und der Spinordnung, welche selbst im Temperaturbereich oberhalb von T_N noch nachweisbar ist. Diese Kopplung bekräftigt die vorherigen Resultate der neuen Spin und Ladungsordnung. Zum Ende dieser Arbeit wird die Möglichkeit der Orbital Ordnung für Temperaturen unterhalb von T_{LT} diskutiert, bei dem keine endgültige Aussage im Rahmen der Messgenauigkeit für solch ein Szenario getroffen werden kann.

1	Introduction	1
2	Correlated electron systems	5
2.1	Ordering phenomena	5
2.1.1	Landau Theory of phase transitions	5
2.1.2	Structural transitions: Lattice order	7
2.1.3	Charge order	7
2.1.4	Orbital order	9
2.1.5	Magnetic order	11
2.1.6	Frustrated order	13
2.2	Coupled order phenomena	14
2.2.1	Magnetoelectric effect	14
2.2.2	Multiferroics	16
2.3	A brief history of LuFe_2O_4	18
3	Experimental Techniques & Theory	27
3.1	Magnetometry	27
3.1.1	DC magnetization	27
3.1.2	AC susceptibility	28
3.2	Scattering Theory	29
3.2.1	Reciprocal space and Bragg scattering	31
3.3	X-ray scattering	32
3.3.1	Crystal structure determination	33
3.3.2	Laboratory single crystal x-ray diffraction	36
3.3.3	6-ID-D: high energy x-ray diffraction	39
3.3.4	Resonant x-ray scattering	39
3.3.5	Polarization analysis in x-ray scattering	42
3.3.6	P09-beamline: full polarization analysis	44
3.3.7	SIM-beamline: soft x-ray magnetic scattering	45
3.3.8	X-ray magnetic circular dichroism	46
3.3.9	4-ID-C: X-ray magnetic circular dichroism	49
3.4	Neutron scattering	50
3.4.1	Nuclear scattering	51
3.4.2	Magnetic scattering	51

3.5	Neutron scattering experiments	53
3.5.1	DNS Diffuse Neutron Scattering instrument	54
3.5.2	D23 Neutron Diffraction	55
3.6	Sample preparation	55
3.6.1	Powder preparation of LuFe_2O_4	55
3.6.2	Single crystal growth	57
4	Macroscopic characterization of LuFe_2O_4	59
4.1	Huge variety in magnetic properties	59
4.2	New magnetic phases	63
4.2.1	Magnetic characterization: different phases in the vicinity of T_N .	63
4.2.2	Near degenerate magnetic phases just below T_N	65
4.2.3	A cluster state below T_{LT}	66
4.2.4	The magnetic phase diagram	71
4.2.5	The “Anomalous field heating effect”: stable disorder	72
4.2.6	Near-degeneracy & antiferromagnetic correlations above T_N . . .	74
4.3	Discussion and Conclusion	75
4.4	Related publications	77
5	The crystallographic structure describing charge order	79
5.1	Long range charge order in samples with reduced quality?	79
5.2	The crystal structure above T_{CO} : No long-range charge order	80
5.3	The monoclinic cell: Putting charge order in new clothes	84
5.3.1	Refining the monoclinic $C2/m$ crystal structure	86
5.3.2	From the refined structure to the CO pattern	91
5.3.3	Solving the structure in Cm -symmetry	95
5.3.4	Influence of electric fields on the charge order	96
5.3.5	Influence of magnetic fields on the charge order	101
5.3.6	The crystal structure below T_{LT}	104
5.4	Discussion and Conclusion	105
5.5	Related publications	107
6	Magnetic phases in LuFe_2O_4	109
6.1	Different magnetic orders for different phases	109
6.1.1	Pure magnetic $(00\frac{3}{2})$ -type reflections	109

6.1.2	New magnetic reflections from neutron scattering	111
6.1.3	Magnetic reflections along the $(\frac{1}{3} \frac{1}{3} \ell)$ -line	113
6.2	A new spin model for both magnetic phases	117
6.2.1	Antiferromagnetic spin order for the low- H phase	120
6.2.2	Ferrimagnetic spin order for the high- H phase	125
6.2.3	The AFM and fM spin structures	128
6.2.4	Magnetic fluctuations above the Néel Temperature	130
6.2.5	The spin structures and symmetry	133
6.3	A glassy transition at T_{LT} : towards disorder	135
6.3.1	The “Anomalous field heating effect”: stable disorder	138
6.4	Discussion and Conclusion	139
6.5	Related publication	140
7	Spin–charge coupling and the question of orbital order	141
7.1	X-ray magnetic circular dichroism	141
7.1.1	XMCD: probing the Fe^{2+} and Fe^{3+} local environment	142
7.1.2	Coupling between spin and charge order above T_N	146
7.2	The question of orbital order	147
7.3	Discussion and Conclusion	151
7.4	Related publications	151
8	Summary and outlook	153
	Acknowledgments	157
I	Appendix	179
A	Own contributions to published work	181
B	List of frequently used symbols and abbreviations	183
C	Relation between $R\bar{3}m(h)$ and $C2/m$ symmetry	185
D	Refinement of the 210 K data in Cm symmetry	189
E	Spin structure candidates	191
E.1	Selection of candidate spin structures	191

INHALTSVERZEICHNIS

F	Spin structure refinements	193
F.1	Refinements of the fM structure proposed in [1]	193
F.2	Refinements of candidate fM spin structures	193
F.3	Refinements of candidate AFM spin structures	194
G	Eidesstattliche Versicherung	195

Introduction

A rapid evolution of digitally stored information was achieved in the last half of the 20th century. This process started during the Second World War with the development of early computers, using vacuum tubes for calculations, punched tape for external storage and relays for internal data storage. The technological limits of such machines were rapidly reached, requiring new approaches. Consequently, the microelectronics century started in 1947 with the development of the first functional transistor, resulting in a continuous downscaling of electronic devices. This still ongoing process is described by Moore's law [2]. It predicts that the number of components in integrated circuits almost doubles every two years. To maintain this rate of development, electronic devices are now reaching the nanometer dimension, a size at which quantum-mechanical effects like electron tunneling appear [3]. Despite these effects, the absolute minimum of the smallest calculating unit is limited by the size of a single atom, making size reductions ad infinitum impossible. Nowadays, the focus of research is on classes of new materials where novel functionalities give rise to new applications, making a temporary downsizing of elements possible. The most prominent effect recently attracting considerable attention is giant magnetoresistance (GMR), observed simultaneously by P. Grünberg and A. Fert in 1988 [4, 5]. Their discovery was honored in 2007 with the Nobel Prize in Physics. So, different approaches for new devices utilizing novel materials are promising. This challenge of finding new materials that have functionalities which are useful in modern information technology is also addressed to solid-state physics.

In condensed matter physics, one scientific objective is, to understand and explain unusual phenomena identified in a large arrangement of interacting atoms. For example, the first theoretical explanation for superconductivity [6], by coupled pairs of electrons (the famous Cooper Pairs), was established in 1957, more than 45 years after the effect was first discovered in 1911 [7]. To interpret such new functionalities it is fundamental to

know the internal crystallographic structure, consisting of the crystal-symmetry and the atomic positions in the unit cell. A reliable structural refinement dealing with these topics is preferable before going into a more detailed analysis. To solve the crystallographic structure, laboratory single crystal x-ray diffraction has improved dramatically in the last decade, making a suitable refinement of complex crystal structures possible. Here, an interesting example is magnetite, the first magnetic material known to mankind. After centuries of scientific interest, the crystal structure below the Verwey-transition at 120 K is still unclear [8, 9] and widely debated.

Another important question before going into detailed study of particular samples is: “How good are my samples?”; for most systems, the answer can be achieved through laboratory experiments. In **Sec. 4** of this thesis, it will be shown, how important an appropriate pre-characterizations is in the case of the material studied in this thesis, LuFe_2O_4 . Through purely magnetic characterizations, new magnetic phases (especially two long range magnetically ordered phases) could be identified in samples which exhibit the best quality behavior in magnetism. Furthermore, the magnetic phase diagram for this kind of sample could be established, intrinsically exhibiting an explanation for some anomalous magnetic behavior observed 20 years ago for this material.

For the charge ordered phase, the crystallographic structure of high quality crystals could be solved in **Sec. 5** within a new monoclinic unit-cell which is consistent with representation analysis. Here, a totally new and unexpected charge order (CO) configuration with charged bilayers is identified. This arrangement is incompatible with the mechanism for ferroelectricity proposed in the literature for this material. Furthermore, in contrast to what was previously assumed, this novel and non polar CO configuration is also stable under high external electric and magnetic fields.

In **Sec. 6**, the two long-range ordered spin structures of LuFe_2O_4 , each separately present in a magnetic phase, could be solved with the help of neutron and soft x-ray diffraction. These two spin-structures exhibit a surprisingly simple geometrical relationship to each other, allowing for a random stacking of still magnetically ordered layers far above the magnetic long-range order temperature. Furthermore, both phases seems equal in energy at the ordering temperature and zero magnetic field, allowing for a novel mechanism for metamagnetic materials based on geometrical frustration.

Finally, in **Sec. 7**, the relationship between spin and charge order could be identified with the help of x-ray magnetic circular dichroism measurements. The evidence of a significant unquenched angular magnetic moment contribution excludes the possibility

of long-range orbital order for both long-range magnetic ordered phases. Since there is a magneto-structural phase transition present at T_{LT} , this exemption is not valid for low temperatures phase. Therefore, the possibility of orbital order is probed by polarized soft x-ray diffraction in the low temperature phase.

Correlated electron systems

Correlated electron systems are an example of complex materials [10] where the electrons interact strongly with each other. For this class of materials, a huge variety of at first unexpected behavior is summarized in the terminology of novel functionalities. Examples for these properties are high T_C superconductivity [11], colossal magnetoresistance (CMR) [12, 13], multiferroic behavior [14, 15] and many more. Most of these functionalities are often technologically useful [16] or on their way to being applicable. They can be explained by electronic ordering processes like charge, spin and orbital order (see Sec. 2.1), though many of these properties are still not fully understood. For example, what drives the pairing in the high- T_C superconductors is still in much debate 25 years after their discovery (in conventional superconductors the repulsive electrostatic electron electron interactions can be compensated by the coupling of two electrons via a phonon to a Cooper-pair, leading to superconductivity at low temperatures only). Some complex transition-metal oxides show multiple functionalities simultaneously present in one physical phase, making them a part of the class of multifunctional materials (see Sec. 2.2). An interesting class of multifunctional materials are the so called multiferroics which show multiple ferroic behavior, for example ferroelectricity and ferromagnetism, in one single phase.

2.1 Ordering phenomena

2.1.1 Landau Theory of phase transitions

The existence of a phase transition can only be detected (in many cases) from the observation of subtle changes in physical properties. At least one property has to differ between the two distinguishable phases separated by the phase transition. We can distinguish between two different ways these transitions can take place, depending on how the derivatives of the free energy F from the system behave.

- First order phase transitions: Transition occurs as an abrupt (discontinuous) change in symmetry, leading to enthalpy (latent heat) and volume jumps. Here, the primary derivatives of the free energy will have a jump at the transition point.
- Second order phase transitions: The symmetry is changed in a continuous way. In temperature-driven structural transitions the symmetry of the low-temperature phase is usually a subgroup of the high-temperature phase. For such a transition, the second derivatives from the free energy, for instance the specific heat, will have a jump.

Generally expressed, the order of a transition is the degree of the derivatives from the free energy F with a jump at the transition point. Landau's idea [17] was that the free energy describing the system could be described in good approximation as a Taylor approximation, as a function of the order parameter η close to the transition point T_c . This description of the thermodynamic potential is a more phenomenological approach, but such theories are very useful to explain experimental results. The phase transition itself can be first or second order, depending on whether the first or second order derivative of the thermodynamic potential with respect to the ordering parameter has a discontinuity. Below, we will discuss the second-order phase transition.

$$F(P, T, \eta) = \Phi_0 + \alpha\eta + A\eta^2 + C\eta^3 + B\eta^4 + \dots \quad (2.1)$$

In Eq.(2.1) the coefficients are functions of P and T . If the states with $\eta = 0$ and $\eta \neq 0$ are different due to the underlying symmetry, the terms linear in η for Eq.(2.1) vanishes. Only the powers of η which are invariant with respect to the symmetry are thus allowed to be present in the $\Phi(\eta)$ polynomial.

If we now consider the onset of magnetic order, we have to consider that by assuming time reversal all spins will change their direction $\vec{S}_i \rightarrow -\vec{S}_i$, leaving the total free energy unchanged. This symmetry is preserved (the Hamiltonian will not change) by using only the even powers in Eq.(2.1):

$$F(P, T, \eta) = \Phi_0 + A\eta^2 + B\eta^4 + \dots \quad (2.2)$$

We know that above T_C the order parameter η vanishes, and below T_C it has some finite value. The value of η should be $\eta \neq 0$ below T_C and 0 for temperatures above. The simplest choice to realize such a case is $A(P, T) = a(T - T_C)$ and $B(P) > 0$, which will give a finite value of η below T_C . It is assumed that the potential is transformed to:

$$F(P, T, \eta) = \Phi_0 + a(P) (T - T_c) \eta^2 + B(P)\eta^4 \quad (2.3)$$

By minimizing the Free energy, Eq.(2.3) will become:

$$\frac{\partial F}{\partial \eta} = 0 \Rightarrow \eta^2 = \frac{a(T_C - T)}{2B} \text{ for } (T < T_c) \text{ and } \eta = 0 \text{ for } (T > T_c) \quad (2.4)$$

So for a second order phase transition the order parameter η will be proportional to $\propto (T_C - T)^{\frac{1}{2}}$ below T_C , with the above assumptions.

Influence of external fields to the phase transition

The influence of an external magnetic field H on a phase transition involving ferro/ferromagnetic states can also be calculated with the Landau theory [17]. The external field will introduce a small perturbation of $-\eta HV$ to the free energy, where V is the volume of the magnetic sample. With this linear extension to the Eq.(2.2), the phase transition will blur out more into the temperature region above the phase transition, for increasing magnetic fields.

2.1.2 Structural transitions: Lattice order

At a structural phase transition, the symmetry of the crystal will change. A characteristic of most phase transitions is that in one phase, some of the symmetry elements of the high-symmetry phase are broken. As discussed in the previous section 2.1.1, there are two different types of structural phase transitions. For a second-order phase transition, the symmetry is lowered and the resulting symmetry is usually a subgroup of the original space group [18].

2.1.3 Charge order

Charge order (CO) occurs in a compound when the specific valence of an element on one particular crystal side is not equally distributed. To achieve this, the average valence is in most cases not an integer value, and consequently, below the charge order temperature T_{CO} the charges will start to localize on sites which were previously equivalent, leading to a disproportionation and a super-lattice due to symmetry lowering. For such a scenario, the intensity of superstructure reflections, which appear due to symmetry lowering, is the order parameter η for the more fundamental valence separation. When the charge ordering scheme breaks spatial inversion symmetry a net electric polarization can be achieved (for details, see Sec 2.2.2). One of the most famous examples, and also the first where a charge order was predicted, is magnetite Fe_2O_3 ; below the Verwey-transition $T_V=120\text{ K}$ the Fe valences on the B site¹ starts to order into more Fe^{2+} and Fe^{3+} -like

¹Magnetite crystallizes in an inverse cubic spinel structure with two different iron sites.

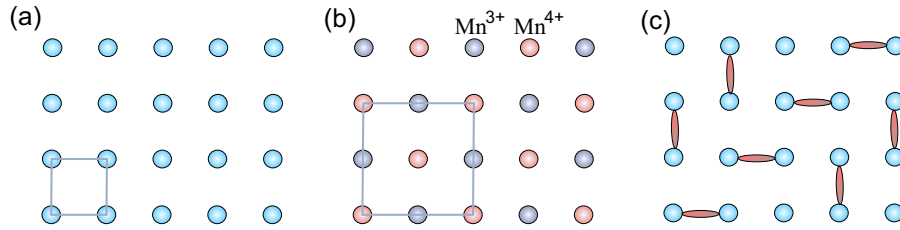


Abbildung 2.1: (a) A layer of manganese atoms, (a) before charge order and (b) after checkerboard charge ordering has taken place. The blue ions in (a) all have the same valence of $\text{Mn}^{+3.5}$. The black line in (b) indicates the charge order unit cell, which in (a) corresponds to the crystallographic unit cell. In (c) the charge order is described as a Zener-polaron state [22] is presented.

valences. Due to the strong geometrical frustration and complex micro-domain formation, the exact charge ordering pattern [19] and the relation to the observed ferroelectricity [20] is still under debate.

Other well studied systems are the half doped manganites $A_xB_{1-x}\text{MnO}_3$, where A is a trivalent ion (like Bi, La, Pr, Sm, Y) and B is a divalent alkaline rare-earth element. The ratio between Mn^{3+} and Mn^{4+} , and thus the charge order pattern, depends strongly on the doping level. Here, a content of $x=0.5$ means, that half of the Mn ions are formally Mn^{3+} and the other half Mn^{4+} . Based on diffraction experiments, two models have been proposed for the charge order, conventional checker-board-like charge ordering [21] in Fig. 2.1a and bond centered charge order, described as Zener-polaron states Fig. 2.1c [22]. The debate over the right model to describe the order has still not been settled.

The ionic character of a charge ordered system is usually not in the range of integer valence states. For example, in Fe_2O_3 the valence separation is only 0.1 from the mean valence of 2.5 on the charge ordering sites [23]. In $\text{EuBaFe}_2\text{O}_5$ one observed 0.68 valence units of charge separation on the average $\text{Fe}^{2.5+}$ valence [24]. An interesting example, where a very strong integer ionic character of the observed Fe valences in the CO pattern is observed, is Fe_2OBO_3 [25, 26]. Here, the sharp valence separation is explained by the fact that B is more electronegative than Fe; consequently, the O prefers to share its electrons with B, resulting in more ionic Fe-O bonds. The class of charge ordered materials this thesis deals with are the $R\text{Fe}_2\text{O}_4$ systems, where R is a rare-earth ion for these compounds. In these systems the iron valences orders on a frustrated triangular arrangement. Here pyroelectric measurements [27] indicate a possible net electric polarization, making this compound a candidate for multiferroicity. For further details on this see e.g. Sec. 2.3.

Detection of charge order

There are different approaches to detect charge order and to determine the valence separation. Three of the most common methods are presented here.

- In Mössbauer spectroscopy the nuclear energy levels, which also depend on the electronic and magnetic environments, are probed. From refined spectra, the isomer shift, quadrupole splitting and magnetic splitting can be obtained. The isomer shift is proportional to the surrounding charges and thus the valence (see e.g. [28]). With this method only a valence separation is detected, so no direct probe of the charge order distribution is possible.
- Resonant x-ray scattering/spectroscopy: This technique can measure the energy shifts for particular element-specific transitions of different valence states in x-ray absorption spectroscopy [29, 30]. By comparing the observed energy shifts with simulations, the particular valence separation of the element can be deduced [31].
- The Bond Valence Sum analysis (BVS) [32, 33] is useful to determine the valences of each atomic site of a properly refined crystal structure. Due to the fact that the electro-static force between a cation and an anion is different for different cation valences, a bond shortening or lengthening is observed. The valences V can be calculated by the sum over all surrounding ligands:

$$V = \sum_i \exp[(d_0 - d_i)/0.37] \quad (2.5)$$

Here, d_i is the experimental bond length to the surrounding ions and d_0 a tabulated empirical value characteristic of the cation-anion pair.

The BVS method is a unique tool which directly relates the observed valence to a particular crystallographic side. The other two are spectroscopy methods, and give only an element-specific valence separation.

2.1.4 Orbital order

The 3d-shell of the transition metal oxides and its five different d -wave functions² (see Fig. 2.2) provides an additional degree of order, which makes the underlying electronic structure more complicated. To understand the concept of orbital order we first discuss the case of an isolated atom with no surrounding ligand atoms. For this case, the five

²The five orbital states can be chosen with a linear combination of spherical harmonics, that they are all real functions.

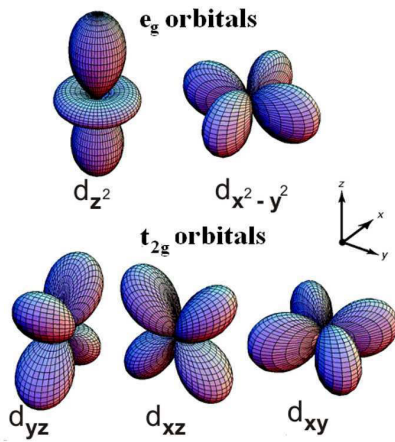


Abbildung 2.2: The 3d-orbitals of the transition metal elements are of five types. Picture taken from [34].

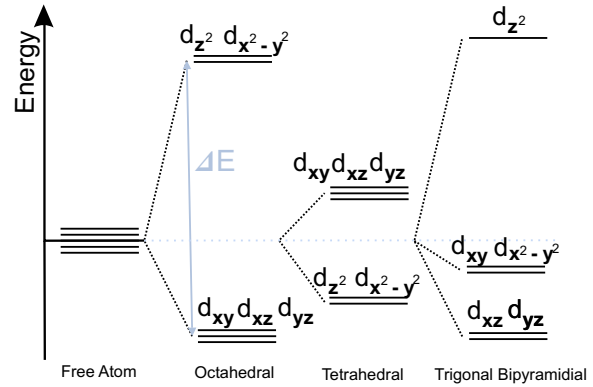


Abbildung 2.3: The crystal field splitting of the 3d orbitals for several surrounding coordinations. The relative values for the octahedral and tetrahedral coordination are approximate in [35]. The splitting for the trigonal bipyramidal coordination is taken from [36].

wave functions are degenerated [35] (see Fig. 2.3), since there is no perturbation involving the energy states of the particular orbital. When the element is embedded in a ligand environment (typical ligands are oxygen atoms), different surroundings are possible. Consequently, the symmetry of the system is lowered in the crystal, resulting in the splitting of the degenerate orbital states [18] into irreducible representations (see Sec. 2.1.5). The reason for this can readily be understood by having a look at the shapes of the orbitals and their environments: for most crystal ligand fields (octahedral, trigonal pyramidal) the spheres of the d_{z^2} orbitals of Fig. 2.2 are pointing towards a ligand atom. This increases the orbital energy and is thus unfavorable for electrons. For the different surroundings, the expected crystal field splitting ΔE is shown in Fig. 2.3; the energy for this splitting is typically in the range of ~ 1 eV. However, it strongly depends on the central atom and ligand geometry. As for the charge ordering in Sec. 2.1.3, it is also possible to develop a long-range ordered pattern of occupied orbitals. When both charge and orbital order are simultaneously present, only those valences with degenerate electronic states can develop orbital order.

This is the case for the half doped manganites $\text{Pr}_{0.5}\text{Ca}_{0.5}\text{MnO}_3$ [37] with an average $\text{Mn}^{3.5+}$ -valence. Here, only the Mn^{3+} is able to develop an orbital order in the charge ordered phase, due to its orbital degeneracy. The orbital order is usually in cooperation with the Jahn-Teller effect. This can be explained, on the one hand, by the fact that orbital states with lower energy are preferentially occupied. On the other hand, however,

orbital ordered systems are expected to be Jahn-Teller distorted (to the lattice) systems as well, so both effects are pointing in the same direction. A prominent example of orbital order is LaMnO_3 [38], which has a distorted perovskite structure, where the cooperative Jahn-Teller distortion [39] elongates the octahedra in the ab -plane in alternating crystal directions. This lifts the degeneracy of the half filled manganese e_g orbitals (see Fig. 2.3), leading to the observation of orbital order below 750 K. The origins of these orbital order transitions are of various natures and still under debate [40]. The scenario of a ferro-like orbital order also exists, for instance in YBaMn_2O_6 [41]. In such a material all orbitals are aligned in the same crystallographic direction, for diffraction resulting in the absence of additional superstructure reflections.

2.1.5 Magnetic order

The magnetic interaction responsible for the formation of (anti)ferromagnetic spin arrangements on a lattice can be described by the Heisenberg model, with the following Hamiltonian.

$$H = -\frac{1}{2} \sum_{i,j} J_{ij} \vec{s}_i \vec{s}_j - \vec{H} \sum_i \vec{s}_i \quad (2.6)$$

Here, the direction of individual spins \vec{s}_i can point in all directions. For a system with sufficiently high magnetic anisotropy the quantization axis will basically be in one direction, and the spins will prefer this easy axis direction upon magnetization. Such a case is described in the Ising spin model, where $\vec{s}_i = \pm 1$ can only point in two discrete directions along the easy axis of the spin system. In both the Heisenberg model and the Ising-model, the remaining magnetic spinstructure depends strongly on the coupling constants J_{ij} , with a resulting antiferromagnetic and ferrimagnetic spin arrangement for $J_{ij} > 0$ and $J_{ij} < 0$, respectively. To describe the observed spinstructure with Ising spins properly, it is important to know the exact magnetic correlations between different sites. For example, the interaction between nearest neighbors can be FM, but AFM between next nearest neighbors, resulting in complicated spin structures. The macroscopic magnetic ordering temperature, the so-called Néel temperature T_N , is observed in magnetization measurements and the underlying spin structure, and thus the magnetic correlations, can be investigated with unpolarized and (half)polarized neutron diffraction experiments (see e.g. Sec. 3.4).

Magnetic anisotropy

The magnetic order in most samples is not isotropic in all directions, so the magnetization tends to lie in certain preferred directions. This can be easily seen by measuring magnetization curves along different crystal directions or by measuring the torque of a sample with varying magnetic-field directions. This magnetic anisotropy, even in an applied magnetic field \vec{H} , originates from inter magnetic dipole-dipole interaction, the shape of the crystal, and spin orbit coupling. In the case of spin orbit coupling, the orbital magnetic moments are coupled via the electron orbital moments to the crystal field. This crystal field depends on the surrounding ligand atoms (see Sec. 2.1.4), which for their part are connected to the crystal structure (lattice). Here, the easy axis of magnetization points along the crystal direction with the largest component of the orbital magnetic moment L (lowest spin orbit energy) [36, 42]. For elements with unquenched orbital magnetic moments, this spin orbit coupling can lead to strong anisotropy energy in magnetization. The spin orbit coupling is a relativistic effect which becomes larger for heavier elements [43].

Spin and orbital contributions of Fe^{2+} and Fe^{3+}

Natural unoxidized iron has the electron configuration of $[\text{Ar}]3d^64s^2$. For the two important oxidation states Fe^{2+} and Fe^{3+} first the $4s$ electrons are lost. This leads to 6 and 5 d -electrons respectively. Because of the Hund's rule, all states of $3d$ -states for the Fe^{3+} valence are half filled, leading to no possible orbital moment and an expected spin moment of $5\mu_B$. For the Fe^{2+} valence the expected spin moment is $4\mu_B$. The orbital moment for this state differs strongly, depending on the interaction with the lattice. In the case of LuFe_2O_4 a strong unquenched orbital moment is reported for Fe^{2+} [36, 44].

Representation analysis

Sec. 2.1.1 discussed how the magnetic phase transition changes the symmetry of the crystal; we could show how the order parameter η changes across the transition. A logical question is, what symmetry changes for a second-order phase transition are allowed. To answer this we first have to point out that the crystal studied belongs to the space group with symmetry elements g_i . These symmetry elements transform the crystal into itself under all operations of the particular space group, and thus the physical properties are invariant under these transformations. Groups in which the time-reversal operator forms

group elements are called magnetic space groups, and the corresponding point groups are called magnetic point groups³.

The analysis of magnetic structures by group theory (representation analysis) [45, 46, 47] is based on the transformation of spins on a given lattice. The site-specific symmetry operations of a crystallographic space group G or a subgroup G_k of the crystal in which the magnetic order is introduced [18] (so above the phase transition) are important for the possible spin arrangement below the magnetic transition. Representational analysis allows the determination of the magnetic structures allowed by the symmetry that can result from a second-order magnetic phase transition (see Landau theory Sec. 2.1.1). The first step in the analysis is the identification of the propagation vector k associated with the phase transition. Usually, the propagation vector is associated with the development of additional peaks in reciprocal space, indicating a bigger periodicity of the magnetic structure. If the magnetic unit cell is identical to the magnetic structure, as in the case of a simple ferromagnet, a $k = (000)$ propagation vector is observed. After finding the right propagation vector the space group symmetry elements g_i are determined, which leave the propagation vector k of the magnetic order invariant. These sets of operations form the subgroup G_k . The magnetic representation of a crystallographic site can then be decomposed in terms of the irreducible representations Γ^μ of G_k :

$$\Gamma_{Mag} = \sum_\nu n_\nu \Gamma_\nu^\mu \quad (2.7)$$

In Eq.(2.7), n_ν is the number of amounts of the particular irreducible representation Γ^μ which is necessary to explain the magnetic order Γ_{Mag} for one specific crystallographic site. The representation analysis is discussed in this section for magnetic transitions, which change the symmetry of a crystal structure. However, this approach is also valid for all other second order phase transitions that change the symmetry. For such a second order phase transition, all sites must order according to one single irreducible representation Γ^μ , in contrast to a first-order transition, where different sites can order according to diverse representations.

2.1.6 Frustrated order

Frustration generally refers to the hindrance of a specific target-oriented action with the physical states resulting from this constraint. The special case of geometrical frustration arises, for example, on a triangular lattice where neighboring atoms have a negative

³A list of these magnetic groups with their subgroups can be found in [18].

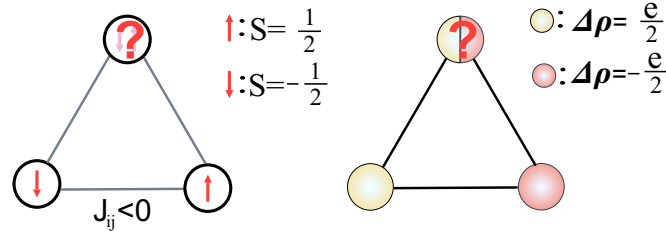


Abbildung 2.4: Spin frustration vs. charge frustration on a 2D hexagonal lattice. The antiferromagnetic ordering will lead to no clear solution \uparrow or \downarrow for the third site on the triangle. A similar case is also possible for the charge order. Figure adopted from [52].

exchange, as shown in Fig. 2.4. In such a system only two of the three spins can be simultaneously aligned anti-parallel on this lattice, according to their exchange interaction. The third spin state is frustrated in its arrangement. This situation is called geometrical magnetic frustration. In such a system, exotic ground states for the spin order can be found, such as spin glasses (spins freeze in a random pattern) [48] and spin liquids (spins remain fluctuating down to temperatures near absolute zero) [49]. It is also possible that, instead of glass or liquid magnetic behavior, a long range ordered phase is established, but often at much lower temperatures than expected from the interaction strength [50, 51] and with very complex and competing magnetic phases. Similar frustration effects are also possible for a charge order scheme on a triangular lattice, as shown in Fig. 2.4.

2.2 Coupled order phenomena

2.2.1 Magnetoelectric effect

The simultaneous presence and dynamic coupling of electricity and magnetism is already proposed by the Maxwell equations, which links both behaviors with a linear term. This coupling can be explained by the Landau theory, where the free energy F is calculated from both electric \vec{E} and magnetic field \vec{H} contributions. For a non-ferroic material, showing no hysteresis in both magnetization and electric polarization, the free energy can, according to [14], be written as:

$$F(\vec{E}, \vec{H}) = F_0 - P_i^S E_i - M_i^S H_i - \frac{1}{2} \epsilon_0 \epsilon_{ij} E_i E_j - \frac{1}{2} \mu_0 \mu_{ij} H_i H_j - \alpha_{ij} E_i H_j - \dots \quad (2.8)$$

Here, P^S and M^S are the spontaneous sample polarization and magnetization, ϵ and μ the electric and magnetic susceptibility in linear dependence. The tensor α_{ij} describes cross coupling between sample magnetization arising from an applied electric field and

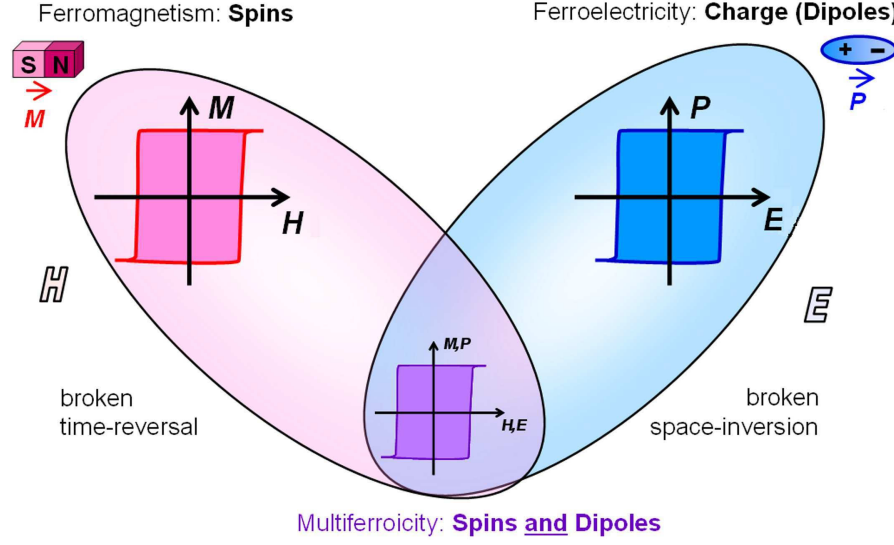


Abbildung 2.5: The control of the sample magnetization \vec{M} and electric polarization \vec{P} by an external magnetic field \vec{H} and electric field \vec{E} . In a ferroic material \vec{P} and \vec{M} arise spontaneously as ferromagnetism and ferroelectricity, indicated by their hysteretic behavior. In a multiferroic, the coexistence of at least two ferroic orders can lead to possible additional interactions. In a magnetoelectric multiferroic, a magnetic field control \vec{P} and an electric field control \vec{M} are achieved (crossing area).

vice versa. This can be seen by calculating the sample polarization and magnetization when minimizing the free energy F .

$$P_i(\vec{E}, \vec{H}) = -\frac{\partial F}{\partial E_i} = P_i^S + \epsilon_0 \epsilon_{ij} E_j + \alpha_{ij} H_j + \dots \quad (2.9)$$

$$M_i(\vec{E}, \vec{H}) = -\frac{\partial F}{\partial H_i} = M_i^S + \mu_0 \mu_{ij} H_j + \alpha_{ij} E_i + \dots \quad (2.10)$$

This coupling effect, which is in first order linear in \vec{H} and \vec{E} , is called the magnetoelectric effect (ME). The strength of the coupling is limited by the upper value of the magnetoelectric susceptibility with: $\alpha_{ij} < \sqrt{\epsilon_0 \epsilon_{ii} \mu_0 \mu_{ii}}$ [53], as observed in different materials like Cr_2O_3 [54] and other antiferromagnetic crystals [55]; but the observed coupling is much too weak for potential applications. Higher orders of coupling are also possible in Eq.(2.10), where the functionality is not linear. It thus appears that the chances of finding substances with large magnetoelectric susceptibilities will be better in ferromagnetic than in antiferromagnetic materials. In order to achieve a stronger coupling, ferromagnetic and/or ferroelectric materials exhibiting sufficiently high ϵ_{ii} and μ_{ii} need to be considered. This will be done in the next chapter.

2.2.2 Multiferroics

The term multiferroics refers to the simultaneous presence (in one phase) of multiple ferroic orders [56], like any type of long-range magnetic order (e.g. ferro- or antiferromagnetism), spontaneous electric polarization (ferroelectricity), and/or ferroelasticity, as shown in Fig. 2.5. Here the word *ferro* (from the Greek word for iron) implies a stable and switchable non-vanishing macroscopic moment/polarization in zero magnetic/electric field. Often, the term is also used to indicate antiferromagnetic and spin-spiral orders, which couple with ferroelectric behavior. The first, brief work on this kind of material was done in the late 1950s by [54]. Over the last ten years, multiferroics have generated much more interest due to their possible application in novel storage devices [16]. Recently, new models were established [57, 58] to understand the underlying coupling mechanism, especially between the magnetic and electric orders. This coupling between different ferroic order parameters holds great potential for future information technology applications [16], e.g. for non-volatile information storage. Here the most interesting materials are magnetoelectric materials in which a coupling between magnetic moments and electric polarization is present [14]. As in superconductivity, the aim of ongoing research to obtain a coupling observable at room temperature or even higher (but for both this is not reached). To this day, the quantity of discovered materials exhibiting multiferroic behavior is small; by further limiting this to coupled multiferroics, only a handful remain. The existence of ferromagnetism and ferroelectricity in the same phase, in their conventional form, is a contradiction, because the traditional mechanism for ferroelectricity is incompatible with ferromagnetism [59]. This is because, according to the Hund's rules, partially filled d -shells with uncompensated spin moments are required for magnetism in transition-oxide-metals. Regretfully, however, these d electrons reduce the tendency for off-center polar distortions, which are necessary for ferroelectricity [60].

Other paths towards multiferroicity therefore needed to be explored: in *proper multiferroics* the ferroelectricity is driven by hybridization and covalency or other purely structural effects. Here the elements with empty d shells have the ability to create a distortion through a strong hybridization with the surrounding ligand atoms. The unequal bonds to ligands produce dipoles, which results in a net electric polarization. This hybridization is strongest for empty shells, making a strong coupling to magnetism difficult. In proper ferroelectric materials, for example BiFeO_3 [61, 62], the order parameter of the phase transition is thus ferroelectricity itself.

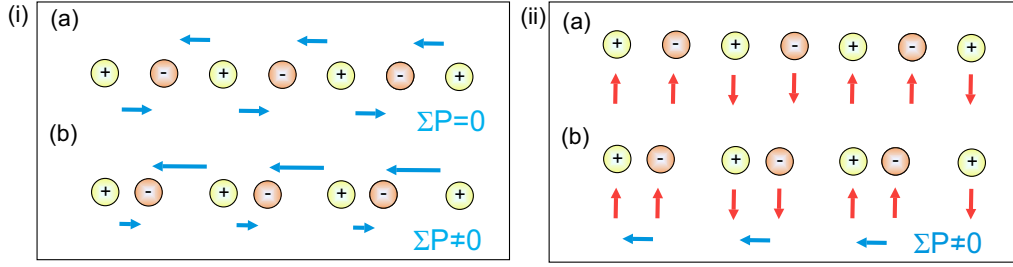


Abbildung 2.6: (i) Example of a neutral one-dimensional chain exhibiting charge ordering. The blue arrows indicate the polarization direction, which is zero for the site centered charge order in (a) but non-zero for the charge order configuration in (b). (ii) Effect of magnetostriction, shortening (in this example) the ferromagnetic bonds, producing a ferroelectric polarization. Figure based on [68].

In *improper multiferroics* the electric polarization appears as a consequence of, or emerges concomitantly with, some other kind of order. For example, in TbMnO_3 the spontaneous electric polarization is driven by an incommensurate helicoidal spin density wave breaking inversion symmetry [58], and thus the electric polarization is intrinsically coupled to the magnetic order [63]. But for this mechanism only weak polarizations are possible due to the reliance on a relativistic effect [64]. For the example of TbMnO_3 presented here, the order parameter indicating ferroelectricity is thus magnetic spin order. In *geometrically-driven ferroelectrics* the ferroelectricity is obtained by a lattice distortion inducing local dipoles. This approach allows for high transition temperatures (e.g. 700K for YMnO_3 [65, 66]) and is coexistent with magnetism by partially filled d shells (like BaNiF_4 [67]); however, the achievable electric polarization is not as high as it is for the case of empty d shells.

Here, a special group of possible multiferroics will be discussed in which the ferroelectricity is caused by a *charge ordering* (CO) process in materials with mixed-valence sites [68]. This class of systems is currently attracting increasing attention, due to the fact that particular charge order configurations can possibly cause enhanced ferroelectricity in magnetic materials. Here, both charge and magnetic occur on the same atomic sites, which could allow for a strong magnetoelectric coupling. As of yet, examples of this new mechanism are extremely rare, and none of the candidate materials is well-understood.

In order to achieve a multiferroic state established by CO, two different scenarios presented in Fig. 2.6, are likely: (i) In a structure where, on different sites, for one type of atom different valences are present, only an antiferroelectric arrangement with no net electric polarization is possible, as long as the charge order does not break spatial inversion symmetry. These antiferroelectric behavior stop when inversion symmetry

is broken, allowing for a net ferroelectric polarization. In such a structure an additional magnetic order on the charge ordered ions is possible. (ii) The spatial inversion symmetry can also be broken by magnetostriction. Here, the presence of inequivalent magnetic ions with different charges is required. With different magnetostriction for antiferromagnetic than for ferromagnetic neighboring ions the spatial inversion symmetry is broken by atomic displacements, and a net electric polarization is achieved. In such materials an additional magnetic order on the different charged ions is required; an example of such a material is $\text{Ca}_3\text{CoMnO}_6$ [69].

In all multiferroic materials found to date know the observed spontaneous ferroelectric polarization is rather small compared with that of conventional ferroelectrics like BaTiO_3 [70, 71]⁴. To find materials that exhibit a sufficiently strong coupling between high net magnetic moments and electric polarizations, which are applicable in storage devices at room temperature, is a challenging task.

Symmetry constraints for Multiferroics

An interesting aspect of multiferroicity is that to achieve both ferroelectricity and ferromagnetism certain crystal symmetries need to be broken. On the one hand, only structures breaking spatial inversion symmetry have the ability to produce a charge imbalance in their structure, leading to a net electric dipole. On the other hand, ferromagnetism, which is produced by the orientation of all or a couple of spins in field direction, is not consistent with time reversal symmetry, due to the fact that time reversal changes the spin direction. Therefore, in multiferroic materials both space-inversion and time-reversal symmetry must be violated.

2.3 A brief history of LuFe_2O_4

In the wide field of strongly correlated electron systems Lutetium ferrate (LuFe_2O_4) is one of the most studied materials because of its possible multiferroic behavior based on the order of the Fe^{2+} and Fe^{3+} valences. LuFe_2O_4 belongs to a class of hexagonal layered materials, generally expressed by $R\text{Fe}_2\text{O}_4$ (R : rare-earth metal) [72, 73, 74, 75] and it is a candidate for room temperature multiferroics based on charge order (CO).

This compound was first synthesized in 1974 as a powder sample by Kimizuka *et al.* [72] under a mixed CO_2/H_2 atmosphere, in order to control the oxygen stoichiometry. The structural phase diagram at 1200°C was established in 1976 by Sekine *et al.* [76]. This

⁴In BaTiO_3 a spontaneous ferroelectric polarization of $80\mu\text{Ccm}^{-2}$ is observed.

phase diagram already indicated a strong influence of the oxygen partial pressure on the sample lattice during synthesis, which could be linked to different oxygen stoichiometry δ in the $\text{LuFe}_2\text{O}_{4-\delta}$ powder. The crystal structure with its atomic distributions was first solved in 1990 by Isobe *et al.* [77] on the single crystals available at that time from [78]. This refinement result is presented in Fig. 2.7; it shows, similar to other materials of the $R\text{Fe}_2\text{O}_4$ class [72], a rhombohedral $R\bar{3}m$ symmetry⁵. Each unit cell contains three sets of

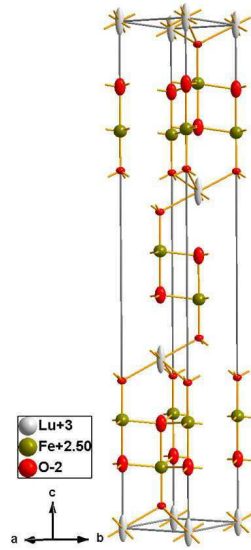


Abbildung 2.7: The high temperature hexagonal crystal structure of LuFe_2O_4 taken from [77]. The anisotropic thermal ellipsoids are shown for each atom. The corresponding lattice parameters in hexagonal representation are $a_{\text{Hex}}=3.4406(1) \text{ \AA}$ and $c_{\text{Hex}}=25.28(1) \text{ \AA}$.

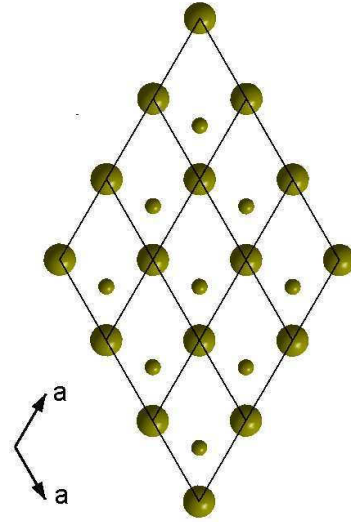


Abbildung 2.8: One iron double layer with a projection along the layer in hexagonal setting. The smaller atoms are positioned in the lower Fe layer.

Fe bilayers, arranged in a triangular pattern and separated by a single triangular lutetium layer. These individual Lu layers make the inter-bilayer Fe distance small compared to the distance between separate double layers. Another important aspect, obtained by the single-crystal refinement, is the large thermal displacement parameter for the Lu atoms in the U_{33} direction. This unusual displacement was already mentioned by Isobe [77]; it can readily be seen in Fig. 2.7 as needle-like displacements for Lu along the c_{Hex} direction.

At that time several reports with magnetization and neutron diffraction measurements showed a very rich magnetic behavior for LuFe_2O_4 . For a temperature range between

⁵The primitive rhombohedral cell is represented in this thesis by the hexagonal notation, as long as not mentioned otherwise.

180 K and 220 K, a highly anomalous field heating effect was observed [79], where the magnetization measured after heating to a temperature in a constant magnetic field is much larger than that measured by the application of the same field after heating to the same temperature in zero field. This highly anomalous effect could not be properly explained until now. In high magnetic field measurements at low temperatures [80, 74], the observed saturation moment suggested a 2:1 ferrimagnetic spin structure with giant coercive fields up to ~ 10 T, in order to switch the magnetization direction. This measurement also indicated a firm magnetic anisotropy with Ising spin behavior along the crystallographic c_{Hex} direction. In the magnetic phase below $T_N \sim 220$ K, a ferrimagnetic cluster state was proposed by Mössbauer spectroscopy methods in combination with neutron diffraction, where a strong Ising spin behavior but no long-range 3D magnetic order could be detected down to 4.2 K [81, 75].

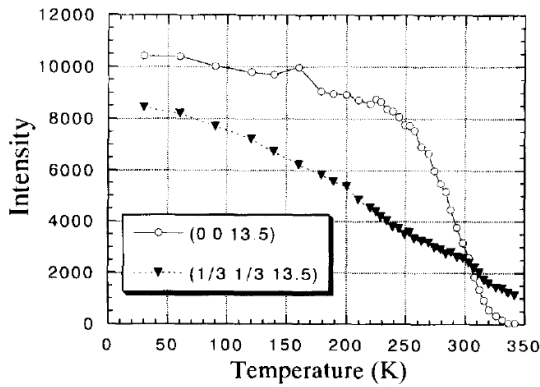


Abbildung 2.9: The temperature variation of the intensity of the two superstructure reflections $(0\ 0\ \frac{1}{3}\ 5)$ and $(\frac{1}{3}\ \frac{1}{3}\ \frac{1}{3}\ 5)$. Figure taken from [82].

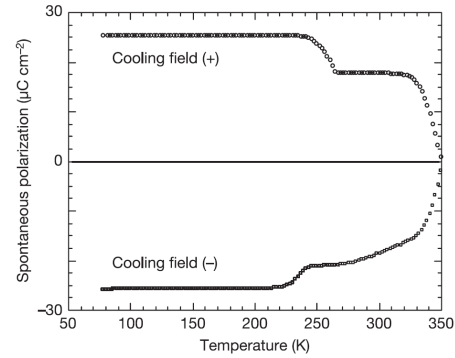


Abbildung 2.10: The integrated pyroelectric current measurement. The current flow from the sample was achieved upon heating after electric field cooling along the c -axis. Figure taken from [27, 83].

Despite the interest in the magnetic behavior, the charge order also attracted considerable attention. The Fe^{2+} and Fe^{3+} charge order is not abrupt in LuFe_2O_4 : between 320 K (just above the CO temperature) and 500 K, a two-dimensional charge order state is observed with diffuse scattering along the $(\frac{1}{3}\ \frac{1}{3}\ \ell)$ diffraction line [84, 85] (see Fig. 2.13) indicating a random stacking of already charge ordered double layers [52]. By cooling through the charge ordering temperature $T_{CO} \sim 320$ K the three dimensional order of the Fe^{2+} and Fe^{3+} valences (in x-ray diffraction) is indicated by the transformation from the diffuse scattering line along $(\frac{1}{3}\ \frac{1}{3}\ \ell)$ into sharp reflections along the same ℓ line. These superstructure reflections were first observed by Ikeda *et al.* in 1997 [82, 52] and later by

others [84, 85]; see Fig. 2.9 and Fig. 2.13(a,b). Detailed analysis of the $(\frac{1}{3} \frac{1}{3} \ell)$ superstructure reflections showed a slightly incommensurable propagation vector of $\delta \sim 0.0028$ [82, 52, 85], away from the straight line in the ℓ direction. As reported in [52, 84], the observed reflections could be explained by the presence of three symmetry-equivalent charge order domains (D1, D2 and D3), related to a 120° rotation around the c_{Hex} direction, with different propagation vectors \vec{k} , pointing away from allowed structural hexagonal reflections $(h k \ell)$. At that time, no clear picture of the exact $\text{Fe}^{2+}/\text{Fe}^{3+}$ charge order arrangement existed.

$$\vec{k}_{D1} = (h k \ell) + \left(\frac{1}{3} + \delta, \frac{1}{3} + \delta, \frac{3}{2} \right) \quad (2.11)$$

$$\vec{k}_{D2} = (h k \ell) + \left(\frac{2}{3} - 2\delta, \frac{1}{3} + \delta, \frac{3}{2} \right) \quad (2.12)$$

$$\vec{k}_{D3} = (h k \ell) + \left(\frac{1}{3} + \delta, \frac{2}{3} - 2\delta, \frac{3}{2} \right) \quad (2.13)$$

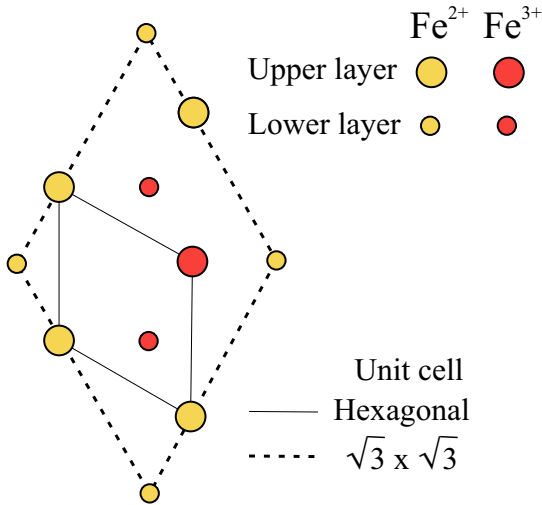


Abbildung 2.11: The polar $\text{Fe}^{2+}/\text{Fe}^{3+}$ charge order configuration for one single Fe bilayer proposed by Ikeda *et al.* in [86]. The polarization is in the c_{Hex} direction.

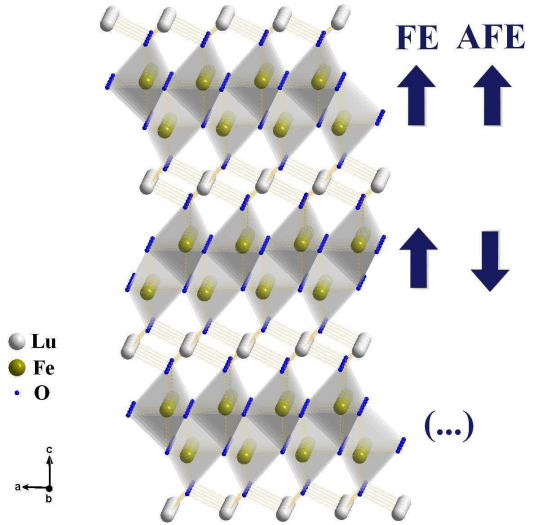


Abbildung 2.12: LuFe_2O_4 crystal structure containing Fe/O bilayers. The $\text{Fe}^{2+}/\text{Fe}^{3+}$ ordering in these double layers involves a charge imbalance between upper and lower layers, with near degenerate AFE and FE stacking indicated by blue arrows following [85].

Below T_{CO} the colossal dielectric constants measured by Ikeda *et al.* [86] suggested for LuFe_2O_4 a freezing of polar domains with antiphase boundaries of short-range charge ordered patches. This result would be consistent with the presence of spontaneous ferroelectric polarization in the CO phase below T_{CO} . They proposed that the domains

were ferroelectric, due to the charge order configuration in Fig. 2.11, where a majority amount of Fe^{2+} in one layer of the bilayer and a majority amount of Fe^{3+} in the other layer is present. Bilayers with such a charge order configuration, exhibiting an inherent Fe^{3+} to Fe^{2+} imbalance, are intrinsically polar. Together with additional pyroelectric current measurements indicating a remanent polarization, this was taken as proof of ferroelectricity originating from charge order, and, as the material is also magnetic below 240 K, of a novel type of multiferroicity [27]. However, the question of how the charge configurations and thus the polarization in different Fe double layers is stacked was not resolved at that time. In all studies, it was assumed that each polar bilayer will have an equal amount of Fe^{2+} and Fe^{3+} , making it non-charged.

The result of polar bilayers has been drawing much attention, since this would be the first observation of ferroelectricity of electronic origin. The serious electric polarization of $26\mu\text{Ccm}^{-2}$ measured at low temperatures⁶ in combination with the high transition temperature to ferroelectricity of ~ 320 K, were at that time very promising results for this material. Furthermore, under the application of small magnetic fields, large changes in the dielectric constant of LuFe_2O_4 were already observed at room temperature by Subramanian *et al.* [87], indicating a strong coupling of spins and the electric dipoles at room temperature.

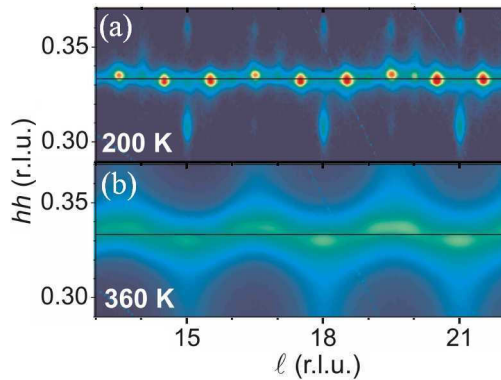


Abbildung 2.13: Scattered intensity in the $(h h \ell)$ plane at (a) 200 K and (b) 360 K. Horizontal lines mark $hh = \frac{1}{3}$. Figure taken from [85].

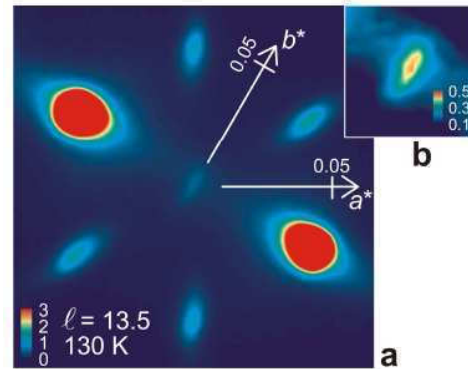


Abbildung 2.14: Incommensurate satellites. (a) Intensity at $(h k 13.5)$ at 130 K. (b) Detail around $(0 0 13.5)$. Figure taken from [85].

An analysis of the diffuse x-ray scattering above T_{CO} in Fig 2.13 by Angst *et al.* [85] reveals broad and strongly overlapping peaks, where some peaks corresponded to a propagation vector of $(\frac{1}{3} \frac{1}{3} 0)$. These suggest strong short-range correlations, and from

⁶compared to other multiferroics; for example, TbMnO_3 has a spontaneous polarization of 800nCcm^{-2} [63].

representation analysis resulting ferroelectric correlations between neighboring bilayers, consistent with the $(\frac{1}{3} \frac{1}{3} 0)$ propagation. This contrast between dominant correlations in the charge-disordered state above T_{CO} and the actual charge order established at lower temperatures indicates that ferro- and antiferroelectric charge configurations in Fig. 2.12 are almost degenerated. This near degeneracy most likely affects the different stacking sequence of the possible bilayers net polarization, as it is indicated in Fig. 2.12 with a ferroelectric (FE) and an antiferroelectric (AFE) sequence. It is thus conceivable that a ferroelectric charge order is established when the sample is cooled in an electric field of sufficient strength, making (at that time) the possibility of spontaneous ferroelectricity likely [27]. This near degeneracy of both orders would explain the remanent polarization observed by Ikeda *et al.* [27] in his pyroelectric current measurements (only) under cooling through T_{CO} in an electric field.

More recently, the magnetic properties of LuFe_2O_4 have also been investigated using magnetization and Mössbauer spectroscopy methods in combination with neutron diffraction. The Néel temperature T_N was found to be in the region between 220 K to 240 K. A consensus emerges in all recent works [1, 36, 44] that the Fe spins have a strong preference to be aligned $\parallel c_{hex}$ below T_N , perpendicular to the bilayers in Fig. 2.15. As mentioned at the beginning of this section, first a ferrimagnetic cluster state was proposed below T_N where no long-range 3D magnetic order could be observed down to 4.2 K [81, 75]. Some other works also report a spin glass state below T_N , indicated by strong frequency splitting in AC magnetization [88] measurements. In current neutron scattering experiments, sharp magnetic Bragg peaks along the $(\frac{1}{3} \frac{1}{3} \ell)$ diffraction line were observed [1, 89], suggesting the existence of long-range magnetic spin order with $(\frac{1}{3} \frac{1}{3} 0), (\frac{2}{3} \frac{1}{3} 0)$ and $(\frac{1}{3} \frac{2}{3} 0)$ symmetry equivalent propagation vectors.

It seems that oxygen off-stoichiometry most easily disturbs the magnetic long range order. Therefore, the discovery of 3D magnetic order was made in samples of higher quality. By only taking $(\frac{1}{3}, \frac{1}{3}, \text{integer})$ magnetic superstructure reflections into account, a ferrimagnetic spin structure in $H = 0$ could be refined by Christianson *et al.* [1] at 220 K, evidencing a 3D magnetic spin order for LuFe_2O_4 . From representation analysis in the parent $R\bar{3}m$ space group with the different propagation vectors, three magnetic domains with 120° rotational symmetry, as shown in Fig. 2.15, are clearly present, a similar case as for the charge order. Furthermore, x-ray magnetic circular dichroism (XMCD) studies under an applied magnetic field were performed [36, 44]; both studies show a strong magnetic orbital moment on the Fe^{2+} valences, and they also predict a 2:1 ferrimagnetic

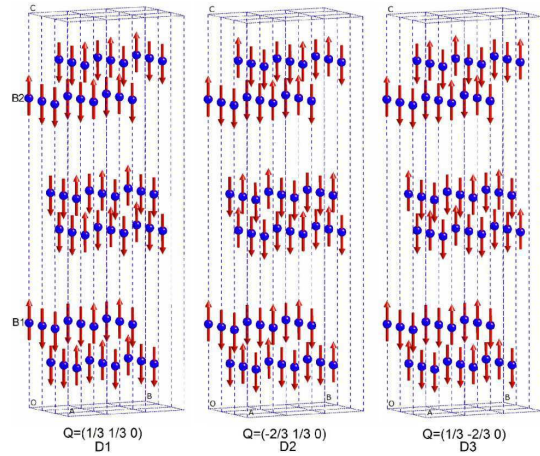


Abbildung 2.15: The three domains of the ferromagnetic spin structure below T_N in $\sqrt{3}\times\sqrt{3}\times 2$ unit cell, proposed by Christianson *et al.*. Figure taken from [1].

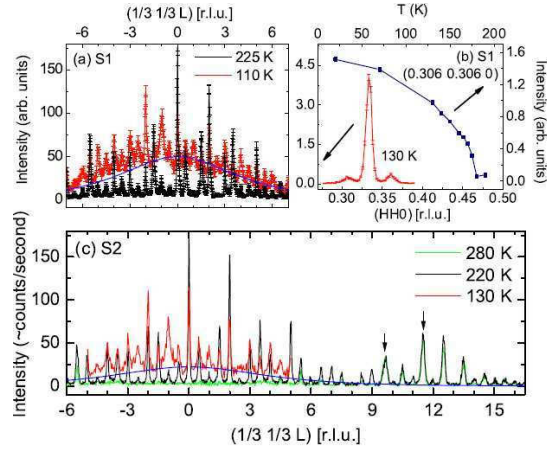


Abbildung 2.16: (a) and (c) Neutron scans along $(\frac{1}{3}, \frac{1}{3}, \ell)$ for S1 and S2. The arrows indicate peaks contaminated by aluminum background scattering. (b) displays data showing the appearance below T_{LT} of a new set of satellites indexed by $(\frac{1}{3} \pm \delta, \frac{1}{3} \pm \delta, \frac{3}{2})$ with $\delta = 0.027$. Figure taken from [1].

total spin configuration. This is in good agreement with the earlier observed saturation moments in $M(H)$ loops [80, 81]. Most interestingly, according to these results, the valences' specific spin structure scheme for Fe^{2+} and Fe^{3+} differs strongly. The strong magnetization anisotropy with its Ising ferrimagnetism for LuFe_2O_4 is attributed in [36, 90] to the strong magnetic anisotropy energy produced by this unquenched orbital moment coupled to the lattice.

Only in highly stoichiometric samples is there a second magnetic phase transition at $T_{LT} \sim 170$ K, where the observed intensity on superstructure reflections is suppressed, accompanied by additional strong diffuse magnetic scattering along the $(\frac{1}{3}, \frac{1}{3}, \ell)$ line [1, 91]. A possible monoclinic distortion affecting the structural reflections is indicated by x-ray diffraction; this magneto-structural transition is induced by magnetic field as well as temperature variations (requiring 14 T at 4 K) [28]. For most of the samples, high coercive fields are observed in order to switch the magnetization direction at low temperatures [80, 74, 92, 28, 88]. This was first explained in terms of kinetic arrest [93] between two different magnetic phases, and in [92, 94] by the formation of the packing configuration of irregular Ising pancakes. They suggest that the enhancement of coercivity is linked to collective freezing of these Ising pancakes for lower temperatures. However, in sum-

mary, the underlying mechanism for giant coercivity and the magneto-structural phase transition are still unclear.

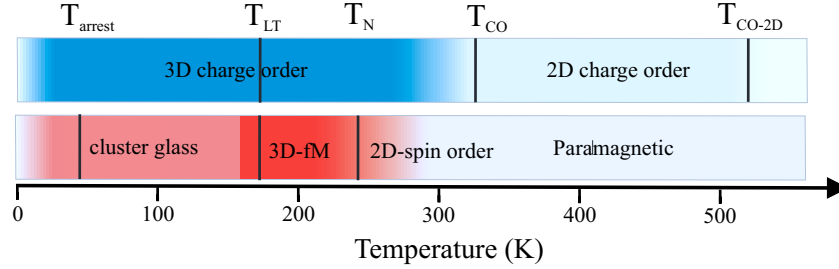


Abbildung 2.17: The actual phase diagram of LuFe_2O_4 , considering samples of best quality, showing the electronic/structural transitions (blue) and the magnetic transitions (red) under cooling in zero field.

In contrast to the charge and spin order, where for both orders in high stoichiometric samples 3D correlations are observed (Fig. 2.17), no long-range orbital ordering scheme has so far been found for LuFe_2O_4 . But according to theoretical work [95, 96] such order is expected. It is suggested that the crystal field of the trigonal bipyramids splits the 3d states of LuFe_2O_4 into two doublets ($d_{xy}=d_{x^2-y^2}$ and $d_{xz}=d_{yz}$) and a singlet (d_{z^2}) [95]. The Fe^{3+} valence with its five 3d electrons is spherical while Fe^{2+} with six 3d electrons exhibits a doubly degenerate orbital degree of freedom in the $d_{xz}=d_{yz}$ ground state [36]; all this is valid for the charge order presented in [52]. In [31] it is also reported that the orbitals exist as an orbital glass, as the observed scattering factors are isotropic, in agreement with the idea of random orientations of the Fe^{2+} orbitals, forming an orbital glass state. A detailed study of orbital order is also presented in [97].

The motivation behind the studies presented in this thesis is to determine what the $\text{LuFe}_2\text{O}_{4-\delta}$ samples of highest quality are. As already explained in this instructional part to LuFe_2O_4 , magnetization measurements seems to be most sensitive to oxygen stoichiometry δ ; this will be elaborated further in this thesis. Another aspect which will be discussed is the crystallographic structure in the charge ordered phase of such high-quality samples. For the charge order presented in this section, all studies assumed polar bilayers (which are generally accepted) where one of the two layers is rich in Fe^{2+} and the other in Fe^{3+} . However, the existence of these polar bilayers was never directly proven by experiments, and it is thus natural to (dis)prove this by direct methods, such as crystal structure refinements. Furthermore, in [85] it was suggested that near-degenerate stacking of the bilayer polarizations could maybe affected by the cooling through T_{CO} under an external applied electric field. In order to demonstrate such a ferroelectric charge

order configuration, in-situ x-ray scattering is the method of choice. Later, different scattering techniques, such as neutron and soft resonant x-ray scattering, are used in a comprehensive study in order to determine the spin configurations in the previously defined magnetic phase diagram. From the particular spin structures, in combination with the phase diagram, some of the effects presented here, until now unexplained (such as the “anomalous field-heating-effect”) can be understood. At the end of this thesis, XMCD studies will provide evidence for a strict coupling between charge and spin order in LuFe_2O_4 , and the idea of orbital order will be discussed.

Experimental Techniques & Theory

3.1 Magnetometry

3.1.1 DC magnetization

The equilibrium value of the magnetization in a sample is extracted by direct current (DC) magnetic measurements. This means that the sample is magnetized by a constant magnetic field and the magnetic moment of the sample is measured as a function of temperature T and magnetic field H applied. Furthermore, $M(H)$ -curves in constant T are also labeled as DC magnetization measurements, because here the magnetic field is increasing or decreasing slowly and in most cases this does not influence the dynamically magnetization processes. The magnetic phase diagram can be established by determining changes in magnetic behavior. In order to investigate the magnetic anisotropy the sample can be mounted in different directions in relation to the applied field, or additionally the sample torque can be measured.

High magnetic field measurements up to 22 T

High magnetic field measurements of up to 22 T were performed on a 10 MW resistive-magnet at the Laboratoire National des Champs Magnétiques Intenses (LCMI) in Grenoble. Here the magnetization was measured by the extraction method, similar to the DC magnetization measurement above. In order to achieve a temperature range from 4 K to 320 K the sample was mounted inside a cryostat.

VSM option at PPMS

The Physical Property Measurement System (PPMS) from Quantum Design has the capability to measure various properties such as magnetization, resistivity, heat capacity and many more [98]. One focus of this work is on magnetic properties, so only the Vibrating Sample Magnetometer (VSM) option will be discussed here. The sample is

mounted inside the PPMS system between two pickup coils connected by a rod to the VSM option with the linear motor (head), vibrating the sample up to 40 Hz through these coils. An electric current proportional to the sample magnetic moment is induced in the coils, and this signal can be separated from electrical noise by lock-in devices. The sample magnetic moment can be measured as a function of the applied magnetic field H (0 T-9 T) and temperature T within the helium cryostat (4 K-400 K) or oven insert (300 K-1200 K). The magnetic sensitivity achievable by the VSM option is $\sim 1 \cdot 10^{-6}$ emu. All quantum design instruments provide the magnetization as electromagnetic unit¹ *emu*.

SQUID option at MPMS

The Magnetic Property Measurement System (MPMS) from Quantum Design [99] is designed to measure small magnetic moments with the use of coils consisting of Josephson-Contacts [100]. The so called Superconducting Quantum Interference Device (SQUID) can measure small changes in magnetization. There are two different ways of measuring the magnetization (of type DC or RSO). The DC technique starts at the lowest point of the scan length and sequentially moves the sample upward through the superconducting pickup loops. This gives a high accuracy for the determined magnetic moment, but is very slow. The Reciprocating Sample Option (RSO) moves² with a typical amplitude of 5 mm through the pickup coils; this method is commonly used when very fast measurements during magnetization versus field $M(H)$ -loops are necessary. The maximum magnetic sensitivity in RSO mode is $\sim 5 \cdot 10^{-9}$ emu. With the laboratory MPMS system, a temperature range of (4-400 K) and field range of (0-7 T) is covered. In order to perform magnetization measurements in almost no field, before the sample is mounted the residual magnetization (even earth's magnetic field) can be compensated for.

3.1.2 AC susceptibility

Because the induced sample moment maybe time-dependent, AC measurements [101] yield information about magnetization dynamics which are not obtained in DC measurements, where the applied moment is constant during the time of measurement. In order to achieve information about the magnetization dynamics, the AC magnetization method is used. For this method, a small oscillating magnetic field is applied to a sample, and the responding AC moment from the sample is measured in real and imaginary parts. Thus, an AC magnetic susceptibility measurement yields two components: the

¹ $M[\mu_B] = M[emu] \cdot 1.079 \cdot 10^{20}$

²The Max Slope technique is described here and is used in this work when RSO is mentioned.

magnitude of the susceptibility, χ , and the phase shift, ϕ (relative to the drive signal). Alternately, one can describe the susceptibility with an in-phase (real part) χ' and an out-of-phase (imaginary part) component χ'' . For our ACMS option inside the PPMS system it is possible to apply a maximum amplitude of 10 Oe as the driven signal with frequencies between 10 Hz and 10 kHz. The AC susceptibility can be measured with a DC field offset up to 9 T from the PPMS magnet in a (4 K-400 K) temperature range.

3.2 Scattering Theory

Scattering techniques are a unique tool to explore the order parameter of a system and its particular phase transitions. These techniques can directly probe the correlations of any ordered parameter inside a system depending on which probing particle, energy and scattering geometry is used for the experiment. Before going into the experimental part of this work, the theoretical fundamentals of scattering theory are explained in this chapter in order to interpret and understand the results presented later. In order to solve the diffraction process of any probing particle with matter, it is necessary to treat this problem as a quantum-mechanical one. The approaching particle, which is scattered by the scattering potential $V(r)$, can be described as an incoming plane wave in space and time. A single scattering event is described by the following Schrödingers equation in (3.1).

$$H\Psi = \left(-\frac{\hbar^2}{2m}\Delta + V(\vec{r}) \right) \Psi = i\hbar \frac{\partial}{\partial t} \Psi \quad (3.1)$$

Here, $\Psi(\vec{r}, t)$ is the amplitude of the probability of presence. For elastic scattering, meaning that approaching and scattered particles have the same energy, the time dependence is separated by $\exp(-i\frac{E}{\hbar}t)$ making the differential equation in (3.1) stationary:

$$\Delta\Psi + k^2(\vec{r})\Psi = 0 \quad \text{with} \quad k^2(\vec{r}) = \frac{2m}{\hbar^2} (E - V(\vec{r})) \quad (3.2)$$

If $V(\vec{r}) = 0$ the solution is a plane wave equal to the incoming wave Ψ^0 . For non vanishing potential $V(\vec{r})$ we can use the Green's function G , which is obtained by solving (3.2) for a point source potential $\delta(\vec{r} - \vec{r}')$:

$$(\Delta + k^2) G(\vec{r}, \vec{r}') = \delta(\vec{r} - \vec{r}') \Rightarrow G(\vec{r}, \vec{r}') = \frac{\exp(ik|\vec{r} - \vec{r}'|)}{4\pi|\vec{r} - \vec{r}'|} \quad (3.3)$$

This solution G transforms the differential Eq.(3.1) into an integral-equation (3.4).

$$\Psi(\vec{r}) = \Psi^0(\vec{r}) + \frac{2m}{\hbar^2} \int G(\vec{r}, \vec{r}') V(\vec{r}') \Psi(\vec{r}') d^3r' \quad (3.4)$$

In order to solve (3.4) the incoming wave Ψ^0 can be used as a first approximation for the solution: $\Psi^1 = \Psi^0 + \int \mathbf{G} V \Psi^0$; this ansatz is known as the first born approximation. It is valid for a weak scattering potential $V(\vec{r})$ and in the case of a small scattering volume, making multiple scattering processes unlikely. For the circumstance that the distance from sample to detector $|\vec{R}| = |\vec{r} - \vec{r}'|$ is much bigger than the size of the sample $|\vec{r}'|$, we can use the far field or Fraunhofer-approximation, transforming (3.4) into (3.5).

$$\Psi^1(\vec{R}) = \underbrace{e^{i\vec{k}\vec{R}}}_{\text{incoming}} + \underbrace{\frac{e^{ikR}}{R} \frac{2m}{4\pi\hbar^2} \int V(\vec{r}') e^{i\vec{Q}\vec{r}'} d^3r'}_{\text{scattered}} \quad (3.5)$$

In Eq.(3.5) we already introduced the scattering vector $\vec{Q} = (\vec{k}_i - \vec{k}_f)$, where \vec{k}_i is the wave vector of the incoming and \vec{k}_f of the scattered plane wave; their absolute values are $|\vec{k}| = 2\pi/\lambda$. The second term in Eq.(3.5) represents the amplitude of the scattered wave. In order to obtain its intensity, we have to calculate the square of the absolute value as shown in (3.6).

$$I(\vec{Q}) \propto |F(\vec{Q})|^2 = \left| \frac{m}{2\pi\hbar^2} \int V(\vec{r}') e^{i\vec{Q}\vec{r}'} d^3r' \right|^2 = |\mathcal{F}[V(\vec{r})]|^2 \quad (3.6)$$

The observed intensity is thus proportional to the square of the Fourier transformation $|\mathcal{F}[V(\vec{r})]|^2$ of the scattering potential. In almost all scattering experiments only the scattered intensity is measured, losing the phase information, and making a direct reconstruction of the scattering density via Fourier transformation impossible. This is the so-called phase problem of scattering; it is compensated by simulating the intensity distribution for a given structure and refining this according to the observed intensity; for more details see Sec. 3.3.1. With a decomposition of \vec{r}' into single scattering particles \vec{r}_p and their distribution in space \vec{r}_s , equation 3.6 becomes:

$$\int_{V_c} V(\vec{r}') e^{i\vec{Q}\vec{r}'} d^3r' = \sum_{j=1}^N e^{i\vec{Q}\vec{r}_j} \int_{V_j} V(\vec{r}') e^{i\vec{Q}\vec{r}'_j} d^3r' \quad (3.7)$$

In Eq.(3.6) the scattering behavior depends on the scattering potential $V(\vec{r})$, determined by the used radiation and the probed material. In 3.7 the scattering process can be treated separately for the lattice and the contained elements. The following sections will provide information on the different radiation probes used in this thesis.

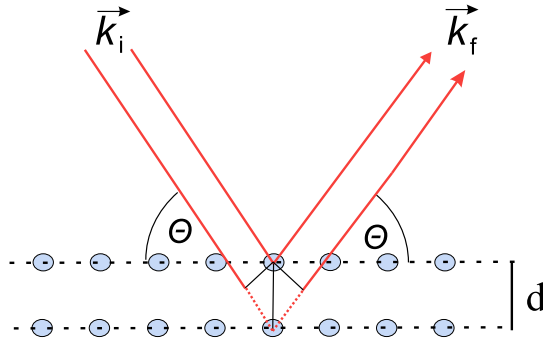


Abbildung 3.1: In Bragg's Law the diffracted waves have constructive interference when the distance between different paths differs by an integer number of wavelengths λ .

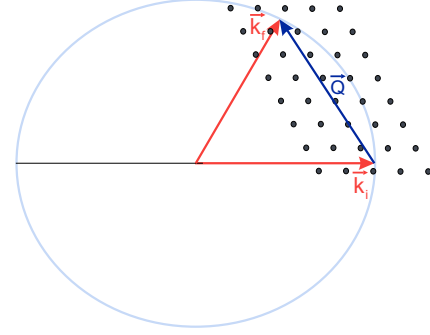


Abbildung 3.2: Bragg reflections are observed for single crystals, when the reciprocal lattice points are on the Ewald's sphere surface and connected by the scattering vector \vec{Q} .

3.2.1 Reciprocal space and Bragg scattering

Before discussing the different types of radiation and their interaction with matter it is worthwhile to take a more detailed look at the general scattering process from a periodic arrangement. In such a structure, constructive interference is observed when the path difference for elastically scattered waves is a multiple integer n of their own wavelength λ . Such a scattering process is illustrated in Fig 3.1(a) with a corresponding path difference of:

$$\Delta s = \vec{d} \cdot (\vec{k}_i - \vec{k}_f) = 2\pi n \quad (3.8)$$

For a given crystal structure, all possible configurations for $\vec{Q} = (\vec{k}_i - \vec{k}_f)$ with constructive interference in 3 dimensions can now be determined; this is called the Ewald sphere. From the periodic arrangement of a crystal, the positions of constructive interference are calculated via the Fourier transformation of its lattice vectors $(\vec{a}, \vec{b}$ and $\vec{c})$. This gives a periodic arrangement with the reciprocal lattice vectors \vec{a}^*, \vec{b}^* and \vec{c}^* and h, k and l integer values.

$$\vec{Q}(h k \ell) = h\vec{a}^* + k\vec{b}^* + \ell\vec{c}^* \quad \text{with} \quad \vec{a}^* = \frac{2\pi(\vec{b} \times \vec{c})}{\vec{a} \cdot (\vec{b} \times \vec{c})} \quad \text{and rotating} \quad (3.9)$$

Bragg's law, as shown in Fig. 3.1, describes the angle of diffraction θ with respect to the scattering planes, with their particular d_{hkl} and used wavelength.

$$n\lambda = 2d_{(h k \ell)} \sin \theta \quad \text{with} \quad d_{(h k \ell)} = \frac{2\pi}{|\vec{Q}(h k \ell)|} \quad (3.10)$$

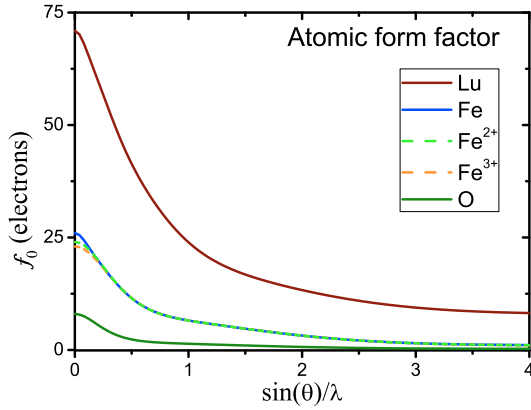


Abbildung 3.3: Atomic x-ray scattering factors for different elements. Note: beside the neutral Fe, the Fe^{2+} and Fe^{3+} valences are displayed [102].

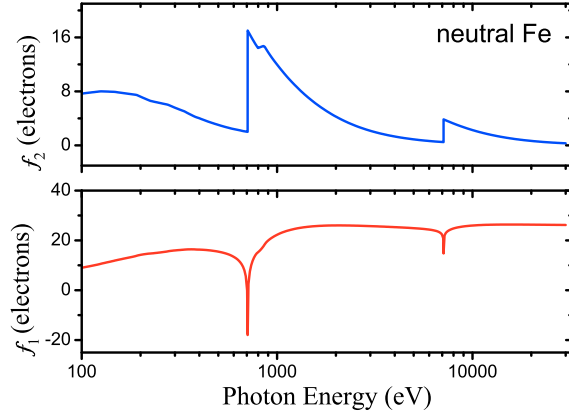


Abbildung 3.4: The real f_1 and imaginary f_2 part of the atomic dispersion correction for a free neutral Fe-atom [103].

Only for reciprocal lattice points coinciding with the surface of the Ewald sphere can the Bragg reflection be fulfilled; a single crystalline sample needs to be aligned to observe a particular reflection. The Bragg equation is not connected to the atomic distribution inside a crystal, and thus it does not give any information about the intensity of different reflections. The scattered intensity can be achieved by introducing all atoms inside the unit cell with their corresponding relative position (u_α , v_α and w_α) to the lattice:

$$\vec{r}_\alpha = u_\alpha \vec{a}_1 + v_\alpha \vec{a}_2 + w_\alpha \vec{a}_3 \quad (3.11)$$

As a result of 3.7, the scattering amplitude will become a convolution of the scattering potential $V(\vec{r})$ considering the atomic positions and the crystal lattice:

$$A_{(h\ k\ \ell)} = \sum_{\alpha} f_{\alpha}(\vec{Q}) e^{-2\pi i(h \cdot u_{\alpha} + k \cdot v_{\alpha} + \ell \cdot w_{\alpha})} \quad (3.12)$$

When the crystal lattice is not primitive, additional selection rules for missing reflections appear where $A_{(h\ k\ \ell)}$ becomes zero. For example, in a base-centered (C) crystal structure the systematically absent reflection condition is $h + k = \text{even}$. This additional x-ray annihilation can be explained by further scattering planes present in the crystal structure.

3.3 X-ray scattering

The atomic form factor $f_{\alpha}(\vec{Q})$ in Eq.(3.12) is element-specific, and it differs strongly for different types of radiation. The scattering process of photons can be described by Thomson scattering: the incoming beam excites the electrons bonded electrostatically

to the atom; and consequently, these atoms, with bonded electrons, are themselves a source of spherical waves of similar radiation. In the case of x-rays, f_α is the Fourier transformation of the charge density distribution $\rho_j(\vec{r}_j)$ of a particular element.

$$f_\alpha(\vec{Q}) = \int_{V_J} \rho_j(\vec{r}_j) e^{i\vec{Q}\vec{r}_j'} d^3r' \quad (3.13)$$

In first approximation, it is independent of the used wavelength and depends solely on the element. An empirical formula is used to reproduce the shape of the measured atomic form factor as a function of diffraction angle θ ; they are tabulated in [102] and some examples are provided in Fig. 3.3. In the case of forward scattering $\theta = 0^\circ$, the integral value from the atomic form factor is equal to the number of electrons (Z) bound to an atom³. As a consequence, the scattered intensity contribution scales with Z^2 [106], making it difficult to perform a sensitive detection of lighter atoms such as hydrogen and oxygen in the unit cell. For structure refinements only the form factor of the neutral atom is used, because the contrast between diverse valences is weak (see Fig. 3.3 for Fe and its different valences). Because the electrons are distributed in a sphere around the atom, there is an increasing destructive interference between different scattered waves, explaining the decay of the atomic form factor for increasing scattering angle. However, the scattering factor is modified by anomalous scattering if the incident wavelength is near an absorption edge of the scattering element, as we will see Sec. 3.3.4.

3.3.1 Crystal structure determination

When studying an unknown crystal, one of the first things of interest is to solve the crystal structure and the internal nuclear distribution. Here, a short introduction to single crystal refinement is given; for further reading see e.g. [107]. In Sec. 3.3 the intensity of a particular reflection ($h k \ell$) can be calculated with the knowledge of the atomic distribution inside the crystallographic unit cell; see e.g. Eq.(3.7). Due to the crystallographic phase problem, caused by the square of the Fourier transformation in Eq.(3.7), this approach does not work the other way around. To obtain the atomic distribution inside the unit cell with the knowledge of the intensities of specific reflections, a different approach is needed. Here, the method of the least square refinement is generally used to solve small-molecule structures:

$$\chi^2 = \sum_i w_{(h k \ell)} (F_{Obs}^2 - F_{Calc}^2)^2, \quad (3.14)$$

³A small Z -dependent energy-independent relativistic correction α is necessary for zero momentum transfer at high energies; tabulated values can be found in [104, 105].

in which the parameters for each atom inside the unit cell are varied until the χ^2 -value between observed and calculated reflections reaches a minimum. The parameters being refined in a crystal structure determination are the x_j , y_j , and z_j positional parameters for each atom⁴ in Eq.(3.15) and the U isotropic or the six U_{ij} anisotropic thermal displacement parameters. The anisotropic displacement parameters describe the thermal elongation from the atomic positions (see Eq.(3.15)), they have a strong impact on refinement. Six parameters are used in a matrix form to describe the anisotropic thermal motion [108, 109]. They are diagonal and off diagonal terms from a three-by-three matrix, where crystal symmetry can reduce the number of non equal parameters [107]. The total calculated intensity is thus given by:

$$I(\vec{Q}) = \left| F(\vec{Q}) \right|^2 = \left| \sum_j f_\alpha e^{i\vec{Q}(h k \ell)r_j} \cdot e^{-\frac{1}{3}\vec{Q}^2|U_{ij}|^2} \right|^2 \quad (3.15)$$

Additional parameters such as extinction, weights and absorption must be refined in order to achieve a good refinement.

Twinning

In x-ray diffraction experiments, it is often observed that the measured sample is not composed of one single crystallite, but that a second or more crystallites are trailed to the original one by one or more definite macroscopic symmetry relations. In crystallography such a case is called twinning; there are different ways the additional grains can be connected to the primary crystal.

- Non-merohedral twins: have two or more crystalline domains with reciprocal lattices that either do not overlap or only partially overlap with the original crystal.
- Merohedral twinning: is a special case of crystallographic twinning where the lattices of twin (different) domains (in a single crystal) overlap in three dimensions. An effect is superimposable lattices when the rotational symmetry of the lattice exceeds the rotational symmetry of the space group.
- Second grain: a second crystallite inside the crystal, which may have a different lattice and symmetry than the original specimen.

Once the nature of the twinning is recognized and included in the model, the structure solution and refinement usually proceed in a normal way.

⁴The atomic structure factor f_α and dispersion correction f_1 and f_2 according to Eq.(3.13) and Eq.(3.26) are obtained for each element specific from [102].

Quality R -indices and weights

The result of a structure refinement yields a list of atom assignments x_j , y_j and z_j in the unit cell and the shape of the anisotropic thermal displacements (thermal parameters U_{ij}). Furthermore, the quality of a solution is assessed by the values of $R1$, $wR2$, and a $Goof$, which all compare the observed intensity with the calculated ones from the refined model.

- $R1$, often called the R -value, is the agreement between the calculated and observed structure factor F . The formula for this value is, with the sum j over all observed reflection:

$$R1 = \frac{\sum_j ||F_{obs}| - |F_{calc}||}{\sum_j |F_{obs}|} \quad (3.16)$$

Ideal solutions would have R -values of zero. However, due to random errors, this is never achieved. R -values (listed as per cents) of less than 5% are considered good solutions; high-quality samples will often result in R -values lower than 2.5%.

- The $wR2$ value is similar to the $R1$ value, but it uses the squared F -values convoluted with the refined weighting scheme w , which corresponds to the intensity measured in a x-ray or neutron experiment. These results always have a higher value in $wR2$ than in $R1$, typically by a factor of two.
- The $Goof$ value refers to the “goodness of fit” of the solution. In addition to the difference in R values, the $Goof$ also takes into account the number of observed reflections and the parameters used. The $Goof$ should approach ~ 1.0 at the end of the refinement.

$$Goof = S = \left(\frac{\sum_j w_{(h\ k\ \ell)} (F_{obs}^2 - F_{calc}^2)^2}{n - p} \right)^{\frac{1}{2}} \quad (3.17)$$

In Eq.(3.16) n is the number of reflections used on refinement and p is the total number of parameters refined.

The weights w used in least squares refinement defines the impact an observation should have on the results. The weights scheme typically includes the statistical error σ of the measured data in a defined form. In Eq.(3.18) a typical scheme for the weighting is shown.

$$w_{(h\ k\ \ell)} = \frac{1}{\sigma^2(F_{obs}^2) + (aF_{obs})^2} \quad (3.18)$$

This weighting scheme gives difficulties for structures showing a broad spectrum of intensity distributions; in such case it is typically defined as:

$$w_{(h\ k\ \ell)} = \frac{1}{\sigma F_{obs}^2(h\ k\ \ell) + (aP)^2 + bP} \quad \text{with} \quad P = \frac{2F_{calc}^2 + \text{Max}(F_{obs}^2)^2}{3} \quad (3.19)$$

The values for a and b in Eq.(3.19) are chosen to give an even distribution of the variances across all groups of data, based on the relative intensities. This is the weighting scheme used in SHELX [110], and it is supposed to give a reduced statistical bias [111] by using P rather than F_{obs}^2 . There are additional parameters for defining a weighting scheme[107], but these are not used in this work and thus are not discussed. The weights are not changed during refinement; the only way to adjust them is a manual procedure where the suggested weights are copied into the SHELX WGHT instruction.

At the end of the refinement all non-hydrogen atoms should be refined with anisotropic displacement U_{ij} parameters (all of them should be positive) provided that there are at least 10 data points (unique reflections) per parameter. There should be no strong residual Q -peaks indicating missing charges in the Fourier transformation. For light-atom structures (up to Na), the maxima and minima should be in the range ± 0.1 to $\pm 0.3e$ per \AA^3 . For systems containing heavy elements, it is normal to find so-called “ghosts” in the Fourier map [112, 113] at a distance up to 1.0\AA from the heavy atom and with up to $\pm 10\%$ of the atomic number Z per \AA^3 . This residual electron density can not be assigned to an particular atom. Even refinements taking anisotropic displacements into account are often not able to describe these residual electron density peaks which are mainly caused by tiny errors in the absorption correction.

3.3.2 Laboratory single crystal x-ray diffraction

Knowing the crystallographic structure is in most cases essential to understand the macroscopic and microscopic physical behavior observed for a sample. In order to solve the crystallographic structure, single crystal and powder diffractions techniques have improved continually over the last decades. With state of the art x-ray diffraction methods, using an area CCD detector, it is possible to collect a couple of reflections simultaneously, accelerating the whole data-acquisition process drastically. The SuperNova dual source diffractometer [114] used in this work is optimized for collecting data from small crystals with a maximum size of $\sim 0.3\text{ mm}$ in radius, depending on absorption. The instrument is equipped with molybdenum ($\lambda(\text{Mo}_{K\alpha}) = 0.709\text{\AA}$) and copper ($\lambda(\text{Cu}_{K\alpha}) = 1.540\text{\AA}$) micro-source x-ray tubes, each with mirror optics to increase the intensity of the x-ray beams



Abbildung 3.5: The OxfordDiffraction SupraNova diffractometer.

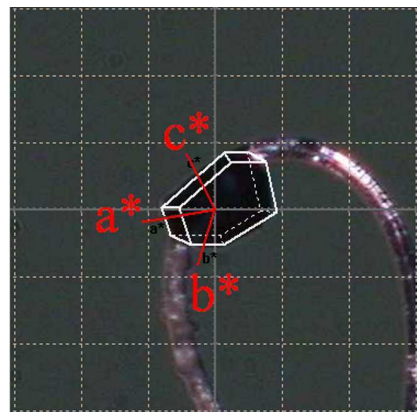


Abbildung 3.6: A LuFe_2O_4 single crystal with indexed phases, ready to apply numerical absorption correction.

at the sample position. This arrangement makes switching between the two sources easy. The scattered intensity is collected on a high sensitivity Atlas area CCD detector. The scattering geometry is horizontal, and the sample movements are achieved by a four circle diffractometer with high positional accuracy. Additionally, the SuperNova system can be operated with a Cryojet using cold N_2 gas to achieve temperatures in a range from 100 K to 490 K.

To refine a given crystal, all unique $(h k \ell)$ reflections should be measured at least once by driving them with the diffractometer into scattering condition with the goniometer from the diffractometer. For a typical single crystal diffraction instrument using a CCD detector, it is always recommendable to collect redundant measurements for each symmetry corresponding set of $(h k \ell)$ reflections. These equivalent reflections are necessary for the absorption correction. The repeated measurements greatly improve the data set quality and require only a little extra effort when using an area CCD detector.

CrysAlis^{Pro}

The instrumental software CrysAlis^{Pro} [115], does not only run the diffractometer and the experiment; it also helps, after performing the experiment, to find the right crystallographic unit cell which best describes the observed reflections. After defining the unit cell inside the program, the Bragg reflection on the recorded CCD images can be integrated. The program is also able to index and integrate the reflections from additionally twinned crystallites inside the original sample (these twins are often discovered after conducting

the whole experiment). After twin indexation (if needed), additional polarization, Lorentz and sample movement corrections are necessary. At the end of this process, an $(h\ k\ \ell)$ file containing the observed intensities and its standard deviation for all measured Bragg reflections is achieved. From all observed reflections, and its intensity distribution, the program guesses what the most likely space group is. For an irregular crystal shape (which is the case for most crystals), additional absorption correction is essential to achieve proper atomic positions and reliable thermal displacement parameters on refinement. This can be done through two different approaches. The first is a numerical correction. Here the crystal shape is assumed to be spherical or cylindrical, and the final crystal shape can be fitted to the intensity deviations for symmetry-equivalent reflections. In the second approach the real shape of the crystal is defined by indexed crystal facets (as seen in Fig. 3.6); absorption can now be calculated from the real transmission path through the crystal for each observed reflection [116]. It is commonly accepted that analytical methods using the crystal shape provide the best absorption corrections. For LuFe_2O_4 the second method was used, due to the large amount of heavily absorbing Lu in this system. A good indication of data quality is the R_{int} -value defined in Eq.(3.20)

$$R_{int} = \sum_j \frac{1}{j+n} \frac{\sum_n (F_n^2 - \langle F^2 \rangle)}{\langle F^2 \rangle} \quad \text{with} \quad \langle F^2 \rangle = \frac{1}{n} \sum_n F_n^2 \quad (3.20)$$

where the inner sum is over the symmetry-equivalent reflections, and the outer sum is over the unique $(h\ k\ \ell)$ data points j . The term n is the number of equivalent data points for given $(h\ k\ \ell)$ reflections being merged. In order to refine a crystal structure properly, the R_{int} value for a collected data set should be at least below 10% after all corrections. After completing the data collection and the corrections here discussed, the crystal structure can be refined with programs such as SHELX [110] and Jana2006. The SHELX [110] package included in the WinGX [117] graphical user interface, is the single-crystal structure refinement program used for data treatment in this thesis. In order to obtain a good refinement, some general data-acquisition parameters are given here: the redundancy should be bigger than six and the completeness (indicating the total measured reflection with respect to the amount of possible measurable reflections) higher than 99% the intensity to noise ratio should be better than 20. For the measurements presented in this work typical exposure times of 20 seconds are used resulting in a total experimental time of approximately five hours.

3.3.3 6-ID-D: high energy x-ray diffraction

The side-station beamline 6-ID-D at the Advanced Photon Source (APS) uses the synchrotron x-ray beam transmitted through the monochromator of the low-energy station. The possible high photon energy range achievable by this set-up is variable in the 28-130 keV range, depending on the chosen facets of silicon crystal monochromators. The experimental hutch is equipped with a single-crystal four-circle diffractometer capable of holding an additional cryostat for low temperatures down to 20 K. The scattered photons are detected on a MAR345 image plate with 345mm sensitive diameter and $10\mu\text{m}$ square pixel size, each with a dynamic range of 17 bit intensity resolution. The detector can be positioned in variable distance from the sample to set up the right Q -resolution. As already shown in Sec. 3.2.1 the radius k_i of the Ewald-sphere will become very broad for high-energy photons with their small wavelength ($|k| = 2\pi/\lambda$). This makes the direct detection of whole reciprocal planes on the 2D-area-detector possible. In order to bring all Bragg reflections into scattering condition an adequate sample movement (rocking) is established. The sample rocking process performed during the experiment was able to measure all Bragg reflections on the image plate, this rocking could be done multiple times (up to 1 h for one exposure) in order to detect very weak reflections or diffuse scattering. Therefore, to avoid over-exposure may be causing damage to the image plate, the most intense Bragg reflections needed to be covered by lead pieces. For experiments conducted in a magnetic field up to 4 T the sample can be mounted inside a cryomagnet, allowing for temperatures down to 20 K. Additionally, a Keithley 2400 SourceMeter was used to apply high voltages to the sample during scattering.

3.3.4 Resonant x-ray scattering

The scattering process, described as Thomson scattering, is only valid for photon energies far away from the absorption edges. In order to describe the interaction of radiation with matter close to the binding energies of electrons of a particular element, a quantum-mechanical treatment of the scattering process is necessary. The Hamiltonian (3.22)

KAPITEL 3. EXPERIMENTAL TECHNIQUES & THEORY

describing this photon electron system can be expressed by the following⁵ according to Blume and Gibbs [118]:

$$H = H_e + H_{rad} = \frac{(\vec{p} + e\vec{A})^2}{2m} + H_{rad} = \frac{\vec{p}^2}{2m} + H_{rad} + \underbrace{\frac{e}{m}\vec{A} \cdot \vec{p} + \frac{e^2\vec{A}(\vec{r}, t)^2}{2m}}_{Interaction} \quad (3.21)$$

Here, H_{rad} is the Hamiltonian for the quantized radiation field and $\vec{A}(\vec{r}, t)$ in Eq.(3.22) describes the vector potential for the quantized electromagnetic field. It is usually expressed by photon creation a and annihilation a^\dagger operators⁶ specified by u and \vec{k} which are the polarization and the propagation vector of the quantized electromagnetic field. The direction of $\vec{A}(\vec{r}, t)$ is specified by \hat{e}_u , the polarization unit vector.

$$\vec{A}(\vec{r}, t) = \sum_{u, \vec{k}} \hat{e}_u \sqrt{\frac{\hbar}{2\epsilon_0 V \omega}} \left[a_{u, \vec{k}} e^{i(\vec{k} \cdot \vec{r} - \omega t)} + a_{u, \vec{k}}^\dagger e^{-i(\vec{k} \cdot \vec{r} - \omega t)} \right] \quad (3.22)$$

The interaction terms in H , combining photon and electron interplay, leads to possible transitions between initial $|i\rangle$ and final $|f\rangle$ states. The transition probability W for a particular transition ($|i\rangle \rightarrow |f\rangle$) is proportional to the cross section and can be determined by applying Fermi's Golden Rule.

$$\frac{d\sigma}{d\Omega} \propto W_{|i\rangle \rightarrow |f\rangle} = \frac{2\pi}{\hbar} |V_{fi}|^2 \rho(\epsilon) \quad (3.23)$$

In Eq.(3.23) $\rho(\epsilon)$ is the density of states from the final states and V_{fi} the transition matrix element for a particular transition. The term $|\langle f | H_{int} | i \rangle|^2$ is of first-order perturbation and gives rise, with the initial part of H_i , which is linear in $\vec{A}(\vec{r}, t)$, to photoelectric absorption. The second contribution of H_i in $|\langle f | H_{int} | i \rangle|^2$ is quadratic, with $\vec{A}(\vec{r}, t)$, and can thus first destroy and then create a photon (not resonant), describing elastic Thomson scattering⁷. Higher transition matrix elements can be calculated by second order time-dependent perturbation theory, with the sum over all possible states $|n\rangle$ and the corresponding energy E_n in Eq.(3.24).

$$\frac{d\sigma}{d\Omega} \propto W_{|i\rangle \rightarrow |f\rangle} = \frac{2\pi}{\hbar} \left| \langle f | H_{int} | i \rangle + \sum_{n=1}^{\infty} \frac{\langle f | H_{int} | n \rangle \langle n | H_{int} | i \rangle}{E_i - E_n} \right|^2 \rho(\epsilon) \quad (3.24)$$

Here, we have to approximate the exponential function in \vec{A} until its linear term, which is the dipole approximation. In this second-order perturbation theory, an electron can

⁵Here interaction of photons with the orbital and spin moment is neglected; this gives only relativistic contributions to the scattering as shown and discussed in Sec. 3.3.5.

⁶The electromagnetic field is thus quantized the same way as the harmonic oscillator with: $a|n\rangle = \sqrt{n}|n-1\rangle$ and $a^\dagger|n\rangle = \sqrt{n+1}|n+1\rangle$, where $|n\rangle$ is an eigenfunction of the Harmonic oscillator.

⁷The electron will be left in the same state $|a\rangle$ as it was before the scattering process, which is not the ground state $|i\rangle$ of the electron-photon system.

make a transition from the ground state $|i\rangle$ into an intermediate virtual state $|n\rangle$. Resonance now occurs when the energy between the intermediate state and the ground state is equal to the incoming photon energy $\hbar\omega = E_n - E_a$ and the denominator thus becomes zero. Resonant scattering is a coherent process merely involving virtual absorption and emission of photons. However, these virtual transitions follow the Pauli exclusion principle which requires that only unoccupied states can be probed with regard to the usual quantum-mechanical selection rule $\Delta m = \pm 1$ in dipole approximation. This makes resonant x-ray scattering a unique tool to explore charge, orbital and spin order. Particularly in the soft x-ray regime, resonant diffraction can directly probe the transition metal $3d$ shells, important for magnetism and orbital order, with a corresponding $2p \rightarrow 3d$ virtual transition at the $L_{2,3}$ -edges.

Anomalous atomic scattering factor

The second term in Eq.(3.24) gives rise to the anomalous atomic scattering factor⁸ $f_1(E) + if_2(E)$, describing the energy-dependent dispersion correction. In Sec. 3.2.1 the atomic form factor $f_0(\vec{Q})$ was introduced. Its energy-independent behavior is only true for energies far away from element-specific absorption edges. Near the absorption edges, the element-specific scattering becomes highly energy-dependent, explained by the real $f_1(E)$ and imaginary $f_2(E)$ part in Eq.(3.25) of the anomalous atomic scattering factor.

$$f(\vec{Q}, E) = f_0(\vec{Q}) + f_1(E) + if_2(E) \quad (3.25)$$

In contrast to $f_0(\vec{Q})$, the two dispersion terms are dominated by electrons in the inner shell close to the nucleus, making the \vec{Q} dependence for $f_1(E)$ and $f_2(E)$ very weak. The absorption cross-section is connected to the imaginary part $f_2(E)$ as follows:

$$I = I_0 \cdot e^{-\mu_m l} \quad \text{with} \quad \mu_m = (2r_0\lambda \frac{N_A}{A})f_2(E) \quad (3.26)$$

Here, r_0 is the classical electron radius, $\frac{N_A}{A}$ the number of atoms per gram and ρ the mass density. The imaginary part $f_2(E)$ and thus the absorption become strong for energies above a transition, as seen in Fig. 3.4(b) for Fe. In contrast to the absorption, the elastic scattering cross-section depends on both $f_1(E)$ and $f_2(E)$.

$$A_{hkl} = \sum_{\alpha} [f_0(\vec{Q}) + f_1(E) + if_2(E)] \cdot e^{-2\pi i(hu_{\alpha} + kv_{\alpha} + lw_{\alpha})} \quad (3.27)$$

Close to the absorption edges, the imaginary part becomes significant, and consequently the observed intensities for symmetric Friedels equivalent reflections can differ by 1-3%;

⁸for further details see e.g. [119, 104, 105].

this anomalous scattering can be used to overcome the phase problem. The resonant scattering part $f_1(E)$ is connected with the absorption through $f_2(E)$ by the Kramers-Kronig relations [120]. It is therefore possible to obtain the anomalous scattering from either scattering or absorption spectroscopy independently.

3.3.5 Polarization analysis in x-ray scattering

In Eq.(3.22) we introduced the interaction Hamiltonian H_i , in which we neglected the interactions of the photons with electron spin and orbital moment. The reason for this is that the intensity ratio between magnetic and charge scattering for a single electron is in the order of 10^{-6} (magnetic scattering is a relativistic correction to charge scattering). In this section we will discuss how to determine and separate the magnetic contribution in scattering. In order to do this, we have to expand the interaction Hamiltonian with the magnetic interactions like spin-orbit coupling and Zeeman splitting of the energy levels [121, 118].

$$H_i^* = H_i + H_{Zeeman} + H_{Spin-Orbit} \quad (3.28)$$

A description related to Sec. 3.3.4 with H_i^* , following Blume [118] in the use of Fermi's Golden Rule and time-dependent perturbation theory up to the second order, similar to Eq.(3.24), leads to the equation:

$$\frac{d\sigma}{d\Omega} \propto W_{\substack{\vec{k}_i, \vec{\epsilon}_i \rightarrow \vec{k}_f, \vec{\epsilon}_f \\ |i\rangle \rightarrow |f\rangle}} = \left(\frac{e^2}{mc^2} \right)^2 \left| \underbrace{\langle f | e^{i\vec{Q}\vec{r}} | i \rangle}_{f_{charge}} \hat{\epsilon}_i \cdot \hat{\epsilon}_f - i \frac{\hbar\omega}{mc^2} \cdot f_{magnetic} \right|^2 \quad (3.29)$$

$$\text{where } f_{magnetic} = \langle f | e^{i\vec{Q}\vec{r}} \left(i \frac{\vec{Q} \times \vec{L}_j}{\hbar k^2} \cdot \hat{\epsilon}_1 + \vec{S}_j \cdot \hat{\epsilon}_2 \right) | i \rangle \rho(\epsilon) \quad (3.30)$$

The sums are taken over all electrons with their particular positions, momenta and spins, which are given by \vec{r} , \vec{L}_j and \vec{S}_j respectively. Polarization-dependent scattering for charge and magnetic contributions is described by the scattering amplitudes f_{charge} and $f_{magnetic}$, respectively⁹. For the scattering process the normalized vectors $\hat{\epsilon}_i$ and $\hat{\epsilon}_f$ describe the polarization dependence of the incoming and the scattered photon. For Thomson scattering from free charges, the scattering cross-section is $r_e^2(\hat{\epsilon}_i \cdot \hat{\epsilon}_f)^2$. For an experiment with linear polarized light, the geometry describing the components of the magnetic moments is changed into a fixed relation with respect to the scattering plane, according to Fig. 3.7. It is also better to omit the $\hat{\epsilon}$ polarization term and change to the σ

⁹with $\hat{\epsilon}_1 = \hat{\epsilon}_f \times \hat{\epsilon}_i$ and $\hat{\epsilon}_2 = \hat{\epsilon}_f \times \hat{\epsilon}_i + (\hat{k}_f \times \hat{\epsilon}_f)(\hat{k}_i \cdot \hat{\epsilon}_i) - (\hat{k}_i \times \hat{\epsilon}_i)(\hat{k}_i \cdot \hat{\epsilon}_f) - (\hat{k}_f \times \hat{\epsilon}_i) \times (\hat{k} \times \hat{\epsilon}_i)$

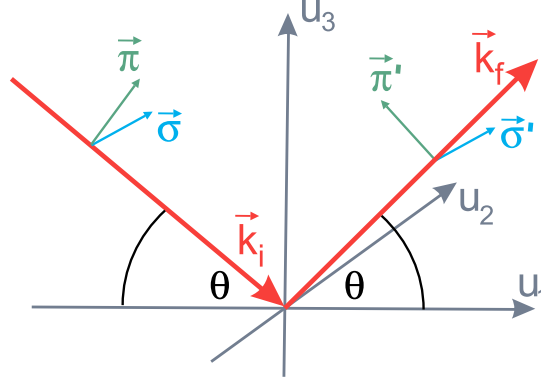


Abbildung 3.7: The definitions and conventions used in this thesis for x-ray full polarization analysis are according to [122].

and π polarization states, which describe the polarization in components perpendicular to and inside the \vec{k}_i and \vec{k}_f scattering plane. Here, S_i and L_i are the components from

Tabelle 3.1: σ and π polarization dependence for pure magnetic scattering.

$ f\rangle \setminus i\rangle$	σ	π
σ'	$S_2 \cos(\theta)$	$[(L_1 + S_1) \cos(\theta) + S_3 \sin(\theta)] \sin(\theta)$
π'	$[-(L_1 + S_2) \cos(\theta) + S_3 \sin(\theta)] \sin(\theta)$	$(2L_2 \sin^2(\theta) + S_2) \cos(\theta)$

the Fourier transformation of the spin and orbital angular momentum along the coordinates u_i respectively [122]. In contrast to charge scattering (see Tab. 3.2), where only diagonal matrix elements exists, for magnetic scattering a change in the polarization state during the scattering process is possible. It is, in principle, even possible for the magnetic part to distinguish between spin and orbital contributions (see Tab. 3.1). Magnetic scattering on separate reflections can only be observed for antiferromagnetic or incommensurate structures, where the magnetic contributions are separate in reciprocal space from the nuclear Bragg peaks. A nice example of separate magnetic reflections is the incommensurate spin order in TbMnO_3 [123] responsible for the multiferroic behavior of this class of materials. For pure isotropic charge scattering, there is no change in the polarization state on scattering as shown in Tab. 3.2. The term proportional to $\cos(2\theta)$ describes the

Tabelle 3.2: σ and π polarization dependence for isotropic charge scattering.

$ f\rangle \setminus i\rangle$	σ	π
σ'	$\rho(\vec{Q})$	0
π'	0	$\rho(\vec{Q}) \cos(2\theta)$

acceleration vector onto a plane perpendicular to the observation direction and thus the

normal dipole field from Thomson scattering. The small magnetic scattering contribution is enhanced by tuning the energy to an element-specific absorption edge.

resonant enhancement scattering

When the energy is tuned close to the absorption edges of a particular element, the transition probability is typically enhanced by a factor of 10^2 for the Fe $L_{2,3}$ edges [124, 125, 126]. Taking only dipole transitions between $|i\rangle$ and $|f\rangle$ into account, the scattering tensor can be expressed by [127]:

$$\begin{aligned} f_{res}^{E1}(E) &= f_0(E) + f_{circ}(E) + f_{lin}(E) \quad \text{with :} \\ f_0(E) &= (\hat{\epsilon}_f \cdot \hat{\epsilon}_i) (F_{+1}^1 + F_{-1}^1) \\ f_{circ}(E) &= i(\hat{\epsilon}_f \times \hat{\epsilon}_i) \cdot \vec{m} (F_{-1}^1 - F_{+1}^1) \\ f_{lin}(E) &= (\hat{\epsilon}_f \cdot \vec{m})(\hat{\epsilon}_i \cdot \vec{m}) (2F_0^1 - F_{+1}^1 - F_{-1}^1), \end{aligned} \quad (3.31)$$

where the $F_m^1 = \alpha_1[(\omega - \omega_{Res}) - \frac{i\Gamma}{2\hbar}]$ terms describes the energy dependent resonator strength as transition probability. The first term describes the anomalous charge scattering and it is independent of the sample magnetization. The second term depends on the direction of the magnetization and consists of matrix elements responsible for the XMCD effect. The polarization dependence shows, that it is possible for magnetic scattering to change the polarization direction of the photons. The last term, depends quadratically on \vec{m} and provides an additional contribution to the magnetic scattering, this term is often neglected.

3.3.6 P09-beamline: full polarization analysis

At the beamline P09 of the PETRA-III synchrotron resonant x-ray experiments were performed. The beamline uses an undulator as x-ray source with a high heat load Si double monochromator followed by a high resolution monochromator, reaching monochromatic photons with 0.3 eV resolution. The available energy range for the photons is from 2.4 keV to 24 keV. The linear incidence polarization from the undulators (99.98% linearly polarized) can be turned from horizontal to vertical (or in in-

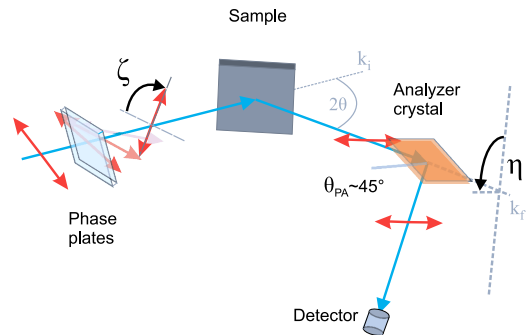


Abbildung 3.8: The scattering geometry for a full polarization analysis experiment, as described in the text. Figure adapted from [128].

intermediate states with any ζ angle), using diamond quarter and half wave plates. The scattered beam can be detected by an APD-detector under an almost $2\Theta_{\text{PA}} \sim 90^\circ$ reflection, from a suitable analyzer crystal¹⁰. To analyze the polarization direction from the scattered beam the whole analyzes setup can be turned around the detector axis (which is parallel to \vec{k}_f) by η . To align different reflections, the sample can be mounted inside a closed cycle cryostat on the six circle diffractometer.

The Stokes' Parameters

In order to achieve the polarization state of the scattered beam \vec{k}_f as a function of incoming beam polarization angle ζ , the intensity for different analyzer angles η is measured by rocking curves of the analyzer crystal. By afterwards fitting the function of Eq.(3.33) to the normalized $I(\eta)$ -curves, as presented in Fig. 3.9, the polarization state can be extract as the commonly used Stokes' parameters P1 and P2 [129].

$$I(\eta) = \frac{I_0}{2} [1 + P1 \cdot \cos(2\eta) + P2 \cdot \sin(2\eta)] \quad (3.32)$$

It is often convenient to collect data at a number of different η positions, in order to achieve a better quality of the fit presented in Fig. 3.9.

The signal is periodic in 180° , thus by rotating the detector with the analyzer crystal stage around \vec{k}_f , as shown in Fig. 3.8, any linear polarization state can be probed. In order to suppress experimental artifacts it is also common to measure the full polarization from the direct beam. Here, it is often found that the polarization behavior is not perfect. This is often an experimental artifact due to $2\Theta_{\text{PA}}$ slightly away from 90° . This can be corrected by changing Eq.(3.32) to:

$$I(\eta) = \frac{I_0}{2} [1 + \cos^2(2\Theta_{\text{PA}}) + P1 \cdot \cos(2\eta) \sin^2(2\Theta_{\text{PA}}) + P2 \cdot \sin(2\eta) \sin^2(2\Theta_{\text{PA}})]. \quad (3.33)$$

3.3.7 SIM-beamline: soft x-ray magnetic scattering

The Surface/Interface Microscopy (SIM) beamline located at the Swiss Light Source (SLS) is a soft x-ray beamline. As already described in Sec. 3.3.4, photons in this energy

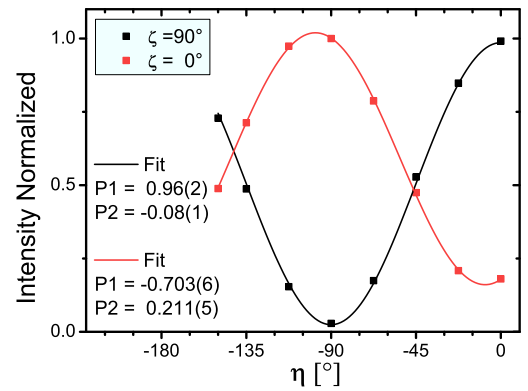


Abbildung 3.9: $I(\eta)$ -curves for different incoming ζ polarization states. The curves for $\zeta = 0^\circ$ and 90° are fitted by Eq.(3.32) in order to achieve the Stokes' parameters P1 and P2. Measured on the $(\tau \tau \frac{27}{2})$ reflection of LuFe_2O_4 at 85 K.

¹⁰This scattering geometry suppresses the π' intensity.

range are a unique tool to probe the magnetism and orbital order in the $3d$ states of the transition metal elements. Due to the short wavelength for soft x-rays, the reciprocal space is very restricted, making it difficult to access Bragg reflections. A good pre-alignment of the sample is essential to bring the Bragg reflections (often only one is accessible) into scattering condition. The x-rays are created by two undulators, capable of producing incident light with any arbitrary polarization within an energy range from 90 eV to 2 keV with full control over the polarization. A collimating mirror is followed by a second mirror and a plane grating monochromator, which then further collimates by slits. The beam can be refocused by an additional mirror to produce a focused spot size of $10\text{ }\mu\text{m} \times 100\text{ }\mu\text{m}$ inside the RESOXS end-station [130]. The scattering inside the RESOXS end station of Fig. 3.10 takes place in a horizontal plane. Here, the polarization analysis is performed using graded multilayers, which are translated and rotated in the vacuum chamber. The polarization analysis of the scattered beam is a rather unique technique. Currently, only two soft x-ray beamlines are capable to offer a full polarization analysis.

For such experiments, the absorption is very high; in order to avoid strong beam attenuation the experiment has to be performed within an ultra-high vacuum (better than 10^{-8} mbar). The sample is mounted on a cold finger, which is connected to a liquid-He cryostat covering a temperature range from ~ 20 to 300 K. The penetration depth for soft x-ray photons is in the range of a couple of hundred nm (depending on probing material and used photon energy see Sec. 3.3.4). Therefore, the sample surface has to be clean (a in-situ cleaved sample is better) to avoid strong surface effects. This set-up is capable of performing full polarization analysis on the Fe $L_{2,3}$ -edges, which is important to determine the origin of the Bragg scattered signals by separating magnetic, charge and orbital contributions.

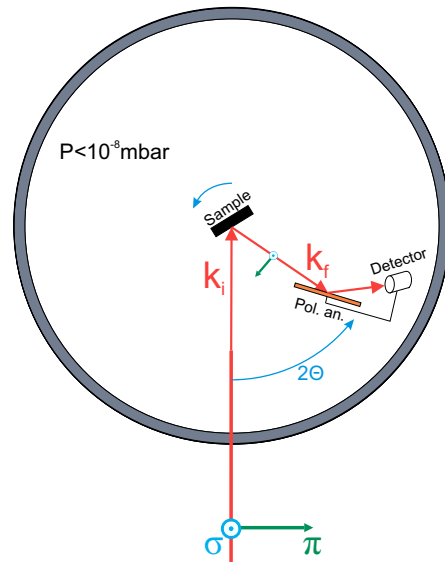


Abbildung 3.10: The RESOXS endstation with the possible π and σ incoming polarization states.

3.3.8 X-ray magnetic circular dichroism

As mentioned in Sec. 3.3.4, for resonant scattering the dipole transition selection rules must be fulfilled to get a non vanishing matrix element; this is obtained only if the orbital

quantum number follows $\Delta l = \pm 1$ for a particular transition. As shown in Sec. 3.3, the absorption probability for a photon, according to Fermi's golden Rule, is proportional to the density of unoccupied states above the Fermi level convoluted with the transition matrix element $V_{if} = \langle f | \vec{A} \cdot \vec{p} | i \rangle$ for a particular dipole transition. The polarization dependence of the incoming light is included in the electro-magnetic-field vector $\vec{A}(\vec{r}, t)$. Circularly polarized light has its own angular momentum depending on the polarization state, $J_z = \hbar$ for right circularly polarized light (RCP) and $J_z = -\hbar$ for left circularly polarized (LCP) light. In the case of spin-polarized photon absorption, the photon angular momentum J_z must be transferred to the sample, giving rise to additional selection rules for the absorption process of both circular polarizations states. These additional selection rules affect both spin $|m_s\rangle$ (spin-flip transitions are forbidden) and angular orbital moment states $|m_l\rangle$ (takes over the photon angular moment), leading to a dichroism in the x-ray absorption spectrum (XAS) $\mu_{\pm}(E)$ between RCP and LCP light. These selection rules describe only the change of dipole fields, because only dipole transitions are considered, as the wavefunction of bound core level electrons only has a small spread in comparison with the used soft x-ray wavelength [131].

$$\Delta m_l = \begin{cases} +1, & \text{RCP} + \text{photons} \\ -1, & \text{LCP} - \text{photons} \end{cases} \quad (3.34)$$

In order to achieve a proper degeneracy of the orbital states by the Zeeman effect, the magnetic field \vec{H} at the sample has to be applied parallel or anti parallel to the photon direction \vec{k} . If the magnetization is antiparallel to the photon wave vector the selection rules for m_l are reversed. For the transition metal elements, an absorbed photon will lead to the transition of electrons into the partially filled $3d$ states from $2p_{3/2}$ (L_3 -edge) and $2p_{1/2}$ (L_2 -edge) core levels. In Fig. 3.11 all allowed transitions are presented with their probability for RCL light ($\Delta m_s = 0$ and $\Delta m_l = +1$). With XMCD it is possible to probe the spin polarization of unoccupied $3d$ -states. The x-ray magnet circular dichroism (XMCD) signal is the difference between both XAS spectra $\mu(E) = \mu_+(E) - \mu_-(E)$.

First, the absorption effect for spin-polarized $3d$ shells is discussed here. The probability of reaching a $3d$ state with $m_s = -1/2$ from the $2p_{1/2}$ state is 75%, and from the $2p_{3/2}$ state it is 37.5%¹¹ according to Fig. 3.11. The spin polarization thus shows an opposite spinpolarization behavior between both L edges. There are twice as many transitions from the $2p_{3/2}$ state as from the $2p_{1/2}$, so a zero total spinpolarization would be

¹¹This means a spin expectation value of $\langle \sigma \rangle = -1/4$ and $\langle \sigma \rangle = 1/8$ for both edges. Note that a value of $\langle \sigma \rangle = 1/2$ means full up spin polarization.

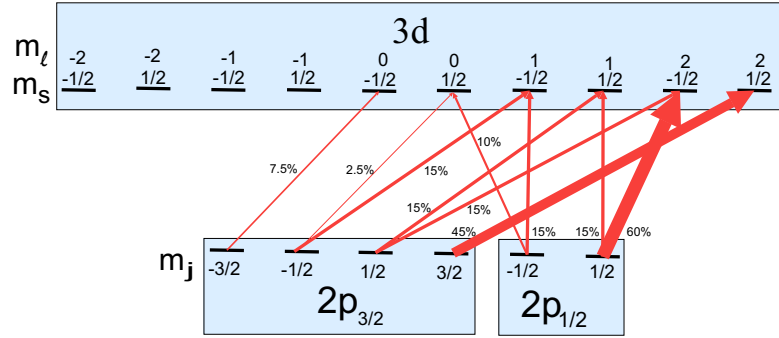


Abbildung 3.11: The transition probability for the different $2p \rightarrow 3d$ excitation with right circularly polarized (RCP) light to empty d continuum states in a solid (according to [132, 126]). The excitation is separated in transitions from the core $2p_{1/2}$ (L_2) levels and the $2p_{3/2}$ (L_3) levels. Note that here the magnetization of the sample is assumed to be anti parallel to the photon wave vector ($\Delta m_l = +1$).

expected. This is not the case, due to the fact that the L_3 and L_2 edges are energetically separated with ~ 14 eV, by spin-orbit-coupling. With these spin-polarized transitions for both edges, the unoccupied spinpolarized states in the $3d$ states can now be probed. The spin polarization from unoccupied states is defined by the sample magnetization: a high absorption is observed if both spin polarizations agree with each other. By turning either the magnetic field or the photon polarization, a lower absorption is observed. The spinpolarization for the L_3 and L_2 edges have opposite behavior, leading to an opposite dichroism signal for the L_3 and L_2 -line.

For the excited states, the same orbital expectancy values $\langle m_l \rangle = 3/2$ for both transitions (see Fig. 3.11) are observed, because only $m_l \geq 0$ are occupied for RCP light (for LCP all signs are changed). When the photon polarization is reversed, the polarization of the excited electron is reversed as well. According to [126], spin-dependent absorption can thus be described as a two-stage process. First, a circularly polarized photon excites a photoelectron from the core level. These initially un-polarized electrons gain a spin polarization during this interaction. In the second state, this electron is captured into an unoccupied valence state. The transition rate depends on the number of available final states with spin parallel to the photoelectron spin. Since the photoelectron spin is governed by the helicity of the absorbed photon, the transition rate becomes different for LCP and RCP light. If the d shell is completely empty or half-filled no dichroism signal is observed, because no or all electronic states with the quantum numbers m_l and m_s are half full. When the $3d$ shell is partially filled and an angular momentum exists the dichroism signal will point in the same direction for the L_3 and L_2 edge.

The XMCD technique has become popular since a direct and separate observation

of orbital moment m_{orb} and spin moment m_{spin} can be obtained from the so-called sum rules. Due to distinctive element specific transition energies (and from the chemical shift even valence-specific), a separation of magnetic contributions for different elements and even valences is possible. These sum rules relate the spin and orbital moment to the integrated intensity from the XMCD dichroism signal over particular absorption edges as follows [133, 134].

$$m_{orb} = -\frac{4 \int_{L_2+L_3} (\mu_+ - \mu_-)}{3 \int_{L_2+L_3} (\mu_+ + \mu_-)} n_h \mu_B \quad (3.35)$$

$$m_{spin} = -\frac{6 \int_{L_3} (\mu_+ - \mu_-) - 4 \int_{L_3+L_2} (\mu_+ - \mu_-)}{3 \int_{L_2+L_3} (\mu_+ + \mu_-)} n_h \mu_B \quad (3.36)$$

For transition metal oxides the observed intensity, according to Fermi's Golden Rule, is proportional to n_h , the number of empty 3d states which are close to the Fermi energy. By dividing the equations by each other the spin to orbital moment relation can be achieved with the values p (the integrated XMCD signal of the L_3 edge) and q (the integrated XMCD signal over the whole $L_{2/3}$ edge), respectively.

$$\frac{m_{orb}}{m_{spin}} = \frac{2q}{9p - 6q} \quad (3.37)$$

These sum rules, however, were derived from a simple model containing a single ion in a crystal field with its valence shells only partially filled. Thus, there are still some questions as to the validity and range of applicability of this sum rule to real condensed matter systems, such as transition metals with their strongly sp -hybridized multiband structure. It has been shown [135, 136] that typical errors for m_{orb}/m_{spin} from the sum rules are in the range of 10% for XMCD measurements.

3.3.9 4-ID-C: X-ray magnetic circular dichroism

In contrast to the experiment discussed in the previous section, the end-tation of the soft x-ray beamline 4-ID-D at the Advanced Photon Source (APS) is used for spectroscopy; this avoids the problem of accessible limited reciprocal space. Similar to diffraction, the spectroscopy methods in this energy range are a unique tool to probe the magnetism from the transition metal elements directly as shown in Sec. 3.3.8. The electromagnetic helical undulator of beamline 4-ID-C provides the connected endstation with x-rays in the soft x-ray regime, with either left circular polarized (LCP) or right circular polarized (RCP) x-rays. The energy is selected by a spherical grating monochromator covering an energy spectrum (500 - 2700 eV) with a typical energy resolution of $E/\Delta E \sim 5000$. The

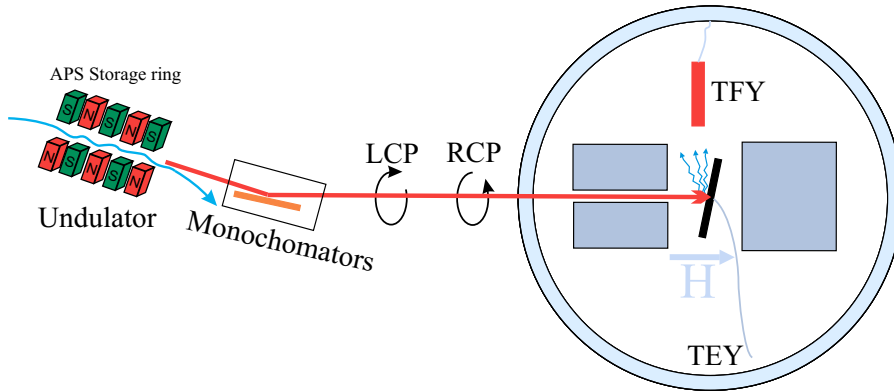


Abbildung 3.12: The 4-ID-C x-ray magnetic circular dichroism endstation. The energy band of the white x-ray beam produced by the undulator is strongly narrowed by different monochromators. The sample is mounted between the pole pieces of a superconducting magnet, where the magnetization direction \vec{H} is (anti)parallel to the incoming beam direction \vec{k}_i with either RCP or LCP light. The x-ray absorption spectra can either be measured by the total electron yield (TEY) signal or by the total fluorescence yield (TFY). The TFY signal is measured by an energy dispersive diode.

x-ray absorption spectrum is measured in the high magnetic field endstation, allowing for magnetic fields up to $H = 6.5 \text{ T}$ parallel and antiparallel to the incoming photon direction. According to the x-ray absorption process discussed in Sec. 3.3.4, there are, in addition to directly observed attenuation of the transmitted beam, two different ways to detect the x-ray absorption spectra necessary for calculating the dichroism signal. First, the absorption spectra can be detected by the electrons detached from the atoms in total electron yield (TEY) mode. To measure the TEY signal, the sample was mounted on a conducting adhesive tape. In addition to the TEY mode, the fluorescence from photonic excited electrons falling back into their ground state can be measured in total fluorescence yield (TFY) mode by an energy-dispersive diode. The undulators from the beamline 4-ID-C are capable of switching rapidly between the generation of right and left circular light, allowing for direct recording the magnetic dichroism signal (XMCD) of Sec. 3.3.8 at each energy position, thereby minimizing the systematic errors and measurement time for a particular spectrum.

3.4 Neutron scattering

The wavelength of neutrons propagating in space can be described in terms of waveparticle duality by the de Broglie formalism $\lambda_n = \sqrt{h^2/2m_n E}$. In contrast to x-rays, neutrons have a strong magnetic moment of $-1.91\mu_N$, making them additionally sensitive to the

magnetic structures. This is considered in the scattering potential $V_n(\vec{r}) = V_N(\vec{r}) + V_M(\vec{r})$, making a separate consideration of nuclear and magnetic scattering for neutrons possible.

3.4.1 Nuclear scattering

The inter-atomic distances for crystals are in the range of Å; to probe this scale with neutrons, they need an energy of about 25 meV to achieve a wavelength of ~ 1 Å. For atomic scattering the neutron is not sensitive to the electronic shell; it only interacts with the nucleus of an atom via the strong nuclear force. Because the size of the nucleus and the radius of the nuclear interaction force are much smaller than the neutron wavelength, the assumption of a delta potential in the Fermi pseudo-potential (3.38), describing the scattering potential, is used.

$$V_N(\vec{r}) = \frac{2\pi\hbar^2}{m_n} b_i \delta(\vec{r} - \vec{r}') \quad (3.38)$$

In Eq.(3.38) the scattering length b_i depends strongly on the nuclei-neutron interaction; it differs intensely for different elements or even for the isotopes of one element. The scattering amplitude for neutrons is similar to that for x-rays, although the atomic form factor is independent of \vec{Q} .

$$N(\vec{Q}) = \sum_j b_j e^{i\vec{Q}\vec{r}_j} \quad (3.39)$$

The values for b_i can be negative, depending on the phase shift the scattered neutron undergoes. Most of the elements in the periodic table consist of different isotopes; the scattering length for different isotopes from one element can vary remarkably, due to the different internal structure of the nuclei. In order to describe a nuclear scattering process, we have to average over the average isotope distribution.

$$\frac{d\sigma}{d\Omega} = \left\langle \sum_j b_j e^{i\vec{Q}\vec{r}_j} \sum_i b_i^* e^{-i\vec{Q}\vec{r}_j} \right\rangle = \langle b \rangle^2 \left| \sum_j b_j e^{i\vec{Q}\vec{r}_j} \right|^2 + N \langle (b - \langle b \rangle)^2 \rangle \quad (3.40)$$

In Eq.(3.40) only the first term contains the phase information. This term can contribute to coherent scattering with constructive interference, whereas the second term does not carry the phase information. It corresponds to incoherent scattering, which contributes equally in all directions and therefore gives rise to an isotropic background in experiments. Values for the scattering length of the isotopes of all elements is given in [137].

3.4.2 Magnetic scattering

Because neutrons have an intrinsic magnetic dipole moment $\vec{\mu}_n$, they interact with the magnetic moment of electrons. The magnetic scattering potential for neutrons $V_M(\vec{r}_M)$,

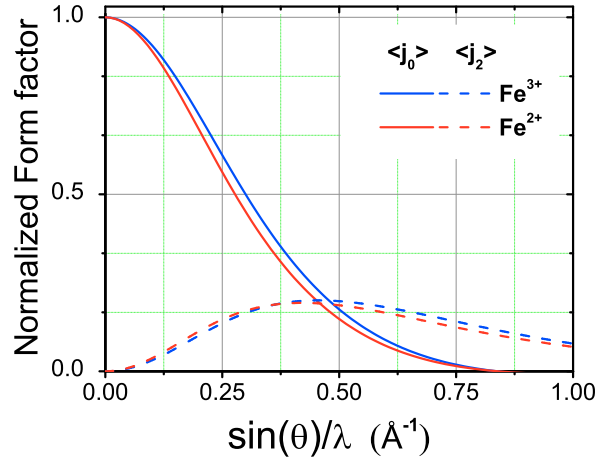


Abbildung 3.13: Neutron magnetic form factors for both spin and their orbital contributions, represented for the different Fe^{2+} and Fe^{3+} valences. Presented data taken from [138].

in (3.41) describes this interaction with magnetic moments from unpaired electrons \vec{B}_{spin} or unquenched orbital moments $\vec{B}_{orbital}$.

$$V_M = -\vec{\mu}_n \cdot \vec{B} \quad \text{with} \quad \vec{B} = \vec{B}_{orbital} + \vec{B}_{spin} \quad (3.41)$$

The magnetic scattering cross section for a process, where the neutron changes its wave vector and the projection of its spin moment from the quantization axis z from σ_z to σ'_z can be expressed in the first Born approximation with the already introduced scattering potential V_M . For further details see [139].

$$I(Q) \propto \frac{d\sigma}{d\Omega} = (\gamma_n r_0)^2 \left| -\frac{1}{2\mu_B} \langle \sigma'_z | \hat{\sigma} \cdot \vec{M}_\perp(\vec{Q}) | \sigma_z \rangle \right|^2 \quad (3.42)$$

In Eq.(3.42), only magnetization contributions perpendicular to the scattering vector $\vec{M}_\perp(\vec{Q})$ can be measured by any sort of neutron scattering experiment.

$$\vec{M}_\perp(\vec{Q}) = \frac{\vec{Q}}{|\vec{Q}|} \times \vec{M}(\vec{Q}) \times \frac{\vec{Q}}{|\vec{Q}|} \quad \text{with} \quad \vec{M}(\vec{Q}) \propto \int \vec{M}(\vec{r}) e^{i\vec{Q} \cdot \vec{r}} d^3r \quad (3.43)$$

In Eq.(3.42) $\vec{M}_\perp(\vec{Q})$ is the perpendicular component to the scattering plane of the Fourier-transformed magnetic moment as seen in Eq.(3.43). In contrast to nuclear scattering, for magnetic scattering there exists a form factor. This can most easily be understood for the case of pure spin scattering (no orbital contributions present). In Eq.(3.43) the macroscopic magnetic moment $\vec{M}(\vec{Q})$ can be treated for every atom and its surrounding electrons with spin moments \vec{s}_i , separate, leading to Eq.(3.44).

$$\vec{M}(\vec{Q}) = -2\mu_B \cdot f_m(\vec{Q}) \cdot \sum_i e^{i\vec{Q} \cdot \vec{r}_i} \cdot \vec{s}_i \quad \text{with} \quad f_m(\vec{Q}) = \int_{Atom} \rho_s(\vec{r}) e^{i\vec{Q} \cdot \vec{r}} d^3r \quad (3.44)$$

Here, f_m is the magnetic form factor as a Fourier transformation of the spin density distribution of a single atom. The magnetic scattering takes place in the electron cloud of the atom; this situation is comparable to the atomic form factor for x-rays. However, only the unpaired electrons in the outer shells contribute to the magnetic moment, and thus a stronger decrease for the \vec{Q} dependence is expected compared to x-ray scattering (for comparison see Fig. 3.13 with Fig. 3.3). The magnetic form factor (in the dipole approximation) describing the Q -dependence of the magnetic neutron scattering cross-section of a single magnetic ion can indeed be described as:

$$F_{mag} = \langle j_0 \rangle(k) + \left(1 - \frac{2}{g}\right) \langle j_2 \rangle(k), \quad (3.45)$$

where different coefficients adequately approximate $\langle j_0 \rangle(k)$ and $\langle j_2 \rangle(k)$, which are determined experimentally [138]. In the case of spin-only scattering the effective gyromagnetic ratio is $g = 2$, which describes the scattering by $\langle j_0 \rangle(k)$.

Neutron polarization analysis

The scattered neutron interacts with the underlying sample magnetic dipole structure, allowing the determination of the sample magnetization direction. The total scattering process can be described by the following equations, derived by Blume [140, 141] and Maleyev [142] where N denotes the nuclear scattering contribution:

$$\begin{aligned} \sigma_{\vec{Q}} = & \sigma_{\vec{Q},coh}^N + \sigma_{\vec{Q},isotop-inc}^N + \sigma_{\vec{Q},spin-inc}^N \\ & + \left| \vec{M}_{\vec{Q}}^\perp \right|^2 + \vec{P} \left(N_{-\vec{Q}} \vec{M}_{\vec{Q}}^\perp + \vec{M}_{-\vec{Q}}^\perp N_{\vec{Q}} \right) + i \vec{P} \left(\vec{M}_{-\vec{Q}}^\perp \times \vec{M}_{\vec{Q}}^\perp \right) \end{aligned} \quad (3.46)$$

From Eq.(3.46) it is clear that for un-polarized neutrons $\vec{P} = 0$ only the square of the structure $N_{\vec{Q}}$ factor and the magnetic component $|\vec{M}_{\vec{Q}}^\perp|^2$ can be achieved. The chiral spin correlations produce a scattering cross-section represented by the cross product, and the nuclear-magnetic interferences are not observable for such a case. For a neutron scattering process on magnetic materials, we can sum up the most important selection rule: the neutron polarization (\vec{P}) direction will be reversed (spin-flip) if the polarization is $\vec{P} \parallel \vec{Q}$ and $\vec{P}, \vec{Q} \perp \vec{M}$. For more details on neutron polarization analysis see e.g. [143].

3.5 Neutron scattering experiments

As already pointed out in Sec. 3.4, neutrons, with their intrinsic magnetic moment, are a perfect probe for determining the magnetic correlations and order parameters inside a particular sample.

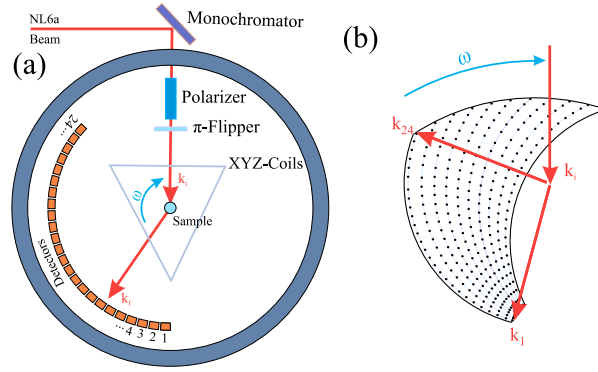


Abbildung 3.14: (a) The DNS instrument with its 24 detectors. The sample can be rotated by ω in the scattering plane, and the polarization direction can be adjusted by the XYZ coils in all directions. (b) Shows a schematic measurement with a sample rotated by 5° ω -steps and the resulting measured map of reciprocal space; where each point on the lines indicates a detector position (one detectorbank position).

3.5.1 DNS Diffuse Neutron Scattering instrument

The Diffuse Neutron Scattering (DNS) instrument located at the FRM2 reactor is designed for collecting intensity from a broad region in reciprocal space in order to observe diffuse magnetic correlations. It is capable of performing full polarization analysis on magnetic single crystals or powder, allowing the separation of nuclear coherent, spin incoherent and magnetic scattering contributions. The PG(002) double focusing monochromator allows a wavelength cover in the range of $2.4 \text{ \AA} < \lambda < 6.0 \text{ \AA}$. The entering beam is polarized, and the polarization direction can be reversed by a π flipper. In order to perform a full polarization analysis, the DNS is equipped with XYZ Helmholtz coils, which have the capability to generate a magnetic field pointing in any direction and thus change the incoming neutron polarization in the same direction [143]. The diffracted neutrons and their remaining polarization direction are detected by 24 detector tubes filled with ^3He gas, making an efficient collection of scattered neutrons possible. For polarization analysis, the detectors are equipped with $m = 3$ super-mirrors. All detectors cover a scattering angle of $0^\circ < \theta < 135^\circ$. Because of the dark angle between individual detectors, multiple detector-bank positions are necessary to ensure a hole-free mapping of the reciprocal space. Low temperatures, down to 10 K, are realized by a He cryostat. The raw data obtained from the detectors during measurement was corrected for deviating detector efficiency by a vanadium reference sample, which is an almost pure spin-incoherent scatterer.

3.5.2 D23 Neutron Diffraction

The thermal neutron two-axis diffractometer D23 at the ILL is devoted to single crystal measurements, either with an un-polarized or half-polarized scattering setup. In contrast to the DNS experiment, it is equipped with a point detector for measuring integrated intensities, necessary for proper magnetic structure refinement. The range of the incident wave length is between $1\text{\AA} < \lambda < 3\text{\AA}$ and is characterized by a high flux and a very good signal to noise ratio. The goniometer can support large sample environments. In our experiment a cryomagnet with horizontal fields up to 4 T was used. The scattered neutrons are detected with a lifting ^3He detector mounted in an arc allowing for rotation around the sample of $\sim \pm 130^\circ$ in the horizontal plane and a possible rotation by $\sim \pm 30^\circ$ out of the horizontal plane.

3.6 Sample preparation

3.6.1 Powder preparation of LuFe_2O_4

The polycrystalline $\text{LuFe}_2\text{O}_{4-\delta}$ samples were prepared via a solid-state reaction. The starting material, a stoichiometric mixture of Lu_2O_3 and Fe_2O_3 powders, was ground in an agate mortar for 120 minutes.

The sample was then heated up to 1290°C in a tube furnace for 8 h in an atmospheric mixture of $(\text{Ar})_{96\%}(\text{H}_2)_{4\%}$ and CO_2 gases in order to control δ , the oxygen stoichiometry. Then the sample was rapidly cooled down to room temperature (in about 10 min) inside the tube furnace, under the corresponding atmospheric conditions. For samples which were cooled down faster under normal atmosphere (outside the furnace) a rapid surface oxidation was observed. The phase homogeneity of the synthesized samples with different gas ratios was afterwards checked by room temperature x-ray powder diffraction in Fig. 3.15 with $\text{CuK}\alpha_1$ radiation. Here, for samples with gas ratios smaller than three, impurity peaks of $\text{Lu}_2\text{Fe}_3\text{O}_7$ [144] are present. These impurities indicate atmos-

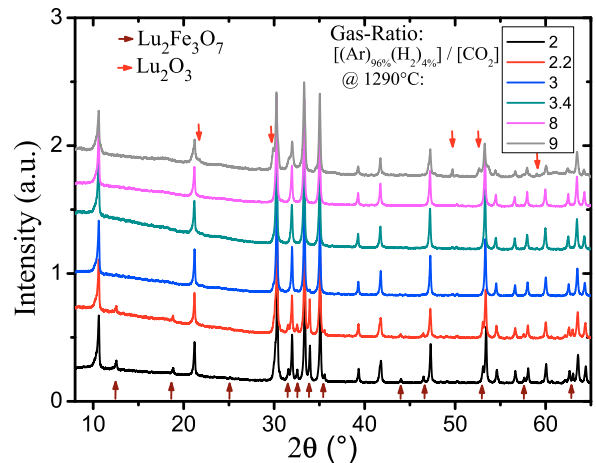


Abbildung 3.15: The LuFe_2O_4 powder grown at 1290°C , in different atmospheric conditions as described in the text. Arrows indicate peaks from impurity phases.

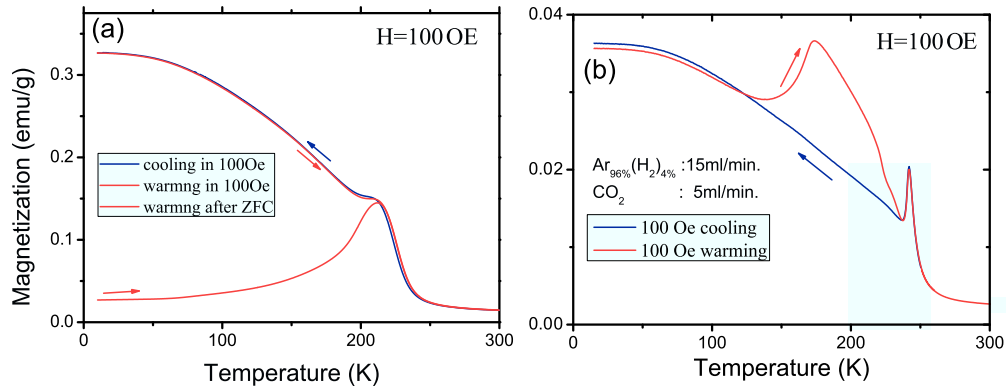


Abbildung 3.16: (a) Magnetization curves as a function of temperature $M(T)$ for a sample with a gas ratio of four, as mentioned in the text. Here the magnetization was measured after Zero Field Cooling (ZFC) in 100 Oe and during field cooling and warming (also 100 Oe). (b) The magnetization curves for samples with a gas ratio close to three.

pheric conditions where the partial pressure of oxygen is too high, following the phase diagram of [76]. According this phase diagram Hematite (Fe_2O_3) should also be present in this inhomogeneous powder. Since Fe_2O_3 is a very weak x-ray scatterer, it is difficult to determine the presence of small amounts by powder diffraction. However, at room temperature there were minor amounts of red material present (even after several sintering processes). This could be separated and identified as Fe_2O_3 . On the other side, for gas ratios bigger than 8 in Fig. 3.15, impurities of FeO and Lu_2O_3 were observed, indicating that the partial pressure of oxygen was too low [76] during synthesis. From the powder preparation here presented it is apparent that at 1290°C a broad region exists, in which a homogeneous phase of LuFe_2O_4 is stable. In order to investigate the properties of LuFe_2O_4 powder in this stable region, all samples were characterized by magnetization measurements in Fig. 3.16. Here, for most of the samples a broad transition at around ~ 220 K into a phase with net magnetic moment is observed (even in Fig. 3.16a at low magnetic fields of 100 Oe). However, for one of the powder samples a sharp transition at about 240 K is in Fig. 3.16b observed on both cooling and warming. The magnetic behavior will be discussed in detail for LuFe_2O_4 single crystals in Sec. 4.1. As will be shown in that section the samples with the sharp magnetic feature at around 240 K seems to be the best in oxygen stoichiometry. For this powder sample a gas ratio at the higher oxygen stoichiometry side of ~ 3 was used. The reproducibility with similar gas ratios was not always successfully. For powders synthesized under similar conditions, huge fluctuations in magnetization were observed. This behavior in synthetization already indicates the fragile region for almost perfect oxygen stoichiometric samples. Furthermore, a similar

behavior was also found in the phase diagram of [76], where only samples synthesized under higher oxygen partial pressure (in the $\text{LuFe}_2\text{O}_{4-\delta}$ single-phase region) show an oxygen stoichiometry very close to four. After high quality LuFe_2O_4 powder is prepared first attempts on stoichiometric single crystal growth are performed.

3.6.2 Single crystal growth

The LuFe_2O_4 single crystal samples studied in this work were grown by the floating zone method, in order to achieve the right oxygen stoichiometry [78] the growth process was carried out under an atmospheric gas mixture of CO_2 and CO gas (both with a purity better than 99,95%). To achieve a high accuracy the gas flow of each gas was controlled separate by a mass flow controller. A couple of crystal syntheses were also performed during the work presented here¹², but none of them show the magnetization behavior

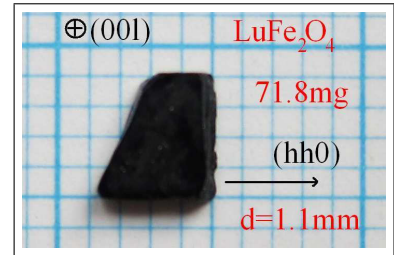


Abbildung 3.17: The LuFe_2O_4 single crystal used for neutron experiments in this and other work [1].

of Fig. 3.16b, which is expected for high stoichiometric samples. As shown in Sec. 4.1, the magnetic behavior [145] of the crystals depend strongly on the oxygen stoichiometry, which is difficult to control [146] precisely during the growth. In parallel to the crystals grown for this work, various samples from the same batch as used in the reference [1, 85] were analyzed for their magnetic behavior. Some crystals of this batch were of the high required quality as proposed in Fig. 3.16b. Some of these samples were already used in previous x-ray, neutron and Mössbauer spectroscopy measurements [85, 28, 93]. All samples used for the various techniques presented later in this work were pre-characterized for their magnetic behavior; see therefore Sec. 4.1. For all the neutron diffraction studies, the biggest LuFe_2O_4 sample, available from the high quality batch (also used in [1]) was used, see Fig. 6.4. Due to the layered structure of LuFe_2O_4 with its extremely long c axis, the sample easily cleaved perpendicular to this direction, providing a high quality surface, e.g. for soft x-ray scattering.

¹²In order to avoid water inclusions into the crystal structure, the single-crystal growth must be performed with CO gas instead of H_2 . Due the toxicity of the CO gas, various security systems needed to be installed, resulting in a substantial time delay for the single crystal growth.

Macroscopic characterization of LuFe_2O_4

4.1 Huge variety in magnetic properties

In the literature, and in the powder preparation of Sec. 3.6.1, a huge variety of magnetic behaviors is reported for LuFe_2O_4 , where LuFe_2O_4 typically exhibits magnetic order or freezing below about 220 K to 240 K. Despite the differences, there is a consensus that the Fe spins have a strong preference to be aligned $\parallel c_{\text{Hex}}$, perpendicular to the layers, as shown for example in [90, 1, 36, 79, 92, 147, 81, 148]. This anisotropy is also found in samples of best quality (type-A in magnetization, see later) where significant differences in magnetization M are found between an applied magnetic field H along c_{Hex} and perpendicular to it; see therefore Fig. 4.1. The magnetic behavior thus arises from Ising spins on triangular lattices. Due to this highly frustrated magnetic arrangement [149] many unusual effects have been observed in different types of samples, including various cluster or spin glass states [147, 89], a magnetostructural transition at $T_{LT} \sim 170$ K [28, 1] and an anomalous “field-heating-effect” [79].

Serious sample-to-sample variations in magnetic behavior are found; these are attributed to tiny variations in oxygen stoichiometry [76, 148]. In this chapter an extensive study of the magnetization behavior of LuFe_2O_4 is presented. For the isostructural compound, $\text{YFe}_2\text{O}_{4\pm\delta}$ (δ indicates off-stoichiometry), a strong sample-to-sample dependence on the physical properties has been found, which are very sensitive to the oxygen stoichiometry. Here, an increasing “parasitic ferrimagnetism” [150] is present for larger δ values, but antiferromagnetic behavior and an additional low T phase transition

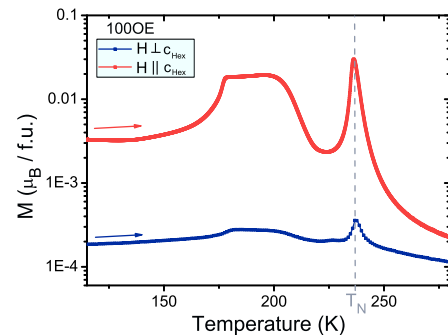


Abbildung 4.1: DC magnetization measurements $M(T)$ of a type A sample at 100 Oe along two different sample orientations, with H parallel (\parallel) and perpendicular (\perp) to the c_{Hex} direction.

for more stoichiometric samples $\delta < 0.03$ [151, 152]. In $\text{ErFe}_2\text{O}_{4\pm\delta}$ similar behavior was observed, but with an even narrower range for δ to reveal an AFM behavior [153]. For LuFe_2O_4 , so far no clear evidence of an AFM behavior has been found. If AFM behavior is an indicator for oxygen stoichiometry in the class of ReFe_2O_4 materials, this would suggest that the region of oxygen stoichiometry is very fragile for LuFe_2O_4 . As already reported by Sekine *et al.* [76], the right conditions for the synthesis of high stoichiometric powder samples are narrow.

In order to estimate the influence of a different oxygen stoichiometry on the sample quality of LuFe_2O_4 , a huge amount of crystals from the same batch as used in [85, 1, 93, 28] was analyzed for their magnetic characteristics. With respect to the strong Ising spin behavior along the c_{Hex} direction, for all DC and AC magnetic measurements (see Sec. 3.1) the field H was applied along this easy magnetic axis. Because of the layered structure of LuFe_2O_4 the crystals cleave easily perpendicular to the c_{Hex} direction creating nice facets in this plane what makes a fast alignment of the samples possible. The results from the magnetization versus temperature measurement are presented in Fig. 4.2; strong deviations are present in $M(T)$ -curves even between samples from one batch. From all

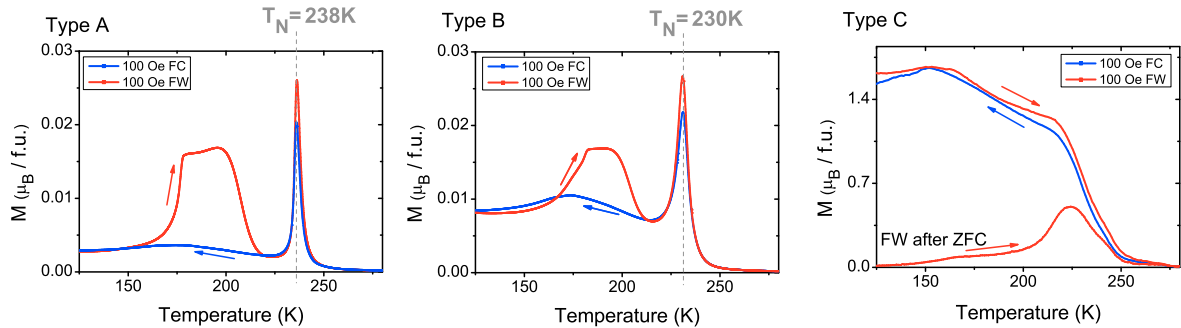


Abbildung 4.2: Magnetization measurements as a function of temperature on both field cooling (FC) and field warming (FW) in a magnetic field of $H = 100 \text{ Oe}$ applied parallel to the hexagonal c_{Hex} direction. The labeled A, B and C type indicates the magnetic behavior for different LuFe_2O_4 oxygen stoichiometry (see text). For the type C sample, a measurement upon warming in 100 Oe after Zero Field Cooling (ZFC) is additionally shown.

of these measured $M(T)$ -curves, the magnetization could roughly be classified into three categories. These different types will be discussed below, and they are presented for comparison in Fig. 4.2 with its representative magnetization curves.

1. The type A samples in Fig 4.2 exhibit a sharp peak at about 238 K in $M(T)$ -curves under cooling in low magnetic fields of 100 Oe. This is the Néel Temperature

T_N where the reported ferrimagnetic 3D long-range spin order first mentioned in [1] appears. At the lower temperature side the magnetization drops in the vicinity of T_N almost to the magnetization value from before the transition. Upon further cooling, there is a small change in the slope of $M(T)$ at ~ 175 K. This is the temperature region where a second phase transition at T_{LT} is reported [28], associated with the development of a structural distortion. Below this transition, the magnetization seems to be stable and no indications for additional transitions are found in $M(T)$ -curves. However, the magnetization behavior changes drastically when the sample is warmed (red curve in Fig. 4.2) across the low-temperature transition T_{LT} : a drastic increase of the magnetization is observed, which reaches a plateau value until ~ 220 K, where it drops back to the initial low value of M already reached under cooling. This behavior was previously observed on polycrystalline LuFe_2O_4 by Iida *et al.* [79] where it was called the “anomalous field-heating-effect”. This unusual magnetic effect disappears at about ~ 218 K, and upon further warming the Néel Temperature T_N is observed at the same temperature as it was on cooling.

Another interesting point for this type of samples is that, in the AC susceptibility measurements with different driving frequencies presented in Fig. 4.3, no frequency splitting could be observed at T_N . This is in contrast to various publications [88, 147] which report the appearance of a magnetic glassy state at T_N , indicated by frequency splitting. In contrast to T_N for the type A samples presented here the transition at T_{LT} is associated with a frequency splitting presented in Sec. 4.2.3.

2. The type B samples presented in Fig. 4.2 show a similar behavior as the type A in $M(T)$ -curves, with a sharp transition at T_N . But the observed transition temperature T_N is shifted to slightly lower temperature values and the remaining magnetization below T_N is much higher compared to the type A samples. Additionally, in AC susceptibility a small frequency splitting is observed. These observations indicate weakened magnetic correlations concomitant with glassiness and parasitic ferrimagnetism. Again, for this kind of samples, upon warming through T_{LT} the anomalous “field-heating-effect” [79] effect could be observed.
3. Compared to the type A and type B samples, the type C samples do not show any sharp peak under cooling in $H = 100$ Oe in the region of $T_N \sim 240$ K. A strong continuous increase of the magnetization M for lower T is observed in Fig. 4.2 around ~ 250 K, indicating the entrance into a phase with a net magnetic moment.

In contrast to both previously discussed types, the magnetization reaches a much higher overall value at lower temperatures (in similar 100 Oe) and no anomalous “field-heating-effect” is observed in this kind of sample upon warming through T_{LT} . For samples showing this behavior, there are no reports about a low-temperature phase transition around T_{LT} . An interesting point to mention here for this type is that the field warming curve after zero field cooling (ZFC) exhibits a considerably lower magnetization, indicating that there are ferro- or ferrimagnetic components stabilized in this sample type by cooling under moderate magnetic fields. The AC susceptibility shows a strong frequency splitting at T_N in Fig. 4.3, indicating the entrance into a state with glassy magnetic dynamics. All this type C behavior is found for LuFe_2O_4 in various publications; see for example [147, 154, 81, 155, 156] as well as [88]. For samples exhibiting these magnetization characteristics no long-range charge order is established. Upon x-ray scattering in Sec. 5.1 this is indicated by the presence of a diffuse line along $(\frac{1}{3} \frac{1}{3} \ell)$, even visible down to low temperatures.

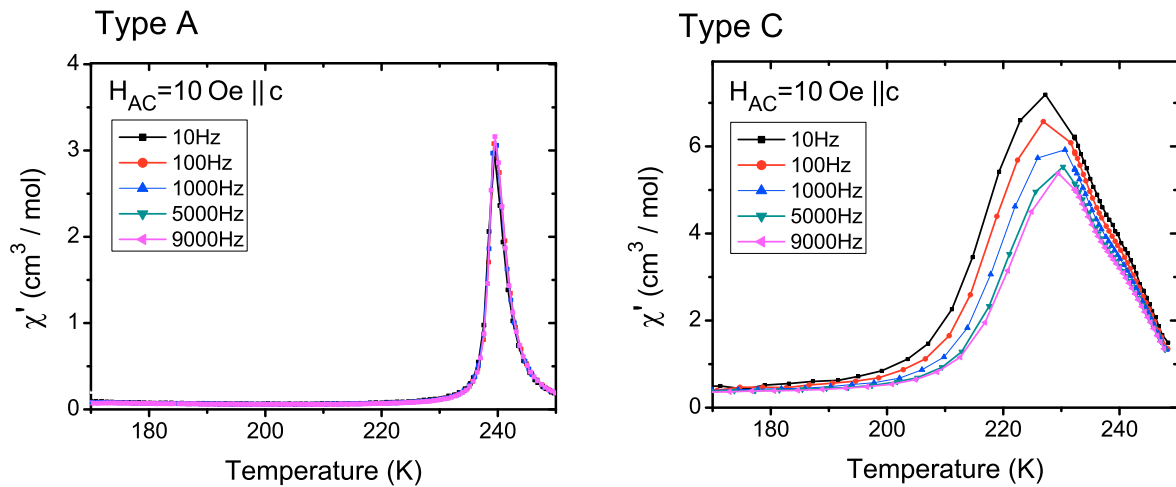


Abbildung 4.3: AC susceptibility measurement with different driving frequencies on cooling with 0.1 K/min. In a temperature region around T_N for the crystals of quality type A and C, defined in this section. The amplitude of the oscillating magnetic field was chosen to be 10 Oe for all the presented frequencies.

In combination with the results reported for the isostructural compound $\text{YFe}_2\text{O}_{4-\delta}$ in [157] it is concluded that the type A species show the magnetic behavior for samples, which are close to stoichiometric in oxygen content. This result is further supported by the fact that for x-ray diffraction, only the samples of type A show sharp charge order superstructure reflections in Sec. 5.1. Unless mentioned otherwise, all the following

characterizations were performed on samples showing the type A magnetization behavior. Due to this sample screening some collaborations with other groups were established in order to conduct experiments, such as infrared phonon spectroscopy [93] and broadband dielectric spectroscopy [158], which are impossible to perform in our laboratories. Also in [88] an additionally detailed magnetic characterization of type C samples was performed by some of our collaborators.

4.2 New magnetic phases

As seen in Sec. 4.1, the observed magnetic properties of LuFe_2O_4 fluctuate strongly, even from samples obtained from one individual growth. This chapter is focused on the macroscopic properties of single crystals exhibiting type A behavior. Here multiple magnetic phase transitions are found below T_N , from which the magnetic phase diagram could be established.

4.2.1 Magnetic characterization: different phases in the vicinity of T_N

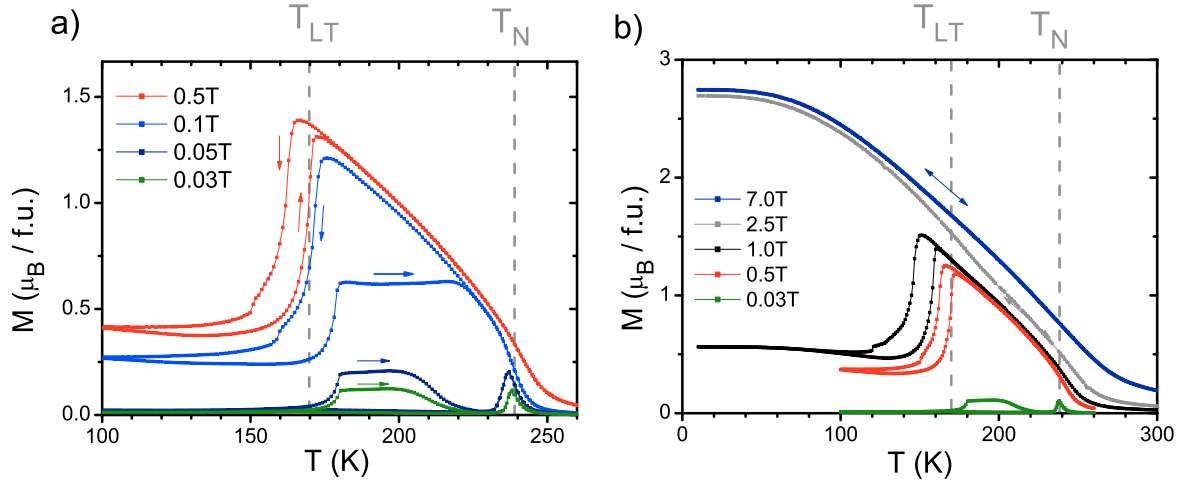


Abbildung 4.4: Magnetization M vs. temperature T on the type A sample for different DC magnetic fields up to 7 T. Arrows indicate the T direction of the particular measurement. The transition temperatures T_N and T_{LT} are marked.

Samples of type A character have been used previously in a few publications [1, 93, 28, 85], but apart from preliminary magnetization measurements in [1] there are no reports about extensive magnetic characterization in order to establish a magnetic phase diagram, in contrast to the type C, which has been more extensively studied in several publications [147, 154, 155]. This missing characterization will be undertaken in the first

part of this thesis. Because of the strong Ising behavior of the Fe-spins in this system, most characterizations were performed along the crystallographic c_{Hex} direction. In the $M(T)$ -curves presented in Fig. 4.4, for small fields (≤ 0.1 T), a low- H phase with almost vanishing net magnetization M is established just below T_N . For other $M(T)$ -curves under increasing magnetic fields, the Néel transition starts to smear out into a region of higher temperatures, a behavior expected for second order phase transitions to a ferromagnetic or ferrimagnetic high- H phase. Additionally, the magnetization measured in the vicinity below T_N increases with increasing H , indicating the growth of ferro/ferrimagnetic contributions. For sufficiently high H (> 0.1 T) the peak shape like transition vanishes and a continual increase of magnetization is observed. The sharp peak in Fig. 4.4a for low- H values, with its corresponding weak magnetization below T_N , contrasts with the continuous magnetization increase for higher- H values. This behavior already suggests the presence of two different magnetic phases in the vicinity of T_N .

For $M(T)$ measurements corresponding to the high- H phase, the magnetization increases until T_{LT}^\downarrow (the \downarrow arrow indicates that it is observed upon cooling) where a sudden suppression of the magnetic moment is observed. Below T_{LT}^\downarrow the remaining magnetization scales with the applied magnetic field. This signifies the presence of increasing areas that have a net magnetic moment. As seen in Fig. 4.4b, the still hysteretic transition temperature of T_{LT}^\downarrow is shifted to lower temperatures for stronger fields (such a behavior was already found in [28]). On further cooling in the phase below T_{LT}^\downarrow there are no more significant changes in $M(T)$, as seen by the 1 T curve in Fig. 4.4b, indicating the existence of this phase until low- T regions. For magnetic fields higher than ~ 1.5 T the transition at T_{LT}^\downarrow is suppressed, and the magnetization increases continuously to low T , where a saturation moment of $2.9 \mu_B/\text{f.u.}$ is reached, in good agreement with previous publications [81, 74, 80] on single crystals with $H \parallel c_{\text{Hex}}$. This total observed magnetic moment in this high- H phase is inconsistent with a pure ferromagnetic spin structure; by only considering the spin moments of Fe^{2+} and Fe^{3+} in the simple ionic limit, a total spin moment of $S = \frac{4\mu_B + 5\mu_B}{2} = 4.5\mu_B$ is expected. However, to explain the spin structure in this phase a more complicated solution, such as ferrimagnetic arrangements similar to those of [1] or [36], must be considered.

Upon warming from low- T under low- H the anomalous “field-heating-effect” introduced in Sec. 4.1 appears as a strong magnetization increase (not observed during cooling) upon warming through T_{LT}^\uparrow . For higher fields $H \geq 0.5$ T this anomalous effect is suppressed, and a transition back to the high- H phase is directly observed at T_{LT}^\uparrow . The

transitions between these different magnetic phases at a constant temperature will be explored in the next chapter. A detailed explanation of the field heating effect is given in Sec. 4.2.5.

4.2.2 Near degenerate magnetic phases just below T_N

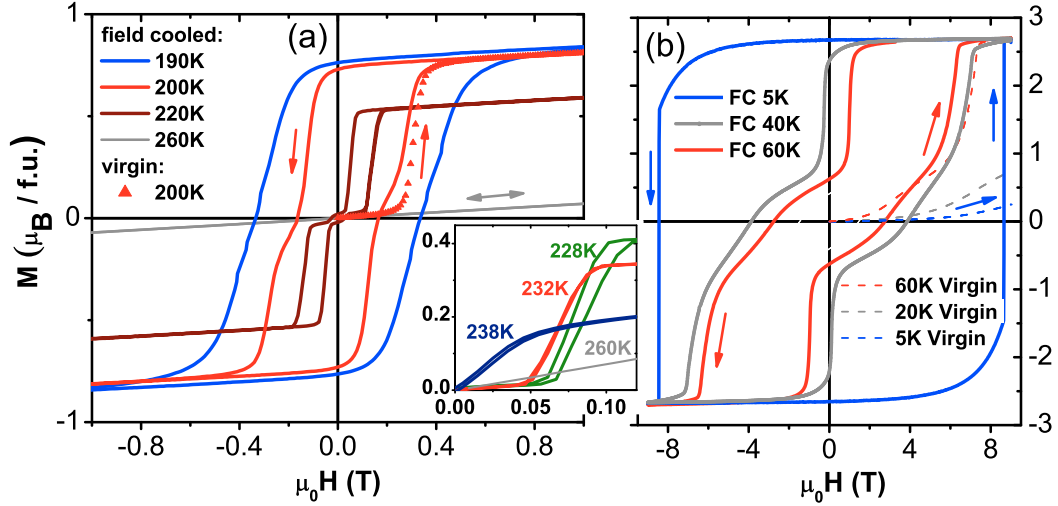


Abbildung 4.5: Magnetization M vs. field $H \parallel c$ for (a) in the temperature region above T_{LT} with inset close to T_N and (b) below T_{LT} . The measurement direction is indicated by arrows. Virgin curves are measured after cooling in $H=0$. $M(H)$ in 5 K, 40 K and 60 K is obtained after cooling in 9 T.

Isothermal magnetization $M(H)$ -loops just below T_N (inset Fig. 4.5a) suggest a first-order metamagnetic transition between the low- H and high- H phase from the previous section. In Sec. 5.3.5 the single crystal x-ray diffraction measurements indicate no change in crystal structure or charge order configuration across this metamagnetic transition. That this is a genuine transition in spin structure, rather than a domain effect, is supported in Sec. 6.1 by the effect of an applied magnetic field on neutron diffraction, as already mentioned in an endnote of [91]. The $M(H)$ -loops clearly show that the high- H phase carries a net magnetic moment. As already described in the last chapter, this phase can be stabilized to low- T in sufficiently high- H (Fig. 4.4b). The low- T saturation moment of $\sim 2.9\mu_B$ /f.u. (Fig. 4.5b) is similar to that found in previous studies [92, 81, 74, 80], and about a third of the full Fe spin moment, implying ferrimagnetic (fM) spin ordering, such as $\uparrow\downarrow\uparrow$. In contrast, the low- H phase near T_N seems to be AFM, with $M \propto H$ and no remanent magnetic moment, as indicated for example by $M(H)$ at 232 K (inset Fig. 4.5a). The loops below ~ 220 K start to resemble fM hysteresis loops with remanent M . However, the virgin $M(H)$ started after cooling are still initially linear and outsi-

de the rest of the loops, as shown in Fig. 4.5a for 200 K. This is typical behavior for strongly hysteretic AFM-fM metamagnetic transitions [159] and it suggests that below 218 K both AFM and fM phases can be stabilized in $H = 0$. In the case of the AFM phase, this is directly clear from the $M(T)$ -curves in Fig. 4.4a. In order to demonstrate the same stability for the fM phase, a half hysteresis curve was measured in Fig. 4.6 at 190 K; afterwards the magnetic field remains zero. For this $H = 0$ procedure, the sample remanent magnetization only changes slightly in a time scale of 12 hours, indicating the stability of the fM phase.

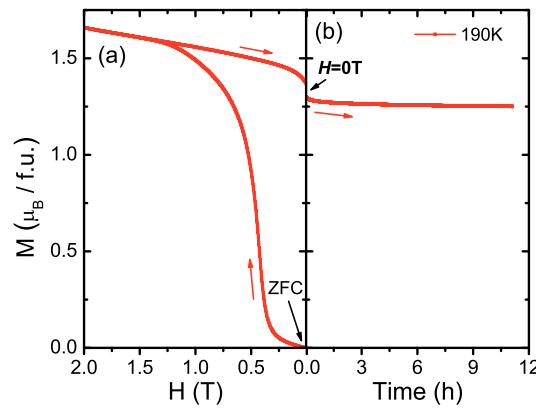


Abbildung 4.6: (a) Magnetization M vs. field $H \parallel c_{\text{Hex}}$ measured after ZFC to the AFM phase. (b) Adjacent time-dependent remanent magnetization measurements up to 12 hours in $H = 0$ performed after reaching the fM phase.

An AFM phase with a metamagnetic transition to fM has not been proposed for LuFe_2O_4 before¹. Here, it is additionally noted that the related YFe_2O_4 shows AFM behavior if, and only if, it is highly stoichiometric [157]. At first sight, an AFM phase at 220 K and $H = 0$ seems to be in contradiction with the neutron diffraction results of [1], which led to the proposed fM spin structure. In [161] it is proposed that an AFM-like phase can be realized by compensating fM clusters with opposite alignments. However, in Sec. 6.2.1 it will be demonstrated that an AFM spin arrangement is in perfect agreement with neutron scattering.

4.2.3 A cluster state below T_{LT}

The transition at $T_{LT}^{\downarrow} = 170$ K on cooling (\downarrow) is associated, as shown in Sec. 6.3, with the development of a strong diffuse magnetic scattering component (already reported in [91, 1]), and accompanied by a structural distortion [28]. Upon cooling through T_{LT}^{\downarrow} , the

¹First publications about such a phase are appearing at the moment of the writing of this thesis [160].

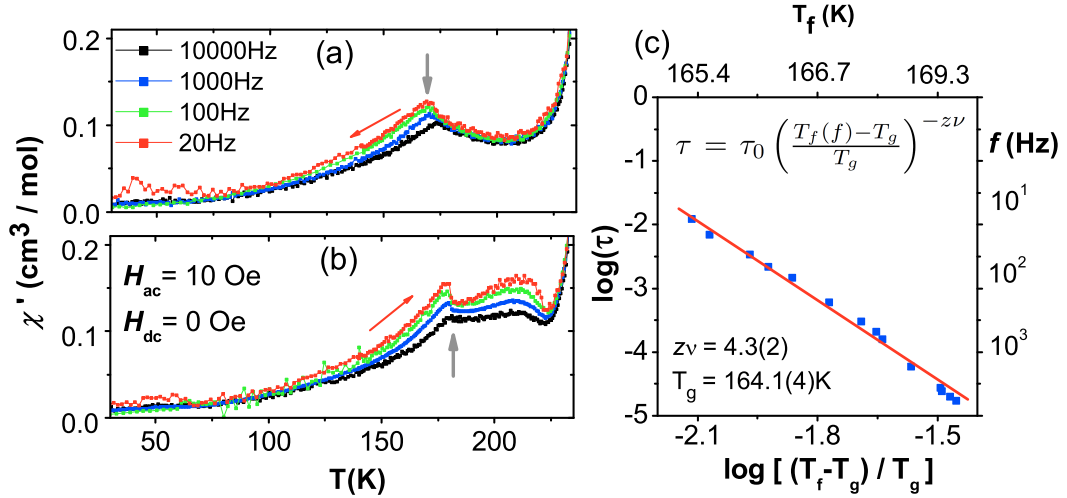


Abbildung 4.7: Real part of AC susceptibility with selected driving frequencies on cooling (a) and warming (b) (thick arrows indicate the structural distortion). (c) Dynamic scaling of the glass temperature versus the maximum relaxation time on cooling described by a power law [162] using the freezing temperature $T_g = 164.1(4)$ K with the fit (red line).

real part χ' in the AC susceptibility (Fig. 4.7a) becomes strongly frequency dependent for LuFe_2O_4 (in contrast to the magnetization reported in Sec. 4.1, where only a small broad peak is observed), suggesting a phase with glassy magnetic dynamics. To quantitatively probe the glass dynamics in LuFe_2O_4 , the χ' signals from the AC susceptibility data have been fitted with a Gaussian peak shape, in order to achieve, for the different driving frequencies, the maximum position in temperature T_f . A scaling analysis (shown in Fig. 4.7c) of the characteristic time $\tau = (2\pi f)^{-1}$ against the frequency-dependent freezing-temperature $T_f(f)$ at maximum χ' following [162], yields a microscopic flipping time of $\tau_0 \sim 10^{-9}$ s. This τ_0 is much larger than for typical spin glasses ($\sim 10^{-12}$ s [162]), but agrees with observations for cluster glass systems [88, 163]. This quantitative analysis indicates that the magnetism below T_{LT}^\downarrow arises out of an assembly of clusters. The dynamic exponent of $z\nu = 4.3(2)$ is small, but it is comparable to values found at T_N for the type C samples, for instance in the study of [88] and [156].

The “glassy nature” of the state below T_{LT}^\downarrow is also apparent in $M(H)$ -curves, with a typical loop at 60 K, as shown in Fig. 4.5b. A butterfly-like shape is visible, resembling $M(H)$ at 220 K and suggesting a first-order metamagnetic transition to the fM high- H phase. However, the loop at 60 K is less sharp, and significant remanent M remains after decreasing H from high values, suggesting that small patches of the sample remain in the fM phase. The highly non-linear behavior of the virgin curve is also notably different

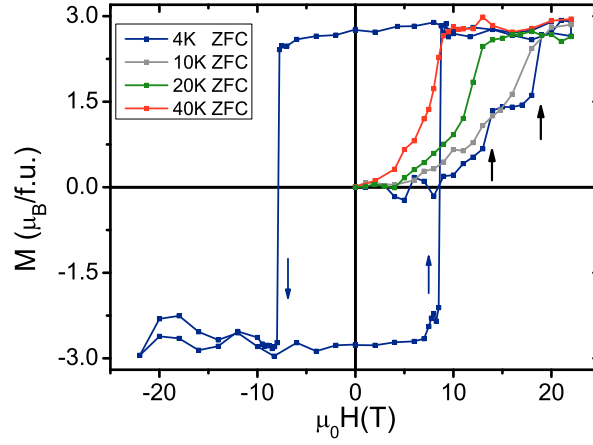


Abbildung 4.8: Magnetization M vs. high magnetic field measurements with $H||c$ up to 22 T. All measurements are performed at different temperatures after a ZFC process. Only for the lowest reachable temperature of 5 K is a full hysteresis $M(H)$ -loop presented. These high magnetic field measurements were done with a 10 MW resistive magnet at the LCNMI in Grenoble.

from the higher T case. The super-linear increase of M with H indicates that fM patches or clusters continuously grow or nucleate until the transition to the full fM phase is triggered. The transition field is lower after the fM phase has been entered, consistent with the significant remanent magnetization. The magnetization curves below T_{LT}^\downarrow after ZFC starts to establish virgin curves where below 40 K the transition into the pure fM phase could not be established in fields up to 9 T, the limit of the PPMS system. For example, in Fig. 4.5b the virgin curve at 5 K shows only a marginal increase of the magnetization at 9 T, compared to the observed saturation moment in Fig. 4.9a after cooling in high fields. In order to study the magnetization behavior in this phase on our laboratory PPMS system, the samples were cooled in fields of 1.5 T and afterwards the $M(H)$ -curves were measured. These curves show a transition from the fM phase to the glassy low- H phase in the temperature region below T_{LT}^\downarrow , indicated by an abrupt drop in magnetization, as shown for the 60 K curve in Fig. 4.5b. For temperatures below 45 K this drop is suppressed in Fig. 4.5b and a direct and sharp reversal of the sample magnetization is observed at 5 K, indicating the sudden flip of all spin moments at ~ 8.5 T. In order to measure the complete virgin magnetization curves below the freezing temperature, a 10 MW resistive magnet with H up to 22 T was used at the LCNMI in Grenoble (for details see Sec. 3.1). Fig. 4.8 shows that the saturation moment for the virgin magnetization curve at 5 K was reached at $H \sim 19$ T, with strong magnetization jumps (indicated by black arrows) suggesting the development of larger magnetic domains [74]. Such a giant coercivity in

$M(H)$ -curves was already observed by Iida *et al.* [80] and Wu *et al.* [92] for LuFe_2O_4 , but not with such sharp in-loop transitions, indicating a total spin-flip of all spins, and it was never connected to the development of a low-temperature phase transition at T_{LT} .

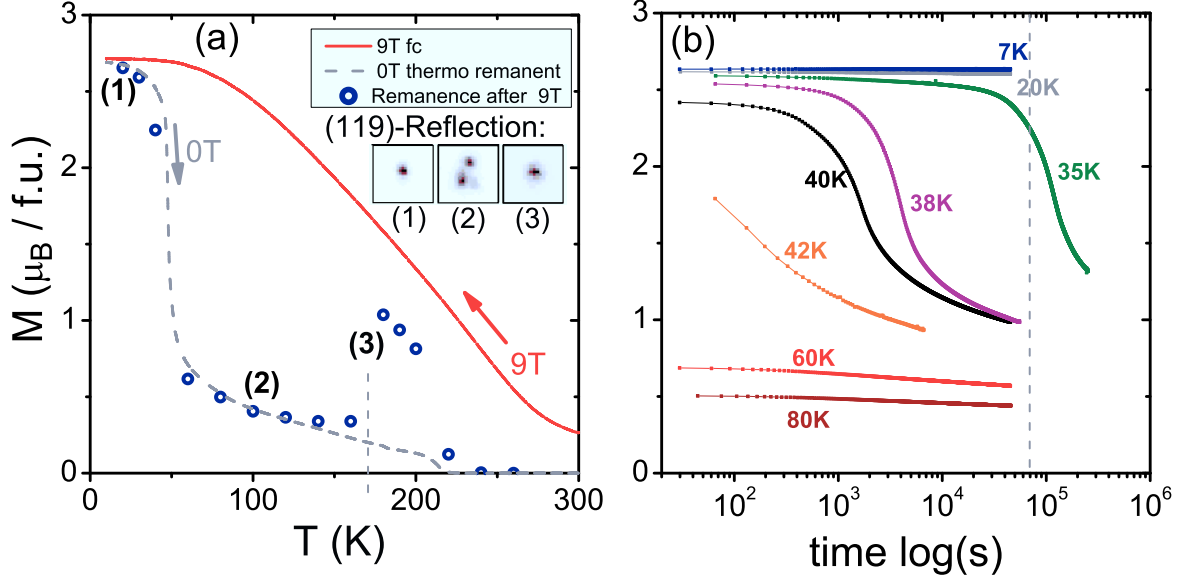


Abbildung 4.9: (a) Thermo-remanent magnetization (TRM) with 1 K/min. after FC in 9 T and warming in zero field; the points indicate the remanence from hysteresis loops at a given temperatures. The inset shows the (119)-reflection at different positions on the TRM curve, additionally measured in the experiment presented in Sec. 5.3.5. (b) Time dependent magnetization measurements after cooling down to 5 K in a field of 9 T and then warming up under 0 T to the mentioned temperature. For clarity, the gray dashed line indicates the 1 day time-line (in log scale).

All this behavior clearly suggests an intrinsically inhomogeneous nature of this magnetic state, reminiscent of the electronic phase separation observed, for example, in mixed valence manganites [164]. As we will discuss in Sec. 6.3, particles of the fM and AFM phases are both evidenced by neutron diffraction in this phase (with a particular imbalance between them, depending on the sample history). We therefore tentatively label this a phase-separated (PS) state. The PS scenario is consistent with the low- T neutron diffraction pattern [1], but a direct proof will require microscopic real-space techniques such as Magnetic Force Microscopy (MFM). The PS \leftrightarrow fM transition below T_{LT}^\downarrow is accompanied by the structural distortion [28] acting as an energy barrier. Here, thermal fluctuations are insufficient to overcome this at lower- T . Upon warming from PS, there is a major point in Sec. 5.3.5, by verifying that on warming, the structural distortion (splitting of e.g. the (119)-reflection inset in Fig. 4.9a) is gone at $T_{LT}^\uparrow \sim T_{LT}^\downarrow + 10 \text{ K}$,

which corresponds to the starting temperature of the “Anomalous field heating effect”, discussed further in Sec. 4.2.5.

The complete suppression of the fM \rightarrow PS transition in H at lower- T is explained in terms of kinetic arrest [165], where the magnetic system becomes fully frozen, as observed in other systems e.g in CeFe_2 [166] and Gd_5Ge_4 [167]. This was also recently proposed for LuFe_2O_4 in [28]. For temperatures below 50 K, the high- H phase remains frozen even after decreasing H to 0 T. Such behavior is indicated in Fig. 4.9a, where the thermo-remanent magnetization (TRM) drops drastically upon continuous warming at the reported freezing temperature of ~ 45 K. Here the entrance into the PS phase is achieved. Since the thermal activation is too low to achieve a direct transition into the PS phase at low temperatures, magnetization dynamics with very long time-scales are thus just below the freezing temperature expected. In order to investigate this, the sample was cooled from RT to about 5 K in a field of 9 T and afterward warmed in $H = 0$ to the temperature mentioned in Fig. 4.9b. As expected for a thermally activated transition, the time for triggering the entrance into the PS phase upon warming, increases for temperatures further away from 42 K to lower T . Here, 35 K was the lowest temperature where the transition could be observed in a reasonable time. Furthermore, the waiting time was about 1 day until the transition took place, for lower T almost no change in magnetization was observed for measuring times of ~ 1 day, indicating the total arrest of the fM phase for $T < 35$ K. Viewed the other way round, the transition temperature depends strongly on the time scale. Kinetic arrest as growing hindrance for the metamagnetic transition at lower temperatures was already reported for various metamagnetic materials such as Co substituted Mn_2Sb [168] and the inter-metallic compound Nd_7Rh_3 [159], which all show a spinglass behavior for low T such as $\text{Ce}(\text{Fe}_{0.96}\text{Ru}_{0.04})_2$ [166] or U_2IrSi_3 [169].

The first indications for this kinetic arrest in LuFe_2O_4 are already found in infrared spectroscopy [93], where the entire spectrum freezes at $T \sim 50$ K, indicating that the dynamic of the structural distortion freezes. Here, the charge order, and the fluctuation of the charge order remains constant below 50 K. This kinetic arrest is the driving force for the observed giant coercivity in LuFe_2O_4 .

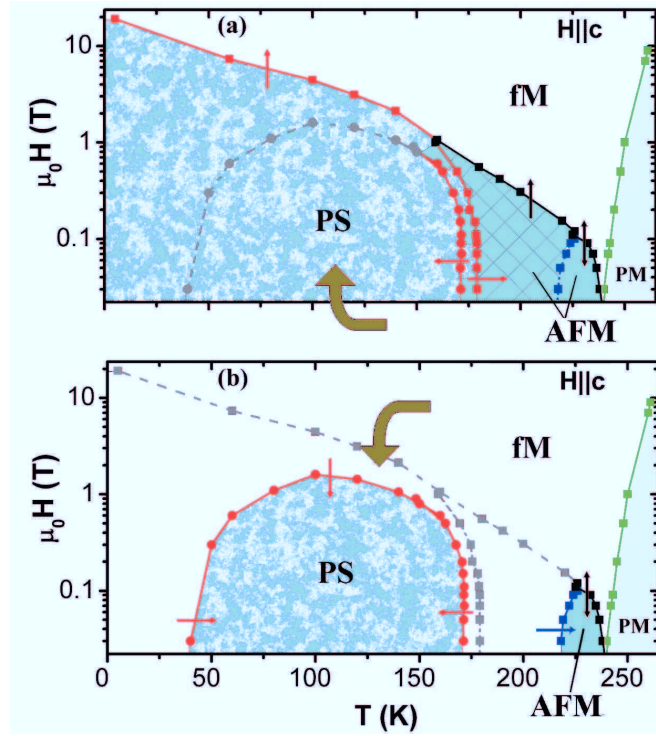


Abbildung 4.10: Magnetic field H – temperature T (logarithmic scale in H) phase diagrams for different starting conditions (indicated by thick arrows): (a) H increasing after zero field cooling and (b) H decreasing after cooling in high- H . Small arrows indicate the direction in which transitions are observed. Red lines are phase transitions accompanied by a structural distortion. Grayed transitions do not occur under given conditions. The three magnetic phases are labeled AFM, fM and PS. The hatched area in (a) delineates a special state reached only by warming from PS (see text).

4.2.4 The magnetic phase diagram

From various $M(T)$ and $M(H)$ -curves, some of which are presented in Fig. 4.4 and Fig. 4.5, the magnetic phase diagram for all the unusual magnetic behavior observed for $H||c_{\text{Hex}}$ could be established in Fig. 4.10a/b. To determine the phase boundary of the paramagnetic phase (PM) against the antiferromagnetic (AFM) phase, which is present only in low H , the peak at T_N was chosen as the transition temperature (only one point in the Fig. 4.10). For the direct transition from PM into the ferrimagnetic (fM) phase under applied H the maximum slope of the magnetization was chosen as transition point. An increase towards higher T is visible for the transition measured in higher H , indicating the magnetic field effects on a phase transition. The PM transition line into AFM or fM is remarkably similar to that reported in [88] on type C samples. However, in contrast to the results reported there, in the study on type A crystals we observed above T_{LT}^{\downarrow} no magnetic cluster states on cooling. The metamagnetic transition from

AFM to fM is achieved from the maximum slope in isothermal $M(H)$ -curves. As already indicated by the strongly hysteretic magnetization curves of Fig. 4.5, for temperatures below ~ 220 K the magnetization shows an AFM character only after zero field cooling; once the high- H phase is achieved it is also stable in $H = 0$. For temperatures higher than 220 K, this decreasing hysteretic character of the metamagnetic transition is included in Fig. 4.10(a/b) by the blue transition line in the phase diagram.

In order to represent all the different ways a magnetic phase can be stabilized in LuFe_2O_4 , the phase diagram is presented in Fig. 4.10a for the case of the magnetic behavior after zero field cooling Fig. 4.10a in contrast to Fig. 4.10b, where all observed phases are indicated by starting from the high- H fM phase. Upon further cooling in $H = 0$, the low-temperature phase transition T_{LT}^\downarrow indicates the entrance into the magnetic inhomogeneous phase reported in Sec. 4.2.3. This transition is indicated by a small broad peak in $M(T)$ -curves. For higher H values upon cooling, the transition is associated with the sudden drop in magnetization indicating the transition from fM into the low temperature PS phase. The metamagnetic transition between the inhomogeneous phase and pure fM reaches very high coercive field values for low temperatures, as already indicated in [28, 92]. This is explained by a kinetic arrest. As seen from the $M(T)$ -curve in $H = 1$ T, the transition at T_{LT} between PS and AFM is also strongly hysteretic in temperature and is accompanied by a structural distortion [28]. This hysteretic region of about 10 K is additionally indicated in the magnetic phase diagram by a thick striped area around 175 K. Upon further warming across T_{LT}^\uparrow , the “Anomalous field heating effect” appears for low fields in the region where the fM phase is stable in $H = 0$; this region is indicated in Fig. 4.10a by a hatched area.

4.2.5 The “Anomalous field heating effect”: stable disorder

An effect that is strongly connected to the cluster state observed below T_{LT}^\downarrow is the anomalous field heating effect, which only appears by leaving upon warming in low H the region below T_{LT}^\uparrow . The strong increase in magnetization is observed at exactly that temperature where the structural distortion (e.g. the (1 1 9) reflection inset in Fig. 4.9a) disappears. Upon warming from PS in low H , M first sharply increases to a high magnetization plateau and then decreases at ~ 218 K (Fig. 4.7b). Very similar behavior, though not as sharp, was already observed 20 years ago [79]. It was denoted “anomalous field heating effect”, but could not be explained.

While in AC susceptibility χ' shows a sharp drop at T_{LT}^\uparrow (Fig. 4.7b), the frequency

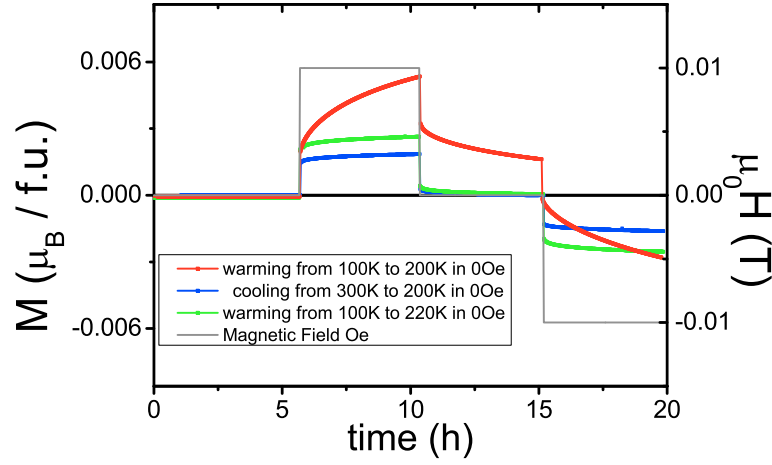


Abbildung 4.11: Time dependent remanent magnetization measurements with $H||c_{\text{Hex}}$ at 200 K after reaching the temperature in zero field for both scenarios, warming from below T_{LT}^{\uparrow} and (warming to 200 K in red and to 220 K in green) also cooling from room temperature to 200 K is presented in blue. The time dependence magnetization is presented following the script for the magnetic field according to the gray line. For each field value, the sample magnetization was collected for 5 hours.

splitting remains in this “plateau-region” (hatched area in Fig. 4.10a), as does the diffuse scattering component in polarized neutron diffraction (see therefore Sec. 6.3.1). To understand this anomalous behavior, consider when warmed above T_{LT}^{\uparrow} the sample enters a H - T region where, according to Fig. 4.10, both AFM and fM phases can be simultaneously stable in low- H . As the sample consists of mesoscopic AFM and fM regions, there is no driving force to settle fully into either the AFM or the fM phase until one of the states becomes unstable. Below T_{LT}^{\uparrow} even a small field promotes the increase of an fM fraction, as indicated by the non-linear virgin magnetization observed at 60 K in Fig. 4.5b. The disappearance of the structural distortion facilitates this increase, resulting in the abrupt rise of M i.e. the anomalous “field-heating effect” [79].

This anomalous behavior is also observed in Fig. 4.11 for time dependent magnetization measurements at 200 K. Here, an enormous difference between the magnetic behavior on cooling (blue) and on warming (red) is present. By applying a magnetic DC field of 100 Oe after ZFC an abrupt increase of magnetization is observed. As expected for AFM behavior, the magnetization saturates rapidly, and it disappears after removing the field. For the same temperature, the behavior strongly differs upon warming from below T_{LT} in zero field, here by setting an field of 100 Oe a continuous increase of magnetization is observed on timescales hard to measure on finite timescales, and after decreasing the field to $H = 0$ a significant remanent magnetization remains. These observations

are consistent with the presence of a cluster state in the temperature region where the “anomalous field-heating-effect” is observed.

Above ~ 218 K the anomalous fM state becomes unstable in low H (Fig. 4.4a), and even in $H = 0$ for the TRM signal in Fig. 4.9. Consequently, the sample re-enters the pure AFM phase. The latter is supported by the fact that both, the frequency splitting in χ' (Fig. 4.7b) and diffuse magnetic scattering (see Sec. 6.3.1) vanish, and the DC magnetization signal drops back to nearly zero (Fig. 4.4b). In the region above ~ 218 K, in Fig. 4.11 no time-dependent magnetic behavior could be observed.

4.2.6 Near-degeneracy & antiferromagnetic correlations above T_N

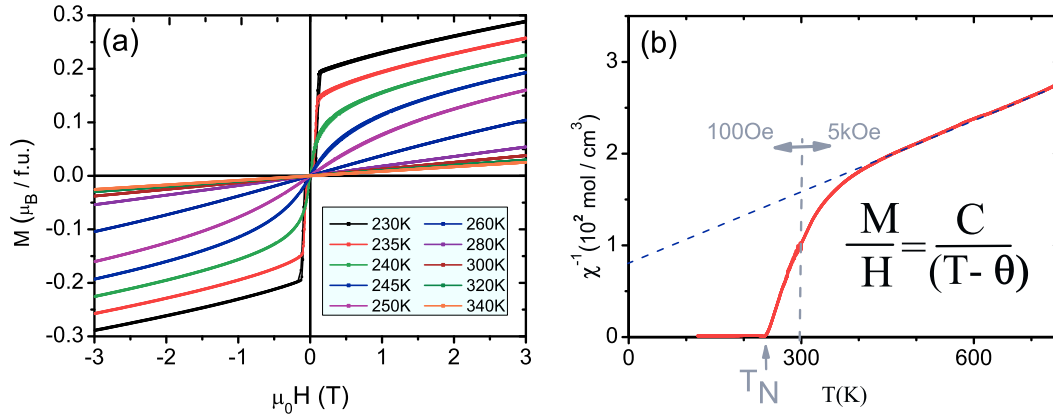


Abbildung 4.12: (a) Magnetization M vs. field $H \parallel c_{\text{Hex}}$ measured in the AFM phase just below T_N and paramagnetic phase above T_N up to 340 K. (b) Inverse susceptibility H/M with Curie-Weiss fit (dashed blue line) in the linear region from 450 K to 750 K. For temperatures below 300 K a field of 100 Oe was used for the measurement, in contrast to the 5000 Oe for above.

The sharp metamagnetic transition between AFM and fM in $M(H)$ -curves presented in Fig. 4.12a is only visible in this edged form below T_N . The $M(H)$ behavior close to T_N is presented in the inset of Fig. 4.5a, where the near degeneracy of both magnetic phases is nicely presented when approaching $T \rightarrow T_N$ in $H \sim 0$. Above this Néel temperature, the increase in magnetization is not linear with H , as expected from pure paramagnetic behavior, but a strongly nonlinear behavior with bending curves at low H is present. This broadening of the metamagnetic transition can be explained, as shown in Sec. 6.2.4 and Sec. 7.1.2, by the alignment of randomly stacked but internally still ordered magnetic bilayers in a magnetic field applied along the c_{Hex} direction.

These strong deviating magnetization characteristics of purely PM behavior are also present in the inverse susceptibility with $\chi^{-1} = H/M$ (inset Fig. 4.12b), where strong

deviations from the linear slope indicate the presence of magnetic fluctuations far above T_N up to ~ 400 K. In the temperature region between 450 K and 750 K, a linear behavior is observed, which could be fitted with a Curie-Weiss law:

$$\frac{1}{\chi} = \frac{3k_B(T - \theta)}{NM_B^2\mu_B^2} \quad (4.1)$$

with the effective moment $\mu_{\text{eff}} = M_B\mu_B = 5.5(2)\mu_B$ expected for equally distributed $\text{Fe}^{2+/3+}$ [170] and a negative Weiss temperature of $\theta = -307(9)$ K, suggesting dominantly antiferromagnetic interactions similar to YFe_2O_4 [157]. Interestingly, there is a discrepancy between the relatively low calculated [90] magnetic exchange parameters (the highest interaction parameter with 7.6 meV corresponding to an ordering temperature of ~ 100 K) and on the other side the high magnetic ordering temperature ($T_N \sim 240$ K) and the Weiss temperature θ determined experimentally [148]. This discrepancy indicates that the theoretical model describing the magnetic interactions in LuFe_2O_4 needs to be improved. The value of μ_{eff} is in good agreement with spin-only magnetic contributions from the different Fe valences with a completely quenched Fe^{2+} orbital magnetic moment. From recent reports [36, 44, 171] it is known that there is a strong orbital magnetic moment present for the Fe^{2+} valence, which is also measured with similar values in the type A samples used in this thesis (see Sec. 7). This would lead to a somewhat higher expected value of μ_{eff} . An explanation for these deviations could be a decay of sample stoichiometry at high-temperatures (already observed at 350°C [145]), which are necessary for this measurement to reach a linear region. With increasing oxygen off-stoichiometry a stronger ferrimagnetic character of the sample could be achieved, which might be influencing the slope of the Curie-Weiss behavior.

4.3 Discussion and Conclusion

Although the magnetic phase-diagram presented in this chapter may not be resolvable in a majority of LuFe_2O_4 samples, the complex phase competition it reveals likely ramifications for all specimens of these materials. For example, if disorder, due to oxygen non-stoichiometry for instance, is added to the competing interactions, glassy freezing is expected to replace the long-range spin order at T_N , as observed in some samples [147, 88]. Furthermore, several of the phenomena explained above in the context of competing magnetic phases have been observed on other samples before. By comparing the phase diagram presented in Fig. 4.10 with the one on type C samples established in [88],

there is much similarity, apart from the fact that fM seems expanded and the AFM phase seems to be replaced by a glassy phase.

A central ingredient in the evolution of the complex phase diagram presented in Fig 4.10 is thus the competition between two nearly-degenerate instabilities at T_N . This competition will be the driving force for the anomalous magnetic behavior observed above T_N and below T_{LT} . For low T the fM \longleftrightarrow PS transition is accompanied by the structural distortion acting as an energy-barrier, which thermal fluctuations are insufficient to overcome at lower T . The observed kinetic arrest completely suppresses the fM \longleftrightarrow PS transition, giving rise to giant coercivity of ~ 8.5 T at 5 K. To understand all this unusual magnetic behavior in detail, a study of the crystallographic and magnetic structure (especially the spin structures) of LuFe_2O_4 is presented in the following chapters by using several of x-ray and neutron scattering techniques. However, as we will see at the end of this thesis, a lot could already be learned from the here presented macroscopic measurements.

4.4 Related publications

The following publications are related to this section:

- “Complex magnetic phases in LuFe_2O_4 ”
M.H. Phana, N.A. Frey, M. Angst, J. de Groot, B.C. Sales, D.G. Mandruse, and H. Srikanth
Solid State Communications **150**, 341 (2010).
- “Lattice dynamical probe of charge order and antipolar bilayer stacking in LuFe_2O_4 ”
X. S. Xu, J. de Groot, Q.-C. Sun, B. C. Sales, D. Mandrus, M. Angst, A. P. Litvinchuk, and J. L. Musfeldt
Phys. Rev. B **82**, 014304 (2010).
- “Dielectric properties of charge ordered LuFe_2O_4 revisited: The apparent influence of contacts”
D. Niermann, F. Waschkowski, J. de Groot, M. Angst, and J. Hemberger
Phys. Rev. Lett. **109**, 016405 (2012).

The following publication is related both to this section and to Sec. 6:

- “Competing Ferri- and Antiferromagnetic Phases in Geometrically Frustrated LuFe_2O_4 ”
J. de Groot, K. Marty, M.D. Lumsden, A.D. Christianson, S.E. Nagler, S. Adiga, W.J.H. Borghols, K. Schmalzl, Z. Yamani, S.R. Bland, R. de Souza, U. Staub, W. Schweika, Y. Su, and M. Angst
Phys. Rev. Lett. **108**, 037206 (2012).

For a detailed declaration of own contributions to the publications see App. A.

The crystallographic structure describing charge order

In this section, the crystallographic cell and its corresponding symmetry elements are presented. They describe the charge order and domain structure for LuFe_2O_4 [172] according to all observations. Below the magnetic and charge ordering temperatures T_N and T_{CO} [90, 173, 85, 28, 27, 44, 1, 174] the $\sqrt{3} \times \sqrt{3} \times 2$ crystallographic cell is usually used to explain both the charge and spin order in theoretical and experimental work. This cell is obtained by expanding the hexagonal unit cell as elaborated in the App. C.

In order to describe the charge order process in this chapter, first the refinements in the high-temperature crystal structure above T_{CO} , and its changes upon charge order, are presented. A transformation between the hexagonal structure and a monoclinic domain is introduced to describe the superstructure reflections appearing in x-ray diffraction upon cooling through T_{CO} . Furthermore, this crystal structure is refined properly according to this novel supposition, and the Bond Valence Method predicts a charge order pattern which is totally unexpected. Importantly, this new charge order scheme does not contain polar bilayers, in contrast to what was previously proposed (e.g. [27, 85]), casting strong doubt on the “ferroelectricity from charge ordering” scenario for LuFe_2O_4 .

At the end of this chapter, measurements are presented which elaborate on the effect of electric and magnetic fields on the charge order configuration, giving additional support to the findings that LuFe_2O_4 cannot be ferroelectric even in electric fields. Furthermore, structural refinements in the temperature region below T_{LT} are performed, where a lattice distortion is reported which interacts strongly with the magnetic structure.

5.1 Long range charge order in samples with reduced quality?

Single crystal diffraction measurements were done on samples exhibiting the type C quality in magnetization from Sec. 4.1, where no sharp magnetic transition at $T_N \sim 240$ K was observable. As expected for this and other kinds of samples strong diffuse scattering

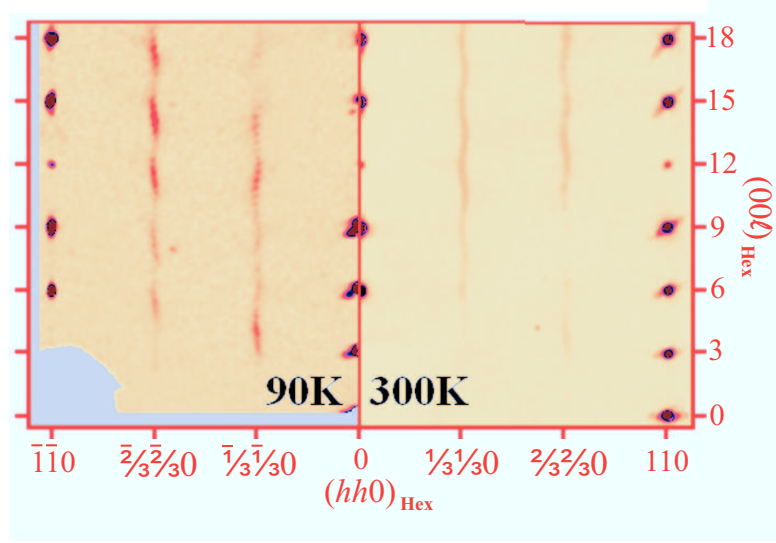


Abbildung 5.1: Composite precession image of a LuFe_2O_4 single crystal of type C magnetic behavior in the $(h h \ell)$ plane constructed from about 1200 individual frames measured at 210 K with $\text{Cu-K}\alpha$ radiation; all reflections are indexed in the hexagonal cell. Two measurements at different temperatures are presented 90 K (left) and 300 K (right). For 90 K the measurement did not reach a completeness of 100 % during data collection, and the missing reciprocal space is marked in gray.

along the $(\frac{1}{3} \frac{1}{3} \ell)$ line is observed above T_{CO} . However, even below T_{CO} at 90 K, the lowest temperature possible to stabilize with the Cryojet-HT, no long-range charge order was established in this type of samples, as indicated in the left of Fig. 5.1. This behavior confirms the idea that only samples showing the sharp transitions at T_N (to the long-range spin ordered AFM phase) are close enough to perfect stoichiometric in order to also establish long-range charge order. The observed speckled diffuse scattering at 90 K for type C is similar to observations in [175] on YbFe_2O_4 , where such a pattern was explained by a charge density wave. A comparable explanation was also given in various publications for the charge ordered state of LuFe_2O_4 [176, 52, 177].

5.2 The crystal structure above T_{CO} : No long-range charge order

Above the charge order temperature, the crystallographic structure was analyzed by x-ray diffraction. As a result of the macroscopic magnetic characterization in Sec. 4.1, it was stated that samples showing a sharp magnetic transition at $T_N \sim 240$ K are close to stoichiometric in oxygen content. In order to perform the single-crystal structure refinement one LuFe_2O_4 single crystal showing the best magnetic behavior (type A from Sec. 4.1) was crushed to obtain smaller crystals suitable for the diffractometer.

5.2. THE CRYSTAL STRUCTURE ABOVE T_{CO} : NO LONG-RANGE CHARGE ORDER

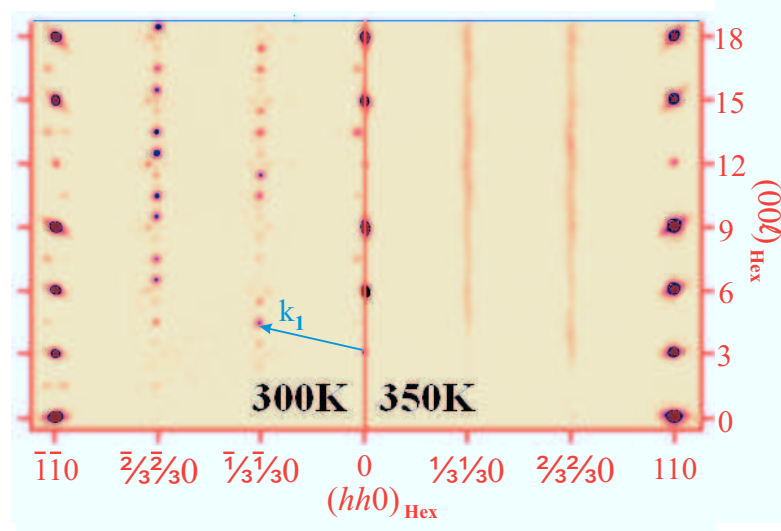


Abbildung 5.2: Composite precession image of a LuFe_2O_4 single crystal of type A in the $(hh\ell)$ plane constructed from ~ 1200 individual frames measured at 210 K with $\text{Cu-K}\alpha$ radiation; all reflections are indexed in the hexagonal cell. The blue arrow indicates the charge order propagation vector $\vec{k}_1 = (\frac{1}{3} \frac{1}{3} \frac{3}{2})$.

In LuFe_2O_4 the Lu-atoms are by far the heaviest elements in this material with $Z = 71$, leading to an enormous absorption, making a reliable structure refinement difficult. The absorption cross section drops for high-energy photons. By using $\text{MoK}\alpha$ radiation with a wavelength of $\lambda = 0.70926 \text{ \AA}$ instead of $\text{CuK}\alpha$, the extremely high absorption¹ is adequately reduced. The $\text{MoK}\alpha$

radiation has the further advantage that the standard $\text{CuK}\alpha$ radiation is in energy just above the Fe K-edge [178], which would produce an additional fluorescence background in all measurements.

A full dataset of about 412 individual frames was collected on the laboratory Super-Nova x-ray diffractometer, covering the hemisphere for hexagonal setting at 350 K. In total, 664 reflections reduced to 116 unique reflections were observed. To minimize the effect of absorption, a crystal with an almost spherical shape of 0.1 mm in radius was chosen. The $R_{int}=0.057$ and $R_\sigma=0.014$ values shows the high quality of the collected data

Tabelle 5.1: Refinement parameters for the data collection at 350 K.

Parameter	this work	Isobe <i>et al.</i> [77]
Space group	$R\bar{3}m$	$R\bar{3}m$
a	3.4404(4)	3.4406(1)
c	25.280(4)	25.28(1)
R_{int}/R_σ	0.02/0.012	0.018
R_1/wR_2	0.019/0.042	0.029/0.031
Goof S	1.107	2.0
Measured Reflections	664	564
diff. peak and hole, $\text{e}/\text{\AA}^3$	0.76 / -1.73	8.1 / -8.6
ρ_{calc} , $\text{g}\cdot\text{cm}^3$	6.7405(1)	6.74

¹For LuFe_2O_4 the $\text{MoK}\alpha$ radiation absorption is $\mu=36.56\text{mm}^{-1}$ in contrast to $\text{CuK}\alpha$ with $\mu=118.57\text{mm}^{-1}$.

after numerical absorption correction. For the adjacent crystal structure refinement, the WinGX package was used, leading to the results presented in Tab. 5.2, which are almost similar to the early findings reported by Isobe *et al.* in [77].

There is a very good agreement between observed and calculated structure factors in Fig 5.3, also indicated by the low value of $R1=2.0\%$ for this solution. In this structure, the taller overall anisotropic displacement U_{ij} for all sites in Tab. 5.2 can be explained by the higher temperature of the measurement. Although the refinement in [77] was done on data collected below T_{CO} , the same strong anisotropic Lu displacement along the c_{Hex} direction is here also achieved on a type A sample above T_{CO} (at 350 K). This anisotropic behavior is very unlikely, because all other elements show a more

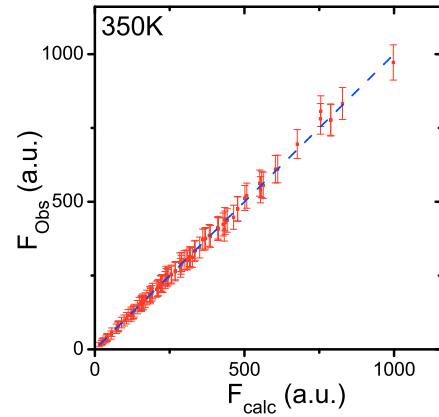


Abbildung 5.3: Observed structure factors against calculated for the refinement in $R\bar{3}m$ symmetry at 350 K, the blue line indicate $f(x)=x$ the ideal distribution

isotropic behavior, and the Lu is by far the heaviest element. This can be interpreted as Lu-displacements along the c_{Hex} direction, which are a precursor effect of the charge order in this system, suggesting that the final crystal structure describing this order, should be different, as shown in Sec. 5.3. Upon refinement, the strongest holes and peaks in the differential electron density map are located close to the Lu atoms and thus not associated to particular atoms, and they can be explained as so-called “ghosts” (see Sec. 3.3.1). The hexagonal lattice in this chapter does not describe the 2D charge order without long-range order reported in [85, 27]. Thus the diffuse intensity along the $(\frac{n}{3} \frac{n}{3} \ell)$ -line remains unexplained by the simple hexagonal structure. This diffuse line is observed e.g. in [52, 85], and also for the type A samples Fig 5.2 (right side). For the refinement in $R\bar{3}m$ the 2D diffuse scattering was neglected upon data collection. The temperature range reported for this diffuse scattering is in the range of 500 K to about 320 K [84]. This could be observed on the type A samples for temperatures up to ~ 380 K with the laboratory x-ray source used for the refinements. Below the charge order temperature T_{CO} , the diffuse line splits up into sharp reflections, as indicated by the precession images in Fig. 5.2 (left side). This result is also consistent with the high energy x-ray diffraction pattern achieved at the 6-ID-D Beamline at the APS presented in Sec. 5.3.4.

5.2. THE CRYSTAL STRUCTURE ABOVE T_{CO} : NO LONG-RANGE CHARGE ORDER

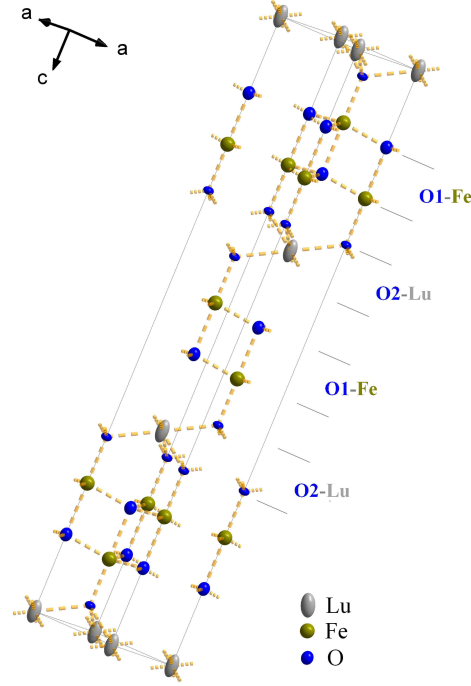


Abbildung 5.4: The hexagonal crystal structure of LuFe_2O_4 in $R\bar{3}m(h)$ space group. The atoms are presented with their refined thermal anisotropic displacement parameters. For better visibility the stacking of [Fe-O1] bilayers and spacer [Lu-O2] single layers are highlighted. The refined data was measured at 350 K.

One part of the sharp charge order reflections can be indexed by a propagation vector close to the symmetry-equivalent direction of $(\frac{1}{3} \frac{1}{3} \frac{3}{2})$ [85, 27], as discussed in the next chapter.

Tabelle 5.2: Refinement parameters for the atomic positions and anisotropic displacement parameters for the refinement on the dataset collected at 350 K.

Parameter	this work	Isobe <i>et al.</i>	Parameter	this work	Isobe <i>et al.</i>
Lu:			O1:		
z	0	0	z	0.1291(2)	0.1281(3)
U_{11}	0.0146(5)	0.0041(1)	U_{11}	0.032(3)	0.019(1)
U_{33}	0.0546(7)	0.0432(2)	U_{33}	0.041(4)	0.047(4)
Fe:			O2:		
z	0.21522(4)	0.21518(3)	z	0.29298(16)	0.2926(2)
U_{11}	0.0202(5)	0.0100(1)	U_{11}	0.0259(19)	0.013(1)
U_{33}	0.0212(7)	0.0090(2)	U_{33}	0.014(2)	0.008(1)

Often, one or two additional sets of CO superstructure reflections appear, due to the particular presence of twin domains (also visible in Fig. 5.2). Such a twinning is expected, since the triangular lattice does not provide a unique orientation for the CO modulation. By considering the $R\bar{3}m$ symmetry, the other two symmetry-equivalent propagation vectors can be expressed as $(\frac{2}{3} \frac{1}{3} \frac{3}{2})$ and $(\frac{1}{3} \frac{2}{3} \frac{3}{2})$, as already presented in [179, 85, 27].

5.3 The monoclinic cell: Putting charge order in new clothes

As already pointed out in the previous chapter, all descriptions of the charge order, until now, have not been based on crystal structure refinements and are therefore only tentative. The suggested charge order scheme in [27, 85] is usually described by a $\sqrt{3} \times \sqrt{3} \times 2$ unit cell, as indicated by \vec{a}' and \vec{b}' in Fig. C.1. However, this unit cell does not describe the domain population with its 120° twinning, as reported in [85].

In this section, a new unit cell is introduced, which describes the observed charge ordering and its domain structure in such a way that all observed reflections are integer and a clear relation to the different domains exists. From symmetry analysis in the hexagonal cell with a $(\frac{1}{3} \frac{1}{3} \frac{3}{2})$ propagation² (as clearly evident for charge ordered LuFe_2O_4 in e.g. [85, 179, 52, 84]), two irreducible representations, presented in Fig. 5.5 are allowed, both of which lower the space group to a monoclinic $C2/m$ cell. These representations correspond to different origin positions (center of inversion) of the monoclinic cell. In one case, it is located at the Lu positions between the bilayers. This structure corresponds to antiferroelectrically (AFE) stacked polar bilayers, as proposed in [85]. In the other case the inversion center is located between the two Fe layers of a bilayer, corresponding to (non-polar) bilayers with a net charge.

The transformed lattice parameters for the monoclinic cell are $|\vec{a}_{\text{Mon}}| = \sqrt{3}a_{\text{Hex}} = 5.959(1)\text{\AA}$, $|\vec{b}_{\text{Mon}}| = 3a_{\text{Hex}} = 10.321(1)\text{\AA}$ and $|\vec{c}_{\text{Mon}}| = \sqrt{\frac{a_{\text{Hex}}^2}{3} + \frac{4c_{\text{Hex}}^2}{9}} = 16.959(1)\text{\AA}$ with a monoclinic distortion of $\beta = 96.72^\circ$ (for detailed information see Appendix. C). The $(h k \ell)$ transformation rules presented in Tab. 5.3 are achieved for the relationship between the hexagonal cell with its three different charge order propagation vectors and the three corresponding monoclinic domains. All three charge order domains contribute to different superstructure

Tabelle 5.3: Transformation rules for the $(h k \ell)$ between the hexagonal and monoclinic unit cell with its three different domains $D1_{0^\circ}$, $D2_{120^\circ}$ and $D3_{-120^\circ}$.

	$D1_{0^\circ}$	$D2_{120^\circ}$	$D3_{-120^\circ}$
$h_{\text{Mon}} =$	$h_{\text{Hex}} - k_{\text{Hex}}$	$3(h_{\text{Hex}} + k_{\text{Hex}})$	$-4h_{\text{Hex}} - 2k_{\text{Hex}}$
$k_{\text{Mon}} =$	$3(h_{\text{Hex}} + k_{\text{Hex}})$	$-4h_{\text{Hex}} - 2k_{\text{Hex}}$	$h_{\text{Hex}} - k_{\text{Hex}}$
$\ell_{\text{Mon}} =$	$\frac{1}{3}(-h_{\text{Hex}} + k_{\text{Hex}} - 2\ell_{\text{Hex}})$	$\frac{1}{3}(-h_{\text{Hex}} + k_{\text{Hex}} - 2\ell_{\text{Hex}})$	$\frac{1}{3}(-h_{\text{Hex}} + k_{\text{Hex}} - 2\ell_{\text{Hex}})$

reflections along the ℓ -line according to Tab. 5.3. For $(\frac{1}{3} \frac{1}{3} \ell)$ superstructure reflections transformed to the monoclinic cell, all reflections corresponding to one domain become integer and fulfill the C-centering conditions in monoclinic setting ($h + k = \text{even}$). This

²This is also valid for the other two propagation vectors $(\frac{2}{3} \frac{1}{3} \frac{3}{2})$ and $(\frac{1}{3} \frac{2}{3} \frac{3}{2})$ giving rise to 120° monoclinic twinning.

5.3. THE MONOCLINIC CELL: PUTTING CHARGE ORDER IN NEW CLOTHES

is also valid for reflections in the hexagonal setting that are obtained from all the structural reflections by adding either $(\frac{1}{3} \frac{1}{3} \frac{3}{2})$ or $(\frac{1}{3} \frac{1}{3} 0)$ or $(00 \frac{3}{2})$. All these superstructure reflections, which belong to one particular charge order domain, can now be described by integer-indexed reflections of the corresponding monoclinic super-cell, in contrast to reflections from the other two domains, which have non-integer-index reflections after the transformation. These facts make the monoclinic cell described in this paragraph the most likely description for the CO in LuFe_2O_4 . This new cell contains 24 Fe-atoms in contrast to the $\sqrt{3} \times \sqrt{3} \times 2$ cell where 36 Fe-atoms are included.

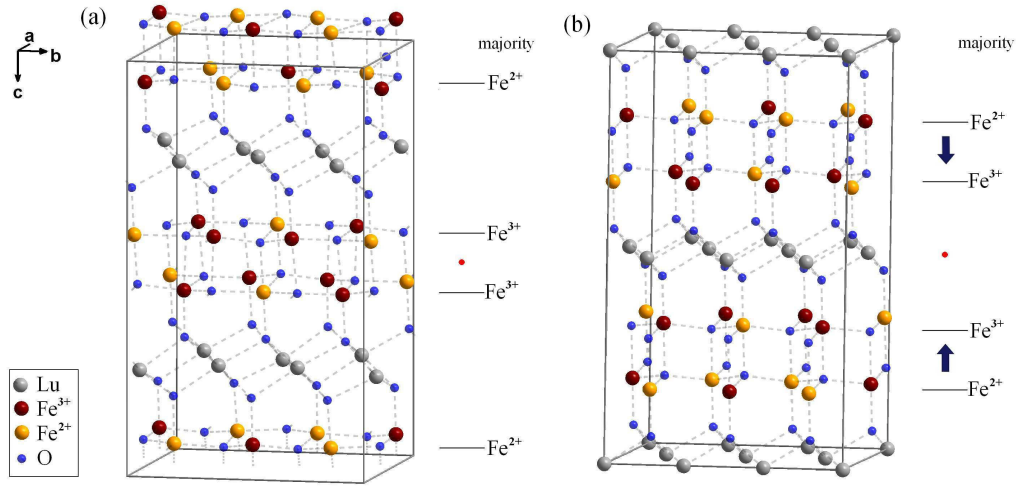


Abbildung 5.5: The two different representations of the monoclinic $C2/m$ cell: (a) with the center of inversion inside a Fe bilayer and (b) with the inversion-center in a Lu single layer. For both structures, the possible charge order configurations are indicated and the particular stacking of majority valences is shown. For solution (b) the potential AFE stacking is indicated by blue arrows.

Due to the reduced symmetry in the $C2/m$ cell, the Wyckoff positions from the $R\bar{3}m$ cell will split into distinct positions, each with a lower symmetry [180]. For example, the single 6c Fe site present in $R\bar{3}m$ will split into 4 not equivalent Fe positions composed of two 4i and two 8j sites. Depending on the origin position (center of inversion), two different representations in the monoclinic subgroup from the hexagonal high-temperature phase ($R\bar{3}m$) of LuFe_2O_4 are possible [181]. In the case of equivalent Fe sites, both representations are equal. However, by introducing a CO to the Fe sites, strong differences appear between both representations, as we will see in the next section.

5.3.1 Refining the monoclinic $C2/m$ crystal structure

As already introduced by the subgroup calculations in the previous section (Sec. 5.3), there is a possible three fold monoclinic twin-structure cell, describing the charge ordered below T_{CO} . In order to refine the crystal structure within this new structure, we collected at 210 K a complete 5-times redundant data set (in monoclinic setting) with extended counting times of 20 seconds. The long counting time was chosen to increase the weak statistics on the charge order superstructure reflections. The chosen temperature of 210 K was, according to [148] and Sec. 4.2.3, low enough to achieve a sufficiently high intensity on the $(\frac{1}{3} \frac{1}{3} \ell)$ diffraction line, but high enough to avoid problems with the strongly hysteretic structural phase transition at $T_{LT} \sim 170$ K (already reported in [28]). This temperature is below $T_N \sim 240$ K, but, as shown in Sec. 5.3.2, the magnetic ordering temperature does not affect the crystallographic structure and the charge order. The $\text{Mo}_{K\alpha}$ radiation was chosen in order to reduce absorption to a tolerable value. To avoid a strong overlap of superstructure reflections, the detector distance was set at 76.95 mm from the sample, which is the maximum value for the SuperNova diffractometer.

For these refinements, the apparently small incommensuration away from $(\frac{1}{3} \frac{1}{3} \ell)$ and $(00 \frac{3}{2})$ type reflections was neglected, because it most likely corresponds not to a “truly incommensurate” structure [182], but rather to a discommensuration from anti-phase-boundaries, as previously proposed for LuFe_2O_4 [84, 85] and also observed in other CO oxides like Fe_2OBO_3 [26].

In order to achieve a proper refinement, a quantity of small crystals, obtained from one crushed sample from the same batch as in [1, 93, 28, 85, 88], showing the best magnetic behavior, was screened for their domain population. In all the low-temperature (with $T < T_{CO}$) x-ray experiments, the three domains could be readily identified by the diffractometer software as a threefold twinned monoclinic cell with $C2/m$ -symmetry (as shown in Fig. 5.7). No violations of the C-centering condition are observed as proposed by the calculations in Sec. 5.3. The exact symmetry description for one domain is $C12/m1$; for monoclinic systems the b -direction is usually used as the unique axis which is parallel to the symmetry axis and is a normal of the symmetry plane. In all measured crystals, the three monoclinic domains could be indexed with the lattice parameters, $a = 5.9483(5)\text{\AA}$, $b = 10.3003(9)\text{\AA}$, $c = 16.9601(12)\text{\AA}$ and $\beta = 96.724(7)^\circ$, which takes into account error bars and thermal expansion corresponds to the values predicted from the calculations in the previous section, but not in their error bars. In [93, 183] a monoclinic cell was also

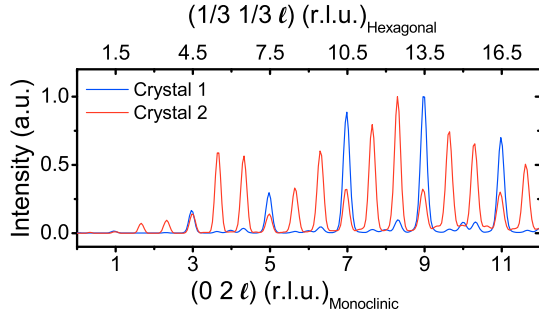


Abbildung 5.6: The intensity distribution along the $(0\ 2\ \ell)$ -line for two different crystals at 210 K. For better comparison, the reflections are indexed in hexagonal and monoclinic settings. The structure refinement here presented is performed on the Crystal-1. Figure from own published work [172].

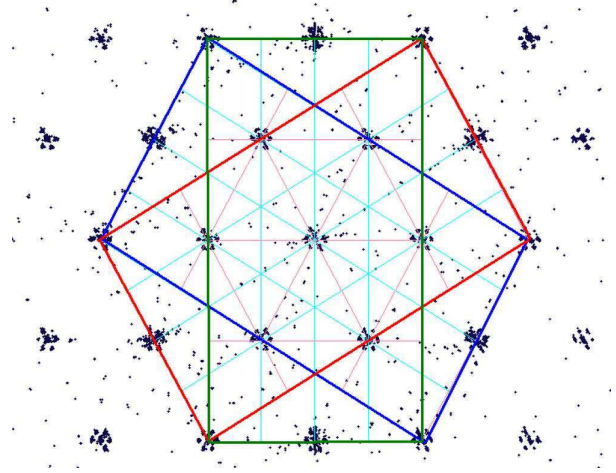


Abbildung 5.7: Observed reflections in reciprocal space for the crystal presented in Fig. 3.6. Almost every reflection could be indexed with the three domains rotated by 120° presented in this chapter and marked by different colors.

used to describe the LuFe_2O_4 crystallographic structure; the different lattice constants $a = 5.95\text{\AA}$, $b = 10.32\text{\AA}$, $c = 17.31\text{\AA}$ and $\beta = 103.2^\circ$ are due to a different cell, chosen for the same monoclinic lattice. The present cell corresponds to the usual crystallographic convention to select the cell with the smallest deviation away from 90° for β .

Upon data integration, the first problems occur, because superstructure reflections along the $(\frac{1}{3}\ \frac{1}{3}\ \ell)$ -line (contributions from the different domains) are located too close to each other for a proper raw data integration³. After screening dozens of samples for their domain population a few samples were found which show an almost mono domain population distribution (see Fig. 5.6 for two different crystals at 210 K); this would improve the integration and crystal structure refinement. This result so far demonstrate, that the domain population of LuFe_2O_4 is strongly sample dependent and not an intrinsic property. This question was already raised by Chrisitanson *et al.* in [1], where for two different samples comparable domain populations of (0:85:0:57:1) were found by neutron diffraction. A similar mono domain approach was also used for the very recent report on the crystal structure refinement of charge ordered magnetite [184], which shows charge order domains below the Verwey transition.

Returning to the crystal structure refinement, after the frame integration for this new single domain crystal was performed (only one domain was addressed) a good R_{int} value

³Even with the smallest possible integration mask, this problem could not be solved.

of 4.5% was achieved for the collection of 8556 reflections (1285 unique). After applying analytical absorption correction (see Sec. 3.3.2), taking the indexed crystal faces into account⁴, the R_{int} value drops to 3.6%. The CrysAlis^{Pro} program for data reduction directly indicated the $C2/m$ -symmetry (space group №12) and no violation of the C-centering condition ($h+k = \text{even}$) was found for all observed reflections. After collecting and integrating the raw data the crystal structure refinement could be performed with the help of the SHELX program package [107].

Crystal structure refinement

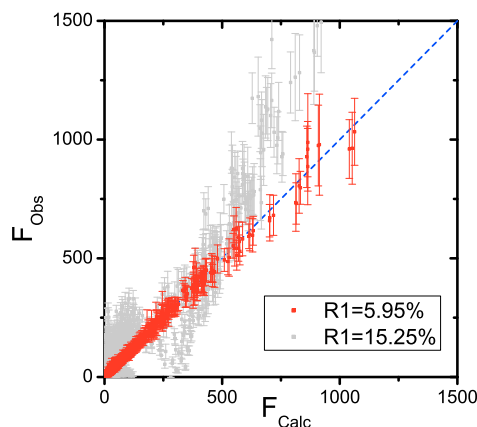


Abbildung 5.8: Observed structure factors against calculated ones from different models. Gray: The solution according to the representation following the charge order distribution of [27, 85]. Red: The solution presented in Fig. 5.9 with the representation presented by the blue dotted lines in Fig. C.2; the blue line indicates $f(x) = x$ the ideal distribution. Different scales are due to distinct weighting schemes (see Sec. 3.3.1).

The $(h k \ell)$ -reflection list containing the integrated intensities and the instruction file containing the lattice parameters and space group were imported into SHELX. Here, the program SIR92 [185, 186] was used for the first guess of the atomic distributions inside the monoclinic unit cell, which gives a reasonable starting point for the following structure refinement. Already at this point, two distinct structural solutions appeared; both were introduced before, in Fig. 5.5, as possible representations for the hexagonal $R\bar{3}m$ solution. They differ from each other by the choice of the center of inversion inside the unit cell. In order to decide which the right one is, crystallographic refinements with both solutions were performed. The first refinement, with the center of inversion located in the Lu layers (the blue domain in Fig. C.2), corresponding to the representation

⁴The particular crystal and its indexed faces are shown in Fig. 3.6.

5.3. THE MONOCLINIC CELL: PUTTING CHARGE ORDER IN NEW CLOTHES

Tabelle 5.5: Refined atomic parameters (positions and thermal displacement parameters) for LuFe_2O_4 at 210 K for the single domain crystal in monoclinic $C2/m$ symmetry in the most likely representation as discussed in the text.

Atom(Wyc)	x	y	z	U_{11}	U_{22}	U_{33}	U_{23}	U_{13}	U_{12}
Lu01 (4i):	.24921(10)	.5000	.23933(6)	.0257(5)	.0281(5)	.0489(5)	.000	.0084(3)	.000
Lu02 (8j):	.25008(6)	.16694(3)	.25543(3)	.0221(5)	.0231(4)	.0313(4)	-.00092(15)	.0031(2)	-.00016(13)
Fe01 (4i):	.3553(4)	.0000	.07430(13)	.0240(11)	.0209(10)	.0223(10)	.000	.0030(8)	.000
Fe02 (8j):	.6434(4)	.16483(14)	.42690(12)	.0283(11)	.0358(12)	.0281(9)	.0016(6)	.0028(7)	.0008(5)
Fe03 (8j):	-.1402(4)	.16892(12)	.07210(10)	.0282(10)	.0249(10)	.0199(8)	-.0010(5)	.0001(6)	.0000(5)
Fe04 (4i):	.1384(5)	.0000	.42740(16)	.0388(15)	.0456(16)	.0305(13)	.000	.0090(10)	.000
O01 (4i):	.207(2)	.0000	.5510(9)	.029(6)	.053(8)	.048(8)	.000	.014(5)	.000
O02 (4i):	-.116(2)	.5000	.1884(6)	.033(6)	.035(6)	.019(5)	.000	.010(4)	.000
O03 (4i):	.673(2)	.0000	.0664(10)	.024(5)	.033(6)	.062(8)	.000	.021(5)	.000
O04 (8j):	.1937(17)	.1570(6)	.0552(5)	.030(4)	.020(3)	.026(4)	-.002(2)	-.001(3)	.003(2)
O05 (8j):	.1089(16)	.3394(5)	.3116(5)	.024(4)	.014(3)	.035(4)	-.004(2)	-.001(3)	.000(2)
O06 (4i):	.0915(18)	.0000	.3112(7)	.021(5)	.019(5)	.030(5)	.000	.007(4)	.000
O07 (8j):	.323(2)	.1809(11)	.4395(11)	.034(6)	.051(6)	.124(12)	.011(6)	.015(6)	-.009(4)
O08 (8j):	.4024(17)	.3255(7)	.1896(5)	.028(4)	.039(5)	.021(4)	.005(3)	.003(3)	.001(3)

with AFE stacked bilayers in [85], puts Lu on symmetric positions and Fe on general positions. In this cell, all 84 atoms on 16 different sites could be found upon refinement. Considering thermal atomic movements leads again to very anisotropic displacement parameters for Lu along the c_{Hex} direction⁵. These displacements are comparable to Sec. 5.2 very unlikely, because the Lu-elements are by far the heaviest elements in this material and should not be that anisotropic. On top of this inconsistency, a relatively poor agreement factor between model and observation was achieved, as illustrated in Fig. 5.8, which plots the observed and calculated structure factors against each other in gray. One sees directly that there is no good agreement, also indicated by the high R -factor of $R1 \sim 15\%$ already introduced in Sec. 3.3.1. All this makes this solution an unlikely one.

For refinements corresponding to the second representation in Fig. 5.5b, with the center of inversion located in the middle of one particular Fe bilayer resulting in Lu atoms on more general positions, a much better agreement factor of $R1 = 5.96\%$ is achieved. In this representation, the positions could be refined with anisotropic thermal displacement parameters for all expected 14 different sites (resulting in a total of 84 atoms inside the unit cell). The corresponding refinement result is presented in Tab. 5.5 and shown in Fig. 5.9.

As indicated by a plot of the measured form factors against the calculated ones in Fig. 5.8, there are no strong deviations of the observed reflections from the calculated

⁵This is similar to the structural solution above T_{CO} in Sec. 5.2 and is most likely due to inaccuracy of the describing structure.

Tabelle 5.4: Refinement parameters for the data collected at 210 K.

Parameter	this work
Space group	$C2/m$
R_{int}/R_{σ}	0.0390/0.0211
R_1/wR_2	0.0596/0.168
Goof S	1.1145
Measured Reflections	1297
diff. peak and hole, $\text{e}/\text{\AA}^3$	3.21/ -2.99
ρ_{calc} , $\text{g}\cdot\text{cm}^3$	6.77064

ones. It is readily seen from Fig. 5.9 that the Lu thermal displacement parameters in this structural refinement are much more isotropic in their distribution than in the high- T solution of Fig. 5.4. This can be explained by the fact that in this structure the Lu-atoms have the possibility to shift along the c_{Hex} direction.

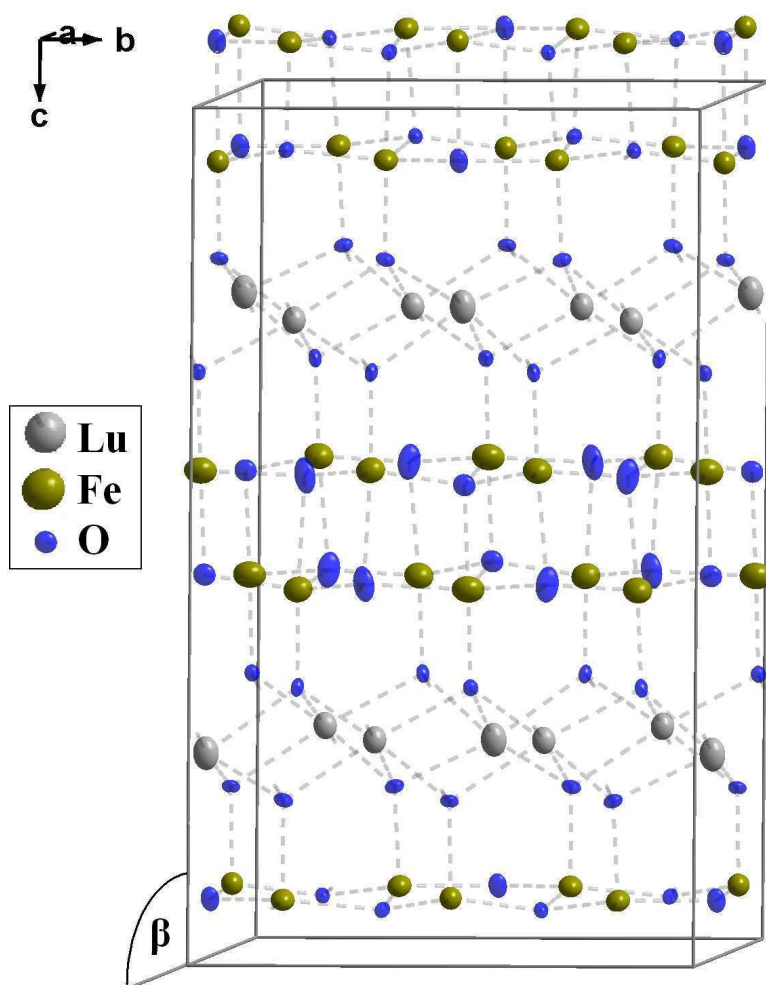


Abbildung 5.9: Monoclinic crystal structure of LuFe_2O_4 in $C2/m$ space group for the charge ordered phase, following the structural representation explained in this chapter. The atoms are presented with their refined thermal anisotropic displacement parameters. The lattice parameters of the cell are: ($a = 5.95 \text{ \AA}$, $b = 10.30 \text{ \AA}$, $c = 16.96 \text{ \AA}$, $\beta = 96.72^\circ$). The refined data was measured at 210 K.

The small atomic displacements explain the poor refinement with large anisotropic displacement parameters for the Lu atoms on high symmetry sites for the first refinement effort. When the Lu positions at 210 K from the second attempt are compared with the ones achieved from refinements with the same monoclinic cell at 350 K, a strong increase of the displacement is visible. This interesting point shows that the Lu distortion along

c_{hex} direction with an amplitude of $\sim 0.14\text{\AA}$ (see Fig. 5.10) is clearly connected to the $\text{Fe}^{2+/3+}$ charge order, involving oxygen shifts on the Fe-O-Lu path. These shifts can be caused by different Fe valences, which favor unequal average bond lengths to the surrounding oxygen atoms [187]. Similar shifts of the rare-earth elements were observed in the isostructural compound YFe_2O_4 [188]. Here the authors claimed that a modulation of the Y-O layer in the c_{Hex} direction plays an important role in the stabilization of the long range periodic $\text{Fe}^{2+/3+}$ charge order for that compound. An equivalent suggestion was already made for LuFe_2O_4 in [87], where the charge order superstructure may arise from the size mismatch between different layers, leading to a distortion on the Lu sites.

One thing to mention here is the bond length between the Fe01 and O03 atoms, which is with $2.3725(171)\text{\AA}$ unusually long compared to a typical Fe-O bond of about 2.03\AA [189]. This can be due to the extremely rare Fe environment with its trigonal pyramidal coordination and the additional charge order, indicating the distortion of individual Lu sites.

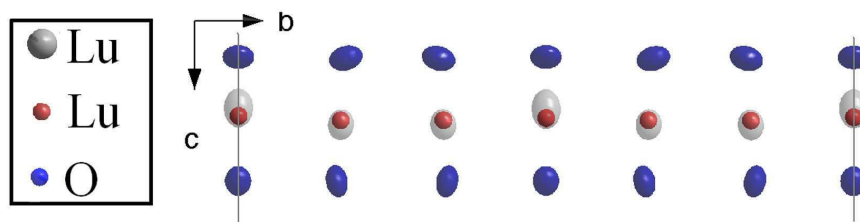


Abbildung 5.10: The Lu and O atoms drawn as thermal ellipsoids in projection along the a_{mon} direction from the refinement at 210 K. For comparison, the Lu positions achieved from the refinement at 350 K are displayed as red spheres. Figure from own published work [172].

5.3.2 From the refined structure to the CO pattern

The correspondence of the cell position with the CO representation analysis, suggests that the structure, with its particular origin (inversion-center), defines the exact CO pattern; but this is no direct proof. The x-ray form factor curves of Fe, Fe^{2+} and Fe^{3+} are identical beyond $\sin(\theta)/\lambda=0.25$ (see Fig. 3.3), and thus a refinement of the different oxidation states cannot be distinguished precisely by a refinement taking different Fe valences on the crystallographic sites into account [190]. Below this resolution value the contrast is still very small, and only very few reflections are accessible (10 reflections from one domain), making such a valence-dependent refinement impossible. Consequently, only the scattering factors of the neutral Fe are used upon refinement for all the Fe-sites.

As will be explained in this chapter for the identification of the different valence states, other methods should be used.

In the previous section, the Lu displacements along the c_{Hex} direction were discussed as a precursor effect from the charge order. These displacements in Fig. 5.10 are a result of the movement of Fe-surrounding oxygen ligands to lower temperatures, as indicated in Fig. 5.11. As already introduced in Sec. 2.1.3, the Bond Valence Sum method (BVS) is a unique tool to explore the different valences on particular sites. Here, the distance to the surrounding ligand atoms is compared to tabulated values for typical bond types and valences. For different Fe sites strong deviations in the positions of surrounding O

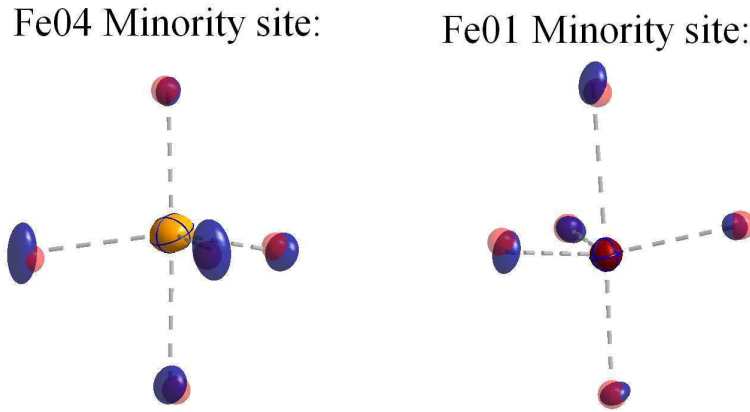


Abbildung 5.11: The oxygen coordination at 210 K and 350 K for Fe^{2+} and Fe^{3+} minority sites (red spheres indicate the oxygen positions obtained from the refinement at 350 K). Figure from own published work [172].

atoms at 210 K are visible in Fig. 5.11 with respect to the high- T structure refined at 350 K, indicating a localized ionic character according to the average site specific Fe-O bond-lengths (see Tab. 5.6). For Fe^{2+} and Fe^{3+} the average Fe-O bond length in a trigonal bipyramidal coordination should be 2.09\AA and 1.98\AA respectively [189]⁶. To determine the valence V from individual cation sites, a Bond Valence analysis [32, 33] was performed:

$$V = \sum_i \exp[(d_0 - d_i)/0.37] \quad (5.1)$$

Here, d_i is the experimental bond length to the surrounding ions and d_0 a tabulated empirical value characteristic for the cation-anion pair [32, 33]. The result of this method strongly depends on the used d_0 , but this value in turn strongly depends on the valence. So, in order not to neglect a potential solution, all possible valence states for particular

⁶The value for Fe^{2+} was extrapolated according to the procedure described in the article.

5.3. THE MONOCLINIC CELL: PUTTING CHARGE ORDER IN NEW CLOTHES

sites are calculated, and the one that is closest to the assumed valence is the most likely. In the case of LuFe_2O_4 the Lu has only an oxidation number which is strict $3+$ ⁷, though only the Fe sites can have different valences of $2+$ and $3+$. By comparing the BVS calculations for both possible Fe valences for each site, the charge order pattern in column 4 of Tab. 5.6 is very close to the assumed valences in calculations and thus the most likely CO distribution.

The result from the BVS method, for the Fe sites from the 210K structure in the previous chapter, are shown in Tab. 5.6 and illustrated by colors for different Fe sites in Fig. 5.13a. It is clear from Tab. 5.6 that Fe atoms on majority sites (higher multiplicity) tend to be less ionic than those located on the minority sites. A strong ionic character of the charge ordered state below T_{CO} was already proposed by Mulders *et al.* [31] from resonant x-ray diffraction, where a chemical shift from the Fe K-edge of 4 eV was deduced, consistent with a full Fe^{2+} and Fe^{3+} charge separation. In order to investigate the tem-

Tabelle 5.6: Calculated valences from the Bond Valence Sum method for different Fe-sites by using the refined crystallographic structure at 210K in Tab. 5.5 and [350K in $R\bar{3}m$ symmetry].

Site	T[K]	$\langle(Fe - O)\rangle [\text{\AA}]$	valence from BVS	valence from BVS	Multiplicity
Fe01	210	1.998	2.91(2) ($3+$)	2.71(1) ($2+$)	4
Fe02	210	1.999	2.75(2) ($3+$)	2.57(2) ($2+$)	8
Fe03	210	2.058	2.10(1) ($2+$)	2.26(1) ($3+$)	8
Fe04	210	2.100	1.92(1) ($2+$)	2.04(1) ($3+$)	4
$\text{Fe}_{R\bar{3}m}$	350	2.030	2.38(3)	2.38(3)	6

perature dependence of the observed charge order pattern, similar structural refinements on the mostly single domain crystal were done at different temperatures. The results are shown in Fig. 5.12. For temperatures below T_{CO} , an onset of charge order is observed, and a plateau value is reached below 260 K for all four sites. The onset of magnetic order at T_N does not affect the crystal structure and the charge order configuration. At $T_{LT} \sim 170$ K there is a magneto-structural phase transition [28] where a splitting from structural reflections is observed by cooling through T_{LT} . This however leads only to very subtle changes of atom positions in the refinements, while not affecting the charge order configuration (120K in Fig. 5.12) observed in BVS calculations and the $C2/m$ symmetry. Above 350 K all valences are close to $2.5+$, indicating no long-range charge order. The valences at this temperature were calculated by using the high-temperature structure above T_{CO} , which refinement is already presented in Sec. 5.2. Because the valence at this temperature tends not to be separated into Fe^{2+} or Fe^{3+} at different sites, the average

⁷The Bond Valence analysis gave 2.940 and 2.947 for the valences on Lu01 and Lu02 sites.

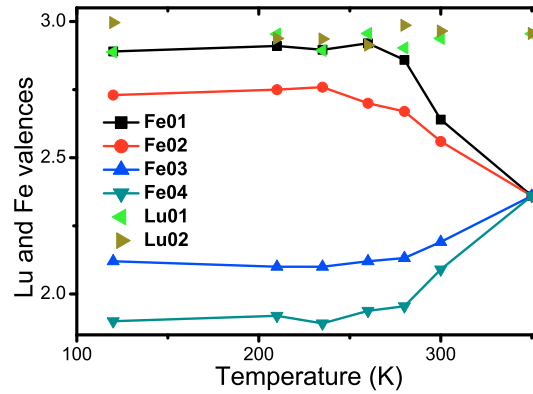


Abbildung 5.12: Fe and Lu valence states for different sites and temperatures calculated from the Bond Valence Sum method. The valence states above T_{CO} are calculated from the hexagonal solution with only one single Fe site presented in Sec. 5.2. Figure from own published work [172].

from both BVS calculations for each type of valences is used⁸. For all temperatures, it is readily seen from Fig. 5.12 that the average valence from different sites is not similar to the expected $\text{Fe}^{2.5+}$; it is slightly lower, because the Fe^{2+} valence contributions are too low. One explanation for this offset behavior could be the extremely rare Fe^{2+} surrounding with its trigonal pyramidal coordination [189, 32] and the perhaps imperfectly estimated tabulated values for such a surrounding. However, for all temperatures the Lu valences are fairly close to the expected value of 3+ for both sides, indicating their ionic behavior.

Before the interesting consequences of this new charge order pattern presented in Fig. 5.13a for the ferroelectric behavior of LuFe_2O_4 are discussed, an additional refinement in the lower possible space group Cm is done in Sec 5.3.3. Afterwards, the stability of this charge order solution is tested under applied external electric and magnetic fields in Sec 5.3.4. However, the valence separation for LuFe_2O_4 observed here, deduced from the BVS analysis, is already considerably larger than that found for other charge ordered Fe oxides, except for Fe_2OBO_3 [26], where a stronger separation into ionic Fe^{2+} and Fe^{3+} is observed. Nevertheless, the valence separation estimated for these two compounds is already considerably greater than, for example, in YBaFe_2O_5 [191], with a valence separation of ~ 0.7 on the iron sites. It is much larger than in the classical, though until now not fully understood, charge-order-example magnetite (~ 0.4) [23], or than in the colossal magneto-resistance manganites with ~ 0.45 valence separation [192].

⁸For the case of Fe^{2+} and Fe^{3+} it would be 2.317 and 2.433 respectively.

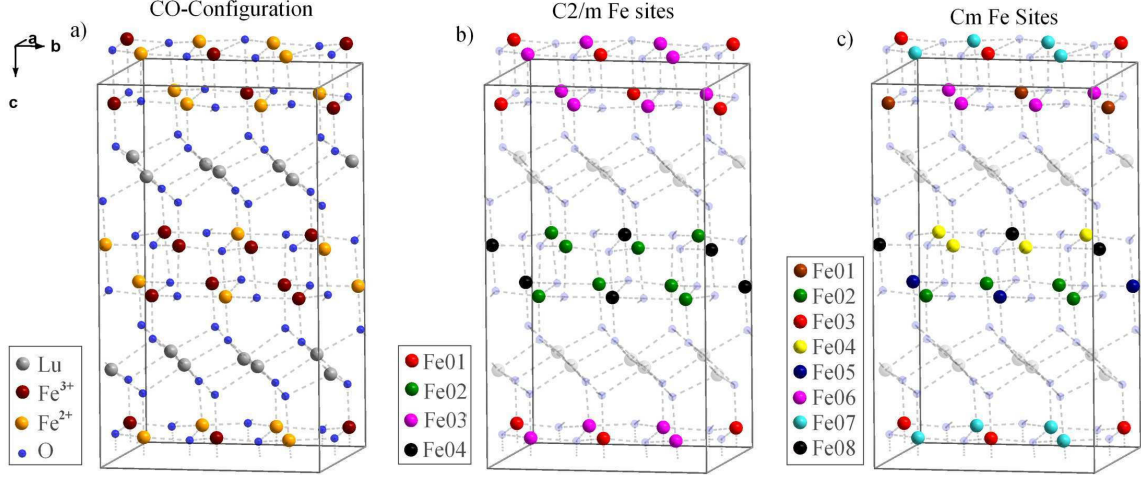
5.3.3 Solving the structure in Cm -symmetry


Abbildung 5.13: (a) Monoclinic crystal structure of LuFe_2O_4 in $C2/m$ symmetry ($a=5.95 \text{ \AA}$, $b=10.30 \text{ \AA}$, $c=16.96 \text{ \AA}$, $\beta=96.72^\circ$). The refined data was measured at 210 K. The same $\text{Fe}^{3+/2+}$ charge order found in both symmetries by the BVS method is represented by the colors. The different Fe Wyckoff sites are distinguishable in each structure by the colors for (b) the $C2/m$ and (c) the lower symmetry Cm cell.

To see if the $C2/m$ space group with its symmetry elements describes the real crystal structure correctly, an additional refinement in the lower symmetry space group Cm was performed. In contrast to the $C2/m$ group, this Cm space group

is non-centrosymmetric, additionally allowing for the ferroelectric charge order scheme reported in [27] (and also the AFE CO suggested in [85]). This is not the case for the $C2/m$ symmetry with the representation used in this thesis. According to this representation, this lower symmetry refinement gives the possibility to see if the observed charge order pattern exhibiting charged bilayers is correct. In order to do this, the reflection list, which now has more reflections with fewer symmetric equivalent Friedel mates, was integrated in the Cm symmetry from the same x-ray data frames as already used in Sec. 5.3.1. For this integration a good data set quality was also achieved, indicated by the low R_{int} value with 3.48% intensity deviation for symmetric equivalent reflections.

Upon crystal structure refinement, all 28 sites, containing 8 sites which belong to Fe, were found. The crystal structure could be refined with a $R1$ value of 4.98%, which is

Tabelle 5.7: The $C2/m$ and Cm refinements.

Space group	$C2/m$	Cm
R_{int}/R_σ	0.0390/0.0211	0.0385/0.031
R_1/wR_2	0.0596/0.168	0.0498/0.128
Goof S	1.1145	1.182
Measured Reflections	1297	2426
diff. peak and hole, $\text{e}/\text{\AA}^3$	3.21/ -2.99	2.35 / -2.99
ρ_{calc} , g/cm^3	6.77064	6.76425

KAPITEL 5. THE CRYSTALLOGRAPHIC STRUCTURE DESCRIBING CHARGE ORDER

Tabelle 5.8: Calculated valences from the Bond Valence Sum method for different Fe-sites by using the refined crystallographic structure in Cm symmetry at 210 K.

Site	T[K]	$\langle(Fe - O)\rangle [\text{\AA}]$	valence from BVS	valence from BVS	Multiplicity
Fe01	210	2.113	1.857(2) (2+)	1.987(1) (3+)	2
Fe02	210	2.085	1.968(2) (2+)	2.105(2) (3+)	4
Fe03	210	2.090	1.948(1) (2+)	2.085(1) (3+)	2
Fe04	210	2.064	2.130(1) (2+)	2.493(1) (3+)	4
Fe05	210	1.951	2.867(1) (3+)	2.680(1) (2+)	2
Fe06	210	1.947	2.802(1) (3+)	2.619(1) (2+)	4
Fe07	210	2.013	2.836(1) (3+)	2.563(1) (2+)	2
Fe08	210	2.041	2.735(1) (3+)	2.651(1) (2+)	4

slightly better than for the case of $C2/m$ symmetry (5.96%). This improved R -value is due to the fact that there are more free parameters for the atomic displacements available to describe the structure. Due to the increase of parameters, only the heavier atoms could be refined adequately with anisotropic thermal displacement parameters. The 16 oxygen atoms could not be refined with anisotropic thermal displacement parameters, because the ratio of data points to parameters would be worse than 8, which would destroy the reliability. The detailed results from these refinements are presented in the Appendix D.

All refined atomic positions in Cm symmetry are close, within three error bars, to the positions found in $C2/m$ symmetry, indicating that there are no significant structural distinctions between the solutions in both symmetries, making $C2/m$ the most likely space group to describe the CO structure. Applying the BVS calculations to this lower symmetry Cm structure, the same charge order pattern as in the previous chapter could be confirmed⁹. These two refinements, in Cm and $C2/m$ symmetry and its corresponding BVS analysis, makes the observed charge order pattern, exhibiting charged double layers instead of polar bilayers, the most likely charge order configuration. Here, the used monoclinic cell seems to be a good approach to describe the charge order in LuFe_2O_4 .

5.3.4 Influence of electric fields on the charge order

After solving the crystal structure in Sec. 5.3.1 and determining the charge order configuration below T_{CO} with its non-polar bilayers, an important question remains to be answered: is an electric field induced ferroelectric charge order configuration for LuFe_2O_4 possible? The best way to answer this question is to perform an in situ x-ray diffraction experiment under applied electric fields (under cooling) along the c_{Hex} direction. This

⁹For the Lu01, Lu02, Lu03 and Lu04 atoms valences of 2.971, 2.994, 2.961 and 2.929 respectively were calculated by the BVS method. This is in good agreement with the results in $C2/m$ symmetry.

5.3. THE MONOCLINIC CELL: PUTTING CHARGE ORDER IN NEW CLOTHES

was already suggested in [85]. One of the main results Ikeda *et al.* [27] presented in his pyroelectric current measurements in Fig. 2.10 was, that the spontaneous electric polarization depends on the direction of the applied electric field ($\pm 10 \text{ kV cm}^{-1}$). In the experiment, the electric field was along the c_{Hex} direction under cooling to low T , and the pyroelectric current flow from the sample was then recorded upon heating without the electric field. This measurement showed that the direction of current flow (and thus the electric polarization) depended strongly (below 350 K) on the sign of the field under cooling. Furthermore, electric voltage versus current measurements on our type A samples in Fig. 5.14a show a firm non linear behavior around T_{CO} . A similar ($I-V$) behavior was also found by other groups for LuFe_2O_4 [193, 194, 195, 196] suggesting a strong interaction between the charge-ordered state and an external electric field.

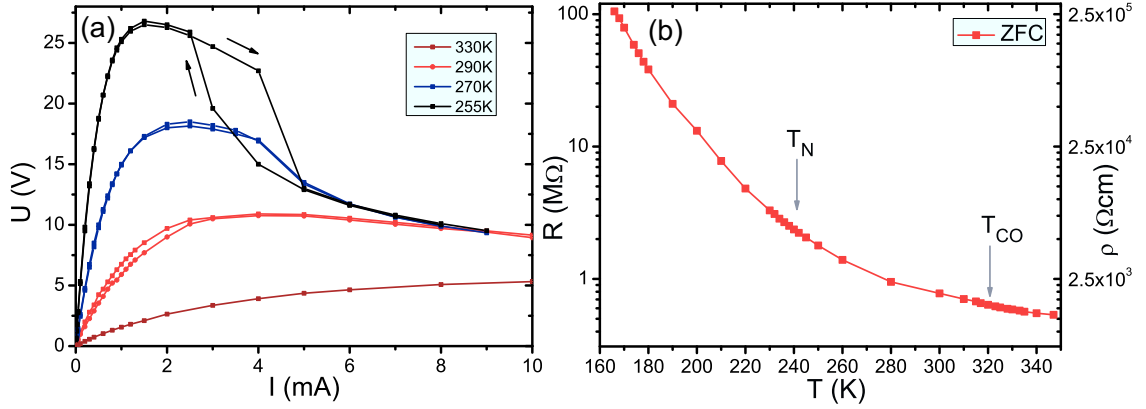


Abbildung 5.14: (a) Voltage versus electric current measurements at different temperatures with $\vec{E} \parallel c_{\text{Hex}}$. Arrows indicate the direction of measurement. (b) Resistivity versus temperature curve measured with low probing currents along the c_{Hex} direction. The resistance below 165 K exceeds the maximum ($\sim 100 \text{ M}\Omega$) of the Keithley2400 Multimeter. The right scale indicates a rough estimation for the specific resistivity of LuFe_2O_4 , due to the uncertainties in sample geometry.

In order to determine the possible influence of electric fields to the CO configuration, a small LuFe_2O_4 single crystal was measured in the $(h h \ell)_{\text{Hex}}$ diffraction plane with high-energy photons¹⁰ of 99.706 keV. The advantage of these highly energetic photons is that the Ewald-sphere in Fig. 3.2 becomes flatter and the absorption inside the sample is minimized. The precise position and orientation (deviation between surface normal and incoming beam) of the image plate were calculated from a standard silicon powder sample, allowing an accurate calculation of the Q values from particular features on the detector. In order to achieve a reasonable Q range, the MAR345 area detector was posi-

¹⁰corresponding to a wavelength of $\lambda = 0.124 \text{ \AA}$.

tioned 160.5 cm away in beam direction from the sample (result from silicon standard), allowing access to a sufficient area of the $(hh\ell)_{Hex}$ plane.

The crystal used in this experiment was of good quality, and it showed nice facets perpendicular to the c_{Hex} direction. It is known from the literature that $LuFe_2O_4$ is a bad conductor, but it is also far from exhibiting perfect insulating behavior [193, 197, 198, 199, 194, 200]. To avoid the establishment of zero net electric inside the crystal by possible charge transfer under an applied external electric field, the silver paint anode and cathode were attached in contact mode to the facets. This non-insulating mounting allows for a current flow through the sample. The result for the $R - T$ curve presented Fig. 5.14b is comparable to the measurements reported in [199, 194] on polycrystalline samples. With the Kitley2400 voltage source, the maximum resistivity measurable is 100 M Ω . This value was already achieved at 165 K, so just in the vicinity of the low-temperature transition T_{LT} .

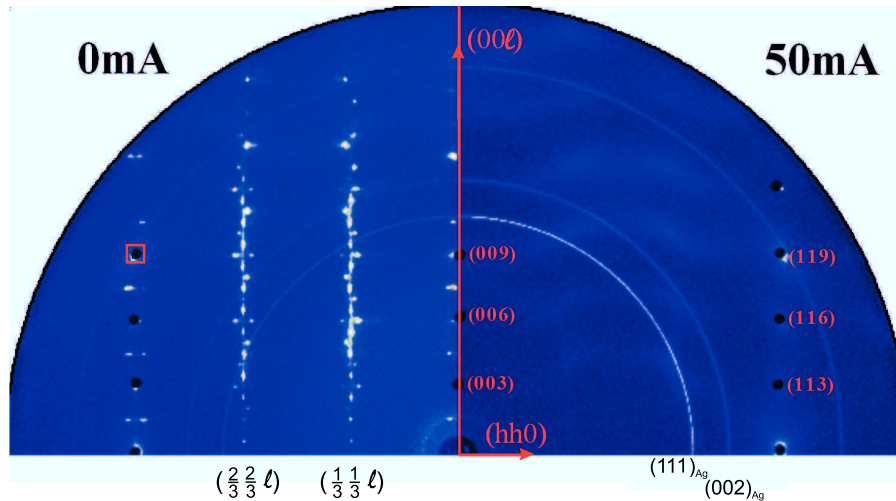


Abbildung 5.15: The $(hh\ell)$ -reciprocal plane measured with the MARE345 area detector at 260 K. The diffraction pattern was collected on the left side with 0 mA and on the right side with 50 mA current flow through the sample. The Ag powder rings additionally measured are indicated by Miller indexes (bottom). Most of the structural reflections from the $R\bar{3}m$ symmetry, indicated by its Miller indexes in red on the right side, are covered by lead pieces in order to protect the detector from overexposure. The red box indicates the $(119)_{Hex}$ reflection, which is studied under magnetic fields in the next section.

Coming back to the diffraction experiment, the sample was mounted on the diffractometer and cooled down to 10 K. The sample was measured with a broad rocking procedure (similar to [201]) in order to achieve as many reflections on the image plate in the $(hh\ell)_{Hex}$ diffraction-plane as possible. The estimated sample temperature was measured with a thermometer on the cold finger located as close to the sample as possible. At

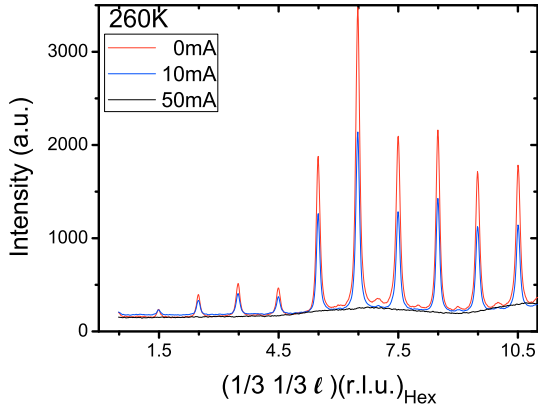


Abbildung 5.16: Charge order domain population at 260 K on the $(\frac{1}{3} \frac{1}{3} \ell)$ line, measured at zero current, 10 mA and 50 mA for comparison. All data was obtained with the same data acquisition script.

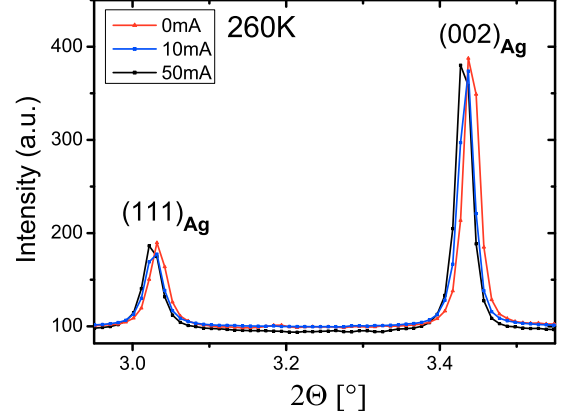


Abbildung 5.17: The observed silver (111) and (002) powder rings in the diffraction experiments and their corresponding 2θ diffraction angles indicating an increase of the silver lattice parameters for higher electric currents.

this low temperature, the applied electric field does not show any influence on the charge order reflections, indicating a robust order, even at very high fields. Afterwards, the sample was heated up to 260 K and the same experiment was repeated (at this temperature the resistance is much lower and therefore, stronger effects are expected). The result for zero field (0 mA) are shown in Fig. 5.15 on the left side¹¹ where $(\frac{1}{3} \frac{1}{3} \ell)$ charge order superstructure reflections are present (similar to the 10 K case), indicating the domain population of this sample. Now, when applying an electric DC voltage and consequently an electric current through the sample, a dramatic change in the superstructure reflections is observed. The observed intensity of these reflections decreases for an increasing voltage/current until there only remains a diffuse line, as indicated on the right side of Fig. 5.15. But for all currents, there is no change of domain population observed, as indicated in Fig. 5.16 by similar intensity ratios along the $(\frac{1}{3} \frac{1}{3} \ell)$ diffraction line.

This effect of “current induced melting of CO domains” has already been observed in LuFe_2O_4 and attracted considerable attention [193, 194, 195, 196]. Recent work [91] based on neutron diffraction under applied electric fields above T_N suggests that this effect is due to the Joule heating effect from the electric current flowing through the samples. This would indicate that there is no direct coupling between the electric field and charge order domain population present. In order to clarify this issue, the diffraction data presented here was analyzed for the Joule heating effect. The Ag powder rings from

¹¹Only a quarter of the image plate is shown due to symmetry reasons.

the electrodes in Fig. 5.15 are a perfect temperature standard for the real temperature at the sample surface. The intensity and position of these rings were obtained by a radial integration from the image plate. In order to avoid overlapping problems, regions with reflections from the crystal were neglected upon integration¹². In Fig. 5.17 the positions from the (1 1 1) and (0 0 2) silver powder rings for different sample currents are shown. For higher currents, there is a shift towards lower 2Θ diffraction angles, indicating an increase of the silver lattice parameters. This increase can only be explained by thermal expansion. The distance of specific lattice planes was calculated by Bragg's law for the particular reflection from the center of a fitted Gaussian peak shape over the powder rings. The corresponding thermal difference is calculated from the relative lattice expansion: $\Delta T = \frac{\Delta L}{L_0 \alpha_{Ag}}$ with the coefficients of linear expansion: $\alpha_{Ag}=19.5 \cdot 10^{-6} \text{ K}^{-1}$ from [202].

Tabelle 5.9: The corresponding real sample temperatures as a function of applied current at a cryostat temperature of 260 K. The temperature deviations are calculated from the thermal expansion observed on lattice d -spacings of the measured silver (1 1 1) and (0 0 2) powder rings in the diffraction experiments.

Current	d-spacing (1 1 1)	d-spacing (0 0 2)	ΔT (1 1 1)	ΔT (0 0 2)
0	2.36243(9) Å	2.04715(2) Å	0 K	0 K
10 mA	2.36506(7) Å	2.04923(3) Å	57(2) K	52.1(9) K
50 mA	2.36988(6) Å	2.05326(3) Å	162(2) K	153.0(9) K

For the electric currents where the “current induced melting of CO domains” is observed, the real sample temperature is already above the charge ordering temperature T_{CO} , as seen in Tab. 5.9. The effect observed is thus simple Joule heating, in agreement with [91, 196], but now with a more direct proof. Additional diffraction experiments where the sample was cooled down with an applied electric field also show no difference in the diffraction patterns compared to the measurements without electric fields. These results indicate that it is impossible to stabilize a new (maybe ferroelectric) charge order pattern by cooling the sample under electric fields parallel to the c_{Hex} direction. Consequently, the pyroelectric current measurements reported by Ikeda *et al.* in [27] thus need to be explained by other effects than ferroelectricity. The fact that the resistivity values and temperature behavior of our type A sample in Fig. 5.14b and the values found in other samples (including type C) [200] are comparable leaky conductive could provide an alternative explanation for the result reported in [27]. The presence of residual conductivity

¹²Before integration the exact image plate position was calculated with the silicon standard.

in non-ferroelectric materials can exhibit currents which strongly resemble ferroelectric depolarization currents which occur due to space-charge effects [203, 204].

5.3.5 Influence of magnetic fields on the charge order

Above the charge ordering temperature T_{CO} , and upon cooling through it, a significant influence of magnetic fields on the observed intensity of superstructure reflections in neutron diffraction is reported in [89]. After exploring the (missing) effects that electric fields have on the charge order in the LuFe_2O_4 samples exhibiting sharp transitions, it is straight forward to ask: is there an influence from magnetic fields on the charge order or domain population which is correlated to the drastic effect in magnetization as seen in Sec. 4.2.1? First, the possible influence of magnetic fields in the region above the low-temperature phase transition T_{LT} is discussed. In order to answer these questions, an x-ray diffraction experiment with similar setup as in Sec 5.3.4 was conducted at the beamline 6-ID-D, with a cryomagnet to allow for low temperatures and magnetic fields up to 4 T. In Sec. 4.2.1, it was already shown that magnetic fields $\parallel c_{\text{Hex}}$ have an intense effect on the magnetic behavior. In order to explore the structural components of this transition, this paragraph focuses on x-ray diffraction experiments (which are not sensitive to magnetic correlations). In the first experiment, the sample was cooled down according to Sec. 4.2.1 to 200 K in zero field in order to achieve the magnetic low- H phase. By applying a magnetic field $H \parallel c_{\text{Hex}}$, high enough to trigger the metamagnetic transition, only a small influence to the $(\frac{1}{3} \frac{1}{3} \ell)$ line with its charge order super structure reflections is observed. This is better illustrated in Fig. 5.18 by the difference (green line) between both measurements. It looks like the charge order reflections becoming significant intense in the fM phase, but the relative intensity distribution along the $(\frac{1}{3} \frac{1}{3} \ell)$ line seems to be unchanged. This result indicates the same charge order and domain distribution for both magnetic long-range ordered phases. The weakly enhanced reflections observed in the fM phase can be explained by sample torque, which possibly aligns the sample moment (present in the fM phase) and thus the sample with the external magnetic field.

Furthermore, in this experiment, the influence of magnetic fields on the structural distortion of the $R\bar{3}m$ reflections, associated to T_{LT} , was studied. Here, the splitting of the (119) reflection (red box in Fig. 5.15) disappeared by going from low- H through the PS→fM metamagnetic transition, similar to the results reported in [28]. It was additionally observed that by cooling under high H the transition at T_{LT} is suppressed; therefore, no peak splitting could be observed (see inset Fig. 4.9). By then warming from

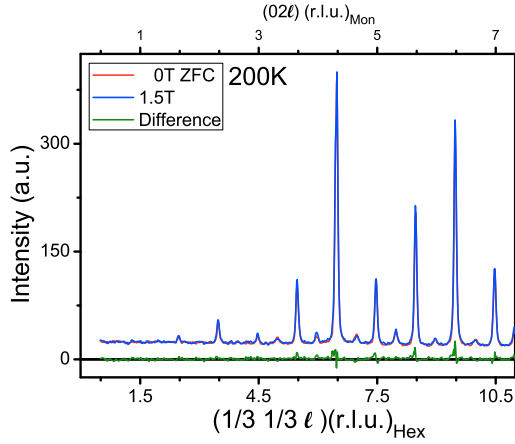


Abbildung 5.18: Observed intensity distribution along the $(\frac{1}{3} \frac{1}{3} l)$ line from different CO domains at 200 K. Two measurements at 200 K in the magnetic AFM and fM phases are presented. The particular intensity difference ($I(\text{fM}) - I(\text{AFM})$) is also presented.

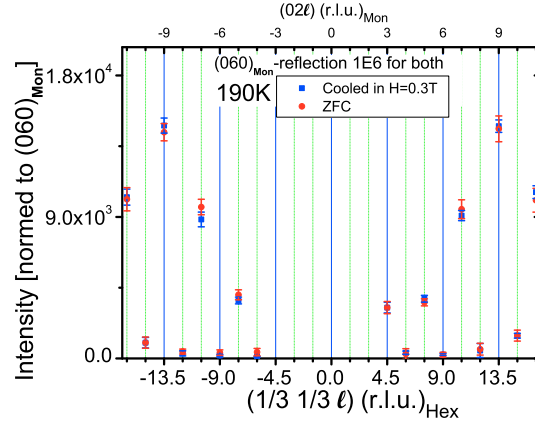


Abbildung 5.19: Observed intensity distribution for the strongest domain of a multiple domain crystal. Two different measurements at 190 K are compared, one in $H = 0$ T and the other one after cooling the sample with $H = 0.3$ T in c_{Hex} -direction. At 190 K the field was removed before the measurement.

low- T in zero field, the splitting appeared again at ~ 50 K, exactly the temperature at which the remanent magnetization in Fig. 4.9 suddenly drops. This suppression of structural reflections in a wide T range already indicates the strength of the kinetic arrest. Upon further warming in $H = 0$ the splitting of the $(119)_{\text{Hex}}$ reflection disappears. This is exactly the temperature at which the increase in magnetization is observed in Fig. 4.9, corresponding to the region where the anomalous field heating effect is present.

In order to verify this result, additional data sets were collected with the laboratory SupaNova diffractometer by applying a magnetic field of ~ 0.3 T with a permanent magnet parallel to the c_{Hex} direction on cooling to 190 K¹³. This field, according to the phase diagram, is more than high enough to stabilize the high- H phase. According to the time-dependent magnetization measurements in Fig. 4.6, this phase, once achieved at 190 K, is also stable in $H = 0$. In order to evaluate the impact of magnetic fields on the domain population a LuFe_2O_4 single crystal was chosen that is not equal in domain population. For comparison, two data sets were collected: The first one after cooling the crystal from room temperature, so far above T_N , to about 190 K with the magnet close to the c_{Hex} direction; and the second one after cooling without a field to the same temperature. The crystal structure from the collected dataset was refined with comparable results and a similar charge order pattern as in Sec. 5.3.1, but due to the more equal

¹³The field at the surface of the permanent magnet was 0.3 T.

domain population for this crystal the R -value did not reach in both magnetic phases such low values upon refinement (6.21% for fM and 6.18% for AFM phase).

The intensity distribution along the $(0\ 2\ \ell)_{\text{Mon}}$ diffraction line is presented in Fig. 5.19 for one particular domain under both collection processes. No difference in charge order superstructure reflections could be observed between the two magnetic phases, indicating that there is no change in charge order configuration for both magnetic phases. The CrysAlis^{Pro} software could also evaluate the domain population to (0.62:0.58:1) and (0.60:0.58:1) for the ZFC and FC measurement respectively, indicating that there is most likely no change in charge order domain population.

The effect magnetic fields have on the intensity of superstructure reflections reported in [89] is likely, because they applied the magnetic field in $H||(\bar{1}\ \bar{1}\ 0)_{\text{Hex}}$ direction (in the plane) by cooling from above T_{CO} . This field direction breaks the rotation symmetry of the hexagonal system, and this might cause a change in domain population.

5.3.6 The crystal structure below T_{LT}

As already mentioned in Sec. 4.2.3 and reported in [28, 1], the transition at T_{LT} is accompanied by a structural distortion (see peak-splitting in inset Fig. 4.9) following the strongly hysteretic temperature behavior reported for the magnetization. In order to investigate the influences of this structural distortion, a crystal structure refinement was performed at 120 K. Surprisingly, the results obtained from this refinement do not differ strongly from the other refinement results below T_{CO} ; a clear charge separation into Fe^{2+} and Fe^{3+} , as shown in Fig. 5.2, is still achieved. The results for the temperature dependence of the monoclinic lattice parameters are presented in Fig. 5.20. Here an increase of the monoclinic c_{Mon} direction and a decrease of the b_{Mon} -direction for lower temperatures, especially for the point below T_{LT} , is observed.

This result is consistent with the report of a contraction (expansion) of the a_{Hex} (c_{Hex}) lattice constant from 350 K to 100 K for the hexagonal cell reported in [1]. As expected for all the measurements at different temperatures, the observed volume of the cell decreases continuously with decreasing temperatures. The strong increase of the c_{Mon} direction could be an indication for the onset of orbital order in LuFe_2O_4 . This lattice expansion in c_{Hex} direction might indicate the presence of an orbital ordered state in the magnetic glassy phase below T_{LT} . This will be further discussed in Sec. 7.2.

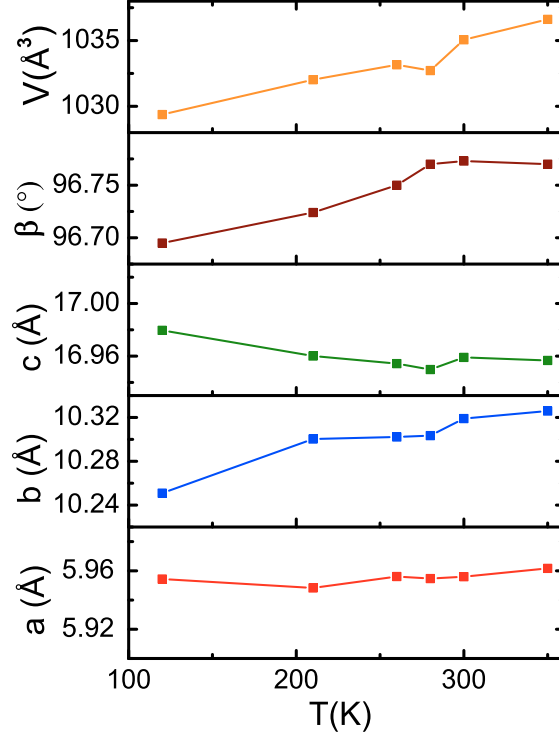


Abbildung 5.20: Monoclinic lattice parameters and cell volume extracted from the crystal structure refinements at different temperatures on cooling presented in this paragraph. The structure above T_{CO} at 350 K was also refined in monoclinic cell.

5.4 Discussion and Conclusion

In this chapter, it was shown that the crystallographic structure of LuFe_2O_4 could be refined with a new monoclinic cell following the $C2/m$ symmetry. This cell can describe the charge order of one single domain species. With the help of the Bond Valence Sum method the different Fe^{2+} and Fe^{3+} valences could clearly be identified, giving rise to an unexpected new charge order arrangement. This charge order arrangement is verified by structural refinements in the lower symmetry Cm space group. Importantly, this new charge order structure resulting out of the crystallographic refinement does not contain polar bilayers, in contrast to what was generally accepted and previously proposed in different articles (e.g. [27, 85]), casting doubt on the “ferroelectricity from charge ordering” scenario. How general is this result given the significant reported (see e.g. [197]) sample-to-sample variations? Clearly, the structure refinement can be expected to be representative for all the kinds of samples where ($\frac{1}{3}$, $\frac{1}{3}$, halfinteger) reflections are observed as the main CO order parameter (e.g. [27, 85, 91, 93, 28, 31, 1, 52, 84]). In particular, the structural refinement results should be valid for the samples for which pyroelectric current measurements have been reported [27].

To explain the pyroelectric current measurements, it was proposed in [85] that a ferroelectric CO might be stabilized by an external electric field (under cooling). However, such a scenario seems less likely when charged bilayers have to be polarized rather than when the AFE stacking of polar bilayers proposed in [85] is changed. Indeed, the observed CO remains complete robust, a fact already reported from diffraction experiments under electric fields by Wen *et al.* [91], based on neutron diffraction. This behavior is moreover confirmed as valid for our magnetic type A samples by an additional x-ray diffraction experiment with in situ electric fields up to 15 kV cm^{-1} . From this experiment, we thus conclude that a ferroelectric charge order cannot be stabilized by external electric fields. In such an in-situ experiment only an electric current induced charge order melting could be observed, which is explained by simple Joule heating from the sample, consistent with the reports of [91, 196].

The relatively low resistivity around T_{CO} [91, 193, 194, 199] could provide an alternative explanation for the observed pyroelectric current measurements [27]; in the presence of residual conductivity non ferroelectrics can exhibit currents strongly resembling ferroelectric depolarization currents, because of space-charge effects [203, 204]. The observed giant dielectric constants attributed as evidence for ferroelectricity in LuFe_2O_4

[87, 173, 177] can be attributed to interface effects [198]. There is an article dealing with this topic in preparation by our co-workers [158].

The lattice parameters in monoclinic c direction showed an abnormal increase below T_{LT} . This might give a weak indication for an orbital ordered state in this region, but further work is required to verify this in detail (see Sec. 7.2). In summary, all the findings reported here for the $\text{Fe}^{2+}/\text{Fe}^{3+}$ charge order configuration of LuFe_2O_4 are in contrast to the indicated ferroelectric behavior. These results cast strong doubts on the prototypical example of CO-based ferroelectricity this material is associated with. Furthermore, examples of oxides where the charge order mechanism occurs are exceedingly rare, and none is really well understood. Magnetite is still under debate as a CO based multiferroic material [20, 205, 68, 206], so a clear example of an oxide material with ferroelectricity originating out of charge order has yet to be identified.

At this point, a question is still open: What is the mechanism by which the non-charge neutral bilayers with each counting a majority of Fe^{2+} and Fe^{3+} are established? Therefore, the strict coupling between charge and spin order, likely already at T_{CO} , is introduced in Sec. 7 and may provide a possible explanation for the exotic charge order pattern presented here. The metamagnetic transition between the AFM and fM order seems not to influence the crystallographic structure, giving a strong indication that the transition is related to different spin structures in both magnetic phases. The question of the right spin structure for both the phases will be discussed in the next chapter.

5.5 Related publications

The following publications are related to this section:

- “*Lattice dynamical probe of charge order and antipolar bilayer stacking in LuFe_2O_4* ”
X. S. Xu, J. de Groot, Q.-C. Sun, B. C. Sales, D. Mandrus, M. Angst, A. P. Litvinchuk, and J. L. Musfeldt
Phys. Rev. B **82**, 014304 (2010).
- “*Dielectric properties of charge ordered LuFe_2O_4 revisited: The apparent influence of contacts*”
D. Niermann, F. Waschkowski, J. de Groot, M. Angst, and J. Hemberger
Phys. Rev. Lett. **109**, 016405 (2012).

The following publication is related both to this section and to Sec. 7:

- “*Charge order in LuFe_2O_4 : an unlikely route to ferroelectricity*”
J. de Groot, T. Mueller, R.A. Rosenberg, D.J. Keavney, Z. Islam, J.-W. Kim, and M. Angst
Phys. Rev. Lett. **108**, 187601 (2012).

For a detailed declaration of own contributions to the publications see App. A.

Magnetic phases in LuFe_2O_4

The magnetic phase diagram presented in Fig. 4.10 was established from various $M(H)$ and $M(T)$ -curves. Below the Néel temperature T_N two different magnetic phases, separated by a metamagnetic transition could clearly be identified. In Sec. 4.1 it was reported that magnetic fields along the c_{Hex} direction will trigger a metamagnetic transition from a low- H phase to a high- H phase. As presented in Sec. 5.3.5, x-ray diffraction does not indicate any structural component for this transition, so the reported magnetic change can only be due to different spin configurations in both magnetic phases. In this chapter, the spin configurations for both magnetic phases are solved [148] within the new monoclinic cell established in Sec. 5.3.1. The corresponding spin configurations and their geometrical relation to each other will also have a strong impact on the magnetic behavior above T_N , as already indicated by the unusual behavior found in the magnetization measurements from Sec. 4.2.6.

6.1 Different magnetic orders for different phases

This chapter, clarifies which reflections are magnetic and what the differences between the two magnetic long-range ordered phases are. New data shows why the ferrimagnetic spin structure proposed in [1] is inconsistent with the low- H phase (likely AFM) by a scenario of compensating ferrimagnetic domains as previously proposed in [161]. Additionally, the solution of [1] also conflicts with new observations in the high- H phase, where a ferrimagnetic spin alignment could be possible.

6.1.1 Pure magnetic $(00\frac{3}{2})$ -type reflections

In order to search for orbital order (the results for orbital order will be discussed in Sec. 7.2 in more detail) in LuFe_2O_4 , a synchrotron scattering experiment at the Swiss Light Source (SLS) with polarization analysis of both the incoming and scattered pho-

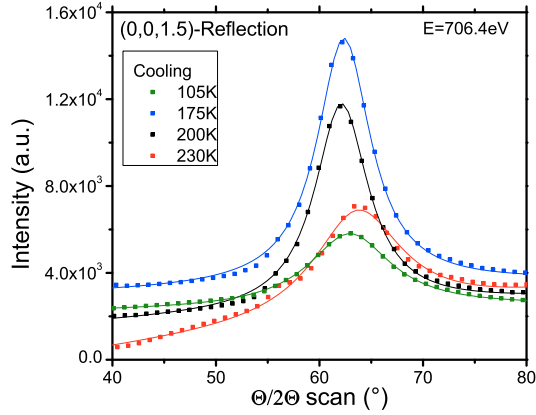


Abbildung 6.1: Measured $\theta/2\theta$ scans at different temperatures on cooling with an incoming photon energy of 706.4 eV. The solid line represents the fitted Lorentzian curve with additional linear background.

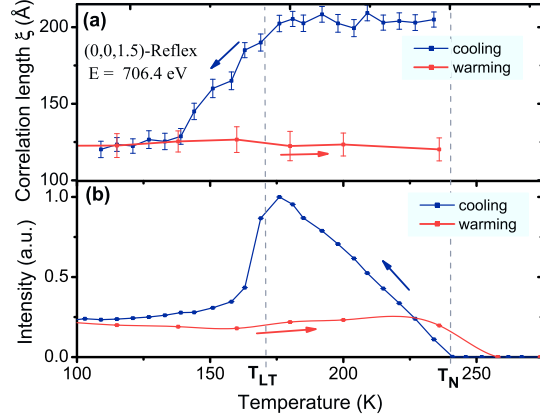


Abbildung 6.2: Temperature dependence on both cooling and warming of (a) the correlation length $\xi_{(00\ell)}$ determined from $\theta/2\theta$ -scans and (b) integrated intensity of the $(00 \frac{1}{2})$ reflection. The warming-curve was measured fast.

tons was performed in the soft x-ray regime. The whole experiment was conducted on the $(00 \frac{3}{2})$ reflection and its corresponding satellites, the only reachable reflection at this energy. A similar reflection structure is observed around the $(00 \frac{27}{2})$ reflection [85] (see also Fig. 2.16). The polarization analysis of the energy scans along the Fe L_3 -edge¹ in Fig. 6.3 shows only contribution in the $\sigma \rightarrow \pi$ and $\pi \rightarrow \sigma$ polarization channels, corresponding, according to Tab. 3.1, to purely magnetic scattering. Furthermore, for the $(00 \frac{3}{2})$ reflection the scattering vector \vec{Q} is parallel to c_{Hex} , and since that there is no intensity in the $\pi \rightarrow \pi$ and $\sigma \rightarrow \sigma$ channel observed, the Fe spin moments must be aligned parallel to \vec{Q} (S_3 according to Fig. 3.7) and therefore c_{Hex} . This confirms the strong Ising spin behavior for LuFe_2O_4 , already reported previously by other groups using different techniques [207, 36, 1, 90, 74]. Additionally, the temperature dependence on cooling of the integrated intensity of $\theta/2\theta$ -scans of this reflection starts to increase at $T_N \sim 240$ K (see Fig. 6.1). Here the maximum of intensity is reached close to T_{LT} (see Fig. 6.2b), matching the boundaries of the low- H phase from the phase-diagram presented in Fig. 4.10. A similar T -dependence of the $(\frac{1}{3} \frac{1}{3} 0)$ reflection intensity is achieved from neutron diffraction in Fig. 6.10 and [1], indicating that both correlations originate from the same spin structure. The observed intensity of this $(00 \frac{3}{2})$ -type reflection is, by its polarization behavior thus, clearly connected to magnetic contributions from the low- H phase. This is an unlikely solution for the low- H phase, because for the reported fM

¹The L_2 edge was too weak to observe while using the polarization analyzer.

spin structure in [1], no intensity of these $(00\frac{3}{2})$ -type reflections is expected, in contrast to the $(\frac{1}{3}\frac{1}{3}0)$ reflection. However, both types of reflections belong to the same structure and thus need to be explained by the final spin structure. An interesting point is that all observed magnetic reflections suggest a commensurate spin order, in contrast to the dis/incommensurate charge order reported in Sec. 5.

In Fig. 6.2a,b there is a drastic drop at T_{LT} in both the observed integrated intensity and the correlation length, determined by the full width at half maximum of the Lorentzian curve fitted to the $\theta/2\theta$ -scans. This drop at T_{LT} indicates a loss in magnetic correlation length $\xi_{(00\ell)}$ along the c_{Hex} direction², as expected for a spin glass system with its frequency splitting in magnetic AC susceptibility measurements observed in Sec. 4.2.3. The $\theta/2\theta$ scans correspond to (00ℓ) scans in reciprocal space and are the only ones possible within the RESOXS endstation.

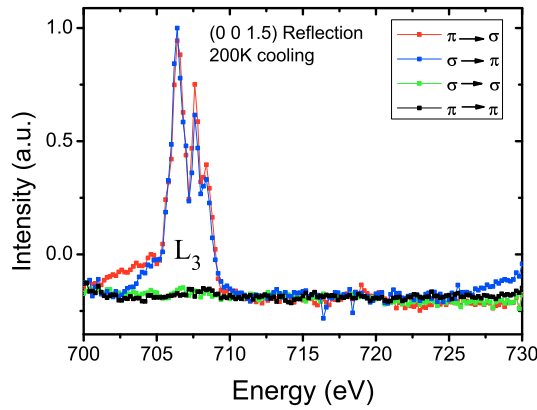


Abbildung 6.3: Energy depend scans across the Fe- L_3 edges of the intensity at the $(00\frac{1}{2})$ reflection with different incoming and outgoing polarization directions. All curves measured at 200 K on cooling.

Upon warming from below T_{LT} , the intensity of the $(00\frac{3}{2})$ reflection and the particular correlation length $\xi_{(00\ell)}$ is still slightly above the transition temperature where the structural distortion disappears (see Sec. 4.2.5), indicating a strong thermal hysteresis of the cluster class state. This cluster state seems to still be present in the region where the “Anomalous field heating effect” of [79] is reported, and it was also observed for the samples of type A used in this thesis and presented in Sec. 4.2.5. Later in Sec. 6.3.1, it will be shown that strong diffuse magnetic scattering is still present on warming in this temperature region above T_{LT} .

6.1.2 New magnetic reflections from neutron scattering

²Calculated from the full width at half maximum in the $\theta/2\theta$ scans by $\xi = 2\pi/\Delta Q_{FWHM}(\text{\AA}^{-1})$.

With the soft x-ray diffraction study presented in the previous paragraph, only a small region of reciprocal space could be explored for additional magnetic reflections. To investigate the spin structures and the metamagnetic transition, further neutron diffraction experiments were performed in both magnetic phases in order to detect more unknown magnetic reflections. In this chapter, data from the D23 diffractometer located at the Institut Laue-Langevin are presented. All neutron data acquisitions are performed on the same crystal (~ 70.1 mg), labeled S2 and already used in previous neutron studies

[1]. This crystal is of type A quality in magnetization, as displayed in the published magnetization in the inset of Fig. 1a of [1] and verified by similar measurements done in our Institute (see Fig. 6.4).

For different types of reflections, a drastic effect of the magnetic field H applied parallel to the c_{Hex} direction is observed on the integrated intensity when going through the metamagnetic transition. An increase of the (magnetic) intensity of structural reflections \mathbf{S} (where \mathbf{S} is any structural reflection from the hexagonal phase) is measured, as shown in Fig. 6.5. For comparison, in Fig. 6.6 both the magnetization M and the integrated intensity show a similar behavior under magnetic fields H , indicating that they originate from the same phase. This additional intensity contribution must be magnetic in origin, since x-ray studies in Sec. 5.3.5 show neither a structural nor a charge order component for this metamagnetic transition. For the measurements presented here, a low temperature of 190 K was chosen in order to increase the relatively weak magnetic contribution on top of the structural reflections. A strong effect of magnetic fields on the observed intensity of particular reflections in neutron diffraction below T_N is already reported in an endnote of [89], but in that case the field was applied $||[1\bar{1}0]$ and the observed effect was not associated with a metamagnetic transition³.

In contrast to the structural reflections \mathbf{S} , the $(\bar{1}0\frac{7}{2})$ reflection shows a drastic suppression of the integrated intensity in Fig. 6.7 when going through the metamagnetic

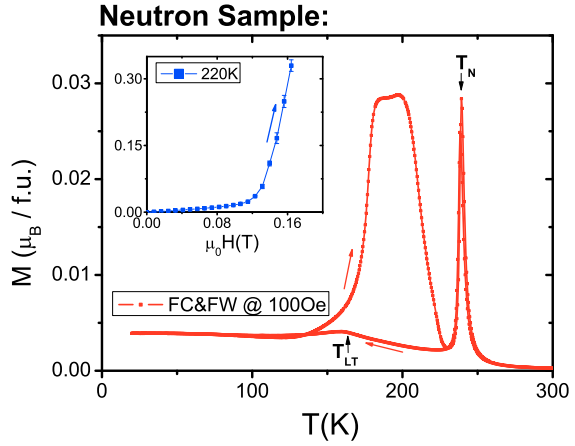


Abbildung 6.4: The magnetization behavior $M(T)$ at 100 Oe of the neutron-sample used in this thesis and other works [1]. The inset shows a partial $M(H)$ -curve at 220 K (The observed moment exceeds the limit of our MPMS system).

³Maybe the sample had a small contribution with $\ell||H$.

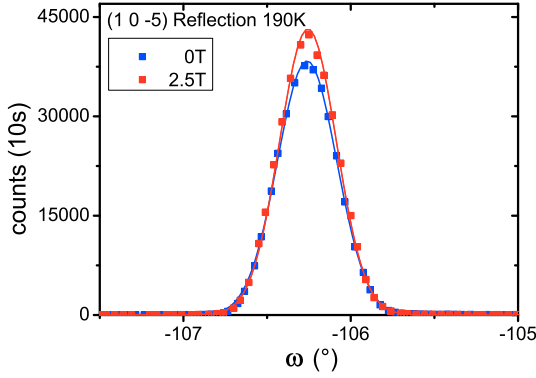


Abbildung 6.5: The measured rocking curves at 190 K from the $(10\bar{5})$ reflection after ZFC and after applying a magnetic field of $H=2.5$ T, both with a fitted Gaussian curve.

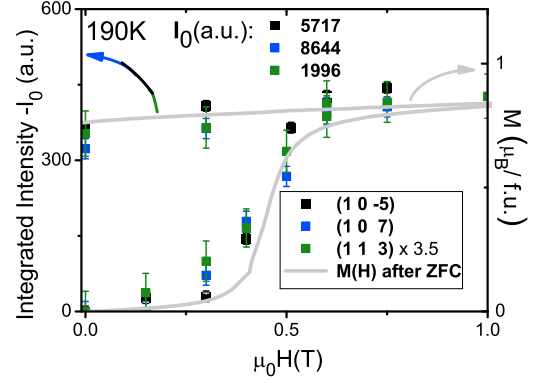


Abbildung 6.6: Integrated intensity changes to I_0 of different structural reflections \mathbf{S} in neutron diffraction versus $H||c_{\text{Hex}}$; compared with a $M(H)$ measurement at 190 K. Figure from own published work [148].

transition. This reflection with $\mathbf{S} + (00\frac{3}{2})$ is of the same type as the $(00\frac{3}{2})$ reflection studied with soft x-ray diffraction. From the integrated intensity behavior under magnetic fields in Fig. 6.8, it is clear that the spin structure which describes the low- H phase should have magnetic contributions on the $\mathbf{S} + (00\frac{3}{2})$ type reflections. For the spin structure reported in [1] no intensity is calculated for this kind of reflection; and it therefore has to be excluded as the right solution. In order to improve the spin structure refinement, the integrated intensities of various reflections of this type were collected in both magnetic phases. The magnetic intensity of structural reflections \mathbf{S} presented in Fig. 6.6 at 190 K remains stable in $H = 0$. Moreover, at 220 K the magnetic phase can switch back from the high- H to the low- H phase. This behavior is measured both in the magnetization curve $M(H)$ and the integrated intensity. Therefore it is also shown that the magnetic contributions to structural reflections will also decrease again in zero magnetic field following to the phase diagram of Fig. 4.10. The majority of the observed intensity on the $(\bar{1}0\frac{7}{2})$ reflection is clearly associated to the low- H phase; the small remaining intensity above 0.3 T in Fig. 6.8 is possibly due to a cross-contamination from the low- H phase, still present in the H -region where the high- H phase is already established.

6.1.3 Magnetic reflections along the $(\frac{1}{3}\frac{1}{3}\ell)$ -line

The N5 diffractometer located at the Chalk River Laboratories was used to measure the $(\frac{1}{3}\frac{1}{3}\ell)$ diffraction line at different temperatures and magnetic fields. Similar to the previous chapter, a drastic effect of $H||c_{\text{Hex}}$ is also found on the intensity distribution

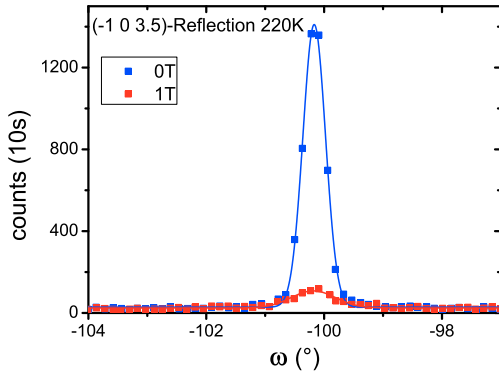


Abbildung 6.7: The measured rocking curves from the $(\bar{1}0\frac{7}{2})$ reflection after ZFC and after applying a magnetic field of $H=1.0\text{ T}$, both with the fitted Gaussian curve.

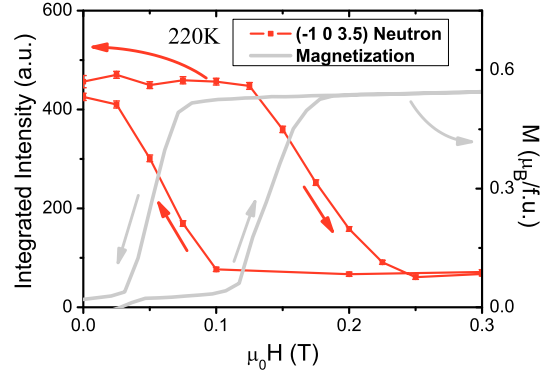


Abbildung 6.8: Integrated intensity of the $(\bar{1}0\frac{7}{2})$ reflection at 220 K in neutron diffraction versus H ; compared with $M(H)$ at 220 K, arrows indicate the field direction. Figure from own published work [148].

along the $(\frac{1}{3}\frac{1}{3}\ell)$ diffraction line, as seen in Fig. 6.9. Interestingly, in both phases the comparative intensities within the sets of $(\frac{1}{3}, \frac{1}{3}, \text{halfinteger})$, as well as the relative intensities of $(\frac{1}{3}, \frac{1}{3}, \text{integer})$, are the same for both magnetic phases in $H=0\text{ T}$ and $H=2.5\text{ T}$. The difference between the phases is mainly that the set of $(\frac{1}{3}, \frac{1}{3}, \text{halfinteger})$ reflections becomes stronger in the high- H phase relative to the $(\frac{1}{3}, \frac{1}{3}, \text{integer})$ reflections. As alrea-

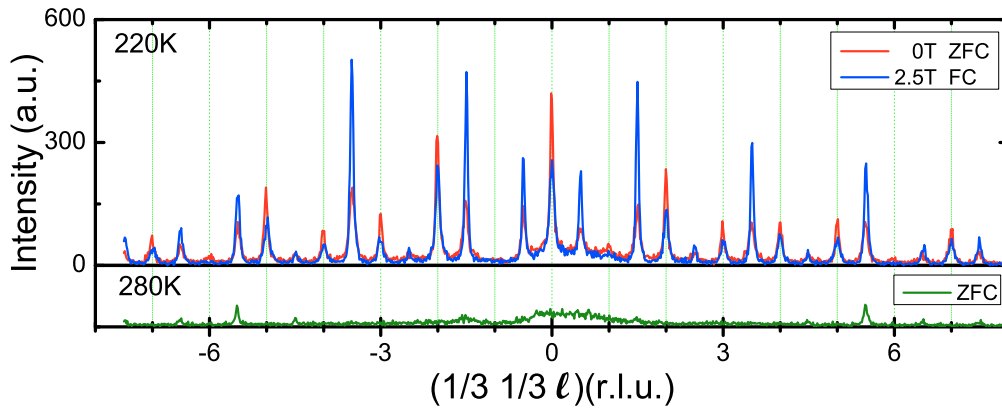


Abbildung 6.9: Neutron diffraction (N5) pattern at 220 K along the $(\frac{1}{3}\frac{1}{3}\ell)$ line in $H=2.5\text{ T}$ (blue) and in $H=0$ (red) with un-polarized neutrons of $\lambda = 2.4\text{ \AA}$. In the lower part of the figure, the charge order intensity contributions of $(\frac{1}{3}, \frac{1}{3}, \text{halfinteger})$ reflections above T_N (needed for correction) are shown with the same intensity scale.

dy mentioned in [1], these intensity contributions measured with neutron diffraction are most likely magnetic in origin, since they appear at low Q , but not at larger Q with $\ell \geq 16$ corresponding to the magnetic form factor in Sec. 3.4.2. The intensity observed

above T_N at 280 K, only at higher ℓ values, is essentially unchanged by cooling through T_{CO} (see [1]). The valence separation in Fig. 5.12 deduced from the BVS method as the order parameter of the charge order (observed with x-ray diffraction) has reached a plateau at 280 K and will not strongly increase further before reaching T_N . This leads to the conclusion that the observed intensity changes on the $(\frac{1}{3}, \frac{1}{3}, \ell)$ diffraction line in Fig. 6.9 between 280 K and 220 K, and also on the high- H phase in 2.5 T, are dominated by magnetic contributions. This is also visible in Fig. 6.10, where a major increase of integrated intensity on the $(\frac{1}{3}, \frac{1}{3}, 0)$ reflection is observed at T_N by cooling in $H = 0$. This increase takes place until T_{LT} , where a sudden drop is observed. Upon warming from below T_{LT} the intensity is lower than under cooling until $T \sim 220$ K, exactly the temperature at which the magnetic phase diagram in Fig. 4.10 re-enters the stable AFM phase upon warming.

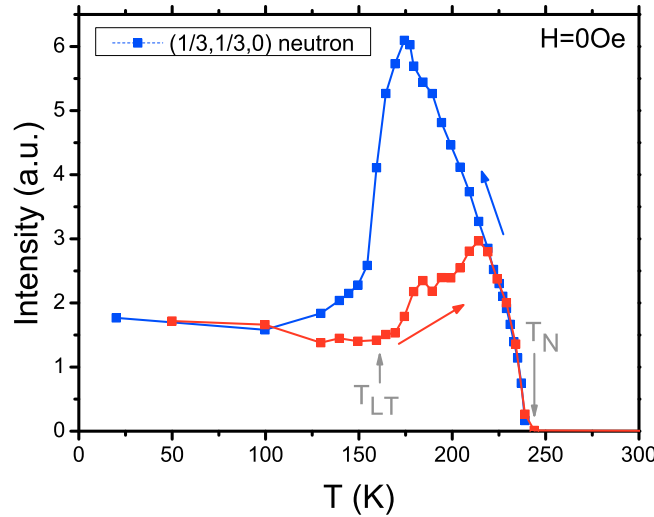


Abbildung 6.10: Temperature dependence on both cooling (blue) and warming (red) of the integrated intensity from the neutron diffraction intensity of the $(\frac{1}{3}, \frac{1}{3}, 0)$ reflection in $H = 0$. Figure from own published work [148].

The refinement presented in [1] was only performed on $(\frac{1}{3}, \frac{1}{3}, \text{integer})$ reflections in $H = 0$ without the $(\frac{1}{3}, \frac{1}{3}, \text{halfinteger})$ reflections. However, for both magnetic phases this single fM solution has to be excluded, because of the discovered changes in magnetization, reported in Sec. 4.2.1 with a metamagnetic transition, and the observed intensity pattern along $(\frac{1}{3}, \frac{1}{3}, \ell)$, which is obviously different. The final spin structures must explain, in their corresponding phases, both the magnetization and the observed magnetic contributions along $(\frac{1}{3}, \frac{1}{3}, \ell)$. Furthermore, for the spin model in [1] zero magnetic intensity is calculated for all these novel reflections. Therefore, this model has to be excluded because these

reflections clearly have magnetic contributions. In addition, the findings of novel magnetic reflections in the previous chapters, Sec. 6.1.2 and Sec. 6.1.1, must also be properly explained by the final spin structures. The approach to solving this problem within the new monoclinic $C2/m$ cell of Sec. 5.3.1 is presented in the next chapter.

6.2 A new spin model for both magnetic phases

The ferrimagnetic spin structure reported in [1] resulted from representation analysis based on the only $R\bar{3}m$ crystallographic cell known at that time, with no charge order and a single Fe site, leading to a very small number of spin structures to be considered. In the following the details of the approach for determining the spin structures of the two magnetic phases in the $6\times$ larger $C2/m$ charge-ordered cell (see Fig. C.1 and C.2 and [28]) are presented. This describes, according to all the observed magnetic reflections in Sec. 6.1, the magnetic cell for one domain (it is clear from the location of the reflections that there are three domains [1]).

From a symmetry analysis in the hexagonal cell with the previously determined $(\frac{1}{3} \frac{1}{3} \frac{3}{2})$ propagation vector for one of the domains (see Sec. 5.3), two irreducible representations are allowed, both of which lower the space group to $C2/m$. These two representations correspond to different origin positions (i.e. center of inversion) in the monoclinic cell (see Fig. C.2). In one case the center of inversion is at the Lu positions between the bilayers, and in the other case the inversion center is located between the two Fe layers of a particular bilayer. As discussed in Sec. 5.3.1, the second case is realized, corresponding to the dashed cell in Fig. C.2 and the Fe positions in Tab. 6.1, which were used for the spin structure refinements. However, as long as no different spin moments for Fe^{2+} and Fe^{3+} are considered, the cell origin has no influence on the refinements result.

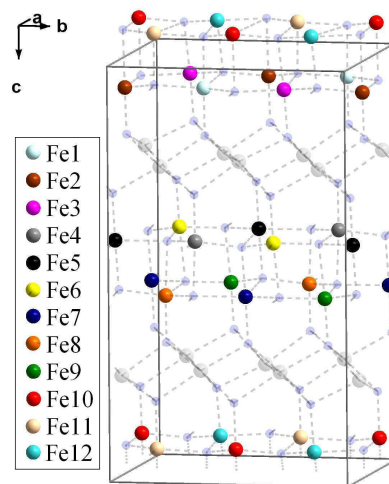


Abbildung 6.11: Monoclinic $C2/m$ crystal structure of LuFe_2O_4 ($a = 5.95 \text{ \AA}$, $b = 10.30 \text{ \AA}$, $c = 16.96 \text{ \AA}$, $\beta = 96.72^\circ$). The Fe positions achieved from the structural refinement with its C-centering condition presented in Tab. 6.1 are used for the spin structure refinement, and are highlighted by different colors.

For tiny deviations in the Fe positions, only small differences are observed upon refinement. This is the case between the Fe positions from the solved monoclinic structure in Sec. 5.3.1 and the transformed positions from the hexagonal representation. Upon refinement, only very small differences of $\Delta\chi^2 \sim 0.05$ are achieved between the two solutions. Consequently, all work presented in this chapter was done on the Fe-position achieved from the structural refinement in Sec. 5.3.1. The transformation rules that describe the $(h k \ell)$ relationship between the hexagonal cell and the monoclinic domains are presented in Tab. 5.3. For comparison with previous work, the hexagonal notation is used for the reflections unless otherwise noted.

The ferrimagnetic spin structure for LuFe_2O_4 proposed in [1] was found by symmetry representation analysis in the only $R\bar{3}m$ cell known at that time. In order to now describe the observed magnetic scattering measured in both magnetic phases, the new monoclinic $C2/m$ cell (with propagation vector $q = 0$ as the magnetic cell is clearly the same) is considered for a similar symmetry representation analysis. But surprisingly, none of the corresponding diffraction patterns from symmetry allowed spin structures comes even close to the ones measured when taking into account all types of observed reflections. Thus another, more general approach is needed to find a right model for the observations. Instead of starting with a limited number of candidate spin structures allowed by symmetry representation analysis, now *all* possible Ising spin structures having the periodicity of the observed magnetic c_{Hex} -centered cell were considered. Very broad-sized restrictions based on measured data from four types of magnetic reflections are used to limit these feasible structures to a small set. These remaining solutions are then refined against experimental data. This approach was necessary because the spin structures obtained by standard representation analysis cannot account for the observation (on either phase). This $C2/m$ cell contains 2×12 Fe atoms (see Tab. 6.1 and Fig. 6.11). The C -centering

Tabelle 6.1: In half of the Fe sites which are used for the spin structure refinement, the atomic positions are from the structural refinement in monoclinic $C2/m$ cell (see Sec. 5.3.1); the other half of the Fe sites is obtained by adding $(\frac{1}{2} \frac{1}{2} 0)$ to the positions presented here.

	P_{ix}	P_{iy}	P_{iz}	Wyck. site		P_{ix}	P_{iy}	P_{iz}	Wyck. site
Fe1	0.8598	0.83106	0.0721	8j ₁	Fe7	0.8617	0.0	0.57256	4i ₂
Fe2	0.8553	0.5	0.07430	4i ₁	Fe8	0.8566	0.66483	0.57311	8j ₂
Fe3	0.8598	0.16894	0.0721	8j ₁	Fe9	0.8566	0.33517	0.57311	8j ₂
Fe4	0.6434	0.83517	0.42689	8j ₂	Fe10	0.6447	0.0	0.9257	4i ₁
Fe5	0.6383	0.5	0.42744	4i ₂	Fe11	0.6402	0.66894	0.9279	8j ₁
Fe6	0.6434	0.16483	0.42689	8j ₂	Fe12	0.6402	0.33106	0.9279	8j ₁

condition is also preserved for the spin orders in both magnetic phases; otherwise additional magnetic reflections would appear, which are absent in all the observations for both magnetic phases. Most generally, the spin configuration is therefore specified by the spins on 12 Fe atoms labeled with different colors in Fig 6.11). All possible spin configurations were considered by ignoring symmetry other than the C-centering and using Ising spins pointing along $\perp \vec{a}$ and $\perp \vec{b}$ in the monoclinic cell. The direction of the Ising spin at the site a_i is represented by either spin up or down $a_i = (1, -1)$ or respective (\uparrow, \downarrow) . For completeness, partial disorder of magnetic moments (sites with $a_i = 0$) were also considered; this magnetic disorder of the spins at particular sites is suggested in [149]. At first, equal magnetic moments for both valences were used; this should be a good approximation, because XMCD measurements suggest a strong orbital magnetic component for the Fe^{2+} ions [36, 44], resulting in a slightly lower total moment than for Fe^{3+} sites⁴. As introduced in Sec. 3.4.2, the intensity (uncorrected for form, polarization and Debey-Waller factor) of each allowed $(h+k=2n)$ reflection in this monoclinic cell is:

$$I(h\ k\ \ell) \sim |F_{(h\ k\ \ell)}|^2 \quad \text{with} \quad F_{(h\ k\ \ell)} = \sum_{i=1}^{12} a_j \cdot e^{i2\pi(p_{jx} \cdot h + p_{jy} \cdot k + p_{jz} \cdot \ell)} \quad (6.1)$$

where h , k and ℓ are coordinates of the reciprocal monoclinic cell. These three particular spin states on 12 separate Fe sites give a total of $3^{12} = 531441$ possible spin structures; this number is too large to refine them all. To narrow the number of candidates to a tractable number, the relative intensities of different magnetic reflections were compared by intensity restrictions in order to exclude solutions that obviously don't match the observations from Sec. 6.1. These restrictions were kept very broad in order to account for uncertainty, for instance in the Debye-Waller factor. Except where noted, the restrictions are completely independent of domain populations.

This approach was followed for the two magnetic phases using a PYTHON program, presented in appendix E.1, yielding different intensities of magnetic reflections. The remaining structures, those fitting the restrictions, were analyzed for symmetry-equivalent structures shifted by $(0\ 0\ \frac{1}{2})$ or $\pm(0\ \frac{1}{3}\ 0)$ with respect to the unit cell or with all spin directions reversed. These equivalent structures are indistinguishable in diffraction and equivalent with regards to symmetry. This equivalence is broken by the two different valence states of Fe, but since the resulting magnetic contrast is not strong, compared to systematic errors, a reliable refinement is difficult, but possible, as presented in the next sections. The final spin structures deduced in Fig. 6.18 are determined just up

⁴As shown in Sec. 7 the refinement result thus depends slightly on the underlying CO pattern.

to this equivalence. The exact relation between spin structure and charge order will be determined in Sec. 7; neutron diffraction can just provide a first glance into this coupling.

6.2.1 Antiferromagnetic spin order for the low- H phase

Tabelle 6.2: Measured integrated intensities in the low- H phase on several reflections (indexed in the $R\bar{3}m$ hexagonal cell) at different temperatures, measured by non-polarized neutron diffraction.

$(h k \ell)_{\text{Hex}}$	$(h k \ell)_{\text{Mon}}$	Integrated Intensity (a.u.)	$Q(\text{\AA}^{-1})$	Temperature (K)
$(\frac{1}{3} \frac{1}{3} 0)$	(0 2 0)	1470(13)	1.22	220
$(\bar{1} 0 \frac{1}{2})$	$(\bar{1} \bar{3} 1)$	154(2)	2.11	220
$(\bar{1} 0 \frac{7}{2})$	$(\bar{1} \bar{3} 3)$	452(3)	2.28	220
$(\frac{1}{3} \frac{1}{3} \frac{3}{2})$	(0 2 1)	601(7)	1.27	220
$(\frac{1}{3} \frac{1}{3} 3)$	(0 2 2)	577(6)	1.43	220
$(\frac{1}{3} \frac{1}{3} \frac{9}{2})$	(0 2 3)	95(2)	1.65	220
$(\frac{1}{3} \frac{1}{3} 6)$	(0 2 4)	97(2)	1.92	220
$(\frac{1}{3} \frac{1}{3} \frac{15}{2})$	(0 2 5)	77(2)	2.23	220
$(1 0 \bar{5})^5$	$(1 3 \bar{4})$	≤ 150	2.45	190
$(1 0 7)^a$	$(1 3 4)$	≤ 150	2.73	190

By comparing all measured integrated intensities (see Tab. 6.2) with the calculated intensities from the model presented in the previous chapter, some broad restrictions for the low- H phase solution can be made. Note that all reflections are indexed in $R\bar{3}m$ (hexagonal setting) crystallographic cell:

- The first set of restrictions suppresses spin structures which have no similar relative intensities on the $I(\frac{1}{3}, \frac{1}{3}, \text{integer})$ as the solution proposed in [1]. Therefore, the following conditions are used: $5.5 < I(\frac{1}{3} \frac{1}{3} 3) < 6.5$ and $0.8 < I(\frac{1}{3} \frac{1}{3} 6) < 1.2$ (all normalized on $I(\frac{1}{3} \frac{1}{3} 0) = 16$). Afterwards ~ 15000 structures remain to be checked, many of which have exactly the same relative intensity on the $(\frac{1}{3} \frac{1}{3} \ell)$ -line.
- Comparing different $(0 0 \frac{3}{2})$ -type reflections according to Tab. 6.2, the following restriction can be made:
 $2 \cdot I(\bar{1} 0 \frac{1}{2}) < I(\bar{1} 0 \frac{7}{2}) < 5 \cdot I(\bar{1} 0 \frac{1}{2})$. Also, from Fig. 6.8 it is clear that both reflections should have intensities > 0 ; at the end, ~ 3800 solutions remain.
- A third restriction compares the integrated intensity from one of the $(0 0 \frac{3}{2})$ -type reflections with the $(\frac{1}{3} \frac{1}{3} 0)$ reflection as follows: $I(\bar{1} 0 \frac{7}{2}) < I(\frac{1}{3} \frac{1}{3} 0)$. Here, the width of the condition was very broad. Based on the domain structure of LuFe_2O_4 it was also taken that the $(0 0 \frac{3}{2})$ -type reflections originate from all three domains, in contrast

to the $(\frac{1}{3}, \frac{1}{3}, \ell)$ -type reflections which originate from a single domain. This condition is valid for any domain population, even the extreme case where only one domain is present. This restriction reduces the number of possible solutions to ~ 1700 .

- Setting only upper limits for the $(\frac{1}{3}, \frac{1}{3}, \text{halfinteger})$ type reflections according to Tab. 6.2 as following:
 $I(\frac{1}{3}, \frac{1}{3}, \frac{3}{2}) < 8$, $I(\frac{1}{3}, \frac{1}{3}, \frac{9}{2}) < 3$ and $I(\frac{1}{3}, \frac{1}{3}, \frac{15}{2}) < 6$. To account for the possibility of cross-contamination from the high- H phase, this restriction also allows for no intensity of the $(\frac{1}{3}, \frac{1}{3}, \text{halfinteger})$ reflections. The total amount of possible solutions is reduced to 252 by this condition.
- The temperature-dependence through the Néel temperature (in $H = 0$) of two structural Bragg reflections indicates no systematic increase below T_N , suggesting that any magnetic contribution is small (see Fig. 6.13b/c; the error bars shown, resulting from fits of rocking curves, obviously underestimate the real error). From the sensitivity of the measurement, upper limits for possible magnetic contributions can be established; normalized to $I(\frac{1}{3}, \frac{1}{3}, 0) = 16$, the condition is $I(1\ 0\ 7) < 5$ and $I(1\ 0\ \bar{5}) < 5$. The value of 5 for both structural reflections takes into account that it originates from all three domains, and these reflections have a large Q -value. In the end, this condition leaves 168 solutions, corresponding to 7 symmetry inequivalent structures, of which only one is fully ordered (see Tab. 6.3).

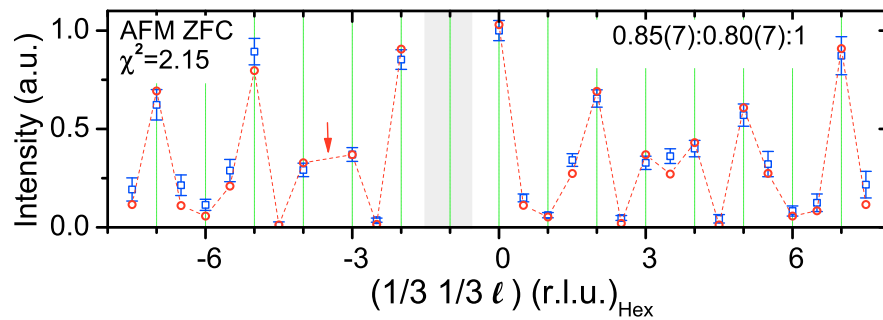


Abbildung 6.12: Integrated intensity for scans along the $(\frac{1}{3}, \frac{1}{3}, \ell)$ neutron diffraction pattern in the AFM magnetic phase (220 K after ZFC), corrected for CO contributions as described in the text. The dashed red line represents the result from the model described in this section for the spin structures N°1 in Tab. 6.3 which is presented Fig. 6.18a. The gray area indicates the magnet's dark angle and the red arrow a reflection affected by a second grain. Figure from own published work [148].

The remaining solutions exhibit different intensity contributions for integer and half-integer ℓ along the $(\frac{1}{3}, \frac{1}{3}, \ell)$ -line. A refinement as described in [1], but including both

$(\frac{1}{3}, \frac{1}{3}, \text{integer})$ and $(\frac{1}{3}, \frac{1}{3}, \text{halfinteger})$ reflections, can decide between those. Before starting the refinement, some reflections need to be excluded due to uncertain conditions in their measurement. An additional neutron diffraction measurement suggests an overlap of $(\frac{1}{3}, \frac{1}{3}, \frac{7}{2})$ with the (006) structural reflection of a small second grain, which puts the experimental intensity of this reflection in doubt. The reflections $(\frac{1}{3}, \frac{1}{3}, \frac{1}{2})$ and $(\frac{1}{3}, \frac{1}{3}, \frac{3}{2})$ are likely affected by the magnet's dark angle, indicated by the intensity drop of the 280 K data in Fig. 6.9 for this ℓ region. They are thus excluded as well. As observed above T_N , the charge order superstructure contributes weak additional (non-magnetic) intensity to the $(\frac{1}{3}, \frac{1}{3}, \text{halfinteger})$ reflections. As x-ray diffraction suggests, no large changes on this charge order reflection intensity [85] is observed on cooling; this could be taken into account as a good approximation by subtracting the intensities measured at 280 K and presented in Fig. 6.9.

Tabelle 6.3: Possible spin structures in the low- H phase obtained from the simulations explained in the text. Only half of the spins in the monoclinic $C2/m$ cell are presented. The other half is obtained by adding $(\frac{1}{2}, \frac{1}{2}, 0)$ with the same spin direction due to the still valid C-centering condition.

Nº(χ^2):	Fe1	Fe2	Fe3	Fe4	Fe5	Fe6	Fe7	Fe8	Fe9	Fe10	Fe11	Fe12
1 (2.15)	↑	↓	↑	↑	↓	↓	↓	↓	↑	↓	↑	↑
2 (15.79)	↓	↓	0	0	0	↑	↓	↑	↓	↓	↑	↓
3 (18.01)	↓	↓	0	0	0	↑	↓	↑	0	↓	↑	0
4 (17.07)	↓	↓	0	↑	0	↑	↓	↑	0	↓	↑	↓
5 (12.31)	↓	↓	↑	↓	0	↑	0	↑	↓	↓	↑	↓
6 (10.45)	↓	↓	↑	0	0	↑	0	↑	0	↓	↑	↓
7 (8.95)	↓	0	↑	↓	0	0	0	0	↓	0	↑	↓

To determine the right spin structure for the low- H phase, a refinement similar to the one in [1] was thus conducted, and only one of the 7 spin structures, N°1 in Tab. 6.3 (it is also the only fully ordered one) has at least a moderately good reduced $\chi^2=2.15$ as presented in Fig. 6.12⁶. Upon refinement of solution N°1 a domain population of 0.85(7):0.80(7):1 and a Debye-Waller factor of 1.9(4) was achieved. The strong deviation between observed and measured intensity on reflections excluded before the refinement would give a significant contribution ($\sim +1.7$) to the reduced χ^2 (see Fig. 6.13), confirming their exemption.

The too high observed intensity of $(\frac{1}{3}, \frac{1}{3}, \text{halfinteger})$ reflections is readily identified (see Fig. 6.13) as the largest contribution to the reduced χ^2 from the correct low- H solution. Here two possible effects were considered as influencing the $(\frac{1}{3}, \frac{1}{3}, \text{halfinteger})$ reflections:

⁶The refinements for the 6 excluded spin structures are presented in Fig. F.3 of the appendix F.3.

- i) As suggested in [1], magnetic intensity could be contributed by the presence of the $\text{Fe}^{2+}/\text{Fe}^{3+}$ contrast. For the refinements presented in Tab. 6.3 (and Appendix F.3), the assumption was that the moments of Fe^{2+} and Fe^{3+} are both equal to $4.5\mu_B$. Corresponding simulations with weaker Fe^{2+} moments indicate that for the new CO presented in Fig. 5.13a, the χ^2 value can be improved to ~ 1 for an optimal Fe^{2+} -moment of $\sim 3.4\mu_B$ (see Fig. 6.14 blue line). This Fe^{2+} moment cannot be realistic; the Fe^{2+} spin moment alone is already $4\mu_B$. Indeed, the weak dependence of χ^2 on the Fe^{2+} moment, in combination with similar improvement of χ^2 by cross-contamination (see below) and a relatively small number of data points per refinement parameters ratio, prevent the determination of the exact size of the Fe^{2+} moment. However, the assumed CO patterns in e.g. [85, 27] in contrast do not show any significant changes for the reduced χ^2 upon refinement for different Fe^{2+} moments.
- ii) Since the intensity contribution of the solution for the high- H phase is strongest in the $(\frac{1}{3}, \frac{1}{3}, \text{halfinteger})$ reflections, which among themselves have the same relative intensities as in the low- H phase (see below), cross-contamination could at least partially explain the systematically higher intensity measured for $(\frac{1}{3}, \frac{1}{3}, \text{halfinteger})$ reflections compared to the model (see Fig. 6.13). By refining the $(\frac{1}{3}, \frac{1}{3}, \text{halfinteger})$ with a scale factor, an overly high intensity of $\sim 40\%$ of this type of reflection could be identified, which would correspond to a cross-contamination of $\sim 15\%$ from the high- H phase. The necessary 15% contamination would give a considerably larger remanent magnetization than the observed 5% in Fig. 6.8. Cross-contamination alone can therefore not explain all the improvement in χ^2 .

The effect these corrections have on the reduced χ^2 values of refinements for the solution N^o1 are presented in Fig. 6.14. Both are able to explain, separately or together in an arbitrary spread, the enhanced intensity on $(\frac{1}{3}, \frac{1}{3}, \text{halfinteger})$ type reflections. A small high- H phase contamination ($< 15\%$) improves the refinement, as seen in Fig. 6.14, but the necessary 15% contamination would lead to a considerably larger remanent magnetization than observed. This can therefore not explain all the improvement in χ^2 , and the idea of CO contributions must be considered. Given the similar effects of cross-contamination and CO, and an increasingly poor ratio of the numbers of data points to refinement parameters, the actual moment difference between the two valences cannot be established. This would explain the unrealistic values achieved for the Fe^{2+} -moment upon refinement. Corresponding simulations with similar $\text{Fe}^{2+}/\text{Fe}^{3+}$ magnetic contrasts

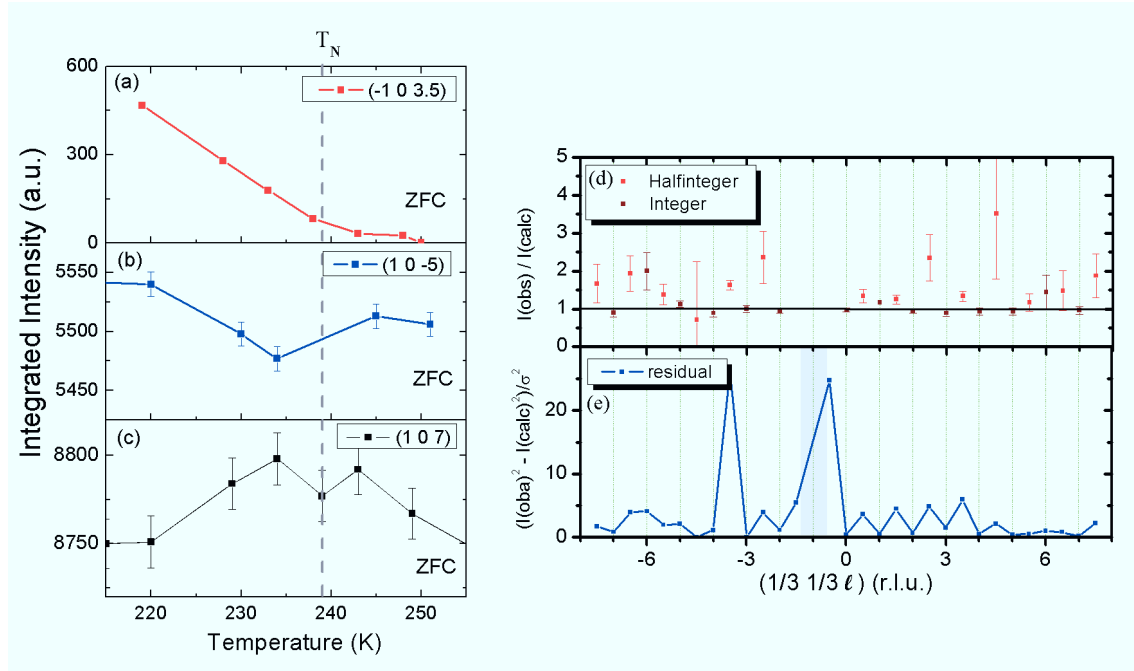


Abbildung 6.13: (a-c) Temperature dependences of the integrated intensity of different types of reflection $(\bar{1}\ 0\ \frac{7}{2})$ (a), $(1\ 0\ \bar{5})$ (b) and $(1\ 0\ 7)$ (c). (d) Ratio between observation and model (AFM spin structure shown in Fig. 1c) for integer and halfinteger $(\frac{1}{3}\ \frac{1}{3}\ \ell)$ reflections in the low- H phase. (e) Residual χ^2 contributions between model and observation for each reflection in the AFM spin structure. The gray area indicates the magnet dark angle. The reflection $(\frac{1}{3}\ \frac{1}{3}\ \frac{7}{2})$ was excluded due to an overlap with the (006) reflection from a small second grain. Figures from own published work [148].

were also carried out for the other spin structures reported for example in [85, 27], but any improvements were always small compared to the large differences in χ^2 for the solution N°1 (see Tab. 6.3) with the charge order reported in Sec. 5.3.2. This result further supports the CO established in Sec. 5.3.2 and suggests a strong spin charge coupling, although uncertainties remain that require another method to verify the exact spin charge coupling in detail (see therefore Sec. 7).

Additionally, a similar refinement was also carried out in the low- H phase for the ferrimagnetic spin structure proposed in [1]. Upon refinement (presented in Fig. F.1 of appendix F.1) this leads to a χ^2 value of 18.12, which is obviously too high compared to the solution N°1, this high value in contrast to [1] is explained by the fact that the half-integer reflections are now considered as well. Before discussing the physical consequences of the spin structure N°1 for this low- H magnetic phase, the similar refinement process for the high- H phase will be presented in the next chapter. Both spin structures will be discussed together in Sec. 6.2.3.

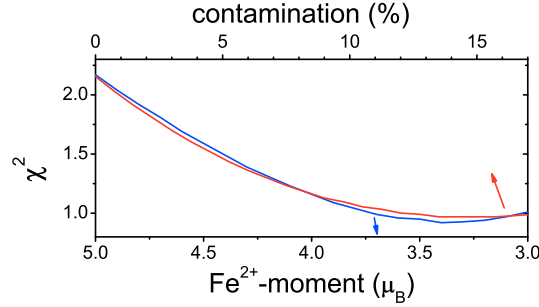


Abbildung 6.14: The reduced χ^2 value obtained by refinement of solution N° 1 for the low- H phase as a function of either contamination percentage from the high- H phase (red line) or Fe^{2+} moment with the Fe^{3+} moment kept fix $5\mu_B$ (blue line). Both valences are according to the CO presented in Sec. 5.3.2.

6.2.2 Ferrimagnetic spin order for the high- H phase

Measured intensities for the high- H phase are given in Tab. 6.4. As already pointed out in Sec. 6.1.3, the difference between the phases is that the relative intensities within the sets of $(\frac{1}{3}, \frac{1}{3}, \text{halfinteger})$, as well as the relative intensities of $(\frac{1}{3}, \frac{1}{3}, \text{integer})$, are the same as in $H = 0$, except that the former become stronger in H relative to the latter. The $(\frac{1}{3}, \frac{1}{3}, \text{integer})$ reflections could, in principle, be a cross-contamination from the low- H phase. Therefore, no lower-limit conditions are used for these reflections, although Fig. 6.8 suggests only a modest cross-contamination of possibly up to 12% when H is applied after zero field cooling; for field cooling it is likely considerably lower.

Tabelle 6.4: Measured integrated intensities in the high- H phase of several reflections (indexed in the $R\bar{3}m$ hexagonal cell) at different temperatures, measured by non-polarized neutron diffraction.

$(h k \ell)_{\text{Hex}}$	$(h k \ell)_{\text{Mon}}$	Integrated Intensity (a.u.)	$Q(\text{\AA}^{-1})$	Temperature (K)
$(\frac{1}{3} \frac{1}{3} 0)$	(020)	899(10)	1.22	220
$(\bar{1} 0 \frac{1}{2})$	$(\bar{1} \bar{3} 1)$	22(2)	2.11	220
$(\bar{1} 0 \frac{7}{2})$	$(\bar{1} \bar{3} 3)$	69(2)	2.28	220
$(\frac{1}{3} \frac{1}{3} \frac{3}{2})$	(021)	1540(16)	1.27	220
$(\frac{1}{3} \frac{1}{3} 3)$	(022)	577(7)	1.43	220
$(\frac{1}{3} \frac{1}{3} \frac{9}{2})$	(023)	130(3)	1.65	220
$(\frac{1}{3} \frac{1}{3} 6)$	(024)	73(2)	1.92	220
$(\frac{1}{3} \frac{1}{3} 9)$	(026)	58(2)	2.47	220
$(10\bar{5})^7$	$(13\bar{4})$	~ 300	2.45	190
$(107)^a$	(134)	~ 300	2.73	190
$(113)^a$	(134)	~ 80	3.73	190

- Comparing all $(\frac{1}{3} \frac{1}{3} \ell)$ with ℓ integer and half-integer values according to the observed in-field neutron diffraction pattern and allowing for cross-contamination from the

AFM phase, ~ 1400 possibilities remain. Conditions: $I(\frac{1}{3} \frac{1}{3} 0) < 9.5$, $I(\frac{1}{3} \frac{1}{3} 3) < 8$, $I(\frac{1}{3} \frac{1}{3} \frac{9}{2}) < 8$ and $I(\frac{1}{3} \frac{1}{3} 6) < 4$. All intensities are normalized to the $I(\frac{1}{3} \frac{1}{3} \frac{3}{2}) = 16$ reflection, the most intense in this phase.

- The $(\bar{1}02)+(00\frac{3}{2})$ reflection is strongly suppressed (by $\sim 85\%$) in the high- H phase. The small intensity remaining is likely due to cross-contamination. Upon considering this, only an upper limit for the reflection was set: $I(\bar{1}0\frac{7}{2}) < \frac{1}{10} \cdot I(\frac{1}{3} \frac{1}{3} \frac{3}{2})$ and $I(\bar{1}0\frac{1}{2}) < \frac{1}{10} \cdot I(\frac{1}{3} \frac{1}{3} \frac{3}{2})$. This was done by taking into account again that the $(\frac{1}{3} \frac{1}{3} \frac{3}{2})$ originates from one domain as above. This restriction reduces the possible solutions to 72.
- After comparing the magnetic contribution on top of different structural reflections $I(10\bar{5}) < 9.5$ and $I(107) < 9.5$ only 26 solutions remain, corresponding to 3 symmetry-inequivalent ones, listed in Tab. 6.5. As in the low- H phase, only one of these solutions is fully ordered. Figure from own published work [148].

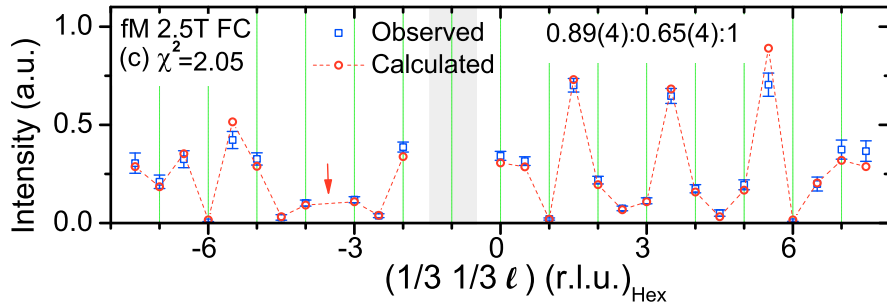


Abbildung 6.15: Integrated intensity of scans along the $(\frac{1}{3} \frac{1}{3} \ell)$ neutron diffraction pattern in the fM magnetic phase at 220 K and 2.5 T, corrected for CO contributions as described in the text. The dashed red line represents the result from the model for the spin structures described in the previous chapter, N°1 in Tab. 6.5, which is presented Fig. 6.18b. The gray area indicates the magnet's dark angle and the red arrow a reflection affected by a second grain. Figure from own published work [148].

As for the low- H phase above, the 3 remaining spin structures presented in Tab. 6.5 were refined, with the same model used in [1], against the experimental data obtained at 220 K and 2.5 T after field cooling. Upon refinement in Fig. 6.15 only the fully-ordered structure N°1 in Tab. 6.5 has a reasonable reduced $\chi^2=2.05$ (after excluding the same reflections as in the low- H phase); this ferrimagnetic solution is presented in Fig. 6.18. Upon refinement, a domain population of 0.89(4):0.65(4):1 and a Debye-Waller factor of 5.1(9) is achieved. It is important to note here that the other possible candidate spin

6.2. A NEW SPIN MODEL FOR BOTH MAGNETIC PHASES

configurations in Tab. 6.5 have a significantly higher χ^2 value upon refinement, presented in Fig. F.2 of appendix F.2.

Tabelle 6.5: Possible spin structures for the high- H phase obtained from the simulations explained in the text. Only half of the spins on the particular Fe sites, according to Tab. 6.2, are presented. The other half is obtained by adding $(\frac{1}{2}, \frac{1}{2}, 0)$ with the same spin direction due to the still valid C-centering condition.

N \circ (χ^2)	Fe1	Fe2	Fe3	Fe4	Fe5	Fe6	Fe7	Fe8	Fe9	Fe10	Fe11	Fe12
1 (2.05)	\uparrow	\downarrow	\uparrow	\downarrow	\uparrow	\uparrow	\uparrow	\uparrow	\downarrow	\downarrow	\uparrow	\uparrow
2 (55.07)	\downarrow	\uparrow	0	\uparrow	0	\uparrow	\downarrow	\uparrow	0	\uparrow	\uparrow	\downarrow
3 (15.29)	\downarrow	0	0	\uparrow	\downarrow	\uparrow	\downarrow	\uparrow	0	\uparrow	\uparrow	\downarrow

Too much intensity on $(\frac{1}{3}, \frac{1}{3}, \text{integer})$ reflections is readily identified (see Fig. 6.16) as the largest contribution to the reduced χ^2 from the correct high- H solution. As for the low- H phase, the refinement can be improved by taking into account a small cross-contamination by the low- H phase or different Fe^{2+} moments following the CO presented in Fig. 5.13a (again the reduced χ^2 did not improve with other previously suggested CO configurations). This result, similar to the case for the AFM phase, gives further support to the newly found CO and a possible spin charge coupling. This is further studied and supported by another method in Sec. 7. In Fig. 6.17 (red line), the results of the Fe^{2+} moment-dependent refinements are presented; a minimum is visible for a Fe^{2+} moment of $\sim 4.5\mu_B$. Within error bars, this is consistent with XMCD results [36, 44] (see also Sec. 7). A small cross-contamination of about $\sim 6\%$ gives a similarly reduced χ^2 value, making it difficult to determine what the right correction is, as was already observed for the low- H phase. Given the similar effects of cross-contamination and CO, and an increasingly poor ratio of the numbers of data points to parameters on refinement for the high- H phase, the actual moment difference between the two valences cannot be established properly.

Additionally, similar refinements were also carried out in the high- H phase for the ferrimagnetic spin structure proposed in [1]. Upon refinement (presented in Fig. F.1 of appendix F.1) this leads to a χ^2 value of 66.46, which is obviously too high compared to the solution N \circ 1. This high value is explained by the fact that the integer reflections are now considered as well.

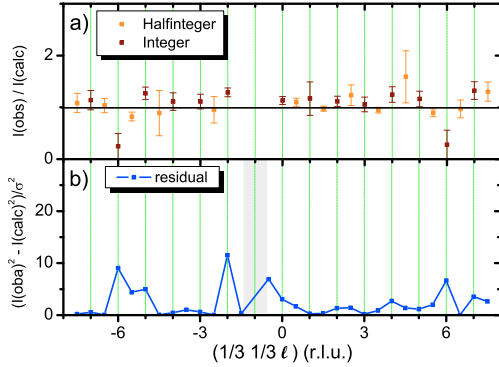


Abbildung 6.16: (a) Deviation between model and observation for both integer and half-integer $(\frac{1}{3} \ \frac{1}{3} \ \ell)$ reflections in the fully ordered fM spin structure. (b) Residual χ^2 contribution between model and observations for each reflection in the fully ordered fM spin structure. The gray area indicates the magnet's dark angle. The reflection $(\frac{1}{3} \ \frac{1}{3} \ \frac{7}{2})$ was excluded due to an overlap with the (006) reflection from a small second grain. Figure from own published work [148].

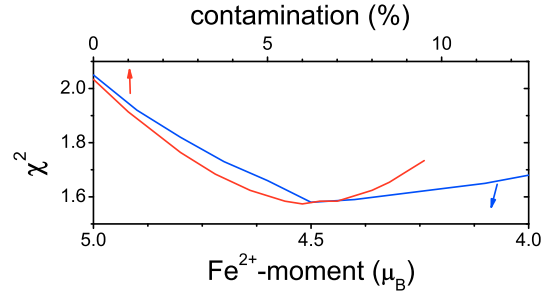


Abbildung 6.17: The reduced χ^2 -value obtained from refinement on solution N°1 in Tab. 6.5 as a function of either contamination percentage from the high- H phase (red line) or Fe^{2+} moment with the Fe^{3+} moment kept fixed $5\mu_B$ (blue line). Both valences are according to the CO presented in Sec. 5.3.2. Figure from own published work [148].

6.2.3 The AFM and fM spin structures

After finding accurate spin models, which are able to explain the observed magnetic intensity of various types of magnetic reflections, it is worthwhile to look at the geometrical relation these two particular spin structures have to each other. Based on the 12 different Fe sites in Fig. 6.11 used upon refinement for the AFM and fM spin models, the solutions which reached the lowest χ^2 value (both solutions N°1 in Tab. 6.3 and 6.5) are shown in Fig. 6.18. These solutions contain magnetic bilayers which each exhibit a 2 : 1 ferrimagnetic spin arrangement, already proposed in [74], with antiferromagnetic nearest neighbor interactions and ferrimagnetic next nearest neighbor interactions following [208]. As indicated in Fig. 6.18 by the gray arrows, in the AFM solution the net magnetization of individual bilayers is stacked antiferromagnetically along the c_{Hex} direction. This stacking leads to a vanishing magnetization in measurements, as already observed in Sec. 4.2 for this phase. Since the AFM solution is a construct of Fe^{2+} and Fe^{3+} spin moments which are not necessarily equal, as mentioned in [36, 44], a minuscule remaining magnetic moment in this phase is possible⁸. This can also be seen from the $M(H)$ -loop at 220 K in Fig. 4.5a. The fM solution is geometrically identical to the AFM

⁸A.D. Christianson reported in private communication about a small beam depolarization effect observed in the low- H phase under neutron diffraction. This could be an effect from a small sample net magnetic moment.

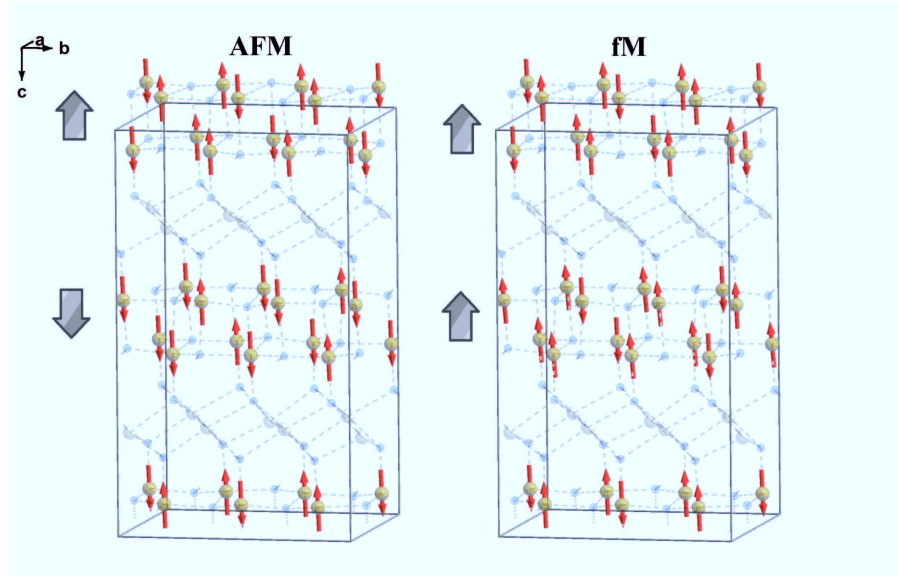


Abbildung 6.18: Results from the spin structure refinement explained in the previous chapters in $C2/m$ cell of the AFM (a) and fM (b) spin structure. Gray arrows indicate the different stacking of bilayer net magnetization. The spin arrangement in each bilayer is similar in both spin structures, except that all spins of one bilayer change their sign. For better visibility, one layer of Fe atoms is added outside the unit cell.

solution, except that all spins in one particular Fe-O bilayer (sites from Fe4 to Fe9 in Tab. 6.5) flip their sign under applied H , leading to the overall 2:1 configuration of \uparrow and \downarrow spins consistent with the observed (Fig. 4.4b) net moment for low- T and high- H . This simple geometrical relation between both spin structures causes the metamagnetic transition and the observed changes in neutron diffraction. A weak antiferromagnetic coupling between the Fe bilayers was already proposed in [81], and if disorder is added, it most likely weakens the inter-bilayer correlations, with its 8.43 Å longer distance and AFM correlations, rather than the intra-bilayer correlations with its 2.45 Å distance and FM correlations.

This different stacking of bilayer net magnetization between the AFM ($\uparrow\downarrow\uparrow \dots$) and the fM ($\uparrow\uparrow\uparrow \dots$) phase has a similarity to the fluctuating CO instabilities at higher T , as already reported in [85]. In Fig. 6.18 the spin structures are not shown with their most likely relation to the charge order distribution as discussed in the previous chapters. This relation will be presented in Sec. 7 with the help of the x-ray magnetic circular dichroism method, giving a similar but much more reliable result.

Intriguingly, as seen in Fig. 4.5b the AFM-fM transition extrapolates to $H \approx 0$ for $T \rightarrow T_N$, i.e. at T_N and $H = 0$ the two phases seem to be essentially degenerate. The

near-degeneracy of both charge and magnetic order is a hallmark of the importance of geometrical frustration in this system. While a ferroelectric charge order cannot be stabilized by an electric field as shown in Sec. 5.3.4 and already reported in [91], the different configurations of the magnetic order can readily be switched by an ambient H . Furthermore, to prevent the occurrence of a spin-flop phase upon increasing H , there must first be a strong anisotropy which constrains the spins to lie either parallel or antiparallel to an easy axis; this is clearly the case for LuFe_2O_4 . Second, in order for the low-temperature phase transition to be first-order for $T > 0$, there must be “competing” interactions between the two magnetic phases. The AFM/fM near-degeneracy in low H can lead to parts of the sample being trapped in fM after cooling through T_N , explaining the increasing parasitic ferrimagnetism described in Sec. 4.2 and already observed for samples with reduced T_N . Disorder will most easily disrupt the weak inter-bilayer correlations, which have by far the longest distances. It is thus natural to expect 3D spin orders to be replaced by “spin-glass-like 2D-ferrimagnetic order”, as reported from early neutron diffraction studies [81]. Phase competition and metamagnetic transitions between $\uparrow\downarrow\uparrow$ and $\uparrow\uparrow\uparrow$ -stacking of net moments along the c_{Hex} direction are expected for layered magnets with a very strong Ising anisotropy⁹ [209], and are also observed in a few model systems at low T , e.g. FeCl_2 [210].

6.2.4 Magnetic fluctuations above the Néel Temperature

The particular differences between the two geometrically related spin structures presented in the previous section and the magnetic near-degeneracy in the phase diagram at T_N both suggest, that the inter-bilayer correlations are far weaker than the intra-bilayer correlations. This was already indicated by [81] for the magnetism in LuFe_2O_4 in a neutron diffraction experiment on a less stoichiometric sample. A question which needs to be answered for such a system is: Above T_N , is a random stacking of the net moment of still medium-range ordered bilayers, i.e. a 2D-order [211], expected?

In magnetic diffraction, this 2D-order would result in strong diffuse magnetic scattering lines through $(\frac{1}{3} \frac{1}{3} \ell)$ above T_N , still reasonably sharp in-plane $(h h 0)$ direction, but featureless along ℓ . Therefore, the crystal already used in [1] and in Sec. 6.1 was measured in the $(h h \ell)$ -plane for magnetic correlations above T_N . In order to do this the DNS instrument (see Sec. 3.5.1), which is capable of mapping whole reciprocal lattice

⁹A “Giant Magnetic Anisotropy” is present for the case of LuFe_2O_4 , as evidenced by the strong orbital moment found by others [36, 44]. They are also present in the type A samples used in present work see Sec. 7.1.1.

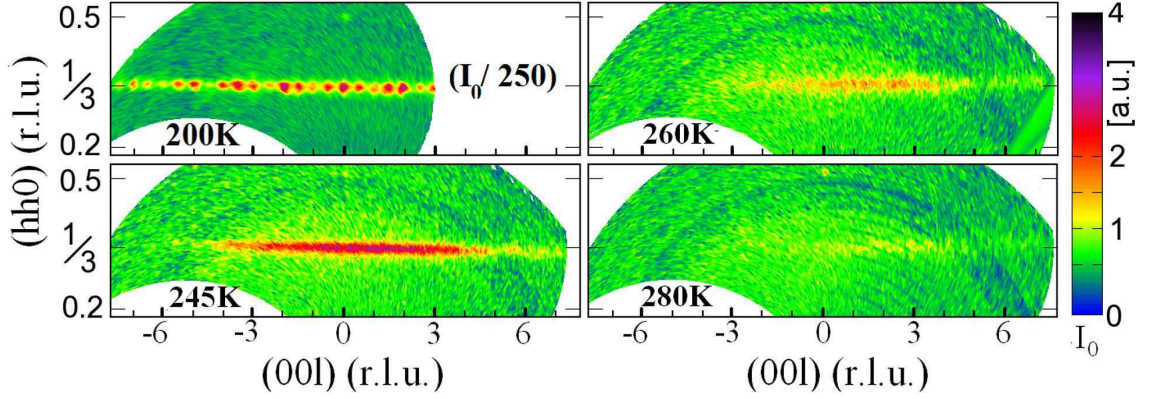


Abbildung 6.19: Reciprocal space map of the scattered magnetic intensity (logarithmic scale) in the $(hh\ell)$ plane, measured with polarized neutrons with $\lambda = 4.6 \text{ \AA}$ in the spin-flip channel (DNS) at different temperatures above and below (200 K), the magnetic ordering temperature T_N . The intensity of the measurement at 200 K is scaled by a factor of 250 in contrast to the observations above T_N . Figure from own published work [148].

planes, was used. The DNS instrument was operated in the neutron spin-flip configuration, making the neutron scattering process sensitive to pure magnetic scattering [143]. The polarization of the incoming neutrons was perpendicular to \vec{Q} and \vec{c}_{Hex} (and thus the sample spin moments \vec{S}) for the whole experimental setup, making a proper detection of magnetic contributions according to Sec. 3.4.2 possible, since all magnetic scattering is in the spin-flip channel. In contrast, the scattering vector \vec{Q} changes its angle with respect to the magnetization \vec{M} along the $(\frac{1}{3} \frac{1}{3} \ell)$ line according to $\alpha = \arccos\left(\frac{Q(\frac{1}{3} \frac{1}{3} \ell)}{Q(\frac{1}{3} \frac{1}{3} 0)}\right)$. Beside the magnetic form factor, this will also reduce the observed intensity for higher ℓ values. In order to achieve a reasonable statistic above T_N , and to separate magnetic and structural correlations, the neutrons were counted in both the spin-flip and the non spin-flip channel for 20 s per sample ω -position. All measurements were corrected by a vanadium standard measurement, as explained in Sec. 3.5.1.

At 200 K, so just below T_N , the intensity distribution in the spin-flip channel along the $(\frac{1}{3} \frac{1}{3} \ell)$ line presented in Fig. 6.19 is comparable to the diffraction pattern in the AFM phase presented in Fig. 6.9. As shown in Fig. 6.19, it exhibits sharp reflections in both the ℓ and the hh directions, indicating the 3D spin order as already previously demonstrated by spinstructure refinement in that phase. By warming above T_N , first to 245 K, the sharp reflections disappear and the observed diffuse line is still sharp along the $(hh0)$ direction but becomes diffuse along the ℓ line, indicating a 2D spin order, consistent with the scattering from a random stacking of still medium-range ordered bilayers.

This result was not observed before, and the integration of the diffuse line at 245 K

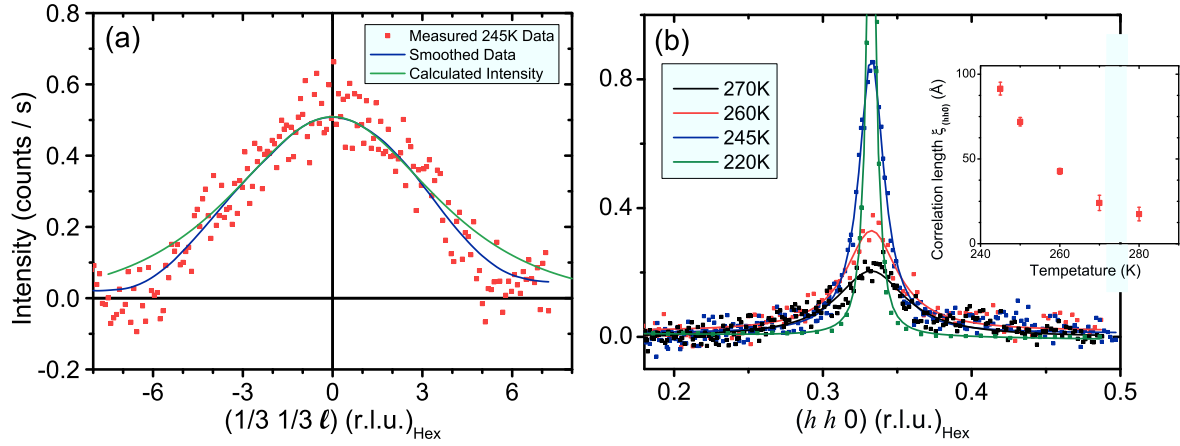


Abbildung 6.20: Cross-section integration of (a) the diffuse spin flip scattering along the $(\frac{1}{3} \frac{1}{3} \ell)$ line. The average of the measured data (blue) and the intensity model for randomly orientated Fe^{2+} and Fe^{3+} spin moments, as described in the text, are both displayed as solid curves. (b) The diffuse scattering in the spin-flip channel along the $(h h 0)$ direction for various temperatures. The data is fitted with a Lorentzian curve (solid lines) to determine the temperature dependence (inset) from the correlation length $\xi_{(h h 0)}$ in this direction. For comparison, the $(\frac{1}{3} \frac{1}{3} 0)$ reflection is shown at 220 K with its intensity divided by 250, with a corresponding correlation length of 252(12) Å. For better visibility the background of all curves is subtracted.

along the $(\frac{1}{3} \frac{1}{3} \ell)$ direction (presented in Fig. 6.20a) is in good agreement with the average magnetic intensity expected for scattering on randomly orientated Fe^{2+} and Fe^{3+} spin moments with its Ising spins pointing along the c_{Hex} direction. To obtain this calculated intensity distribution, the averaged Fe^{2+} and Fe^{3+} from factor squared (see Sec. 3.4.2) is multiplied by the squared polarization factor and the average Debye-Waller factor from both the fM (5.1) and AFM (1.9) spinstructure refinements presented in Sec. 6.2. The calculated intensity distribution presented in Fig. 6.20 is slightly broader than the observed (smoothed) intensity data. This broadening could indicate weak magnetic correlation along the c_{Hex} direction still remaining above T_N , but it could also be due to the fact that the magnetic model does not take the still present internal bilayer spin order into account. However, this model describes the diffuse line along ℓ with reasonable accuracy, indicating the magnetic origin of this behavior with almost no correlations between the still magnetically ordered bilayers. For higher temperatures, the intensity distribution for the diffuse line presented in Fig. 6.19 also becomes broader in the $(h h 0)$ direction (see Fig. 6.20b) and the overall intensity decreases strongly. Due to this decrease, the diffuse line could be measured properly by neutron diffraction only up to a temperature of 280 K. The estimated correlation length $\xi_{(h h 0)}$ below T_N is, with 252(12) Å, longer than that observed in Sec. 6.1.1 along the $(0 0 \ell)$ direction. Above T_N , $\xi_{(h h 0)}$ decreases

drastically for higher temperatures (inset Fig. 6.20b) but remains present, indicating the loss of internal bilayer spin correlations for much higher temperatures than T_N .

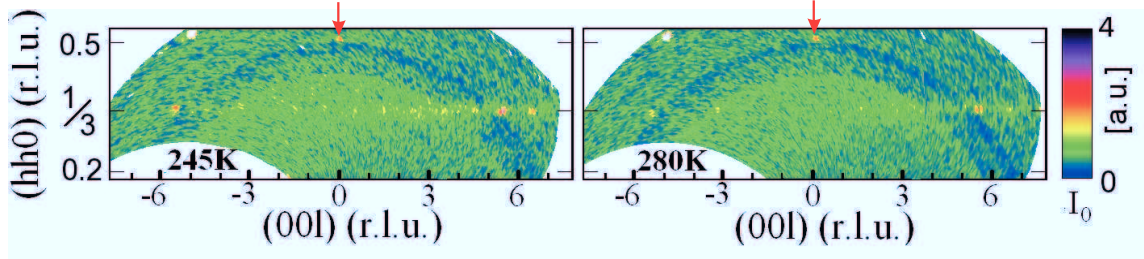


Abbildung 6.21: Reciprocal space map of the scattered non-magnetic intensity (logarithmic scale) in the $(h h \ell)$ plane. Measured with polarized neutrons of $\lambda = 4.6 \text{ \AA}$ in the non spin-flip channel (DNS) at different temperatures above the magnetic ordering temperature T_N . The presented data is corrected for $<100\%$ spin polarization, and the peaks indicated by red arrows at the $(\frac{1}{2} \frac{1}{2} 0)$ positions are a contribution from the $\frac{\lambda}{2}$ radiation on the structural (110) -reflection.

For the measurements in the non spin-flip channel (which is mainly sensitive to the structural correlations) with similar counting times no diffuse scattering could be observed; only sharp reflections from the charge order superstructure are visible in Fig. 6.21 at half-integer reflections for both temperatures. This result is consistent with previously measured data at 280 K (without polarized neutrons) which is already presented in Fig. 6.9.

The polarized neutron diffraction gives clear evidence for short-range magnetic correlations in the temperature range up to at least 280 K. Additionally, the strong deviations from Curie-Weiss behavior up to $\sim 400 \text{ K}$ in Fig. 4.12b [157, 200] imply that these short-range correlations are also significant in a much wider T range, including room temperature and T_{CO} . Furthermore, the hysteresis curves measured above T_N with $H \parallel c_{\text{Hex}}$ do not show a clear linear behavior in Fig. 4.12a, as is expected for a pure paramagnetic material, but exhibit a broad magnetic transition in H . This behavior can be explained by rearranging bilayers in the magnetic field. The competition of AFM and fM correlated fluctuations could be relevant for the giant magneto-dielectric response [87] observed also at room temperature. In Sec. 7.1.2 the idea of still spin ordered bilayers above the magnetic ordering temperature will be extended and coupled to the charge order.

6.2.5 The spin structures and symmetry

For a second-order magnetic phase transition to a spin structure described by a propagation vector with $q=0$ (this means identical magnetic and structural cells), the magnetic

structure established in $H = 0$ on a crystal with the space group $C2/m$, where all sites take part in the spin order, would usually be expected to follow one of the four magnetic space groups $C2/m$, $C2/m'$, $C2'/m'$ or $C2'/m$ [18]¹⁰. Each of these magnetic space groups corresponds to one of four irreducible representations Γ_i , according to which all crystallographic sites involved in the spin order should order (for more information on representation analysis see Sec. 2.1.5). For both spin structures established in this chapter for LuFe_2O_4 this is not the case, even taking into account symmetry-equivalent structures (i.e., a shifted cell) and both possible positions of the inversion center in the monoclinic cell (see Sec. 5.3.1) because the spins on distinct sites inevitably order according to different representations. In Tab. 6.6 the AFM and fM spin structures are presented separately, with their particular Wyckoff sites obtained from the crystal structure refinement in Sec. 5.3.1. They are compared with the possible irreducible representation Γ_i allowed by the $C2/m$ space group calculated by the program SARAh [212]. It is interesting to note, that for a monoclinic system the spins do not point in the crystallographic c_{Mon} direction but according to the monoclinic distortion β , measured for LuFe_2O_4 in Sec. 5.3.1, with an angle of 6.72° away from c_{Mon} . This fact does not play any role in the representation analysis, because the magnetic contributions for each Γ and site are equal along a_{Mon} and c_{Mon} and the spins can thus rotate freely in the monoclinic a, b plane according to Γ . As a result of this analysis, three of the sites are consistent with the Γ_3 representation, and the other is consistent with Γ_1 . This result is valid and presented in Tab 6.6 for both the AFM and fM magnetic phase.

Tabelle 6.6: The AFM and fM spin structure solutions for the low- and high- H magnetic phases obtained from the refinement explained in the previous chapters. For the different sites the possible irreducible representations Γ_i are calculated for the monoclinic structure with the program SARAh [212].

(8J ₂)	AFM	fM	Γ_1	Γ_2	Γ_3	Γ_4	(8J ₁)	AFM	fM	Γ_1	Γ_2	Γ_3	Γ_4
Fe ₆	↓	↑	↑	↑	↑	↑	Fe ₃	↑	↑	↑	↑	↑	↑
Fe ₉	↑	↓	↓	↓	↑	↑	Fe ₁₁	↑	↑	↓	↓	↑	↑
Fe ₈	↓	↑	↑	↓	↑	↓	Fe ₁₂	↑	↑	↑	↓	↑	↓
Fe ₄	↑	↓	↓	↑	↑	↓	Fe ₁	↑	↑	↓	↑	↑	↓
(4i ₁)	AFM	fM	Γ_1	Γ_2	Γ_3	Γ_4	(4i ₂)	AFM	fM	Γ_1	Γ_2	Γ_3	Γ_4
Fe ₂	↓	↓	0	↑	↑	0	Fe ₅	↓	↑	0	↑	↑	0
Fe ₁₀	↓	↓	0	↓	↑	0	Fe ₇	↓	↑	0	↓	↑	0

In fact, requiring all sites to follow the same representation (or remain disordered) corresponds to only 40 individual structures in $C2/m$ symmetry; the diffraction pattern

¹⁰Here ' denotes the time-inversion symmetry element.

of all of these structures is clearly inconsistent with the observed neutron diffraction pattern along the $(\frac{1}{3} \frac{1}{3} \ell)$ line. Different irreducible representations on different sites are incompatible with magnetic ordering occurring via a single second order phase transition. In the case of LuFe_2O_4 , the apparent degeneracy of two phases at $T=T_N$ and $H=0$ indeed makes a simple second-order transition unlikely. It is expected that the representation analysis will give the same result for both phases, because the only difference between the magnetic structures is a spin-reversal of 2 sites ($8J_2$ and $4i_2$) not involving the spin distribution for the irreducible representation. In summary, each site is for itself consistent with the $C2/m$ symmetry, but all the sites together are not compatible with the same irreducible representation Γ_i for this space group.

The question which now arises is: how to explain this order according to different Γ_i for different sites. One explanation could be that the transition is not purely second-order. This is supported by the fact that the bilayers are still ordered above T_N , as shown in Sec. 6.2.4, and the metamagnetic transition observed below T_N between AFM and fM is first-order (see magnetization curves in Fig. 4.5), which therefore must not follow the representation analysis. One other explanation relies on the fact that a magnetic triple point is present at $T = T_N$ and $H = 0$, a similar case to that already observed in a few model systems at low T , e.g. FeCl_2 [210]. For these metamagnetic model systems, the transition is only present under ambient H and very low T [209]. This is in strong contrast to our findings for LuFe_2O_4 , where the triple point is just present for $H = 0$ at ambient temperatures of $T_N \sim 240$ K. If there is a magnetic triple point present at the transition point into the long-range ordered magnetic phases (either AFM or fM), the transition cannot be second-order, and the need to follow the same irreducible representations vanishes. However, in the case of a first-order transition (the most likely case for this transition), sites ordering according to different irreducible representations is allowed, but still a highly unusual behavior.

6.3 A glassy transition at T_{LT} : towards disorder

The magnetic and structural behavior of LuFe_2O_4 changes drastically by cooling through the low-temperature transition T_{LT} , as indicated by the DC and AC magnetization curves presented in Sec. 4.2 and the structural transition observed in Sec. 5.3.6. In Fig. 2.16b taken from [1] a strong increase of diffuse magnetic scattering is reported below T_{LT} , accompanied by the appearance of an incommensurate peak structure around the $(\frac{1}{3} \frac{1}{3} 0)$ reflection. This increasingly diffuse scattering accompanied by the satellite structure was

also observed in a similar DNS measurement taken at 100 K, as already presented in Sec. 6.2.4. In Fig. 6.22 the $(h h \ell)$ plane is measured with polarized neutrons in the spin flip channel. In this measurement below T_{LT} an additional diffuse component to the

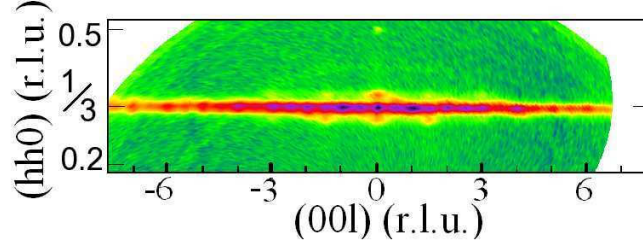


Abbildung 6.22: Reciprocal space map (DNS) of the scattered magnetic intensity (logarithmic scale) in the $(h h \ell)$ plane measured with polarized neutrons of $\lambda = 4.6 \text{ \AA}$ in the spin-flip channel below T_{LT} at 100 K.

3D scattering builds up, which is extremely broad along $(\frac{1}{3} \frac{1}{3} \ell)$ but sharp along $(h h 0)$ (similar to the case above T_N presented in the previous chapter). This diffuse scattering appears to be magnetic in origin, indicated by the fact that it only appears in the spin-flip channel, which is sensitive to magnetic correlations. The increase in line width on the $(\frac{1}{3} \frac{1}{3} \ell)$ magnetic peaks below T_{LT} is consistent with the introduction of stacking faults at the structural phase transition [28]. These stacking faults can also be an indication for the growth of fM and/or AFM cluster states, which will have a reduced size and thus exhibit a lower correlation length. An interesting point is that the formation of AFM/fM clusters is nothing else than a local stacking fold for the particular long range ordered phase.

The idea of an AFM and an fM cluster state is also supported by additional neutron diffraction measurements along the $(\frac{1}{3} \frac{1}{3} \ell)$ line which are presented in Fig. 6.23. These measurements are similar to Fig. 6.9, where the relative intensity contribution of integer and half-integer reflections is very sensitive to the particular sample history in the PS phase at 130 K. These different peak ratios according to history explain the presence of slightly more fM contributions, with stronger half-integer reflections, for the first scenario (blue line represents the 2.5 T FC case to 3 K with later warming in 0 T to 130 K), and AFM contributions, with stronger integer reflections, for the second scenario (red line represents direct ZFC to 130 K) in the diffraction pattern. For both scenarios, a strong diffuse magnetic background is present, indicating the loss of homogeneous long-range magnetic order in the phase below T_{LT} . That this diffuse scattering is magnetic in origin

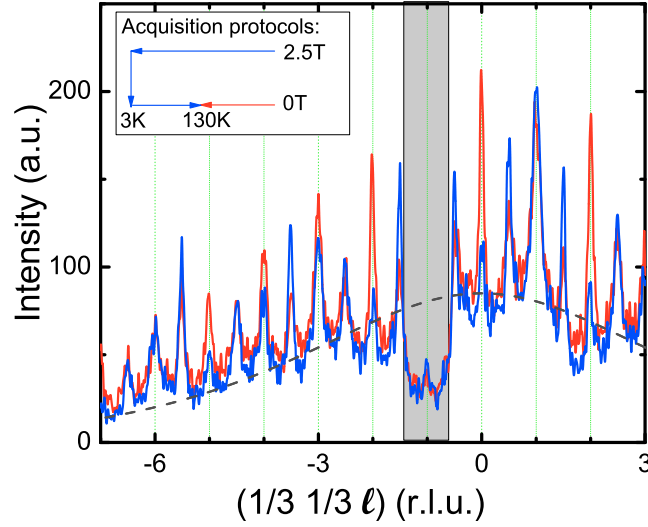


Abbildung 6.23: Neutron diffraction (N5) pattern at 130 K along the $(\frac{1}{3} \frac{1}{3} l)$ -line with different sample history with un-polarized neutrons of $\lambda = 2.4 \text{ \AA}$: The blue data represents the measurement after a 2.5 T FC to 3 K with afterwards warming in 0 T up to 130 K and the red data corresponds to a direct ZFC to 130 K. The gray area indicates the magnet coils with the corresponding dark angle in the diffraction pattern. The dashed dark gray line represents the model for random orientated Fe^{2+} and Fe^{3+} spin moments pointing along c_{Hex} which was already used in Sec. 6.2.4.

is supported by the fact that it fits to the same model (dashed green line) which describes a random stacking of medium-ranged ordered bilayers above T_N (see Sec. 6.2.4).

The incommensurate diffuse peak structure around the $(\frac{1}{3} \frac{1}{3} 0)$ reflection in Fig. 6.22 has also been observed in [1]. Although the line width of the peaks below T_{LT} and the broad diffuse component of the scattering makes a full solution of the low T magnetic structure very difficult, some general conclusions are possible. The 3D magnetic correlations in LuFe_2O_4 are intrinsically sensitive to disruptions along the c_{Hex} -axis, as the super-exchange path between Fe-O bilayers must pass through not one but two oxygen ions; and thus the driving force for the changes in the magnetic structure below T_{LT} may be related to the introduction of stacking faults as discussed above. Another possibility, not inconsistent with the magnetic cluster state, could be the onset of orbital order at T_{LT} . For this scenario the large orbital magnetic moments on Fe^{2+} valence should disappear, which can be observed by the drop on magnetization curves in Fig. 4.4. But this drop is too big to be explained by the orbital order scenario alone.

Most interesting in the orbital order scenario is that the magneto-crystalline anisotropy of Fe^{2+} may be necessary to stabilize the fM and AFM long-range magnetic ordered phases. If the transition at T_{LT} is associated with the order of Fe^{2+} orbitals, this

would destroy the anisotropy and could thus explain the appearance of diffuse magnetic scattering as an indication of broken magnetic long-range order in that phase.

6.3.1 The “Anomalous field heating effect”: stable disorder

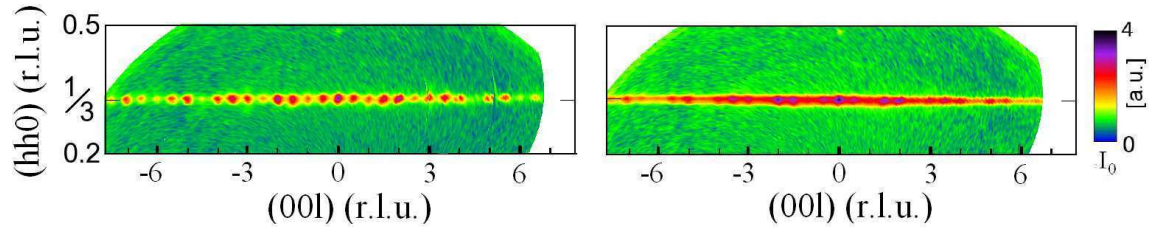


Abbildung 6.24: Reciprocal space map of the scattered magnetic intensity (logarithmic scale) in the $(hh\ell)$ -plane measured by polarized neutrons in the spin-flip channel (DNS) in the region where the anomalous “field heating effect” is observed [79]. The measurement temperature was 200 K on cooling (left) and the identical temperature on warming from below T_{LT} (right). Both measurements were done with the same data-acquisition script.

An interesting point is that the diffuse scattering is still present upon warming in the region where the structural distortion already disappeared, as indicated in Fig. 6.24b and reported in [28]. A remaining strong frequency splitting is measured for the AC susceptibility measurement on warming, in contrast to the observations upon cooling for this region. Additionally, upon warming from the PS phase in low H , M first sharply increases to a high magnetization plateau and then decreases at ~ 218 K, which is presented in Fig. 4.2 for the type A samples. Very similar, though not as sharp, behavior was already observed 20 years ago [79]. It was denoted “anomalous field-heating-effect”, but could not be explained. The rise of M on warming coincides with the structural transition $T_{LT}^\uparrow \sim 180$ K where peak splitting disappears. While χ' shows a sharp drop at T_{LT}^\uparrow in Fig. 4.7b, the frequency-splitting remains in this “plateau-region” (hatched area in Fig. 4.10a), as does the diffuse component in neutron diffraction in Fig. 6.24. To understand this anomalous behavior, consider that by warming above T_{LT}^\uparrow , the sample enters a H - T region where both AFM and fM phases can be stable. As the sample consists of mesoscopic AFM and fM regions, there is no driving force to settle fully into either the AFM or fM phase until one of the states becomes unstable. Below T_{LT} even a small field promotes the increase of an fM fraction, as indicated by the non-linear virgin magnetization. The disappearance of the structural distortion facilitates this increase, resulting in the abrupt rise of M , i.e. the anomalous “field-heating effect” [79]. Above ~ 218 K the fM state becomes unstable in low- H (Fig. 4.7b), and consequently,

the sample re-enters the pure AFM phase. This is supported by the fact that both the frequency splitting (Fig. 4.7b) and diffuse magnetic scattering vanish at ~ 218 K and the DC magnetization signal drops back to nearly zero (Fig. 4.7b). Another interesting point is that the temperature-dependent intensity of the $(\frac{1}{3} \frac{1}{3} 0)$ reflection in Fig. 6.10 reaches, in $H = 0$, equal values for both cooling and warming at ~ 218 K, indicating re-entry into the long-range spin ordered AFM phase.

6.4 Discussion and Conclusion

In summary, with the help of neutron diffraction and the monoclinic crystallographic model, the long-range spin ordered structures present in the magnetic phase diagram of LuFe_2O_4 (Fig. 6.18) are solved. A central ingredient in the evolution of the complex phase diagram is the competition between two nearly-degenerate instabilities at T_N . This competition between the fully ordered AFM and fM spin alignments, similar to the two competing CO instabilities proposed at higher T [85], arises from geometrical frustration. The particular difference between the two nearly degenerate spin structures is the reversal of all the spin moments in one Fe bilayer. This behavior, together with the crystallographic structure, implies that the intra-bilayer correlations are more dominant than the inter-bilayer correlations.

Diffuse magnetic scattering below the low-temperature phase transition T_{LT} indicates the entrance into a “magnetic glassy” state with a weaker coupling between the bilayers. Neutron diffractions in the low temperature phase suggest that both the AFM and fM correlations are simultaneously present in this phase, depending strongly on the sample history. Together with the results from the macroscopic magnetization measurements in Sec. 4.2.3, both methods demonstrate the intrinsically inhomogeneous nature of this magnetic state, most likely linked to magnetic phase separation. This diffuse scattering is still present upon warming above T_{LT} , indicating a region where both AFM and fM phases are simultaneously stable. In the magnetization measurements of Sec. 4.2.5 these fM patches are also observed as a sudden increase in M , which was previously labeled [79] as anomalous “field-heating effect”.

Just above T_N therefore, a random stacking of the net moment of still medium range ordered bilayers, i.e. a 2D order, is observed. Strong deviations from Curie-Weiss behavior (already presented in Sec. 4.2.6) up to ~ 400 K, imply that these short-range correlations are significant in a wide T -range including T_{CO} and may influence the establishing of CO with the spin charge coupling presented in Sec. 7. This competition also strongly

influences the magnetic properties in samples where the phase diagram could not be resolved, giving rise to apparently inconsistent observations in earlier studies, such as glassy freezing instead of long-range order. The complexity of the H - T phase diagram delineated in this work will, hopefully guide future experiments and restrict theoretical models of this material.

6.5 Related publication

The following publication is related to this section:

- “*Competing Ferri- and Antiferromagnetic Phases in Geometrically Frustrated LuFe_2O_4* ”
J. de Groot, K. Marty, M.D. Lumsden, A.D. Christianson, S.E. Nagler, S. Adiga,
W.J.H. Borghols, K. Schmalzl, Z. Yamani, S.R. Bland, R. de Souza, U. Staub, W.
Schweika, Y. Su, and M. Angst
Phys. Rev. Lett. **108**, 037206 (2012).

For a detailed declaration of own contributions to this publication see App. A.

Spin–charge coupling and the question of orbital order

The refinements on neutron diffraction with different moments for the Fe^{2+} ions, presented in Sec. 6, already provided a first indication for the possible coupling between the charge and the spin orders in LuFe_2O_4 . In this section, more elaborate methods are used to answer the following questions: Is the new CO arrangement with charged bilayers presented in Sec. 5.3 consistent with the magnetic structure presented in Sec. 6? Are the magnetic structures predetermined by the CO? At the end of this section the question of possible orbital order in the low temperature phase is addressed.

7.1 X-ray magnetic circular dichroism

The ideal tool to address these questions is x-ray magnetic circular dichroism (XMCD) at the Fe $L_{2/3}$ edges. Two previous XMCD studies on LuFe_2O_4 are reported [44, 36], but both were performed on samples for which no long-range charge and magnetic order has been demonstrated. To test whether the strong spin-charge coupling deduced in [44, 36] also applies to the type A samples presented in this thesis, which exhibit both long-range spin and charge order, a similar XMCD experiment to [44, 36] was performed at the soft x-ray beamline 4-ID-C of the Advanced Photon Source (APS). Here magnetic fields up to 4 T $\parallel c_{\text{Hex}}$ were used. The incoming beam and the total electron yield, as x-ray absorption spectra (XAS), was dominated by re-absorption, but confirmed the bulk signal of the XMCD signal. The XMCD signal was calculated from the difference between the XAS for positive and negative circular polarization (μ_+ and μ_-). To eliminate possible non-magnetic dichroic contributions, the XMCD spectra with \vec{H} parallel and antiparallel to the incoming beam were subtracted from each other. The diffraction data in $H \parallel c_{\text{Hex}}$ up to 2.5 T, show in Sec. 5.3.5 neither a change in the CO configuration nor a structural transition.

7.1.1 XMCD: probing the Fe^{2+} and Fe^{3+} local environment

In the high-field phase with the ferrimagnetic spin structure refined in Sec. 6, the measured shape of the XMCD spectra $\Delta\mu$ obtained from the total electron yield (TEY) signal in Fig. 7.1 is close to the ones shown in [44, 36]. With the sum rule [133, 134] of Eq.(3.37) applied to the integrated dichroism signal $\sum(\Delta\mu)$, before and far after the Fe L_2 edge with p and q , respectively, a similar orbital to spin moment ratio of ~ 0.3 as that reported in [44, 36] could be extracted:

$$\frac{m_{orb}}{m_{spin}} = \frac{2q}{9p - 6q} \quad (7.1)$$

By considering the total spin magnetic moment of $m_{spin} = 2.33\mu_B/\text{f.u.}$ in the simple ionic limit ($4\mu_B$ for Fe^{2+} and $5\mu_B$ for Fe^{3+}), corresponding, according to the extracted orbital to spin moment ratio, to a pure orbital magnetic moment of $\sim 0.7\mu_B/\text{f.u.}$ for Fe^{2+} (explaining the observed saturation moment of $\sim 2.9\mu_B/\text{f.u.}$ in magnetization measurements from Sec. 4). This angular magnetic moment also explains the strong magneto-crystalline anisotropy along c_{Hex} , due to possible spin orbit coupling [213]. According to the integrated XMCD signal-direction the Fe^{2+} angular-magnetic moment points in field direction; this is also in agreement with the third Hund's rule for more than half-filled shells [214]. Because of its electronic configuration for the Fe^{3+} valence, no orbital contributions to the magnetism are expected.

The Fe^{3+} with five $3d$ electrons is spherical, while the Fe^{2+} with six $3d$ electrons exhibits a doubly degenerate orbital degree of freedom in the $d_{zx}=d_{yz}$ ground state of Fig. 2.3 [36]. Furthermore, from these observed unquenched orbital magnetic moments for the Fe^{2+} valence the possibility of long-range orbital magnetic order can be excluded. This is due to the fact that the orbital contributions must be real functions with a complex linear combination of d_{zx} and d_{yz} orbitals, since only such a complex state can carry non-zero angular momentum. This avoids the splitting of the orbital ground state, and thus there is no origin for an orbital order scenario in the fM phase. Furthermore, as reported in [36] the proposed splitting of the e_g'' and e_g' doublets is incompatible with orbital angular magnetic moments in the xy plane and so a strong spin-orbit coupling $-\xi\Delta\vec{L} \cdot \vec{S}$ is therefore expected.

On the other hand, for the presence of the strong spin-orbit interaction, the ground state has no orbital ordering. Instead, a large orbital magnetic moment is induced, similar as it is observed for V_2O_3 [215]. This absence of long-range orbital order is also valid for the paramagnetic, and the AFM long-range ordered magnetic phases. For the AFM

and paramagnetic phase this evidence of absence is indirect, since there is no structural component involved in the corresponding metamagnetic transitions which would indicate an orbital ordered state. In contrast to this, for the low-temperature phase transition at T_{LT} a structural component is indeed observed (see Sec. 5.3.6 and [28]). Upon this transition, the orbital magnetic moments on the Fe^{2+} might be quenched, and therefore long-range orbital order in this low-temperature phase cannot be excluded.

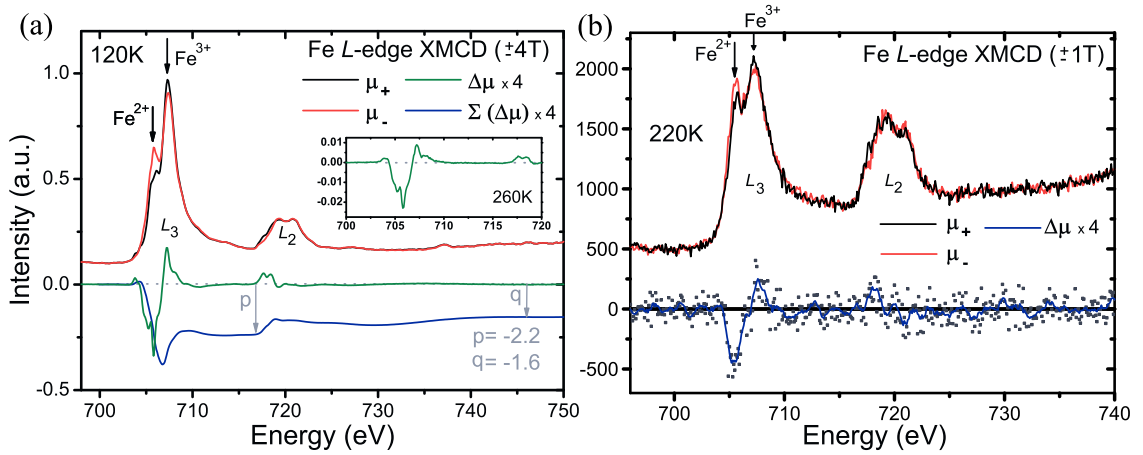


Abbildung 7.1: (a) Fe $L_{2/3}$ edge XMCD spectra from TEY of LuFe_2O_4 at 120 K and 260 K (inset) in $\pm 4T$. Fe^{2+} and Fe^{3+} white lines in the L_3 region are indicated by arrows. The dichroism spectrum ($\Delta\mu = \mu_+ - \mu_-$) is obtained from the difference of the absorption spectra and multiplied by a factor of 4 for better visibility. (b) A XMCD spectra from TFY, for comparison, to verify the bulk behavior of the XMCD signal from TEY. For better comparison with the TEY signal, the solid blue line is the five points smoothed TFY-XMCD signal. Both (a,b) signals are measured in the fM phase according to Fig. 4.10 and the data was averaged from positive and negative field measurements.

Another interesting point is that in the XMCD spectra the valence state of Fe also has an influence on the energy position in the absorption spectra. A large downward peak at ~ 708 eV for the Fe^{2+} valence and a smaller upward peak at ~ 709.5 eV for the Fe^{3+} valence are present [216, 29]¹.

In the L_3 -region of the TEY-XAS (Fig. 7.1a), the Fe^{3+} peak is higher than the Fe^{2+} peak suggesting an Fe^{3+} contribution of more than 50% [218]. Because TEY has a very short probing depth, and because the structure refinement and other bulk-sensitive techniques (e.g. Mössbauer spectroscopy [28]) clearly show a $\text{Fe}^{2+}:\text{Fe}^{3+}$ ratio close to 1 : 1, this is most likely an effect of surface oxidation (for this experiment the crystals were cleaved ex-situ in normal atmosphere). Indeed, the peak ratio is close to the one shown in [44], who cleaved their crystals in $5 \cdot 10^{-8}$ mbar, whereas crystals cleaved in

¹Furthermore, an influence of the local environment on the $\text{Fe}^{2+/3+}$ XAS spectra is reported [217]. However, there is no report for such a behavior for the trigonal-bipyramidal coordination in [36, 44].

higher vacuum of $7 \cdot 10^{-10}$ mbar [36] resulted in peaks closer in height. To verify this, XAS and XMCD were also measured in total fluorescence yield TFY (Fig. 7.1b), which is more bulk-sensitive, due to the much longer photons free path of the fluorescence signal compared to that of the electrons. Indeed, the $\text{Fe}^{2+} : \text{Fe}^{3+}$ peak ratio in the L_3 region is close to 1 : 1 in fluorescence yield. Strong self-absorption (clearly visible in the changed $L_3:L_2$ intensity ratio) results in a somewhat noisy XMCD signal in fluorescence-yield, but despite this the main feature of the XMCD, a large downward peak at the Fe^{2+} position and a smaller ($\sim 50\%$) upward peak at the Fe^{3+} position, is also clearly visible in fluorescence-yield, confirming its bulk nature (Fig. 7.1b). However, this surface effect should not contribute to the XMCD signal [44, 36], which is only sensitive to the differences from both XAS channels.

The main feature in XMCD, a downward peak at the Fe^{2+} and a smaller upward peak at the Fe^{3+} position directly implies that the net magnetic moment of the Fe^{2+} -sites is in field-direction and a net moment of the Fe^{3+} sites points to the opposite direction. Because the spin-value of Fe^{3+} is larger than the one of Fe^{2+} , the considerably smaller XMCD intensity at the Fe^{3+} position

Tabelle 7.1: Possible Fe^{2+} and Fe^{3+} spin configurations according to the measured XMCD signal. The magnetic moments of Fe^{2+} and Fe^{3+} are given in brackets. Here, the $4.7 \mu_B$ spin-moment plus orbital magnetic moment on Fe^{2+} and the pure spin-moment of $5.0 \mu_B$ on Fe^{3+} are used.

N _o	Fe^{2+} ($4.7 \mu_B$)	N _o	Fe^{3+} ($5.0 \mu_B$)
1	↑ ↑ ↑ ↑ ↑ ↑	1*	↓ ↓ ↓ ↓ ↓ ↑
2	↑ ↑ ↑ ↑ ↑ ↓	2*	↓ ↓ ↓ ↓ ↑ ↑
3	↑ ↑ ↑ ↑ ↓ ↓		

implies that fewer Fe^{3+} spins are aligned antiparallel to field than Fe^{2+} spins are aligned $\parallel H$. This is consistent with the local valence-specific spin configuration proposed in both [44] and [36]. Together with the well-known magnetic saturation moment of $\sim 3 \mu_B/\text{f.u.}$ and two facts of the recently published spin-model from neutron diffraction [148] it can readily be shown that this is indeed the only possible local valence-specific spin configuration. The first fact, that the magnetic and crystallographic cell are equal [148], implies that there are only 12 Fe-sites (i.e. 6 each 3+ and 2+), and the second fact, that this is an Ising-system with all sites fully ordered implies that each site contributes parallel or antiparallel. From the above direct implications of the XMCD, this leaves only three possible arrangements, tabulated in Tab. 7.2. All other combination of Tab. 7.1 are inconsistent with the XMCD implication that more Fe^{2+} spin moments are parallel to the field than Fe^{3+} are antiparallel.

Here, $N^{\circ}(1 + 2^*)$ is the only combination of local spin environments, which gives a reasonable net moment of $3.03 \mu_B/\text{f.u.}$, very close to the measured saturation moment of $\sim 3 \mu_B/\text{f.u.}$ found in literature [148, 81, 92], which is also valid for the sample used in this work. All other combinations of possible spin configurations in Tab. 7.2, will result in much lower overall net moments (the next highest is $N^{\circ}(2 + 2^*)$ and $N^{\circ}(1 + 1^*)$ both with $\sim 1.4 \mu_B/\text{f.u.}$, all others combinations have negative values), and therefore can be excluded. Furthermore, $N^{\circ}(1 + 2^*)$ to be the favored local spin configuration does not depend strongly on the actual Fe^{2+} and Fe^{3+} moments. By changing the total Fe^{2+} magnetic contribution to $4 \mu_B/\text{f.u.}$ and the Fe^{3+} moment to $5 \mu_B/\text{f.u.}$, or both valences equal to $4.5 \mu_B/\text{f.u.}$, the solution $N^{\circ}(1 + 2^*)$ is still the configuration which is the closest to the observed saturation moment.

Tabelle 7.2: Magnetic saturation moment of the three local spin configurations according Tab. 7.1.

Combination	$\mu_B/\text{f.u.}$
$N^{\circ}(1 + 2^*)$	3.03
$N^{\circ}(2 + 2^*)$	1.46
$N^{\circ}(1 + 1^*)$	1.36

Given the CO configuration shown in Fig. 5.13a of Sec. 5.3.3, there are only 15 inequivalent spin structures possible, neglecting partial disorder. In all observations with neutron and soft x-ray diffraction in Sec. 6 the C-centering condition is still preserved for the fM phase. According to the XMCD result, all spins on the six Fe^{2+} sites should point in the H -direction. There are only six Fe^{3+} sites left in the monoclinic cell where four \downarrow and two \uparrow spins must be arranged. Of these possible solutions, 14 lead to magnetic diffraction patterns clearly inconsistent with observations; the remaining solution, indicated by arrows in Fig. 7.2, is the same as the one presented (without relation to the CO) in Fig. 6.18 for the ferrimagnetic phase. The new CO configuration presented in this thesis, obtained from structure refinement and the local spin structure from XMCD, together lead to the long-range spin order reported in this thesis.

More important, the above implications of the XMCD signal, combined with the ferrimagnetic model of Sec. 6, verify the novel CO configuration. Given the absence of partial disorder only three valence specific local spin configurations are possible, of which only one is consistent with the overall magnetic saturation moment of $\sim 3 \mu_B/\text{f.u.}$: All Fe^{2+} as well as $\frac{1}{3}$ of the Fe^{3+} spins are aligned in H -direction, $\frac{2}{3}$ of the Fe^{3+} spins point opposite to H , the same model as proposed in [36, 44]. Combining this local spin-charge configuration with the ferrimagnetic spin order of Sec. 6 directly excludes any (anti)ferroelectric model preserving mirror symmetry. Ignoring mirror symmetry, 28 CO

configurations are possible ², of which however only the one presented in Fig. 7.2a fits to the right intensity distribution along the $(0\ 2\ \ell)_{\text{Mon}}$ line (Fig. 5.6b); this is also the only one of the 28 preserving mirror symmetry. Furthermore, as noted in Sec. 6.2, the refinement of spin structures can be slightly improved by introducing different moments for Fe^{2+} and Fe^{3+} according to the charged bilayer CO model of Sec. 5.3, but not for any CO with polar bilayers such as those reported, for instance, in [27, 85, 160]. This provides a further support for the charge order configuration presented in Sec. 5.

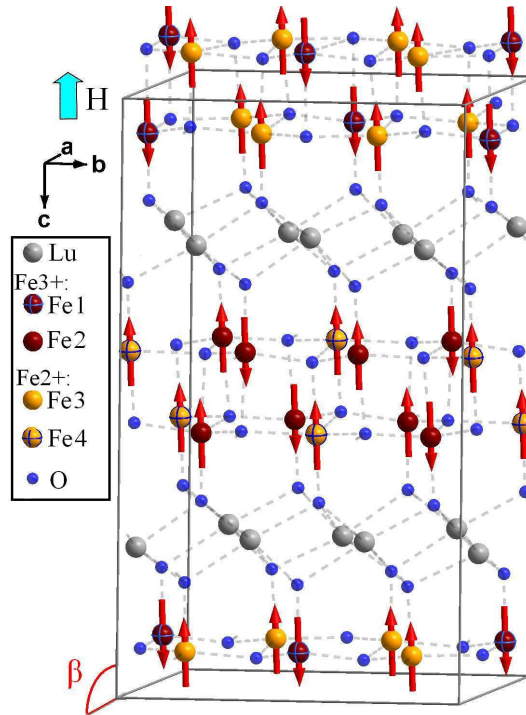


Abbildung 7.2: The relation between the Fe^{2+} and Fe^{3+} CO presented in Fig. 5.13a and the local valence spin order obtained from the XMCD signal measured at 120 K and $H = \pm 4$ T (in fM according to the phase diagram in Fig. 4.10) following the interpretation of [44, 36]. Both the CO and the fM spin orders for the different Fe sites in the $C2/m$ monoclinic cell already introduced in Sec 5.3 are presented in this figure. Figure from own published work [172].

7.1.2 Coupling between spin and charge order above T_N

The analysis of the XMCD signal in this chapter not only shows the consistency of the charged bilayer CO and the spin order, but also implies a strict coupling of these orders. Interestingly, XMCD spectra taken at 260 K, thus above T_N , presented in the inset for Fig. 7.1, have a small amplitude in ± 4 T, but they indicate the identical $\text{Fe}^{2+/3+}$ spin

²All four \downarrow -sites must be Fe^{3+} , and the number of possibilities to distribute two remaining Fe^{3+} among the 8 \uparrow -sites is given by: $\binom{8}{2} = 28$.

configuration as in the ferrimagnetic phase. This is consistent with the conclusion for $H = 0$ of randomly-stacked bilayers that are still magnetically ordered based on diffuse magnetic scattering in Fig. 6.19: partial polarization by a magnetic field is then expected to lead to the same relative net moments on Fe^{2+} and Fe^{3+} . These results signify already ordered Fe-bilayers in the paramagnetic phase, with strictly coupled charge and spin order persisting well above T_N . The magnetic hysteresis curves in Fig. 4.12a show a persisting strong deviation from linear behavior above T_N , indicating this coupling. From susceptibility measurements in Fig. 4.12b, this spin charge coupling is also likely present in the temperature region above T_{CO} , indicated by the appreciable deviation from the Curie-Weiss law in this region. This suggests short-range precursors at high T , with already coupled local spin and CO. This coupling, so far present above T_{CO} , is probable the origin of the magnetic field control of the charge configuration reported in [89].

7.2 The question of orbital order

Both, a new 3D charge order pattern, coupled to complex 3D magnetic spin order could be identified in this thesis. In contrast to this, there is no experimental evidence so far for a (long range) orbital ordered state, despite the orbital glass of [31]. But, in contradiction of the experimental results, a long-range ordered phase is theoretically expected [95, 219]. However, in LuFe_2O_4 no additional reflection which could be connected to orbital order was ever observed, so any ordered state of the orbitals would have to be in a ferro-like alignment³. Such a scenario will lead to anisotropic scattering contributions on charge order reflections [220] for long-range order of the Fe^{2+} orbitals that is distinct from that of the spherical Fe^{3+} ions. For LuFe_2O_4 it is reported, that the crystal field of the trigonal bipyramidal coordination splits the $3d$ states into two doublets ($d_{xy}/d_{x^2+y^2}$ and d_{xz}/d_{yz}) and a singlet d_{z^2} [95, 31]. The Fe^{3+} with its five $3d$ electrons is spherical, while the Fe^{2+} with six $3d$ electrons exhibits a doubly degenerate orbital degree of freedom in the d_{xz} and d_{yz} ground states. In the previous chapter the presence of orbital order could be excluded in the fM and AFM magnetic phases through the observation of strong magnetic orbital moments on the Fe^{2+} valence. The question which still needs to be answered: could there be a ferro orbital order state present in the low temperature region below T_{LT} ?

In order to exclude the possibility of a small anisotropic component in the scattering, indicating the presence of orbital order in LuFe_2O_4 , a soft x-ray diffraction experiment with polarization analysis was performed on the $(00\frac{3}{2})$ reflection and the corresponding

³The propagation vector of such an ordered state should be $\vec{k} = (000)$, identical to the structure.

satellites, allowing a direct access to the Fe 3d bands. This was the initial study presented in Sec. 6.1.1, where the intensity of the central $(00\frac{3}{2})$ reflection was identified as a pure magnetic contribution to the scattering. This behavior seems to be stable down to low temperatures as indicated in Fig. 7.3 by the temperature-dependent analysis of energy scans with both π and σ incoming polarization. In order to take care of the anomalous field heating effect all scans were done at 200 K in cooling and warming. The shape of both spectra in the π and σ channel looks similar for all measured temperatures, indicating that they have the same origin. For a better comparison with the results obtained for the much weaker $(\tau\overline{2\tau}\frac{3}{2})$ satellite reflection the analysis on the $(00\frac{3}{2})$ reflection presented here was performed without a polarization analyzer for the scattered beam.

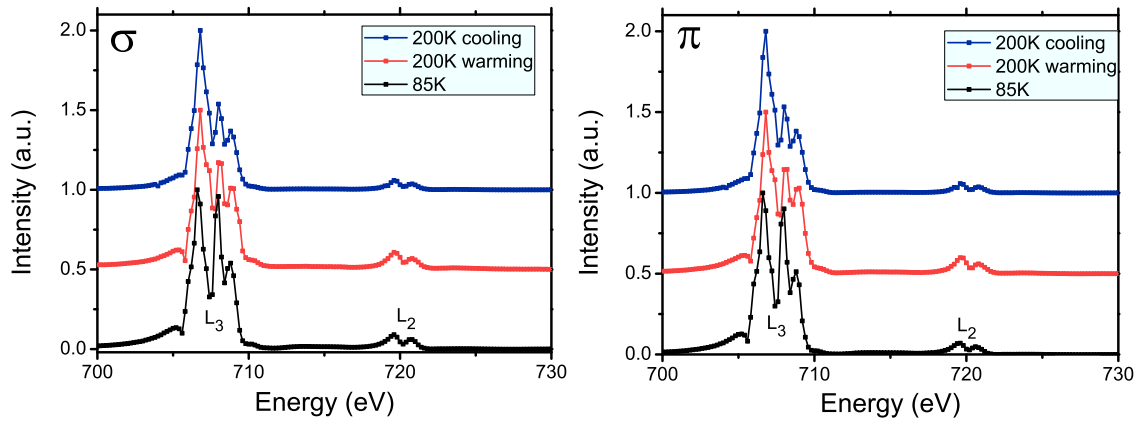


Abbildung 7.3: Energy dependence of the intensity of the $(00\frac{1}{2})$ reflection of LuFe_2O_4 with incident linear σ (left) and π (right) polarization recorded over the Fe L_2 and the L_3 edges at constant wave vector \vec{Q} but different temperatures. For a better visibility all presented curves are shifted.

In order to elaborate the possibility of orbital order in LuFe_2O_4 , the $(\tau\overline{2\tau}\frac{3}{2})$ reflection was additionally studied. Here the results are presented in Fig. 7.4 for both π and σ incoming polarization. The intensity on this type of satellite reflections is very weak, and thus the polarization analyzes of the scattered light was neglected. For the σ channel in Fig. 7.4 the shape of the energy scans seems to be unchanged, except for the overall increase of intensity at lower temperatures. For isotropic charge scattering the same energy dependence in the σ and π channel is expected; this is clearly not the case for the reflection presented here by comparing Fig. 7.4a and b. This anisotropy contribution is even present at 285 K, the T region where orbital order already could be excluded from the XMCD results presented in the previous section. Despite this high temperature anisotropy at all temperatures, a strong change of the π incident channel at the L_2 and L_3 edge is also present below T_{LT} . In principle, the observed changes below T_{LT} could be

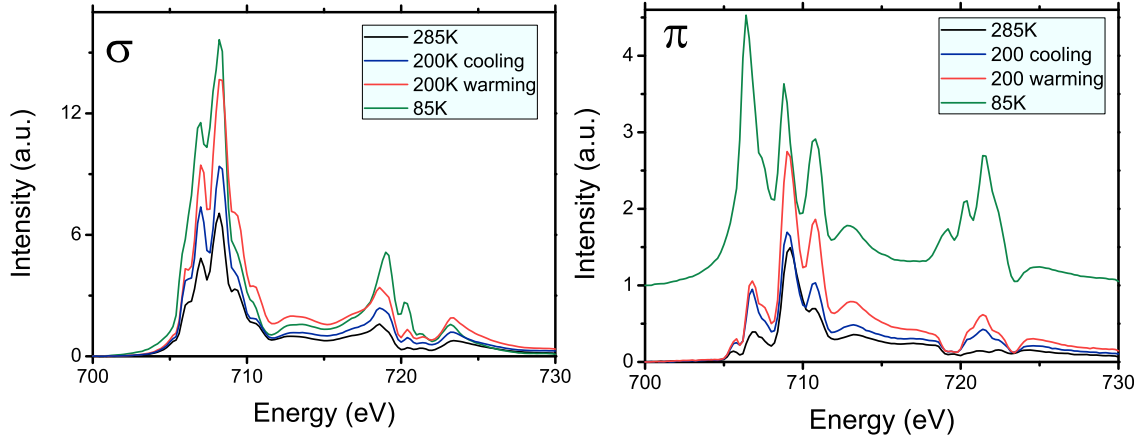


Abbildung 7.4: Energy dependence from the intensity of the $(\tau \overline{2\tau} \frac{3}{2})$ reflection of LuFe_2O_4 with incident linear σ (left) and π (right) polarization recorded over the Fe L_2 and the L_3 edges at constant wave vector \vec{Q} but different probe temperatures. The curve measured at 85 K in the right panel is shifted for clarity.

magnetic in origin; however, the DNS measurement evidence that only the $(00 \frac{3}{2})$ central reflection is purely magnetic. The strong intensity increase on the L_2 relative to the L_3 edge in the π channel suggests an order of the Fe^{2+} orbitals [221, 222]. Furthermore, for this temperature region the orbital order scenario can not be excluded by our previous XMCD studies, due to the structural distortion associated with this phase below T_{LT} .

In order to elaborate this in more detail, the aim of a second experiment at beamline P09 of the Petra-III synchrotron was, to check if there is any anisotropic contribution in the polarization dependent scattering from charge order super structure reflections in LuFe_2O_4 single crystals present. This anisotropy could indicate Fe orbital order or correlations (in contrast to the orbital glass reported in [31]). For this, some indications from the previous soft x-ray experiment [97] were present. We also performed a hard x-ray diffraction experiment (mainly sensitive to structural anisotropy) at the ESRF on beamline ID20 at a temperature of 200 K, where no indications for anisotropy connected to orbital order could be found [97]. In this follow up experiment, it is tested whether there is an anisotropic signal, and if so is it truly an orbital order contributi-

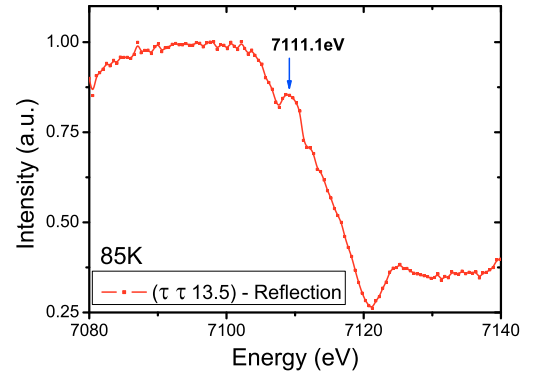


Abbildung 7.5: Energy scan at fixed wavevector of the $(\tau \tau \frac{27}{2})$ reflection intensity, measured at 85 K, with π incident polarization.

on, or merely a manifestation of an anisotropic structural distortion present below T_{LT} . After performing an energy scan on the $(\tau\tau\frac{27}{2})$ reflection, around the Fe K edge (see Fig. 7.5) at 85 K, it was decided to perform the polarization analysis on the feature which appears at 7111.1 eV on the edge. For this reason, the arization analysis [25], was extracted from the polarization analysis of the scattered beam, under different incoming linear polarization states, see therefore Fig. 3.9 of Sec 3.3.6.

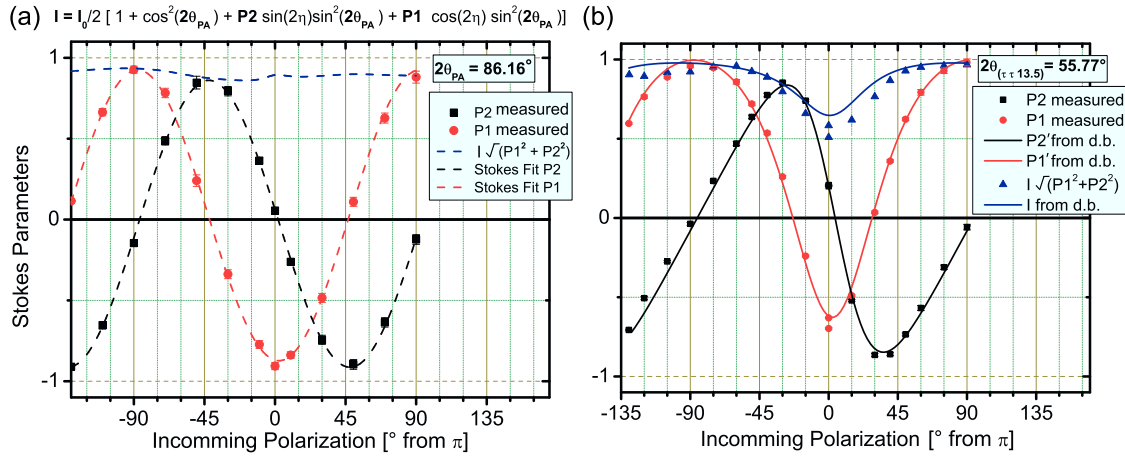


Abbildung 7.6: Full linear polarization analysis on the direct beam (a) and the $(\tau\tau\frac{27}{2})$ superstructure reflection (b), both are measured at an energy of 7111.1 eV and a temperature of 85 K in $H = 0$ after ZFC. In (a) the Stokes' parameters of the direct beam were fitted, concerning the Cu(220) reflection under $2\theta_{PA} = 86.16^\circ$ from the polarization analyzer crystal. In (b) the solid lines show the behavior expected from the direct beam for P1 and P2 in case of isotropic Thomson scattering under $2\theta_{(\tau\tau\frac{27}{2})} = 55.77^\circ$.

The result of the full polarization analysis (Fig. 7.6b) shows no clear indication for an anisotropic contribution to the polarization dependent scattering from a ferro type orbital order. The differences between the direct beam (also measured in order to exclude experimental artifacts) in Fig. 7.6a and the $(\tau\tau\frac{27}{2})$ reflection in Fig. 7.6b are explained, with high accuracy, by the higher $2\theta_{(\tau\tau\frac{27}{2})}$ value⁴ of 55.77° for this reflection. Here, the calculated values for P1' and P2' (solid lines in Fig. 7.6b) are obtained according to:

$$P1' = \frac{1 - x^2 + P1(1 + x^2)}{1 + x^2 + P1(1 - x^2)} \quad \text{and} \quad P2' = \frac{2 \cdot x^2 \cdot P2}{1 + x^2 + P1(1 - x^2)}, \quad (7.2)$$

with $x = \cos(2\theta_{(\tau\tau\frac{27}{2})})$ from the fitted direct beam P1 and P2 curves [223]. Similar polarization analysis performed on the $(\tau\tau\frac{15}{2})$ reflection, leading to comparable results, also indicating only contributions from the isotropic Thomson “charge” scattering. In conclusion, no clear indication for anisotropic behavior on the charge order superstructure

⁴The signal in the π' channel is very sensitive to the 2θ value of the corresponding reflection, for $2\theta = 90^\circ$ only the σ' component survives in Thomson scattering.

reflections, possibly indicating orbital order in the low temperature phase of LuFe_2O_4 , were found. However, given the measurement uncertainty it is maybe possible that there is a weak orbital contribution below the measured signal, as there is a large isotropic scattering term present. Therefore, this negative result is not fully conclusive for an orbital ordered state below T_{LT} .

7.3 Discussion and Conclusion

In this section, it was shown that a remarkably large unquenched angular magnetic moment is present in the Fe^{2+} . This orbital magnetic moment is incompatible with an orbital order scenario for both the long range magnetic ordered phases (fM and AFM) and for the paramagnetic phase. Additionally, the relationship between the spin and the charge order could be established from the shape of the XMCD spectra. Furthermore, it was shown that the charge order of Sec. 5 and the ferrimagnetic spin order of Sec. 6 are in a perfect agreement with each other, considering the local $\text{Fe}^{2+/3+}$ spin configuration determined by XMCD. This spin charge coupling also persists into the region where no 3D magnetic order is present. Most likely, it is also present above T_{CO} . At the end of this section there were indications for an orbital ordered state below T_{LT} , in the low temperature phase. In this phase an orbital ordered state could not be fully excluded.

7.4 Related publications

The following publications are related to this section:

- “Charge order in LuFe_2O_4 : an unlikely route to ferroelectricity”
J. de Groot, T. Mueller, R.A. Rosenberg, D.J. Keavney, Z. Islam, J.-W. Kim, and M. Angst
Phys. Rev. Lett. **108**, 187601 (2012).
- “Direct Observation of Charge and Orbital Order in LuFe_2O_4 ”
S.R. Bland, J. De Groot, T.A.W. Beale, U. Staub, R.A. de Souza, S.S. Dhesi, F. Yakhou, M. Angst, and P.D. Hatton
In preparation.

For a detailed declaration of own contributions to the publications see App. A.

Summary and outlook

In this work, the crystallographic and magnetic structure of the charge order-based candidate multiferroic material LuFe_2O_4 was investigated. In Sec. 4, macroscopic magnetization measurements of LuFe_2O_4 show the presence of previously unobserved antiferromagnetic (AFM), ferrimagnetic (fM) and phase separated (PS) phases. After comparing the temperature dependence of the magnetic behavior of a huge variety of samples, these could roughly be classified into three different categories. The observed differences are most likely due to tiny differences in oxygen stoichiometry. The type A samples, showing the sharpest magnetic behavior, also exhibit the strongest charge order superstructure reflections at room temperature. Additionally, the magnetic phase diagram for this type of sample could be established. Here, the metamagnetic transition between the AFM and fM phase approaches $H = 0$ for $T \rightarrow T_N$, indicating the simultaneous presence of both phases at T_N (the magnetic ordering temperature).

After identifying the best type of sample and the corresponding magnetic phase diagram, the crystallographic structure in the charge ordered phase could be solved as a monoclinic structure following the $C2/m$ symmetry. In this symmetry, previously observed strong unphysical Lu thermal anisotropies along the c_{Hex} direction could be explained by Lu distortions. For the new monoclinic structure, a totally new charge order pattern could be identified by evaluating the average Fe-O bond length with the help of the Bond Valence Sum method. Importantly, this new charge order structure resulting out of the crystallographic refinement does not contain polar bilayers, in contrast to what was generally accepted and previously proposed in different articles, casting heavy doubt on the ferroelectricity from charge ordering scenario favored for this material.

Also, the idea that a ferroelectric charge order configuration might be stabilized by an external electric field (under cooling) applied parallel to c_{Hex} was excluded by an in situ diffraction x-ray experiment under electric fields of up to up to 15 kVcm^{-1} . In

such an in situ experiment only an electric current-induced charge order melting could be observed, which can be explained by simple Joule heating from the electric current flow through the sample. Furthermore, the stability of the charge order pattern under external magnetic fields shows no influence on the crystallographic structure above T_{LT} . The structure presented here can be expected to be representative of all types of samples where $(\frac{1}{3}, \frac{1}{3}, \text{halfinteger})$ reflections are observed as main charge order ordering parameter. In particular, these structural refinement results should also be valid for the samples on which pyroelectric current measurements have been previously reported. All reported macroscopic indications of ferroelectric behavior in LuFe_2O_4 are most likely due to extrinsic effects; a clear example of an oxide material with ferroelectricity originating from charge order has yet to be identified.

With the help of the new monoclinic cell and the particular Fe distribution inside the crystal, the long-range ordered spin structures present in the magnetic phase diagram of LuFe_2O_4 (Fig. 4.10) could be solved using neutron diffraction. A central ingredient in the evolution of this complex phase diagram is the competition between the two nearly degenerate instabilities at T_N . This competition between the fully ordered AFM and fM spin alignments arises from geometrical frustration. The particular difference between the two near-degenerate spin structures is the total reversal of all the spin moments in one particular Fe bilayer. This behavior, together with the crystallographic structure, implies that the intra-bilayer correlations are more dominant than the inter-bilayer correlations. Therefore, just above T_N a random stacking of the bilayer net moment of still medium-range ordered bilayers, i.e. a 2D order, is also observed in neutron diffraction. Strong deviations from Curie-Weiss behavior (already presented in Sec. 4.2.6) up to ~ 400 K, imply that these short-range correlations are significant in a wide T range including T_{CO} and may influence the establishing of charge order, provided there is a strict spincharge coupling. This competition also strongly influences the magnetic properties in samples where the phase diagram could not be resolved, giving rise to apparently inconsistent observations in earlier studies, such as glassy freezing instead of long-range order. The complexity of the H - T phase diagram delineated in this work will hopefully guide future experiments and restrict theoretical models of near-degenerate metamagnetic phases in this material.

The strict coupling between the spin and charge orders was studied by x-ray magnetic circular dichroism, signifying still ordered Fe bilayers in the paramagnetic phase with strictly coupled charge and spin orders persisting well above T_N , from susceptibility

also likely above T_{CO} . This suggests short-range precursors at high T , with already coupled local spin and charge orders. This coupling already above T_{CO} is most likely the origin of the magnetic field control of charge structures reported in [89]. In the high field ferrimagnetic phase, an orbital magnetic moment of $\sim 0.7\mu_B/\text{f.u.}$ could be extracted from the shape of the XMCD spectra (explaining the observed saturation moment observed in magnetization measurements). This observed unquenched orbital magnetic moment excludes the possibility of long-range orbital order for the paramagnetic and both long-range ordered magnetic phases. Due to the structural transition at T_{LT} we cannot exclude long-range orbital order in this low temperature phase. Such an orbital order below T_{LT} could be consistent with the observed lattice parameter changes, but a detailed discussion is beyond the scope of the present study.

In summary, this work gives a comprehensive overview of microscopic magnetic and structural investigations of LuFe_2O_4 , including their mutual coupling. In particular, the correlation of the local atomic structure and the spatial magnetization distribution within the new monoclinic cell may contribute to a better understanding of fundamental properties such as a strong spin orbit coupling. The new charge order pattern evidenced by single crystal structure refinement exhibiting charged bilayers makes a strong ferroelectric character for this material unlikely, and the search for a “real” charge order-based multiferroic must continue.

Despite all the progress presented here in the understanding of the charge, spin and orbital order, a number of problems remain to be solved. The most obvious point is the question of a possible orbital order state present in the low temperature phase. Here, a more detailed analysis of the lattice parameters, together with a more detailed polarized synchrotron x-ray experiment, may lend additional support to an orbital ordered state. It would also be interesting to perform magnetic force microscopy (MFM) experiments in the low temperature phase in order to provide real space evidence for the magnetically phase-separated state. I hope that this thesis will guide further experimental and theoretical work on LuFe_2O_4 in particular, and on the whole $R\text{Fe}_2\text{O}_4$ system in general. Despite disproving ferroelectricity for LuFe_2O_4 , in this class of complex materials many still undiscovered phenomena need to be explored.

Acknowledgments

Here, I would like to thank the following people who supported this project over the last three years and without their support this work would be almost impossible. I thank here as many people as I can remember, but in case I miss anybody, I am very sorry.

Prof. Manuel Angst for an extremely well assistance during my whole thesis. I enjoyed our discussions in the coffee kitchen and during uncountable cigarette breaks. You were always supportive and have given me the freedom to pursue various scientific projects without objection. I would also like to thank you for the interesting beamtimes we carried out together with always very nice discussions.

Prof. Matthias Wuttig who agreed to take the second revision of this thesis.

Prof. Thomas Brückel for the opportunity to work in his institute, without his support this thesis would be impossible.

Steward Blend and **Prof. Peter Hatton** for their great support and the nice time during uncountable synchrotron experiments.

Werner Schweika, **Karin Schmalzl**, **Wouter Borghols** and **Yixi Su** for their help and scientific support at the DNS and D23 neutron scattering experiments, which helped a lot to understand the microscopic magnetic behavior in detail.

Karol Marty, **Mark Lumsden**, **Andrew Christianson**, **Steven Nagler** for their strong support on the spinstructure refinements on the data from the N5 instrument, which are an essential part of this work.

Urs Staub for the nice measurements we carried out together on the SIM beamline.

Richard Rosenberg and **David Keavney** for the assistance during the 4-ID-C beamtime and a lot of nice discussions about the XMCD results.

Jörg Stremper for his support during the P09 measurements at the Petra-III synchrotron.

Jörg Persson for his help on the single crystal growth and especially for the installation of the CO sensor.

Arlei Antunes from the LNCMI Grenoble High Magnetic Field Laboratory for his great support on the high magnetic field measurements.

Furthermore, I would like to thank all the people from the institute for scattering techniques PGI-4 and JCNS for the great time and nice support during my thesis. Here, I want to thank in particular my closest colleagues, the members of the Young Investigator Group “Complex Ordering Phenomena in Multifunctional Oxides” **Shilpa Adiga**, **Tho-**

mas Müller, Pankaj Thakuria and Hailey Williamson; I really enjoyed working in this institute.

Especially I would like to thank my **family** who always supported me and motivated me to go on. I know I always have my family to count on when things becomes rough. I would give my special thanks to **Julia** whose patient love enabled me to finish this work.

- [1] A. D. Christianson, M. D. Lumsden, M. Angst, Z. Yamani, W. Tian, R. Jin, E. A. Payzant, S. E. Nagler, B. C. Sales, and D. Mandrus, “*Three-Dimensional Magnetic Correlations in Multiferroic LuFe_2O_4* ”, Phys. Rev. Lett. **100**, 107601 (2008).
- [2] G. E. Moore, “*Cramming more components onto integrated circuits*”, Electronics **38** (1965).
- [3] K. Hisao, S. Toshitsugu, and B. Toshio, “*Observation of source-to-drain direct tunneling current in 8 nm gate electrically variable shallow junction metaloxide-semiconductor field-effect transistors*”, Appl. Phys. Lett. **76**, 3810 (2000).
- [4] G. Binasch, P. Grünberg, F. Saurenbach, and W. Zinn, “*Enhanced magnetoresistance in layered magnetic structures with antiferromagnetic interlayer exchange*”, Phys. Rev. B **39**, 4828 (1989).
- [5] M. N. Baibich, J. M. Broto, A. Fert, F. N. Van Dau, F. Petroff, P. Etienne, G. Creuzet, A. Friederich, and J. Chazelas, “*Giant Magnetoresistance of $(001)\text{Fe}/(001)\text{Cr}$ Magnetic Superlattices*”, Phys. Rev. Lett. **61**, 2472 (1988).
- [6] J. Bardeen, L. N. Cooper, and J. R. Schrieffer, “*Theory of Superconductivity*”, Phys. Rev. **108**, 1175 (1957).
- [7] H. Onnes, “*The Superconductivity of Mercury*”, Comm. Phys. Lab. Univ. Leiden **122** (1911).
- [8] Y. Joly, J. E. Lorenzo, E. Nazarenko, J.-L. Hodeau, D. Mannix, and C. Marin, “*Low-temperature structure of magnetite studied using resonant x-ray scattering*”, Phys. Rev. B **78**, 134110 (2008).
- [9] J. P. Wright, J. P. Attfield, and P. G. Radaelli, “*Charge ordered structure of magnetite Fe_3O_4 below the Verwey transition*”, Phys. Rev. B **66**, 214422 (2002).
- [10] E. Dagotto, “*Complexity in Strongly Correlated Electronic Systems*”, Science **309**, 257 (2005).
- [11] C. P. Poole, H. A. Farach, R. J. Creswick, and R. Prozorov, *Superconductivity, second edition* (Elsevier, 2007).
- [12] J. Volger, “*Further experimental investigations on some ferromagnetic oxidic compounds of manganese with perovskite structure*”, Physica **40**, 49 (1954).

- [13] A. Urushibara, Y. Moritomo, T. Arima, A. Asamitsu, G. Kido, and Y. Tokura, “*Insulator-metal transition and giant magnetoresistance in $La_{1-x}Sr_xMnO_3$* ”, Phys. Rev. B **51**, 14103 (1995).
- [14] W. Eerenstein, N. D. Mathur, and J. F. Scott, “*Multiferroic and magnetoelectric materials*”, Nature **442**, 759 (2006).
- [15] M. Fiebig, “*Revival of the magnetoelectric effect*”, Journal of Physics D: Applied Physics **38**, R123 (2005).
- [16] M. Bibes and Agnès Barthélémy, “*Multiferroics: Towards a magnetoelectric memory*”, Nature Materials **7**, 425 (2008).
- [17] L. Landau, E. Lifschitz, and L. Pitajewski, *Lehrbuch der Theoretischen Physik* (Akademie-Verlag Berlin, 1987).
- [18] M. S. Dresselhaus, G. Dresselhaus, and A. Jorio, *Group theory: application to the physics of condensed matter* (Springer-Verlag, Berlin Heidelberg, 2008).
- [19] E. Verwey and P. Haayman, “*Electronic conductivity and transition point of magnetite Fe_3O_4* ”, Physica **8**, 979 (1941).
- [20] Y. Miyamoto and M. Shindo, “*Magnetoelectric Measurement of Magnetite (Fe_3O_4) at Low Temperatures and Direct Evidence for Nonexistence of ac Mirror Plane*”, J. Phys. Soc. Jpn. **62**, 1423 (1993).
- [21] J. B. Goodenough, “*Theory of the Role of Covalence in the Perovskite-Type Manganites $[La, M(II)]MnO_3$* ”, Phys. Rev. **100**, 564 (1955).
- [22] A. Daoud-Aladine, J. Rodríguez-Carvajal, L. Pinsard-Gaudart, M. T. Fernández-Díaz, and A. Revcolevschi, “*Zener Polaron Ordering in Half-Doped Manganites*”, Phys. Rev. Lett. **89**, 097205 (2002).
- [23] J. P. Wright, J. P. Attfield, and P. G. Radaelli, “*Long Range Charge Ordering in Magnetite Below the Verwey Transition*”, Phys. Rev. Lett. **87**, 266401 (2001).
- [24] P. Karen, K. Gustafsson, and J. Lindn, “ *$EuBaFe_2O_5$: Extent of charge ordering by Mössbauer spectroscopy and high-intensity high-resolution powder diffraction*”, Journal of Solid State Chemistry **180**, 138 (2007).

- [25] S. R. Bland, M. Angst, S. Adiga, V. Scagnoli, R. D. Johnson, J. Herrero-Martn, and P. D. Hatton, “*Symmetry and charge order in Fe_2OBO_3 studied through polarized resonant x-ray diffraction*”, Phys. Rev. B **82**, 115110 (2010).
- [26] M. Angst, P. Khalifah, R. P. Hermann, H. J. Xiang, M.-H. Whangbo, V. Varadarajan, J. W. Brill, B. C. Sales, and D. Mandrus, “*Charge Order Superstructure with Integer Iron Valence in Fe_2OBO_3* ”, Phys. Rev. Lett. **99**, 086403 (2007).
- [27] N. Ikeda, H. Ohsumi, K. Ohwada, K. Ishii, T. Inami, K. Kakurai, Y. Murakam, K. Yoshii, S. Mori, Y. Horibe, et al., “*Ferroelectricity from iron valence ordering in the charge-frustrated system LuFe_2O_4* ”, Nature **436**, 1136 (2005).
- [28] X. S. Xu, M. Angst, T. V. Brinzari, R. P. Hermann, J. L. Musfeldt, A. D. Christianson, D. Mandrus, B. C. Sales, S. McGill, J.-W. Kim, et al., “*Charge Order, Dynamics, and Magnetostructural Transition in Multiferroic LuFe_2O_4* ”, Phys. Rev. Lett. **101**, 227602 (2008).
- [29] B.-G. Park, Y.-H. Jeong, J.-H. Park, J. H. Song, J.-Y. Kim, H.-J. Noh, H.-J. Lin, and C. T. Chen, “*Physical properties and electronic evolution of $\text{Sr}_2\text{FeMo}_{1-x}\text{Nb}_x\text{O}_6$ ($0 \leq x \leq 1$)*”, Phys. Rev. B **79**, 035105 (2009).
- [30] M. Benfatto, J. A. Solera, J. G. Ruiz, and J. Chaboy, “*Double-channel excitation in the X-ray absorption spectrum of Fe^{3+} water solutions*”, Chemical Physics **282**, 441 (2002).
- [31] A. M. Mulders, S. M. Lawrence, U. Staub, M. Garcia-Fernandez, V. Scagnoli, C. Mazzoli, E. Pomjakushina, K. Conder, and Y. Wang, “*Direct Observation of Charge Order and an Orbital Glass State in Multiferroic LuFe_2O_4* ”, Phys. Rev. Lett. **103**, 077602 (2009).
- [32] N. E. Brese and M. O’Keeffe, “*Bond-Valence Parameters for Solids*”, Acta Cryst. **B47**, 192 (1991).
- [33] I. D. Brown, *The Chemical Bond in Inorganic Chemistry: The Bond Valence Model*. (Oxford University Press, 2002).
- [34] Y. Tokura and N. Nagaosa, “*Orbital Physics in transition-Metal Oxides*”, Science **288**, 462 (2000).
- [35] J. J. Zuckerman, “*Crystal field splitting diagrams*”, Journal of Chemical Education **42**, 315 (1965).

- [36] K.-T. Ko, H.-J. Noh, J.-Y. Kim, B.-G. Park, J.-H. Park, A. Tanaka, S. B. Kim, C. L. Zhang, and S.-W. Cheong, “*Electronic Origin of Giant Magnetic Anisotropy in Multiferroic LuFe_2O_4* ”, Phys. Rev. Lett. **103**, 207202 (2009).
- [37] R. J. Goff and J. P. Attfield, “*Charge ordering in half-doped manganites*”, Phys. Rev. B **70**, 140404 (2004).
- [38] Y. Murakami, J. P. Hill, D. Gibbs, M. Blume, I. Koyama, M. Tanaka, H. Kawata, T. Arima, Y. Tokura, K. Hirota, et al., “*Resonant X-Ray Scattering from Orbital Ordering in LaMnO_3* ”, Phys. Rev. Lett. **81**, 582 (1998).
- [39] J. Kanamori, “*Crystal Distortion in Magnetic Compounds*”, J. Appl. Phys. **31**, S14 (1960).
- [40] E. Pavarini and E. Koch, “*Origin of Jahn-Teller Distortion and Orbital Order in LaMnO_3* ”, Phys. Rev. Lett. **104**, 086402 (2010).
- [41] A. J. Williams and J. P. Attfield, “*Ferro-orbital order in the charge- and cation-ordered manganite YBaMn_2O_6* ”, Phys. Rev. B **72**, 024436 (2005).
- [42] H. A. Dürr, G. Y. Guo, G. van der Laan, J. Lee, G. Lauhoff, and J. A. C. Bland, “*Element-Specific Magnetic Anisotropy Determined by Transverse Magnetic Circular X-ray Dichroism*”, Science **277**, 213 (1997).
- [43] M. Darby and E. Isaac, “*Magnetocrystalline anisotropy of ferro- and ferrimagnetics*”, Magnetism, IEEE Transactions on **10**, 259 (1974).
- [44] K. Kuepper, M. Raekers, C. Taubitz, M. Prinz, C. Derks, M. Neumann, A. V. Postnikov, F. M. F. de Groot, C. Piamonteze, D. Prabhakaran, et al., “*Charge order, enhanced orbital moment, and absence of magnetic frustration in layered multiferroic LuFe_2O_4* ”, Phys. Rev. B **80**, 220409 (2009).
- [45] V. Petříček, J. Fuksa, and M. Dušek, “*Magnetic space and superspace groups, representation analysis: competing or friendly concepts?*”, Acta Cryst. **A66**, 649 (2010).
- [46] E. F. Bertaut, “*Magnetic structure analysis and group theory*”, Journal de Physique Colloque **C1**, 462 (1971).
- [47] E. F. Bertaut, “*Representation analysis of magnetic structures*”, Acta Cryst. **A24**, 217 (1968).

- [48] J. S. Gardner, B. D. Gaulin, S.-H. Lee, C. Broholm, N. P. Raju, and J. E. Greedan, “*Glassy Statics and Dynamics in the Chemically Ordered Pyrochlore Antiferromagnet $Y_2Mo_2O_7$* ”, Phys. Rev. Lett. **83**, 211 (1999).
- [49] M. J. Harris, S. T. Bramwell, D. F. McMorrow, T. Zeiske, and K. W. Godfrey, “*Geometrical Frustration in the Ferromagnetic Pyrochlore $Ho_2Ti_2O_7$* ”, Phys. Rev. Lett. **79**, 2554 (1997).
- [50] C. Schröder, H. Nojiri, J. Schnack, P. Hage, M. Luban, and P. Kögerler, “*Competing Spin Phases in Geometrically Frustrated Magnetic Molecules*”, Phys. Rev. Lett. **94**, 017205 (2005).
- [51] G. Lawes, M. Kenzelmann, N. Rogado, K. H. Kim, G. A. Jorge, R. J. Cava, A. Aharony, O. Entin-Wohlman, A. B. Harris, T. Yildirim, et al., “*Competing Magnetic Phases on a Kagomé Staircase*”, Phys. Rev. Lett. **93**, 247201 (2004).
- [52] Y. Yamada, S. Nohdo, and N. Ikeda, “*Incommensurate Charge Ordering in Charge-Frustrated $LuFe_2O_4$ System*”, J. Phys. Soc. Jpn. **66**, 3733 (1997).
- [53] W. F. Brown, R. M. Hornreich, and S. Shtrikman, “*Upper Bound on the Magnetoelectric Susceptibility*”, Phys. Rev. **168**, 574 (1968).
- [54] I. E. Dzyaloshinskii, “*On the magneto-electrical effects in antiferromagnets*”, Sov. Phys. JETP **10**, 628629 (1959).
- [55] N. Hur, S. Park, P. A. Sharma, J. S. Ahn, S. Guha, and S.-W. Cheong, “*Electric polarization reversal and memory in a multiferroic material induced by magnetic fields*”, Nature **429**, 392 (2004).
- [56] N. A. Spaldin and M. Fiebig, “*The Renaissance of Magnetoelectric Multiferroics*”, Science **309**, 391 (2005).
- [57] Z. J. Huang, Y. Cao, Y. Y. Sun, Y. Y. Xue, and C. W. Chu, “*Coupling between the ferroelectric and antiferromagnetic orders in $YMnO_3$* ”, Phys. Rev. B **56**, 2623 (1997).
- [58] M. Kenzelmann, A. B. Harris, S. Jonas, C. Broholm, J. Schefer, S. B. Kim, C. L. Zhang, S.-W. Cheong, O. P. Vajk, and J. W. Lynn, “*Magnetic Inversion Symmetry Breaking and Ferroelectricity in $TbMnO_3$* ”, Phys. Rev. Lett. **95**, 087206 (2005).

- [59] K. Aizu, “*Possible Species of Ferromagnetic, Ferroelectric, and Ferroelastic Crystals*”, Phys. Rev. B **2**, 754 (1970).
- [60] N. A. Hill, “*Why Are There so Few Magnetic Ferroelectrics?*”, J. Phys. Chem. B **104**, 6694 (2000).
- [61] P. Ravindran, R. Vidya, A. Kjekshus, H. Fjellvåg, and O. Eriksson, “*Theoretical investigation of magnetoelectric behavior in BiFeO₃*”, Phys. Rev. B **74**, 224412 (2006).
- [62] H. Béa, B. Dupé, S. Fusil, R. Mattana, E. Jacquet, B. Warot-Fonrose, F. Wilhelm, A. Rogalev, S. Petit, V. Cros, et al., “*Evidence for Room-Temperature Multiferroicity in a Compound with a Giant Axial Ratio*”, Phys. Rev. Lett. **102**, 217603 (2009).
- [63] T. Kimura, T. Goto, H. Shintani, K. Ishizaka, T. Arima, and Y. Tokura, “*Magnetic control of ferroelectric polarization*”, Nature **426**, 55 (2003).
- [64] M. Mostovoy, “*Ferroelectricity in Spiral Magnets*”, Phys. Rev. Lett. **96**, 067601 (2006).
- [65] van Aken, T. T. Palstra, A. Filippetti, and N. A. Spaldin, “*The origin of ferroelectricity in magnetoelectric YMnO₃*”, Nature Materials **3**, 164 (2004).
- [66] C. J. Fennie and K. M. Rabe, “*Ferroelectric transition in YMnO₃ from first principles*”, Phys. Rev. B **72**, 100103 (2005).
- [67] C. Ederer and N. A. Spaldin, “*Electric-field-switchable magnets: The case of BaNiF₄*”, Phys. Rev. B **74**, 020401 (2006).
- [68] J. van den Brink and D. I. Khomskii, “*Multiferroicity due to charge ordering*”, Journal of Physics: Condensed Matter **20**, 434217 (2008).
- [69] Y. J. Choi, H. T. Yi, S. Lee, Q. Huang, V. Kiryukhin, and S.-W. Cheong, “*Ferroelectricity in an Ising Chain Magnet*”, Phys. Rev. Lett. **100**, 047601 (2008).
- [70] K. Wang, J.-M. Liu, and Z. Ren, “*Multiferroicity: the coupling between magnetic and polarization orders*”, Adv. Phys. **58**, 321448 (2009).
- [71] R. E. Cohen, “*Origin of ferroelectricity in perovskite oxides*”, Nature **358**, 136 (1992).

- [72] N. Kimizuka, A. Takenaka, Y. Sasada, and T. Katsura, “*A series of new compounds $A^{3+}Fe_2O_4$ ($A = Ho, Er, Tm, Yb, \text{ and } Lu$)*”, Sol. Sta. Commun. **15**, 1321 (1974).
- [73] M. Tanaka, K. Siratori, and N. Kimizuka, “*Mössbauer Study of RFe_2O_4* ”, J. Phys. Soc. Jpn. **53**, 760 (1984).
- [74] J. Iida, S. Kakugawa, G. Kido, Y. Nakagawa, S. Takekawa, and N. Kimizuka, “*High field magnetization of single crystals YFe_2O_4 , $YbFe_2O_4$ and $LuFe_2O_4$* ”, Physica B: Condensed Matter **155**, 307 (1989).
- [75] M. Tanaka, “*Mössbauer study of RFe_2O_4 family: A two-dimensional antiferromagnet on a triangular lattice*”, Nuclear Instruments and Methods in Physics Research Section B: Beam Interactions with Materials and Atoms **76**, 149 (1993).
- [76] T. Sekine and T. Katsura, “*Phase Equilibria in the System $Fe-Fe_2O_3-Lu_2O_3$ at $1200^\circ C$* ”, Jour. of Sol. State Chemistry **17**, 49 (1976).
- [77] M. Isobe, N. Kimizuka, J. Iida, and S. Takekawa, “*Structures of $LuFeCoO_4$ and $LuFe_2O_4$* ”, Acta Cryst. **C46**, 1917 (1990).
- [78] J. Iida, S. Takekawa, and N. Kimizuka, “*Single crystal growth of $LuFe_2O_4$, $LuFeCoO_4$ and $YbFeMgO_4$ by the floating zone method*”, Journal of Crystal Growth **102**, 398 (1990).
- [79] J. Iida, Y. Nakagawa, and N. Kimizuka, “*Field Heating Effect Anomalous Thermomagnetization Curves Observed in Hexagonal $LuFe_2O_4$* ”, J. Phys. Soc. Jpn. **55**, 1434 (1986).
- [80] J. Iida, Y. Nakagawa, S. Takekawa, and N. Kimizuka, “*High Field Magnetization of Single Crystal $LuFe_2O_4$* ”, J. Phys. Soc. Jpn. **56**, 3746 (1987).
- [81] J. Iida, M. Tanaka, Y. Nakagawa, S. Funahashi, N. Kimizuka, and S. Takekawa, “*Magnetization and Spin Correlation of Two-Dimensional Triangular Antiferromagnet $LuFe_2O_4$* ”, J. Phys. Soc. Jpn. **62**, 1723 (1993).
- [82] N. Ikeda, Y. Yamada, S. Nohdo, T. Inami, and S. Katano, “*Incommensurate charge ordering in mixed valence system $LuFe_2O_4$* ”, Physica B: Condensed Matter **241-243**, 820 (1997).
- [83] N. Ikeda, “*Ferroelectric properties of triangular charge-frustrated $LuFe_2O_4$* ”, Journal of Physics: Condensed Matter **20**, 434218 (2008).

- [84] Y. Yamada, K. Kitsuda, S. Nohdo, and N. Ikeda, “*Charge and spin ordering process in the mixed-valence system LuFe_2O_4 : Charge ordering*”, Phys. Rev. B. **62**, 12167 (2000).
- [85] M. Angst, R. P. Hermann, A. D. Christianson, M. D. Lumsden, C. Lee, M.-H. Whangbo, J.-W. Kim, P. J. Ryan, S. E. Nagler, W. Tian, et al., “*Charge Order in LuFe_2O_4 : Antiferroelectric Ground State and Coupling to Magnetism*”, Phys. Rev. Lett. **101**, 227601 (2008).
- [86] N. Ikeda, K. Kohn, N. Myouga, E. Takahashi, H. Kitôh, and S. Takekawa, “*Charge Frustration and Dielectric Dispersion in LuFe_2O_4* ”, J. Phys. Soc. Jpn. **69**, 1526 (2000).
- [87] M. A. Subramanian, T. He, J. Chen, N. S. Rogado, T. G. Calvarese, and A. W. Sleight, “*Giant Room Temperature Magnetodielectric Response in the Electronic Ferroelectric LuFe_2O_4* ”, Advanced Materials **18**, 1737 (2006).
- [88] M. Phan, N. Frey, M. Angst, J. de Groot, B. Sales, D. Mandrus, and H. Srikanth, “*Complex magnetic phases in LuFe_2O_4* ”, Sol. Sta. Commun. **150**, 341 (2010).
- [89] J. Wen, G. Xu, G. Gu, and S. M. Shapiro, “*Magnetic-field control of charge structures in the magnetically disordered phase of multiferroic LuFe_2O_4* ”, Phys. Rev. B **80**, 020403 (2009).
- [90] H. J. Xiang, E. J. Kan, S.-H. Wei, M.-H. Whangbo, and J. Yang, “*Origin of the Ising ferrimagnetism and spin-charge coupling in LuFe_2O_4* ”, Phys. Rev. B **80**, 132408 (2009).
- [91] J. Wen, G. Xu, G. Gu, and S. M. Shapiro, “*Robust charge and magnetic orders under electric field and current in multiferroic LuFe_2O_4* ”, Phys. Rev. B **81**, 144121 (2010).
- [92] W. Wu, V. Kiryukhin, H.-J. Noh, K.-T. Ko, J.-H. Park, W. Ratcliff, P. A. Sharma, N. Harrison, Y. J. Choi, Y. Horibe, et al., “*Formation of Pancakelike Ising Domains and Giant Magnetic Coercivity in Ferrimagnetic LuFe_2O_4* ”, Phys. Rev. Lett. **101**, 137203 (2008).
- [93] X. S. Xu, J. de Groot, Q.-C. Sun, B. C. Sales, D. Mandrus, M. Angst, A. P. Litvinchuk, and J. L. Musfeldt, “*Lattice dynamical probe of charge order and antipolar bilayer stacking in LuFe_2O_4* ”, Phys. Rev. B **82**, 014304 (2010).

- [94] S. Park, Y. Horibe, Y. J. Choi, C. L. Zhang, S.-W. Cheong, and W. Wu, “*Pancake-like Ising domains and charge-ordered superlattice domains in LuFe_2O_4* ”, Phys. Rev. B **79**, 180401 (2009).
- [95] A. Nagano, M. Naka, J. Nasu, and S. Ishihara, “*Electric Polarization, Magnetoelectric Effect, and Orbital State of a Layered Iron Oxide with Frustrated Geometry*”, Phys. Rev. Lett. **99**, 217202 (2007).
- [96] M. Naka, A. Nagano, and S. Ishihara, “*Magnetodielectric phenomena in a charge- and spin-frustrated system of layered iron oxide*”, Phys. Rev. B **77**, 224441 (2008).
- [97] S. R. Bland, Ph.D. thesis, Durham University (2010).
- [98] <http://www.lot-oriel.com/files/downloads/qd/en/ppms.pdf> (2012).
- [99] <http://www.qdusa.com/products/mpms.html> (2012).
- [100] W. Buckel and R. Kleiner, *Supraleitung- Grundlagen und Anwendung* (Wiley-VCH, 2004).
- [101] http://www.lot-oriel.com/files/downloads/qd/eu/PPMS_Magnetometry_eu.pdf (2012).
- [102] A. Wilson, ed., *International Tables for Crystallography, Volume C* (Kluwer Academic Publishers, Dordrecht, 1992).
- [103] B. Henke, E. Gullikson, and J. Davis, “*X-ray interactions: photoabsorption, scattering, transmission, and reflection at $E=50\text{-}30000\text{ eV}$, $Z=1\text{-}92$* ”, Atomic Data and Nuclear Data Tables **54**, 181 (1993).
- [104] L. Kissel and R. H. Pratt, “*Corrections to tabulated anomalous-scattering factors*”, Acta Cryst. **A46**, 170 (1990).
- [105] D. Schaupp, M. Schumacher, F. Smend, P. Rullhusen, and J. H. Hubbell, “*Small-Angle Rayleigh Scattering of Photons at High Energies: Tabulations of Relativistic HFS Modified Atomic Form Factors*”, J. Phys. Chem. Ref. Data **12**, 467 (1983).
- [106] M. Ben-Nun, T. J. Martinez, P. M. Weber, and K. R. Wilson, “*Direct imaging of excited electronic states using diffraction techniques: theoretical considerations*”, Chemical Physics Letters **262**, 405 (1996).

- [107] P. Mueller, R. Herbst-Irmer, A. L. Spek, T. R. Schneider, and M. R. Sawaya, *Crystal Structure Refinement. A Crystallographers's Guide to SHELXL* (Oxford Science Publications, 2006).
- [108] K. N. Trueblood, H.-B. Bürgi, H. Burzlaff, J. D. Dunitz, C. M. Gramaccioli, H. H. Schulz, U. Shmueli, and S. C. Abrahams, "Atomic Displacement Parameter Nomenclature. Report of a Subcommittee on Atomic Displacement Parameter Nomenclature", *Acta Cryst.* **A52**, 770 (1996).
- [109] R. W. Grosse-Kunstleve and P. D. Adams, "On the handling of atomic anisotropic displacement parameters", *Journal of Applied Crystallography* **35**, 477 (2002).
- [110] G. M. Sheldrick, "A short history of SHELX", *Acta Cryst.* **A64**, 112 (2008).
- [111] A. J. C. Wilson, "Statistical bias in least-squares refinement", *Acta Cryst.* **A32**, 994 (1976).
- [112] Q. Huang, X. Wu, Q. Wang, T. Sheng, and J. Lu, "Heterometallic Polymeric Cluster Compounds Derived from Tetrathiotungstate and Silver(I): Syntheses and Crystal Structures of $[AgWS_4]_n [NH_4]_n$ and $[W_4Ag_5S_{16}]_n [M(DMF)_8]_n$ ($M = Nd$ and La)", *Angewandte Chemie International Edition in English* **35**, 868 (1996).
- [113] *manual_ShelxTL.pdf* (2012).
- [114] <http://www.chem.agilent.com/Library/brochures/SuperNova> (2012).
- [115] <http://www.chem.agilent.com/en-US/Products/Software/x-ray/crysalis/Pages/default.aspx> (2012).
- [116] R. C. Clark and J. S. Reid, "The analytical calculation of absorption in multifaceted crystals", *Acta. Cryst.* **A51**, 887897 (1995).
- [117] L. J. Farrugia, "WinGX suite for small-molecule single-crystal crystallography", *J. Appl. Cryst.* **32**, 837 (1999).
- [118] M. Blume, "Magnetic scattering of x rays (invited)", *J. Appl. Phys.* **57**, 3615 (1985).
- [119] J. A. Nielson and D. McMorrow, *Elements of modern X-ray physics* (John Wiley & Sons, New York, 2001).
- [120] R. D. L. Kronig, "On the Theory of dispersion of X-rays", *J. Opt. Soc. Am.* **12**, 547 (1926).

- [121] D. Moncton, D. Gibbs, and J. Bohr, “*Magnetic X-ray scattering with synchrotron radiation*”, Nuclear Instruments and Methods in Physics Research Section A: Accelerators, Spectrometers, Detectors and Associated Equipment **246**, 839 (1986).
- [122] M. Blume and D. Gibbs, “*Polarization dependence of magnetic x-ray scattering*”, Phys. Rev. B **37**, 1779 (1988).
- [123] D. Mannix, D. F. McMorrow, R. A. Ewings, A. T. Boothroyd, D. Prabhakaran, Y. Joly, B. Janousova, C. Mazzoli, L. Paolasini, and S. B. Wilkins, “*X-ray scattering study of the order parameters in multiferroic TbMnO₃*”, Phys. Rev. B **76**, 184420 (2007).
- [124] J. P. Hannon, G. T. Trammell, M. Blume, and D. Gibbs, “*X-Ray Resonance Exchange Scattering*”, Phys. Rev. Lett. **61**, 1245 (1988).
- [125] S. B. Wilkins, P. D. Hatton, M. D. Roper, D. Prabhakaran, and A. T. Boothroyd, “*Soft X-Ray Resonant Magnetic Diffraction*”, Phys. Rev. Lett. **90**, 187201 (2003).
- [126] W. S. Lovesey and S. P. Collins, *X-ray scattering and absorption by magnetic materials* (Oxford : Clarendon Pr., 1996).
- [127] J. P. Hill and D. F. McMorrow, “*Resonant Exchange Scattering: Polarization Dependence and Correlation Function*”, Acta Cryst. **A52**, 236 (1996).
- [128] C. Mazzoli, S. B. Wilkins, S. Di Matteo, B. Detlefs, C. Detlefs, V. Scagnoli, L. Paolasini, and P. Ghigna, “*Disentangling multipole resonances through a full x-ray polarization analysis*”, Phys. Rev. B **76**, 195118 (2007).
- [129] E. Hecht, *Optics* (Addison-Wesley, 2002).
- [130] U. Staub, V. Scagnoli, Y. Bodenthin, M. Garca-Fernndez, R. Wetter, A. M. Mulders, H. Grimmer, and M. Horisberger, “*Polarization analysis in soft X-ray diffraction to study magnetic and orbital ordering*”, J. Synchrotron Rad. **15**, 469 (2008).
- [131] J.-M. Mariot and C. Brouder, “*Spectroscopy and Magnetism: An Introduction*”, Spectroscopy and Magnetism **565**, 24 (2001).
- [132] C. Kapusta, P. Fischer, and G. Schtz, “*Magnetic X-ray absorption spectroscopy*”, Journal of Alloys and Compounds **286**, 37 (1999).

- [133] C. T. Chen, Y. U. Idzerda, H.-J. Lin, N. V. Smith, G. Meigs, E. Chaban, G. H. Ho, E. Pellegrin, and F. Sette, “*Experimental Confirmation of the X-Ray Magnetic Circular Dichroism Sum Rules for Iron and Cobalt*”, Phys. Rev. Lett. **75**, 152 (1995).
- [134] B. T. Thole, P. Carra, F. Sette, and G. van der Laan, “*X-ray circular dichroism as a probe of orbital magnetization*”, Phys. Rev. Lett. **68**, 1943 (1992).
- [135] R. Wu, D. Wang, and A. J. Freeman, “*First principles investigation of the validity and range of applicability of the x-ray magnetic circular dichroism sum rule*”, Phys. Rev. Lett. **71**, 3581 (1993).
- [136] R. Wu, D. Wang, and A. J. Freeman, “*Validity and the applicability of magnetic-circular-dichroism sum rules for transition metals (invited)*”, J. Appl. Phys. **75**, 5802 (1994).
- [137] NIST, “*Special Feature section of neutron scattering lengths and cross sections of the elements and their isotopes*”, Neutron News **3**, 29 (1992).
- [138] P. J. Brown, “*Magnetic form factors*”, International tables for crystallography vol. C C, 391 (1990).
- [139] R. Celotta and J. Levine, *Methods of experimental physics: Neutron scattering, Volume 23, Part 3* (Academic Press, INC:, 1987).
- [140] M. Blume, “*Polarization Effects in the Magnetic Elastic Scattering of Slow Neutrons*”, Phys. Rev. **130**, 1670 (1963).
- [141] M. Blume, “*Polarization Effects in Slow Neutron Scattering II. Spin-Orbit Scattering and Interference*”, Phys. Rev. **133**, A1366 (1964).
- [142] S. Maleev, V. Baryakhtar, and R. Suris, “*The Scattering of Slow Neutrons by Complex Magnetic Structures*”, Soviet Phys.-Solid State (English Transl.) **4**, 25332539 (1963).
- [143] W. Schweika, “*XYZ-polarisation analysis of diffuse magnetic neutron scattering from single crystals*”, Journal of Physics: Conference Series **211**, 012026 (2010).
- [144] N. Kimizuka, A. Takenaka, Y. Sasada, and T. Katsura, “*New Compounds $\text{Yb}_2\text{Fe}_3\text{O}_7$ and $\text{Lu}_2\text{Fe}_3\text{O}_7$* ”, Sol. Sta. Commun. **15**, 1199 (1974).

- [145] S. Patankar, S. K. Pandey, V. R. Reddy, A. Gupta, A. Banerjee, and P. Chaddah, “*Tuning the magnetic properties of the multiferroic LuFe_2O_4 by moderate thermal treatment*”, EPL (Europhysics Letters) **90**, 57007 (2010).
- [146] M. V. Kumara, K. Kuribayashi, and K. Kitazono, “*Formation of LuFe_2O_4 phase from an undercooled LuFeO_3 melt in reduced oxygen partial pressure*”, J. Mater. Res. **23**, 2996 (2008).
- [147] F. Wang, J. Kim, Y.-J. Kim, and G. D. Gu, “*Spin-glass behavior in $\text{LuFe}_2\text{O}_{4+\delta}$* ”, Phys. Rev. B **80**, 024419 (2009).
- [148] J. de Groot, K. Marty, M. D. Lumsden, A. D. Christianson, S. E. Nagler, S. Adiga, W. J. H. Borghols, K. Schmalzl, Z. Yamani, S. R. Bland, et al., “*Competing Ferri- and Antiferromagnetic Phases in Geometrically Frustrated LuFe_2O_4* ”, Phys. Rev. Lett. **108**, 037206 (2012).
- [149] A. B. Harris and T. Yildirim, “*Charge and spin ordering in the mixed-valence compound LuFe_2O_4* ”, Phys. Rev. B **81**, 134417 (2010).
- [150] T. Sugihara, K. Siratori, I. Shindo, and T. Katsura, “*Parasitic Ferrimagnetism of YFe_2O_4* ”, J. Phys. Soc. Jpn. **45**, 1191 (1978).
- [151] M. Inazumi, Y. Nakagawa, M. Tanaka, N. Kimizuka, and K. Siratori, “*Magnetizations and Mössbauer Spectra of $\text{YFe}_2\text{O}_{4-x}$* ”, J. Phys. Soc. Jpn. **50**, 438 (1981).
- [152] Y. Nakagawa, M. Inazumi, N. Kimizuka, and K. Siratori, “*Low Temperature Phase Transitions and Magnetic Properties of YFe_2O_4* ”, J. Phys. Soc. Jpn. **47**, 1369 (1979).
- [153] J. Iida, M. Tana, H. Kito, and J. Akimitsu, “*Successive Phase Transitions in Nearly Stoichiometric ErFe_2O_4* ”, J. Phys. Soc. Jpn. **45**, 1191 (1990).
- [154] J. Kim, S. B. Kim, C. U. Jung, and B. W. Lee, “*Magnetic Anisotropy in LuFe_2O_4* ”, IEEE Transactions on Magnetism **45**, 2608 (2009).
- [155] D. S. F. Viana, R. A. M. Gotardo, L. F. Cótica, I. A. Santos, M. Olzon-Dionysio, S. D. Souza, D. Garcia, J. A. Eiras, and A. A. Coelho, “*Ferroic investigations in LuFe_2O_4 multiferroic ceramics*”, J. Appl. Phys. **110**, 034108 (2011).

- [156] S. Taran, C. C. Chou, J. L. Her, C. P. Sun, C. C. Lin, C. L. Chan, C. L. Huang, and H. D. Yang, “*Study of magnetic dynamics of LuFe_2O_4* ”, Journal of Physics: Conference Series **150**, 042205 (2009).
- [157] T. Matsumoto, N. Môri, J. Iida, M. Tanaka, and K. Siratori, “*Magnetic Properties of the Two Dimensional Antiferromagnets RFe_2O_4 ($\text{R}=\text{Y}, \text{Er}$) at High Pressure*”, J. Phys. Soc. Jpn. **61**, 2916 (1992).
- [158] D. Niermann, F. Waschkowski, J. de Groot, M. Angst, and J. Hemberger, “*Dielectric properties of charge ordered LuFe_2O_4 revisited: The apparent influence of contacts*”, Phys. Rev. Lett. **109**, 016405 (2012).
- [159] K. Sengupta and E. V. Sampathkumaran, “*Field-induced first-order magnetic phase transition in an intermetallic compound Nd_7Rh_3 : Evidence for kinetic hindrance, phase coexistence, and percolative electrical conduction*”, Phys. Rev. B **73**, 020406 (2006).
- [160] A. M. Mulders, M. Bartkowiak, J. R. Hester, E. Pomjakushina, and K. Conder, “*Ferroelectric charge order stabilized by antiferromagnetism in multiferroic LuFe_2O_4* ”, Phys. Rev. B **84**, 140403 (2011).
- [161] S. Nakamura, H. Kitô, and M. Tanaka, “*An approach to specify the spin configuration in the RFe_2O_4 ($\text{R}=\text{Y}, \text{Ho}, \text{Er}, \text{Tm}, \text{Yb}, \text{and Lu}$) family: ^{57}Fe Mössbauer study on a single crystal LuFe_2O_4* ”, Journal of Alloys and Compounds **275-277**, 574 (1998).
- [162] J. A. Mydosh, *Spin Glasses: An Experimental Introduction* (Taylor Francis, 1993).
- [163] D. N. H. Nam, R. Mathieu, P. Nordblad, N. V. Khiem, and N. X. Phuc, “*Spin-glass dynamics of $\text{La}_{0.95}\text{Sr}_{0.05}\text{CoO}_3$* ”, Phys. Rev. B **62**, 8989 (2000).
- [164] M. Uehara, S. Mori, C. H. Chen, and S.-W. Cheong, “*Percolative phase separation underlies colossal magnetoresistance in mixed-valent manganites*”, Nature **399**, 560 (1999).
- [165] K. Kumar, A. K. Pramanik, A. Banerjee, P. Chaddah, S. B. Roy, S. Park, C. L. Zhang, and S.-W. Cheong, “*Relating supercooling and glass-like arrest of kinetics for phase separated systems: Doped CeFe_2 and $(\text{La}, \text{Pr}, \text{Ca}) \text{MnO}_3$* ”, Phys. Rev. B **73**, 184435 (2006).

- [166] M. K. Chattopadhyay, S. B. Roy, and P. Chaddah, “*Kinetic arrest of the first-order ferromagnetic-to-antiferromagnetic transition in $\text{Ce}(\text{Fe}_{0.96}\text{Ru}_{0.04})_2$: Formation of a magnetic glass*”, Phys. Rev. B **72**, 180401 (2005).
- [167] J. D. Moore, G. K. Perkins, K. Morrison, L. Ghivelder, M. K. Chattopadhyay, S. B. Roy, P. Chaddah, K. A. G. Jr, V. K. Pecharsky, and L. F. Cohen, “*Local probing of arrested kinetics in Gd_5Ge_4* ”, Journal of Physics: Condensed Matter **20**, 465212 (2008).
- [168] P. Kushwaha, R. Rawat, and P. Chaddah, “*Metastability in the ferrimagnetic - antiferromagnetic phase transition in Cosubstituted Mn_2Sb* ”, Journal of Physics: Condensed Matter **20**, 022204 (2008).
- [169] D. X. Li, S. Nimori, Y. Shiokawa, Y. Haga, E. Yamamoto, and Y. Onuki, “*Ferromagnetic cluster glass behavior in U_2IrSi_3* ”, Phys. Rev. B **68**, 172405 (2003).
- [170] H. Akamatsu, S. Oku, K. Fujita, S. Murai, and K. Tanaka, “*Magnetic properties of mixed-valence iron phosphate glasses*”, Phys. Rev. B **80**, 134408 (2009).
- [171] H.-J. Noh, H. Sung, J. Jeong, J. Jeong, S. B. Kim, J.-Y. Kim, J. Y. Kim, and B. K. Cho, “*Effect of structural distortion on ferrimagnetic order in $\text{Lu}_{1-x}\text{L}_x\text{Fe}_2\text{O}_4$ ($\text{L}=\text{Y}$ and Er ; $x = 0.0, 0.1$, and 0.5)*”, Phys. Rev. B **82**, 024423 (2010).
- [172] J. de Groot, T. Mueller, R. Rosenberg, D. Keavney, Z. Islam, J.-W. Kim, and M. Angst, “*Charge order in LuFe_2O_4 : an unlikely route to ferroelectricity*”, Phys. Rev. Lett. **108**, 187601 (2012).
- [173] H. J. Xiang and M.-H. Whangbo, “*Charge Order and the Origin of Giant Magnetocapacitance in LuFe_2O_4* ”, Phys. Rev. Lett. **98**, 246403 (2007).
- [174] S. Li, S. Luo, R. Fu, B. Jin, K. Wang, J.-M. Liu, J. Ding, and X. Li, “*Terahertz spectroscopy of central and soft phonon modes in LuFe_2O_4* ”, Applied Physics A: Materials Science & Processing **96**, 893 (2009).
- [175] A. J. Hearmon, D. Prabhakaran, H. Nowell, F. Fabrizi, M. J. Gutmann, and P. G. Radaelli, “*Helical scattering signatures of strain and electronic textures in YbFe_2O_4 from three-dimensional reciprocal-space imaging*”, Phys. Rev. B **85**, 014115 (2012).
- [176] Y. Zhang, H. X. Yang, C. Ma, H. F. Tian, and J. Q. Li, “*Charge-Stripe Order in the Electronic Ferroelectric LuFe_2O_4* ”, Phys. Rev. Lett. **98**, 247602 (2007).

- [177] Y. Zhang, H. X. Yang, Y. Q. Guo, C. Ma, H. F. Tian, J. L. Luo, and J. Q. Li, “*Structure, charge ordering and physical properties of LuFe_2O_4* ”, Phys. Rev. B **76**, 184105 (2007).
- [178] A. C. Thompson and D. Vaughan, eds., *X-ray Data Booklet* (Lawrence Berkeley National Laboratory, University of California, 2001), 2nd ed.
- [179] H. Yang, H. Tian, Y. Zhang, Y. Qin, L. Zeng, C. Ma, H. Shi, and J. Lu, “*Phase separation and ferroelectric ordering in charge-frustrated $\text{LuFe}_2\text{O}_{4-\delta}$* ”, Sol. Sta. Commun. **150**, 1467 (2010).
- [180] E. Kroumova, J. M. Perez-Mato, and M. I. Aroyo, “*WYCKSPLIT: a computer program for determination of the relations of Wyckoff positions for a group-subgroup pair*”, J. Appl. Cryst. **31**, 646 (1998).
- [181] M. I. Aroyo, J. M. Perez-Mato, C. Capillas, E. Kroumova, S. Ivantchev, G. Madariaga, A. Kirov, and H. Wondratschek, “*Bilbao Crystallographic Server: I. Databases and crystallographic computing programs*”, Zeitschrift für Kristallographie **221**, 15 (2006).
- [182] H. J. Kim, C. D. Malliakas, A. T. Tomić, S. H. Tessmer, M. G. Kanatzidis, and S. J. L. Billinge, “*Local Atomic Structure and Discommensurations in the Charge Density Wave of CeTe_3* ”, Phys. Rev. Lett. **96**, 226401 (2006).
- [183] J. Rouquette, J. Haines, A. Al-Zein, P. Papet, F. Damay, J. Bourgeois, T. Hamouda, F. Doré, A. Maignan, M. Hervieu, et al., “*Pressure-Induced Structural Transition in LuFe_2O_4 : Towards a New Charge Ordered State.*”, Phys. Rev. Lett. **105**, 237203 (2010).
- [184] M. S. Senn, J. P. Wright, and J. P. Attfield, “*Charge order and three-site distortions in the Verwey structure of magnetite*”, Nature **advance online publication** (2011).
- [185] M. Burla, M. Camalli, G. Cascarano, C. Giacovazzo, G. Polidori, R. Spagna, and D. Viterbo, “*SIR88 - a direct-methods program for the automatic solution of crystal structures*”, J. Appl. Cryst. **22**, 389 (1989).
- [186] A. Altomare, G. Cascarano, C. Giacovazzo, A. Guagliardi, M. C. Burla, G. Polidori, and M. Camalli, “*SIR92 - a program for automatic solution of crystal structures by direct methods*”, J. Appl. Cryst. **27**, 435 (1994).

- [187] I. D. Brown and D. Altermatt, “*Bond-valence parameters obtained from a systematic analysis of the Inorganic Crystal Structure Database*”, Acta Cryst. **B41**, 244 (1985).
- [188] Y. Horibe, N. Ikeda, K. Yoshii, and S. Mori, “*Direct observation of low-temperature superstructure in spin- and charge-frustrated ferrite $YFe_2O_{4-\delta}$* ”, Phys. Rev. B **82**, 184119 (2010).
- [189] R. D. Shannon, “*Revised effective ionic radii and systematic studies of interatomic distances in halides and chalcogenides*”, Acta Cryst. **A32**, 751 (1976).
- [190] F. C. Hawthorne, L. Ungaretti, and R. Oberti, “*Site populations in minerals: Terminology and representation of results of crystal-structure refinement*”, The canadian mineralogist **33**, 907 (1995).
- [191] P. M. Woodward and P. Karen, “*Mixed Valence in $YBaFe_2O_5$* ”, Inorganic Chemistry **42**, 1121 (2003).
- [192] J. Garca and G. Subas, “*The Verwey transition - a new perspective*”, Journal of Physics: Condensed Matter **16**, R145 (2004).
- [193] L. J. Zeng, H. X. Yang, Y. Zhang, H. F. Tian, C. Ma, Y. B. Qin, Y. G. Zhao, and J. Q. Li, “*Nonlinear current-voltage behavior and electrically driven phase transition in charge-frustrated $LuFe_2O_4$* ”, EPL (Europhysics Letters) **84**, 57011 (2008).
- [194] C. Li, X. Zhang, Z. Cheng, and Y. Suna, “*Electric field induced phase transition in charge-ordered $LuFe_2O_4$* ”, Appl. Phys. Lett. **93**, 152103 (2008).
- [195] N. Ikeda, M. Kubota, H. Hayakawa, H. Akahama, D. Ohishi, A. Nakanishi, T. Funabiki, Y. Matsuo, N. Kimizuka, T. Kambe, et al., “*Electric Field Response of Stoichiometric $LuFe_2O_4$* ”, Ferroelectrics **414**, 41 (2011).
- [196] S. Cao, J. Li, H. F. Tian, Y. B. Qin, L. J. Zeng, H. X. Yang, and J. Q. Li, “*Nonlinear transport properties and Joule heating effect in charge ordered $LuFe_2O_4$* ”, Appl. Phys. Lett. **98**, 102102 (2011).
- [197] T. Michiuchi, Y. Yokota, T. Komatsu, H. Hayakawa, T. Kuroda, D. Maeda, Y. Matsuo, S. Mori, K. Yoshii, N. Hanasaki, et al., “*Stoichiometric Study of the Dielectric and Magnetic Properties in Charge Frustrated System $LuFe_2O_4$* ”, Ferroelectrics **378**, 175 (2009).

- [198] P. Ren, Z. Yang, W. G. Zhu, C. H. A. Huan, and L. Wang, “*Origin of the colossal dielectric permittivity and magnetocapacitance in LuFe_2O_4* ”, J. Appl. Phys. **109**, 074109 (2011).
- [199] B. Fisher, J. Genossar, L. Patlagan, and G. M. Reisner, “*Electronic transport and I - V characteristics of polycrystalline LuFe_2O_4* ”, J. Appl. Phys. **109**, 084111 (2011).
- [200] K. Yoshii, N. Ikeda, Y. Matsuo, Y. Horibe, and S. Mori, “*Magnetic and dielectric properties of RFe_2O_4 , RFeMO_4 , and RGaCuO_4 ($R = \text{Yb}$ and Lu , $M = \text{Co}$ and Cu)*”, Phys. Rev. B **76**, 024423 (2007).
- [201] A. Kreyssig, S. Chang, Y. Janssen, J. W. Kim, S. Nandi, J. Q. Yan, L. Tan, R. J. McQueeney, P. C. Canfield, and A. I. Goldman, “*Crystallographic phase transition within the magnetically ordered state of $\text{Ce}_2\text{Fe}_{17}$* ”, Phys. Rev. B **76**, 054421 (2007).
- [202] Y. S. Touloukian, *Thermal Expansion, Metallic elements and alloys. Vol.12* (IFI,Plenum, New York, 1975).
- [203] M. Maglione and M. A. Subramanian, “*Dielectric and polarization experiments in high loss dielectrics: A word of caution*”, J. Appl. Phys. **93**, 032902 (2008).
- [204] J. F. Scott, “*Ferroelectrics go bananas*”, Journal of Physics: Condensed Matter **20**, 021001 (2008).
- [205] D.I. and Khomskii, “*Multiferroics: Different ways to combine magnetism and ferroelectricity*”, Journal of Magnetism and Magnetic Materials **306**, 1 (2006).
- [206] K. Yamauchi, T. Fukushima, and S. Picozzi, “*Ferroelectricity in multiferroic magnetite Fe_3O_4 driven by noncentrosymmetric $\text{Fe}^{2+}/\text{Fe}^{3+}$ charge-ordering: First-principles study*”, Phys. Rev. B **79**, 212404 (2009).
- [207] S. Park, Y. Horibe, Y. J. Choi, C. L. Zhang, S.-W. Cheong, and W. Wu, “*Pancake-like Ising domains and charge-ordered superlattice domains in LuFe_2O_4* ”, Phys. Rev. B **79**, 180401 (2009).
- [208] M. Mekata, “*Antiferro-Ferrimagnetic Transition in Triangular Ising Lattice*”, J. Phys. Soc. Jpn. **42**, 76 (1977).
- [209] E. Strykowski and N. Giordano, “*Metamagnetism*”, Adv. Phys. **26**, 487 (1977).

- [210] M. K. Wilkinson, J. W. Cable, E. O. Wollan, and W. C. Koehler, “*Neutron Diffraction Investigations of the Magnetic Ordering in FeBr₂, CoBr₂, FeCl₂, and CoCl₂*”, Phys. Rev. **113**, 497 (1959).
- [211] S. Funahashi, J. Akimitsu, K. Siratori, N. Kimizuka, M. Tanaka, and H. Fujishita, “*Two-Dimensional Spin Correlation in YFe₂O₄*”, J. Phys. Soc. Jpn. **53**, 2688 (1984).
- [212] A. Wills, “*A new protocol for the determination of magnetic structures using simulated annealing and representational analysis (SARAh)*”, Physica B: Condensed Matter **276**, 680 (2000).
- [213] P. Gambardella, S. Rusponi, M. Veronese, S. S. Dhesi, C. Grazioli, A. Dallmeyer, I. Cabria, R. Zeller, P. H. Dederichs, K. Kern, et al., “*Giant Magnetic Anisotropy of Single Cobalt Atoms and Nanoparticles*”, Science **300**, 1130 (2003).
- [214] F. Wilhelm, P. Pouloupoulos, H. Wende, A. Scherz, K. Baberschke, M. Angelakeris, N. K. Flevaris, and A. Rogalev, “*Systematics of the Induced Magnetic Moments in 5d Layers and the Violation of the Third Hund’s Rule*”, Phys. Rev. Lett. **87**, 207202 (2001).
- [215] A. Tanaka, “*Electronic Structure and Phase Transition in V₂O₃: Importance of 3d Spin-Orbit Interaction and Lattice Distortion*”, Journal of the Physical Society of Japan **71**, 1091 (2002).
- [216] P. A. van Aken and B. Liebscher, “*Quantification of ferrous/ferric ratios in minerals: new evaluation schemes of Fe L_{2/3} electron energy-loss near-edge spectra*”, Physics and Chemistry of Minerals **29**, 188 (2002).
- [217] J. P. Crocombette, M. Pollak, F. Jollet, N. Thromat, and M. Gautier-Soyer, “*X-ray-absorption spectroscopy at the FeL_{2,3} threshold in iron oxides*”, Phys. Rev. B **52**, 3143 (1995).
- [218] W. L. Yang, A. P. Sorini, C.-C. Chen, B. Moritz, W.-S. Lee, F. Vernay, P. Olalde-Velasco, J. D. Denlinger, B. Delley, J.-H. Chu, et al., “*Evidence for weak electronic correlations in iron pnictides*”, Phys. Rev. B **80**, 014508 (2009).
- [219] A. Nagano and S. Ishihara, “*Spin-charge-orbital structures and frustration in multiferroic RFe₂O₄*”, Journal of Physics: Condensed Matter **19**, 145263 (2007).

- [220] S. Ishihara and S. Maekawa, “*Theory of Anomalous X-Ray Scattering in Orbital-Ordered Manganites*”, Phys. Rev. Lett. **80**, 3799 (1998).
- [221] C. W. M. Castleton and M. Altarelli, “*Orbital ordering in the manganites: Resonant x-ray scattering predictions at the manganese L_{II} and L_{III} edges*”, Phys. Rev. B **62**, 1033 (2000).
- [222] J. Schlappa, C. Schüssler-Langeheine, C. F. Chang, H. Ott, A. Tanaka, Z. Hu, M. W. Haverkort, E. Schierle, E. Weschke, G. Kaindl, et al., “*Direct Observation of t_{2g} Orbital Ordering in Magnetite*”, Phys. Rev. Lett. **100**, 026406 (2008).
- [223] C. Detlefs, M. S. del Rio, and C. Mazzoli, “*X-ray polarization: General formalism and polarization analysis*”, *arXiv* p. 1106.4446v1 (2011).

Teil I

Appendix



Own contributions to published work

Declaration of own contributions to the first author publications.

- **“Competing Ferri- and Antiferromagnetic Phases in Geometrically Frustrated LuFe_2O_4 ”**

Phys. Rev. Lett. **108**, 037206 (2012) and the corresponding Supplement

J. de Groot, K. Marty, M.D. Lumsden, A.D. Christianson, S.E. Nagler, S. Adiga, W.J.H. Borghols, K. Schmalzl, Z. Yamani, S.R. Bland, R. de Souza, U. Staub, W. Schweika, Y. Su, and M. Angst

Both, the article and its corresponding supplement were written by myself in close cooperation with the co-authors. Apart from the neutron measurements presented in Fig. 4, all measurements and data analysis were done by myself in cooperation with the coworkers mentioned in the paper. The data presented in Fig. 4 was measured by M. Angst, A.D. Christianson, S.E. Nagler, Z. Yamani and M.D. Lumsden at the Chalk River Laboratories.

- **“Charge order in LuFe_2O_4 : an unlikely route to ferroelectricity”**

Phys. Rev. Lett. **108**, 187601 (2012) and the corresponding Supplement

J. de Groot, T. Mueller, R.A. Rosenberg, D.J. Keavney, Z. Islam, J.-W. Kim, and M. Angst

Both, the article and the corresponding supplement were written by me in close cooperation with the co-authors. All measurements and data analysis presented in the manuscript were done by myself in close cooperation with the coworkers mentioned in the paper.

B

List of frequently used symbols and abbreviations

- CO - Charge order
- BVS - Bond-Valence-Sum
- T_{CO} - Charge ordering temperature
- T_N - Néel temperature
- T_{LT} - Low temperature phase transition
- λ - radiation wavelength
- r.l.u. - Relative lattice units
- FM - Ferromagnetic
- fM - Ferrimagnetic
- PS - Phase separated
- AFM - Antiferromagnetic
- H - Magnetic field
- M - Magnetization
- E - Electric Field
- P - Electric polarization
- ξ - Correlation length
- $FWHM$ - Full width at half maximum
- Hex - Hexagonal

ANHANG B. LIST OF FREQUENTLY USED SYMBOLS AND ABBREVIATIONS

- Mon - Monoclinic
- a.u. - Arbitrary units
- \vec{Q} - Scattering vector
- Å- Ångström
- k_i - Incident wave vector
- k_f - Scattered wave vector
- σ - Polarization perpendicular to scattering plane
- π - Polarization inside the scattering plane
- S - Structural hexagonal reflection
- μ_B - Bohr magneton
- emu - Electromagnetic units
- LCP - Left circular polarized light
- RCP - Right circular polarized light
- XMCD - X-ray magnetic circular dichroism
- RT - Room temperature



Relation between $R\bar{3}m(h)$ and $C2/m$ symmetry

It is important to find the right $(h\ k\ \ell)$ -transformation rules between the normal cell in hexagonal setting and the super-cell. It is possible to represent the space group $R\bar{3}m$ by a subgroup with lower symmetry. This $C2/m$ cell already used in [93, 183], and its primitive cell, can fully describe the ground-state antiferroelectric charge order as well as the alternative ferroelectric charge order supposed in [85]. The transformation matrix in Eq.(C.1) between the rhomboidal space group $R\bar{3}m$ (N° 166) and the possible monoclinic $C2/m$ subgroup (N° 12) (describing the charge order) in relation to the hexagonal lattice vectors¹.

$$\mathbf{M} = \begin{pmatrix} 1 & 3 & -1/3 \\ -1 & 3 & 1/3 \\ 0 & 0 & -2/3 \end{pmatrix} \quad (\text{C.1})$$

The monoclinic lattice vectors are then explained by the hexagonal lattice vectors through the following equations:

$$\vec{a}_{mon} = \mathbf{M} \cdot (\mathbf{R} \cdot \vec{a}_{hex}) \quad (\text{C.2})$$

$$\vec{b}_{mon} = \mathbf{M} \cdot (\mathbf{R} \cdot \vec{b}_{hex}) \quad (\text{C.3})$$

$$\vec{c}_{mon} = \mathbf{M} \cdot (\mathbf{R} \cdot \vec{c}_{hex}) \quad (\text{C.4})$$

The additional transformation matrix \mathbf{R} addresses according to Fig. C.1 the two other domains with their particular rotation of $\Delta\omega = \pm 120^\circ$ in the (a,b)-plane. As a result from this multiplication we obtain the monoclinic vectors described in hexagonal unit vectors:

$$\vec{a}_{mon} = \begin{pmatrix} 1 \\ -1 \\ 0 \end{pmatrix}, \vec{b}_{mon} = \begin{pmatrix} 3 \\ 3 \\ 0 \end{pmatrix} \quad \text{with} \quad \vec{c}_{mon} = \begin{pmatrix} -1/3 \\ 1/3 \\ -2/3 \end{pmatrix} \quad (\text{C.5})$$

¹This lattice vectors are: $\vec{a}_{hex} = (1, 0, 0)$, $\vec{b}_{hex} = (0, 1, 0)$ and $\vec{c}_{hex} = (0, 0, 1)$ with $\angle(\vec{a}_{hex}, \vec{b}_{hex}) = 120^\circ$.

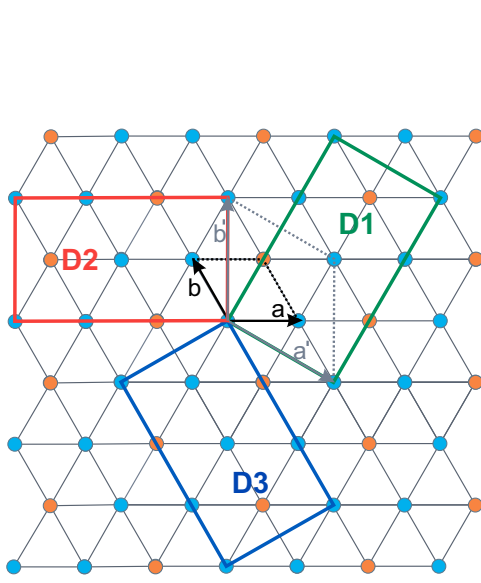


Abbildung C.1: The transformation between the hexagonal cell in black and the three monoclinic domains (D1, D2 and D3) in the a, b -plane. For clarity also the $\sqrt{3} \times \sqrt{3}$ cell used in previous work [1] is indicated in gray.

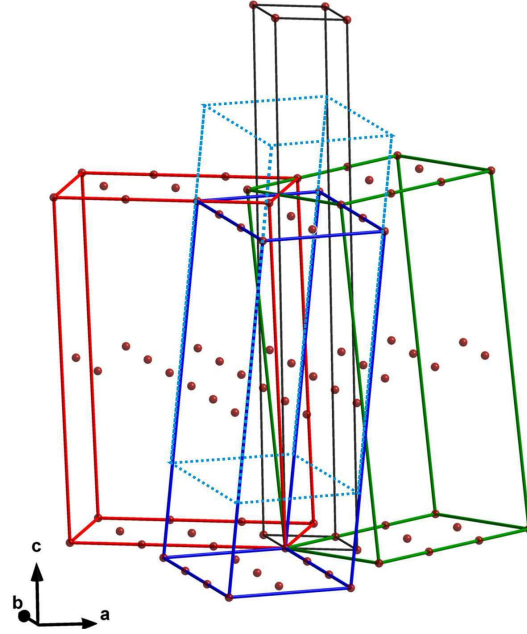


Abbildung C.2: Relation between the hexagonal lattice and the three monoclinic domains (only Lu Atoms are presented). The final domains positions are achieved by shifting them $1/4$ along the c lattice direction as indicated for the domain D3 by dotted lines the others shifted domains are omitted for clarity.

From these vectors it is easy to produce the monoclinic lattice vectors in Cartesian coordinates by using the hexagonal vectors in Cartesian coordinates². From this Cartesian lattice vectors describing the monoclinic cell, we can calculate the monoclinic lattice vectors in Eq.(C.6):

$$\vec{a}_{mon}^* = \begin{pmatrix} (3/2)a_{hex} \\ -(\sqrt{3}/2)a_{hex} \\ 0 \end{pmatrix}, \vec{b}_{mon}^* = \begin{pmatrix} (3/2)a_{hex} \\ (3\sqrt{3}/2)a_{hex} \\ 0 \end{pmatrix} \quad \text{and} \quad \vec{c}_{mon}^* = \begin{pmatrix} -(1/2)a_{hex} \\ (\sqrt{3}/6)a_{hex} \\ -(2/3)c_{hex} \end{pmatrix} \quad (\text{C.6})$$

The corresponding lattice parameters for the monoclinic cell are $|\vec{a}_{mon}| = \sqrt{3}a_{hex} = 5.959(1)\text{\AA}$, $|\vec{b}_{mon}| = 3a_{hex} = 10.321(1)\text{\AA}$ and $|\vec{c}_{mon}| = \sqrt{\frac{a_{hex}^2}{3} + \frac{4c_{hex}^2}{9}} = 16.959(1)\text{\AA}$ and a monoclinic distortion of $\beta = 96.72^\circ$. The corresponding reciprocal lattice is calculated according to Eq.(7.2). Each point in reciprocal space is described by different sets of (h, k, ℓ) from the

²The hexagonal lattice vectors in Cartesian coordinates: $\vec{a}_{hex} = (a, 0, 0)$, $\vec{b}_{hex} = (-a/2, \sqrt{3}a/2, 0)$ and $\vec{c}_{hex} = (0, 0, c)$.

hexagonal unit cell and the monoclinic cell with the following transformation between both descriptions:

$$h_{mon} \cdot \vec{a}_{mon}^* + k_{mon} \cdot \vec{b}_{mon}^* + \ell_{mon} \cdot \vec{c}_{mon}^* = h_{hex} \cdot \vec{a}_{hex}^* + k_{hex} \cdot \vec{b}_{hex}^* + \ell_{hex} \cdot \vec{c}_{hex}^* \quad (C.7)$$

By solving Eq.(C.7) the transformation rules presented in Tab. C.1 are achieved for the relationship between the hexagonal cell and the three monoclinic domains.

Tabelle C.1: Transformation rules for the (h, k, ℓ) between the hexagonal and monoclinic unit cell with its three different domains $D1_{0^\circ}$, $D2_{120^\circ}$ and $D3_{-120^\circ}$.

	$D1_{0^\circ}$	$D2_{120^\circ}$	$D3_{-120^\circ}$
$h_{mon} =$	$h_{hex} - k_{hex}$	$3(h_{hex} + k_{hex})$	$-4h_{hex} - 2k_{hex}$
$k_{mon} =$	$3(h_{hex} + k_{hex})$	$-4h_{hex} - 2k_{hex}$	$h_{hex} - k_{hex}$
$\ell_{mon} =$	$\frac{1}{3}(-h_{hex} + k_{hex} - 2\ell_{hex})$	$\frac{1}{3}(-h_{hex} + k_{hex} - 2\ell_{hex})$	$\frac{1}{3}(-h_{hex} + k_{hex} - 2\ell_{hex})$



Refinement of the 210 K data in Cm symmetry

The refinement in Cm symmetry.

Tabelle D.1: Refined atomic parameters (positions and thermal displacement parameters) for LuFe_2O_4 at 210 K for the single domain crystal in monoclinic Cm symmetry.

Atom	(Wyc)	U_{11}	U_{22}	U_{33}	U_{23}	U_{13}	U_{12}
Lu01	2a	.0327(5)	.0262(5)	.0334(5)	.000	.0084(3)	.000
Lu02	2a	.0321(5)	.0243(4)	.0373(4)	-.00024(10)	.0031(2)	-.0006(13)
Lu03	4b	.0278(5)	.0225(4)	.0301(4)	-.00040(9)	.0035(2)	-.0006(13)
Lu04	4b	.0321(5)	.0241(4)	.0292(4)	-.00041(11)	.0027(2)	-.0006(13)
Fe01	2a	.0370(12)	.0339(11)	.0243(10)	.000	.0036(8)	.000
Fe02	4b	.0243(12)	.0348(21)	.0224(12)	.000	.0028(5)	.000
Fe03	2a	.0322(20)	.0259(20)	.0293(11)	.000	.0011(3)	.000
Fe04	4b	.0311(11)	.0254(19)	.0245(11)	.000	.0079(12)	.000
Fe05	2a	.0298(09)	.0316(08)	.0312(09)	.000	.0065(12)	.000
Fe06	4b	.0263(10)	.0371(13)	.0311(14)	.000	.0070(12)	.000
Fe07	2a	.0331(13)	.0299(13)	.0295(09)	.000	.0061(12)	.000
Fe08	4b	.0372(07)	.0331(11)	.0261(17)	.000	.0063(12)	.000

ANHANG D. REFINEMENT OF THE 210 K DATA IN Cm SYMMETRY

Tabelle D.2: Refined atomic parameters (positions and thermal displacement parameters) for LuFe_2O_4 at 210 K for the single domain crystal in monoclinic Cm symmetry.

Atom	(Wyc)	x	y	z	U_{Iso}
Lu01	2a	0.90009(16)	0	-0.24093(10)	ATP
Lu02	2a	1.40156(16)	0	-0.72147(10)	ATP
Lu03	4b	1.39844(14)	-0.33306(12)	-0.74076(8)	ATP
Lu04	4b	1.39765(11)	-0.16782(11)	-0.23159(5)	ATP
Fe01	2a	1.0149(10)	0	-0.9093(5)	ATP
Fe02	4b	1.0062(7)	-0.1682(3)	-0.4122(3)	ATP
Fe03	2a	1.2919(11)	0	-1.0537(6)	ATP
Fe04	4b	1.2875(8)	-0.1689(3)	-0.5568(3)	ATP
Fe05	2a	1.0049(9)	-1/2	-0.4085(5)	ATP
Fe06	4b	1.5062(7)	-0.1641(3)	-0.9093(3)	ATP
Fe07	2a	1.7927(9)	0	-0.5586(5)	ATP
Fe08	4b	1.7918(8)	-0.1654(3)	-1.0548(3)	ATP
O01	2a	1.356(4)	0	-0.9307(14)	0.011(4)
O02	4b	0.841(3)	-0.3453(12)	-0.4361(9)	0.009(3)
O03	2a	1.461(3)	0 -0.566(1)	0.013(4)	0.008(3)
O04	2a	1.245(4)	0	-1.1695(17)	0.011(5)
O05	2a	1.763(4)	0	-0.6746(16)	0.009(5)
O06	4b	1.243(4)	-0.1753(15)	-0.6755(12)	0.015(4)
O07	4b	1.753(3)	-0.1625(12)	-1.1712(10)	0.009(3)
O08	4b	1.474(3)	-0.1767(17)	-1.0441(12)	0.014(5)
O09	4b	0.949(3)	-0.1629(15)	-0.5439(12)	0.015(4)
O10	2a	0.949(4)	0	-1.0375(15)	0.011(5)
O11	2a	1.059(3)	0	-0.7957(12)	0.010(4)
O12	4b	1.048(3)	-0.1708(12)	-0.2944(10)	0.009(4)
O13	4b	1.324(2)	-0.3189(14)	-0.9225(8)	0.013(3)
O14	2a	1.309(3)	-1/2	-0.4331(12)	0.009(3)
O15	2a	1.033(4)	-1/2	-0.2970(16)	0.014(4)
O16	4b	1.535(3)	-0.1574(12)	-0.7965(10)	0.015(3)



Spin structure candidates

In this Appendix the PYTHON program searching for the candidate spin structures is presented.

E.1 Selection of candidate spin structures

```
import sys
import cmath

#Atomic positions:

p1x = 0.8598
p1y = 0.83106
p1z = 0.0721+0.25
p2x = 0.8553
p2y = 0.5
p2z = 0.07430+0.25
p3x = 0.8598
p3y = 0.16894
p3z = 0.0721+0.25

p4x = -0.3566
p4y = -0.16483
p4z = 0.42689+0.25
p5x = -0.3617
p5y = 0.5
p5z = 0.42744+0.25
p6x = -0.3566
p6y = 0.16483
p6z = -0.57311+0.25

p7x = 0.8617
p7y = 1.0
p7z = 0.57256+0.25
p8x = 0.8566
p8y = 0.66483
p8z = 0.57311+0.25
p9x = 0.8566
p9y = 0.33517
p9z = 0.57311+0.25

p10x = 0.6447
p10y = 0.0
p10z = 0.9257+0.25
p11x = 0.6402
p11y = 0.66894
p11z = 0.9279+0.25
p12x = 0.6402
p12y = 0.33106
p12z = 0.9279+0.25

count = 1
Pi = cmath.pi

#Calculate Intensity for (h,k,l)-reflection in monoclinic notation:

def Inthkl(h,k,l)
    test1 = a1 cmath.exp(1j 2 Pi (p1x h + p1y k + p1z l)) + a2 cmath.exp(1j 2 Pi (p2x h + p2y k + p2z l))
    test2 = a3 cmath.exp(1j 2 Pi (p3x h + p3y k + p3z l)) + a4 cmath.exp(1j 2 Pi (p4x h + p4y k + p4z l))
    + a5 cmath.exp(1j 2 Pi (p5x h + p5y k + p5z l)) + a6 cmath.exp(1j 2 Pi (p6x h + p6y k + p6z l))
    test3 = a7 cmath.exp(1j 2 Pi (p7x h + p7y k + p7z l)) + a8 cmath.exp(1j 2 Pi (p8x h + p8y k + p8z l))
    test4 = a9 cmath.exp(1j 2 Pi (p9x h + p9y k + p9z l)) + a10 cmath.exp(1j 2 Pi (p10x h + p10y k + p10z l))
```

ANHANG E. SPIN STRUCTURE CANDIDATES

```
+ a11 cmath.exp(1j 2 Pi (p11x h + p11y k + p11z l)) + a12 cmath.exp(1j 2 Pi (p12x h + p12y k + p12z l))
zusammen = test1 + test2 + test3 + test4
Int = zusammen.real +zusammen.imag +zusammen.imag
return Int

def Intnorm(h,k,l):
    if Inthkl(0,2,0)>0.0:
        Intnorm = Inthkl(h,k,l) / Inthkl(0,2,0)    16.0
    else:
        Intnorm = 0.0
    return Intnorm
a1, a2, a3, a4 , a5, a6 ,a7 ,a8 a9, a10, a11, a12

summ=0
f=open('/home/joost/work', 'w')
for a1 in range(-1,2):
    for a2 in range(-1,2):
        for a3 in range(-1,2):
            for a4 in range(-1,2):
                for a5 in range(-1,2):
                    for a6 in range(-1,2):
                        for a7 in range(-1,2):
                            for a8 in range(-1,2):
                                for a9 in range(-1,2):
                                    for a10 in range(-1,2):
                                        for a11 in range(-1,2):
                                            for a12 in range(-1,2):
                                                summ = a1 + a2 + a3 + a4 + a5 + a6 + a7 + a8 + a9 + a10 + a11 + a12
                                                abssumm = abs(a1) + abs(a2) + abs(a3) + abs(a4) + abs(a5) + abs(a6)
                                                    + abs(a7) + abs(a8) + abs(a9) + abs(a10) + abs(a11) + abs(a12)
                                                if abs(summ) <= 12:
#Restrictions for AFM:
                                if Intnorm(0,2,-2) > 5.5:
                                    if Intnorm(0,2,-2) < 6.5:
                                        if Intnorm(0,2,4) > 0.8:
                                            if Intnorm(0,2,4) < 1.2 :
                                                if abssumm >= 0 and <=12:
                                                    if Intnorm(0,2,-1) < 8 and Intnorm(0,2,-3) < 3 and Intnorm(0,2,-5) < 6:
                                                        if Intnorm(1,3,-5) < 5 and Intnorm(1,3,3)<5:
                                                            if 2 Intnorm(-1,-3,0)<Intnorm(-1,-3,-2) and 5 Intnorm(-1,-3,0)>Intnorm(-1,-3,-2)
                                                                and Intnorm(-1,-3,-2) > 0.1 and Intnorm(-1,-3,0) > 0.1:
                                                                    if Intnorm(0,2,0)>1 Intnorm(-1,-3,-2):
#Restrictions for fM:
                                if Intnorm(0,2,-1) < 8 and Intnorm(0,2,-3) < 3 and Intnorm(0,2,-5) < 6:
                                    if Intnorm(1,3,-5) < 5 and Intnorm(1,3,3)<5:
                                        if 2 Intnorm(-1,-3,0)<Intnorm(-1,-3,-2) and 5 Intnorm(-1,-3,0)>Intnorm(-1,-3,-2)
                                            and Intnorm(-1,-3,-2) > 0.1 and Intnorm(-1,-3,0) > 0.1:
                                                if Intnorm(0,2,0)>1 Intnorm(-1,-3,-2):
#Output of candidates:
                                f.writelines(" (a1,a2,a3,a4,a5,a6,a7,a8,a9,a10,a11,a12,summ))
                                print (count, summ,Intnorm(1,3,-4))
                                count+=1
```

Spin structure refinements

In this Appendix the refinements for the candidate spin structures achieved from the program presented in App. E.1 are presented for both magnetic phases.

F.1 Refinements of the fM structure proposed in [1]

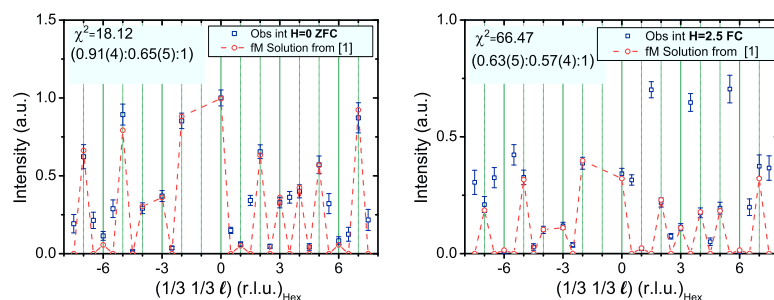


Abbildung F.1: Observed structure factors against calculated ones for both magnetic phases from the model proposed in [1].

F.2 Refinements of candidate fM spin structures

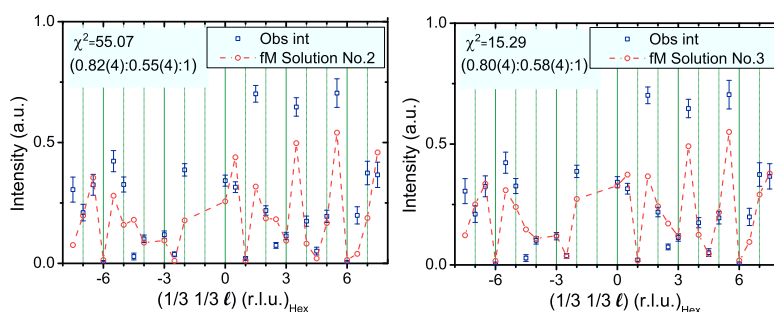


Abbildung F.2: Observed structure factors in the high- H phase at 220 K against calculated ones from different models.

F.3 Refinements of candidate AFM spin structures

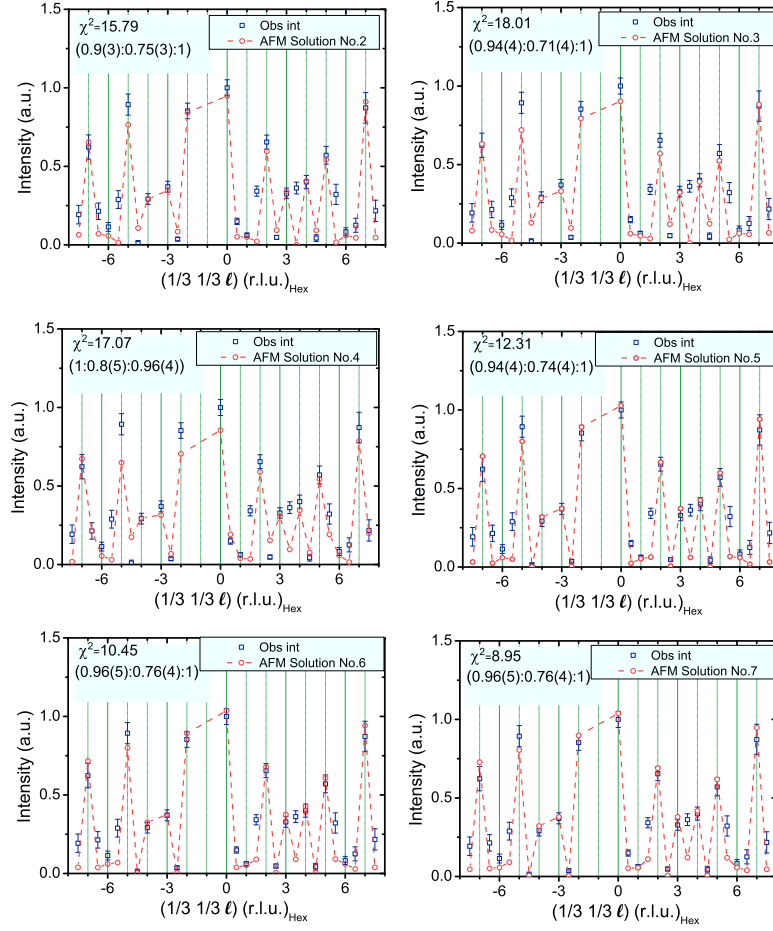


Abbildung F.3: Observed structure factors in the low- H phase at 220 K against calculated ones from different models.



Eidesstattliche Versicherung

Ich erkläre hiermit an Eides Statt, dass ich die vorliegende Arbeit ohne unzulässige Hilfe Dritter und ohne Benutzung anderer als der angegebenen Hilfsmittel angefertigt habe. Die aus anderen Quellen direkt oder indirekt übernommenen Daten und Konzepte sind unter Angabe der Quelle gekennzeichnet.

Die Arbeit wurde bisher weder im In- noch im Ausland in gleicher oder ähnlicher Form einer anderen Prüfungsbehörde vorgelegt.

Ort, Datum

Unterzeichner

Lebenslauf

Joost de Groot

Geburtsdatum / Ort: 14. Mai 1981 / Nordhorn

Nationalität: niederländisch

28. Juni 2012 Tag der mündlichen Prüfung

13. März 2012 Abgabe der Dissertation

**Oktober 2008
bis März 2012** Dissertation am Peter Grünberg Institut 4 des Forschungszentrums Jülich GmbH / RWTH-Aachen
Prof. Dr. M. Angst
Thema der Arbeit:
„Charge, spin and orbital order in the candidate multiferroic material LuFe_2O_4 “

**Oktober 2002
bis Juni 2008** Studium der Physik an der RWTH-Aachen
Diplomarbeit in Physik am Peter Grünberg Institut 4 des Forschungszentrums Jülich GmbH
Prof. Dr. Th. Brückel
Thema der Arbeit: „Strukturelle und magnetische Ordnung in multiferroischem TbMnO_3 , Untersuchungen an Dünnschichten und Einkristallen“

**August 1999
bis Juli 2002** Abitur
Technisches Gymnasium Nordhorn